NOTICE

The quality of this microform is heavily dependent upon the quality of the original thesis submitted for microfilming. Every effort has been made to ensure the highest quality of reproduction possible.

If pages are missing, contact the university which granted the degree.

Some pages may have indistinct print especially if the original pages were typed with a poor typewriter ribbon or if the university sent us an inferior photocopy.

Reproduction in full or in part of this microform is governed by the Canadian Copyright Act, R.S.C. 1970, c. C-30, and subsequent amendments.

AVIS

La qualité de cette microforme dépend grandement de la qualité de la thèse soumise au microfilmage. Nous avons tout fait pour assurer une qualité supérieure de reproduction.

S'il manque des pages, veuillez communiquer avec l'université qui a conféré le grade.

La qualité d'impression de certaines pages peut laisser à désirer, surtout si les pages originales ont été dactylographiées à l'aide d'un ruban usé ou si l'université nous a fait parvenir une photocopie de qualité inférieure.

La reproduction, même partielle, de cette microforme est soumise à la Loi canadienne sur le droit d'auteur, SRC 1970, c. C-30, et ses amendements subséquents.

Gravity and Magnetic Interpretation of the Kapuskasing Structural Zone in the Val Rita and Groundhog River Blocks Northwestern Ontario, Canada

by

Estella Akweseh Nkwate

Submitted in partial fulfillment of the requirements
for the degree of Doctor of Philosophy

at

Dalhousie University
Halifax, Nova Scotia
December, 1990

ISBN 0-315-64500-8

DALHOUSIE UNIVERSITY

FACULTY OF GRADUATE STUDIES

The undersigned hereby certify that they have read and recommend to the Faculty of Graduate Studies for acceptance a thesis entitled " Gravity and Magnetic Interpretation of the Kapuskasing Structural Zone in the Val Rita and Groundhog River Blocks, Northwestern Ontario, Canada"

by Estella Akwesh Nkwate

in partial fulfillment of the requirements for the degree of Doctor of Philosophy.

Dated December 3, 1998

External Examiner

Research Supervisor

Examining Committee

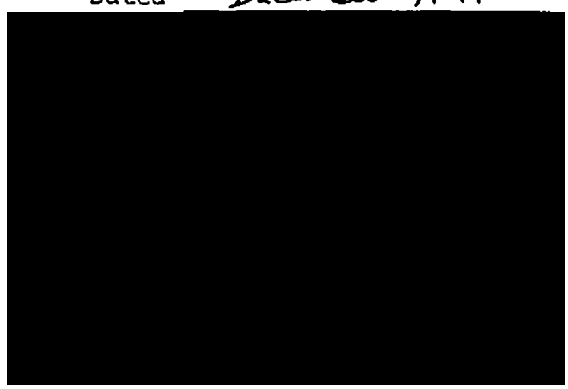

DALHOUSIE UNIVERSITY

Date December 1, 1990

Author Estella Akweseh Nkwate

Title Gravity and Magnetic Interpretation of the Kapuskasing Structural Zone in the Val Rita and Groundhog River Blocks Northwestern Ontario, Canada

Department or School Geology

Degree: PhD Convocation February Year 1991

Permission is herewith granted to Dalhousie University to circulate and to have copied for non-commercial purposes, at its discretion, the above title upon the request of individuals or institutions.

[redacted]

Signature of Author

This dissertation is dedicated to my father for giving me the opportunity to dream, and for ensuring that my dreams come true. To God Almighty, for providing me with the strength to complete this work.

TABLE OF CONTENTS

PAGE #

TABLE OF CONTENTS

PAGE #

TABLE OF CONTENTS

PAGE #

LIST OF FIGURES

PAGE #

LIST OF FIGURES

Page #

LIST OF FIGURES

Page #

LIST OF FIGURES

Page #

LIST OF TABLES

ABSTRACT

The Kapuskasing Structural Zone (KSZ) in Ontario consists of four separate tectonic blocks with distinctive gravity and magnetic anomalies. From south to north, these include the Chapleau Block (CB), the Groundhog River Block (GRB), the Val Rita Block (VRB) found west of the GRB and the Fraserdale-Moosonee Block (FMB). Previous gravity studies, based on sparse data coverage, failed to satisfactorily explain the cause of the potential field anomalies within the VRB and the GRB in the central portion of the KSZ. Hence, a detailed gravity survey was conducted over the VRB and GRB in order to constrain interpretations of deep crustal structure based on seismic, geologic and physical properties data.

Gravity and magnetic models across the VRB suggest that uplift of dense granulites from depths of 10-25 km to shallow levels of the crust is responsible for the gravity anomaly observed over this block. These granulites are generally not exposed but are buried underneath a thin veneer of amphibolite facies tonalite gneiss. Furthermore, the models suggest that the crust is 48-50 km thick beneath the VRB and its associated gravity high compared to 40-43 km beneath adjacent areas.

Model results from the GRB suggest that the granulites associated with the GRB must be thin (1-4 km, increasing in thickness from north to south). Although magnetic susceptibilities are variable throughout this block, magnetic modelling indicates that they are sufficient to account for the strong magnetic anomaly associated with the block. Model results from the CB are consistent with previous results (e.g., Percival and Card, 1983) and indicate that uplift of dense granulites from depths of 15-30 km is responsible for its high gravity anomaly. A thick crust of 52 km underlies the CB and is also coincident with the region of high gravity anomaly.

The VRB is interpreted as a broad, southerly plunging antiform and the GRB as a thin thrust sheet. Arching within the VRB was caused by ramping and was probably coeval with thrusting in the GRB. The interpreted geometries of antiformal folding and thrusting within the VRB and GRB are analogous to the geometry of the Limpopo Belt of Southern Africa. The CB is interpreted as a west dipping slab consistent with previous interpretations, and is analogous to the Boothia Uplift in arctic Canada. The interpreted structures of the KSZ are similar to those in fold and thrust belts.

LIST OF ABBREVIATIONS

2D	Two-dimensional
3D	Three-dimensional
AB	Abitibi Belt
AGC	Atlantic Geoscience Centre
BU	Boothia Uplift
CB	Chapleau Block
FMB	Fraserdale Moosonee Block
GRB	Groundhog River Block
GSC	Geological Survey of Canada
IGRF	International Geomagnetic Reference Field
ILCZ	Ivanhoe Lake Cataclastic Zone
ILF	Ivanhoe Lake Fault
KSZ	Kapuskasing Structural Zone
KU	Kapuskasing Uplift
KZ	Kapuskasing Zone
LB	Limpopo Belt
LF	Lepage Fault
MB	Michipicoten Belt
MT	Magnetotelluric
QB	Quetico Belt
SLF	Saganash Lake Fault
SLMV	Saganash Lake Metavolcanic Belt
VRB	Val Rita Block
WGT	Wawa Gneiss Terrane
WR	Wind River
WRF	Wakusimi River Fault

ACKNOWLEDGEMENTS

I would like to thank my supervisor, Dr. Matthew Salisbury, for accepting me as his student, proposing this project, and for his encouragement towards the completion of this study. Appreciation is also expressed to the other members of my supervisory committee, for their excellent supervision during the course of this study.

I was fortunate to have had the opportunity of working at the Atlantic Geoscience Centre, initially under the supervision of Dr. John Woodside and later on under Dr. Jacob Verhoef and Dr. Walter Roest. I shall forever be grateful to them for teaching me much about the processing of potential filed data and for their patience and valuable guidance during this study. Appreciation is also expressed to all the staff of the Regional Reconnaissance Division, especially to G. Bassi, C. Currie, F. Marillier, K. Usow, G. Oakey, S. Srivastava, K. Shih, S. Levesque, P. Girouard, R. Macnab and S. Perry for providing me with a friendly atmosphere to work in.

Interpretations of the structures were developed through useful discussions with Dr. Nick Culshaw and Alan Leclair. Special thanks are expressed to Dr. Pat Ryall and his family, for their love, friendship and support during my stay in Halifax. My stay in Halifax would not have been the same without friends like Nigel and Pauline Kemp (my host family), Kimberley Jenner and Joe and Mercy Umoh. I would also like to thank Alice Giddy, Isaac, Valentine, Bindzile, Nellie and Judy, for helping out with baby sitting.

Finally, I wish to thank my family, especially my husband for giving me the love and encouragement that I needed; and my son, for being a source of joy and comfort to me during the difficult times. Sincere appreciation is also expressed to my mother-in-law, Elizabeth Atekwana, and sister-in-law, Patricia Atekwana, for their support and help with the baby and to my mother, for all her moral support and encouragement. I shall forever be indebted to Carmelita Fisher for her support and for helping with the typing and arrangement of the final draft of this dissertation.

I wish to acknowledge financial support from the Dalhousie University Fellowship program.

CHAPTER ONE: INTRODUCTION

The Kapuskasing Structural Zone (KSZ) is a linear, northeast trending belt of high grade metamorphic rocks located within the central Archean Superior Province of the Canadian Shield (Figure 1-1). Characterized by high gravity and magnetic anomalies (Garland, 1950; Innes, 1960; Bennett et al., 1967; Maclaren et al., 1968), it extends northward about 500 km from Lake Superior into James Bay, transecting the predominant east-west structural trends of the metavolcanic and metasedimentary plutonic belts of the Archean Superior Province (Card and Ciesielski, 1986; Figure 1-1). For the most part, the KSZ is bounded to the east by a major shear zone, the Ivanhoe Lake Cataclastic Zone (ILCZ) and to the west by several normal faults (Figure 1-2) (Percival and Card, 1983, 1985).

The KSZ consists of four fault-bounded tectonic blocks with distinct lithology, internal structure and geophysical characteristics (Percival and McGrath, 1986; Leclair, 1990). From south to north the blocks are: the Chapleau Block (CB), the Groundhog River Block (GRB), the Val Rita Block (VRB) which lies west of the GRB and the Fraserdale-Moosonee Block (FMB) (Figure 1-2). Previous geological and recent LITHOPROBE studies have concentrated on the CB. These studies have demonstrated that the high gravity anomaly and anomalously high seismic velocities underneath the core of this block are caused by the uplift of high density rocks from lower crustal depths to the surface. As a result of these studies, the deep crustal structure of the CB is better defined than that of the other blocks. On the contrary,

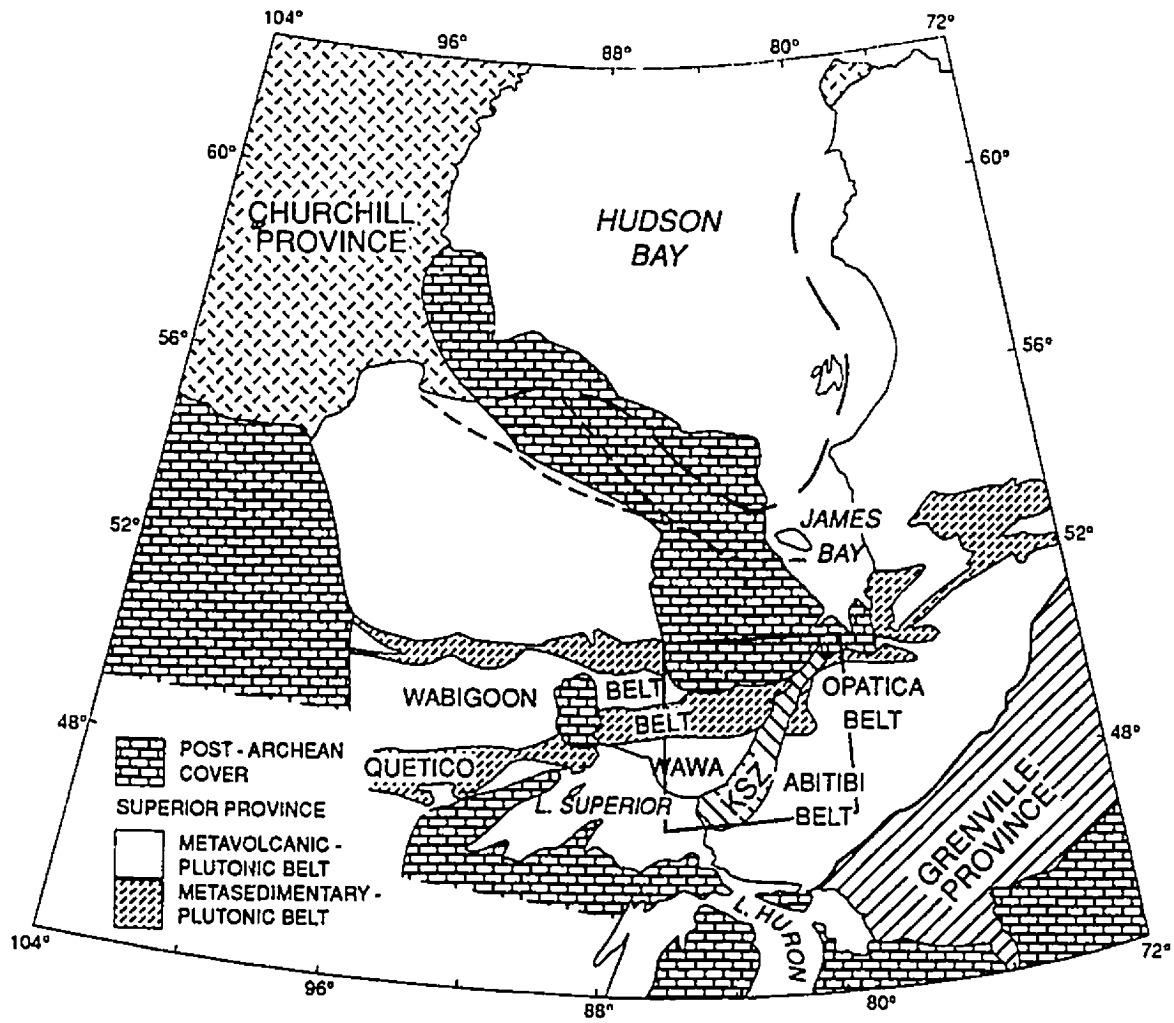

Figure 1-1. Location of the Kapuskasing Structural Zone (KSZ) within the Canadian Shield. Rectangular block shows the location area for Figures 1-2 and 2-1 (From Percival and McGrath, 1986).

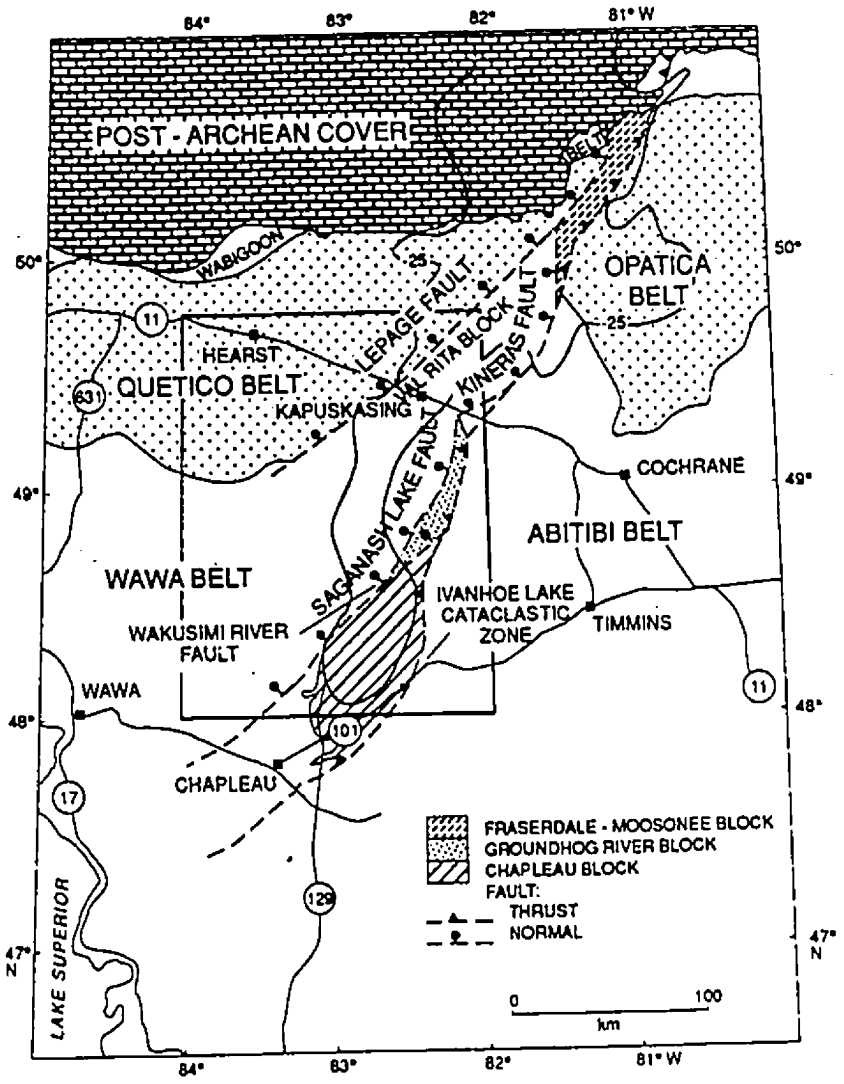

Figure 1-2. Map showing the different tectonic blocks of the KSZ. The regional gravity high is outlined by the -25 mGal Bouguer anomaly contour. Rectangular block shows the location area for Figures 3-3 and maps discussed in chapter 4 (from Leclair and Nagerl, 1988).

contrary, the VRB and GRB, which make up the central part of the KSZ are poorly understood, partly due to sparse rock exposure and partly because of limited geological and geophysical mapping. Consequently, their deep crustal structure remains relatively unknown. Previous studies (Percival and McGrath, 1986) identified several problems which could not be resolved within this central portion of the KSZ because the limited geophysical data available does not correlate with the geology. For example, the high gravity anomaly which coincides with dense granulite facies rocks in most of the other blocks of the KSZ is absent within the GRB; instead a strong aeromagnetic anomaly which is only subtle in the other blocks, is present within this block. Furthermore, the CB gravity anomaly extends into the VRB, which is characterized by lower density, amphibolite facies rocks. These disparities in the geophysical characteristics of the blocks raise questions concerning the structure of the GRB and VRB at depth and their relationship to the CB.

Therefore, this study was initiated as part of a multidisciplinary investigation of the KSZ to determine the deep crustal structure of the central KSZ. The primary objectives of this study are thus:

1) to determine the deep crustal structure of the VRB and GRB,
2) to determine the relationships between these blocks and the CB, and
3) to provide insight into the structural evolution of the KSZ and the role of the VRB and GRB in this evolution.

Achievement of these objectives will involve the following:

1) the collection of detailed gravity data for the GRB, VRB and northern CB,
2) modelling the boundary faults to obtain their geometry at depth,
3) modelling the depth and shape of the Moho beneath the KSZ as a means of substantiating the refraction and reflection results,
4) comparing the gravity and magnetic signatures with different structural elements found in the area, and
5) relating the field geology and geobarometric data to potential field and seismic data in order to provide structural interpretations for the different tectonic blocks.

In this study, gravity and magnetic modelling constrained by refraction and reflection results is thus combined with geology to develop crustal models for the different tectonic blocks of the central KSZ and to provide interpretations and insights into the structural evolution of the KSZ as a whole.

CHAPTER TWO: GEOLOGICAL AND GEOPHYSICAL SETTING

2.1 GEOLOGICAL SETTING

The Superior Province, which hosts the KSZ, represents the nucleus of the North American continental craton and contains the world's largest continuous area of exposed Precambrian rocks. It is made up of a complex of igneous and metamorphic rocks, consisting mainly of granitoid gneisses and plutons and preserved east-west striking greenstone belts of metamorphosed and deformed volcanic and sedimentary rocks (Goodwin, 1972; Percival and Card, 1983). These greenstone belts, with metavolcanic subprovinces, contain most of the mineral deposits for which the Superior Province is known. The continuity of the east-west structural grain of the Superior Province is interrupted by the northeast trending KSZ (Figure 1-2; Thurston et al., 1977; Gibb, 1978; Card, 1979), a zone of high grade metamorphic rocks separating the Abitibi and Wawa metavolcanic-plutonic belts in the south, and the Quetico and Opatica metasedimentary-plutonic belts in the north (Bennett et al., 1967). The region defined by the Kapuskasing gravity anomaly (the -25 mGal contour in Figure 1-2) is wide in the north (about 240 km) and narrows to the south (about 50 km). The abrupt change in width of this anomaly coincides approximately with the boundary between the Wawa and Quetico belts to the west and the Abitibi and Opatica belts to the east (Gibb, 1978).

Granulite facies metamorphic rocks, high geobarometric pressures (7-9 kbars) (Percival and McGrath, 1986; Leclair, 1990), high densities (average of 2.9 g/cm^3),

high magnetic susceptibilities and high seismic velocities (6.6 km/s) (Boland and Ellis, 1989; Fountain et al., 1990) are common within the core of the KSZ. The strong contrast in physical properties between the Kapuskasing related-rocks and the adjacent belts gives rise to prominent gravity, magnetic and seismic anomalies which have been especially useful in outlining the limits of this zone. Percival and McGrath (1986), have determined the formation pressures for the various lithologies within the KSZ based on the geobarometry of metamorphic assemblages. In the south of the mapped region (Figure 2-1) a traverse from west to east shows a progressive increase in paleopressures and metamorphic grade from 2-3 kbars in the low grade greenschist facies rocks of the Michipicoten Belt (MB), through 4-6 kbars in the amphibolite facies rocks of the Wawa Gneiss Terrane (WGT), to 7-9 kbars in the high grade upper amphibolite to granulite facies rocks of the KSZ. The Ivanhoe Lake Cataclastic Zone marks an abrupt return to lower pressures (2-3 kbars) and lower grade rocks (greenschist to lower amphibolite facies) of the Abitibi greenstone belt (AB) to the east (Percival and Card, 1983; 1985). These results suggest a difference in formational level of about 20 km between the MB and the KSZ due to thrusting (Percival and Krogh, 1983). The above transition from low grade to high grade rocks has been interpreted as an oblique cross section through the upper two thirds of the crust (Percival and Card, 1983; Percival and Fountain, 1989). The amphibolite/granulite transition which represents the boundary between the WGT and the KSZ corresponds to an increase in seismic velocities of between 0.2 to 0.3 km/s (Fountain and Salisbury, 1986; Fountain et al., 1990), and an average increase

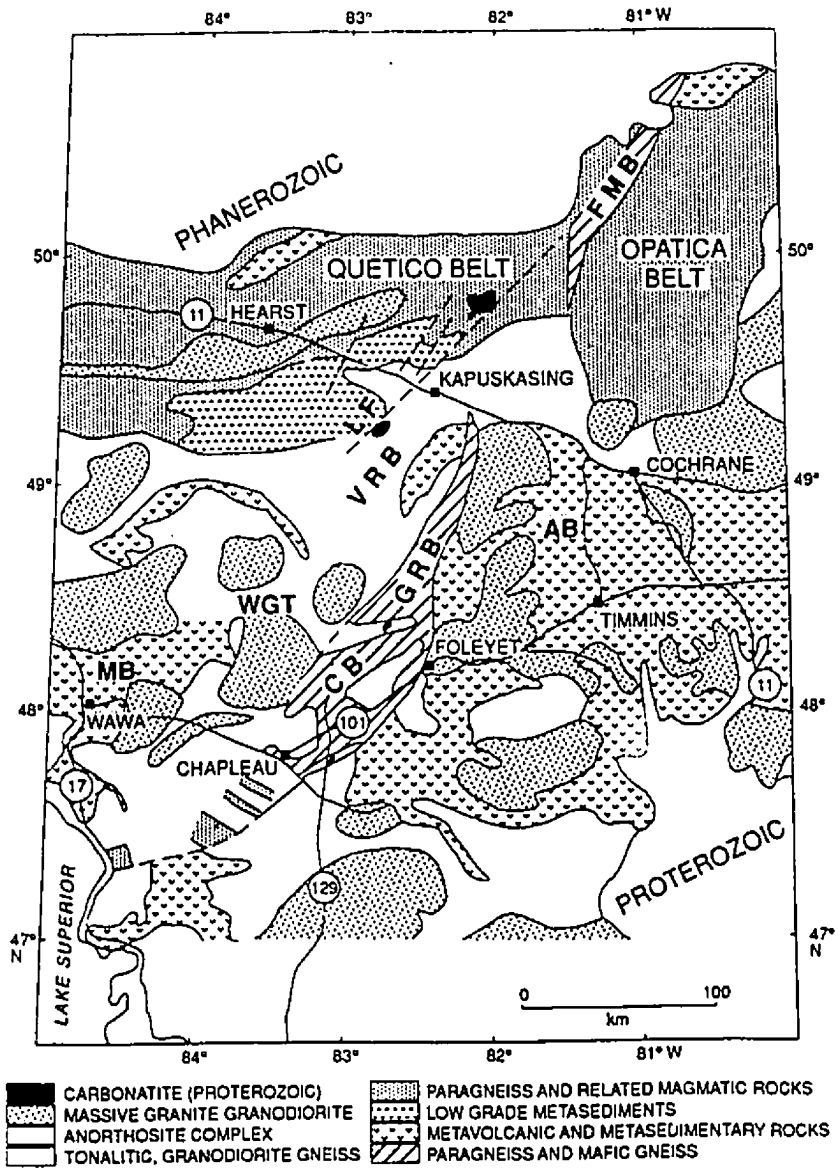

Figure 2-1. Generalized geology map of the Kapuskasing region in the central Superior Province (from West, 1988). Abbreviations used include: Lepage Fault (LF), Chapleau Block (CB), Groundhog River Block (GRB), Val Rita Block (VRB), Fraserdale-Moosonee Block (FMB), Wawa Gneiss Terrane (WGT), Abitibi Greenstone Belt (AB), Michipicoten Belt (MB).

in density from 2.70 g/cm^3 to 2.82 g/cm^3 (Percival, 1986) and has been interpreted as the mid crustal velocity discontinuity (i.e., the Conrad discontinuity) which has been detected seismically at depth in many shield areas (Berry and Fuchs, 1973; Hall and Hajnal, 1973; Green et al., 1979).

Many of the characteristics exhibited by the KSZ have been observed in other regions of the world such as the Ivrea Zone in northern Italy (Fountain, 1976), the Pikwitonei Belt of northern Manitoba (Weber and Scoates, 1978), the Musgrave Block of central Australia (Forman and Shaw, 1973), the Fraser Range of western Australia (Mathur, 1974) and the Kasila Group in Sierra Leone (Williams, 1978). Fountain and Salisbury (1981) suggest that such areas represent portions of the lower crust which have been exposed at the surface by crustal scale thrust faulting and erosion. Therefore, the rocks exposed within the KSZ provide a unique opportunity to study the composition, structure and physical properties of the lower continental crust beneath the Superior Province.

Geochronological studies (e.g., K-Ar, U-Pb, Rb-Sr) have been carried out in the area to determine the age of the zone and to date the uplift. The ages of the rock units within the Wawa and Abitibi belts range between 2650 and 2750 Ma (Percival and Krogh, 1983). The mafic gneisses of the Kapuskasing structure give concordant dates of 2650 and 2627 Ma from rounded zircons of metamorphic origin (Percival and Krogh, 1983). The uplift of the granulites from lower crustal depths is inferred to have occurred before 1907 Ma from the age of alkaline plutons and carbonatite intrusives that cut the post-thrust normal faults in the region (Percival and

McGrath, 1986). From analysis of isotopic systems in the KSZ, the Ivanhoe Lake Cataclastic Zone (ILCZ) is constrained to be 2250-2200 or 1950-1900 Ma in age (Percival et al.,1988).

2.2 GEOLOGY OF STUDY AREA

The region surrounding and including the KSZ, characterized by a continuous transition from low to high grade metamorphic rocks (defined as the Kapuskasing Uplift (KU) by Percival and McGrath, 1986), can be divided into four zones on the basis of lithological, metamorphic and structural characteristics. From west to east these zones are: (1) the Michipicoten belt (MB), (2) the Wawa Gneiss Terrane (WGT), (3) the KSZ, and (4) the Abitibi greenstone belt (AB) (Figure 2-1).

The MB (Figure 2-1) is predominantly composed of metavolcanic rocks of ultramafic, mafic and felsic compositions with intercalated greywacke, conglomerates, iron formation and chert (Percival and Card, 1983). The rocks within this belt have been metamorphosed to the greenschist and lower amphibolite facies (Studemeister, 1983; Fraser et al., 1978). Intrusive rocks are also common and include synvolcanic peridotites, granodiorites, granite and syenite plutons (Card, 1982). Large scale dome and basin structures and overturned strata predominate within this belt (Goodwin, 1962; Attoh, 1980). The supracrustal rocks of the MB are intruded to the southeast by tonalitic gneiss and plutons of the WGT.

The WGT consists mainly of amphibolite facies granodiorite to tonalite gneisses (Figure 2-1) intruded by granite, granodiorite and tonalite plutons (Percival

and Krogh, 1983). Inclusions of amphibolite, ranging from a few centimetres to hundreds of meters wide, occur within the gneisses west of the WGT. Domal structures on the 20-25 km scale, defined by trends of foliation and fold axial surfaces, are common (Percival and Card, 1985; Percival, 1986).

The KSZ is lithologically and structurally different from the belts mentioned above. It contains the highest grade of metamorphic rocks found within the uplift and consists mostly of paragneiss, mafic gneiss, tonalitic, dioritic, and anorthositic rocks and several early to mid-Proterozoic carbonatite intrusions. Metamorphic grade ranges from the upper amphibolite to granulite facies, with paleo-temperature and pressure conditions in the range of 700 to 800°C and 6 to 9 kbar (Percival and Card, 1983). Dome and basin structures which are prominent in the other belts, are absent in the KSZ and are replaced by northeasterly trending features with northwesterly dips (Percival and Card, 1983; 1985). The geology of the four tectonic blocks which make up the KSZ is discussed below:

1) Chapleau Block (CB)

The CB (Figure 2-1) is composed of northeast striking belts of paragneiss, mafic gneiss, tonalite gneiss, foliated diorite, mafic tonalites and anorthosites, including the Shawmere anorthosite complex (Thurston et al., 1977; Percival, 1985). The ILCZ forms the eastern boundary between the CB and the Abitibi greenstone belt to the east, juxtaposing the high grade metamorphic rocks (granulite facies) of the CB with low grade rocks of the Abitibi belt (greenschist facies). The CB has a

high gravity anomaly (Figure 1-2) associated with its dense granulites and a subtle magnetic anomaly. Seismic refraction experiments indicate high velocities at the surface (6.5-6.7 km/s) and a considerable crustal thickening beneath the CB (Northey and West, 1986; Boland and Ellis, 1988; Wu and Mereu, 1988). These results are substantiated by laboratory velocity results which also indicate high velocities at the surface (Fountain et al., 1990). Paleopressures based on garnet-orthopyroxene-plagioclase-quartz geobarometry yield pressures of up to 10.1 kbars (Leclair, 1990; Percival and McGrath, 1986). The southern part of the western boundary of the CB is gradational, consisting of a continuous transition from greenschist to upper amphibolite facies, and is interpreted as an exposed Conrad discontinuity (Percival, 1986).

2) Groundhog River Block (GRB)

The GRB has been suggested by Percival and McGrath (1986) to be the apparent continuation of the CB. Granulite facies metamorphic rocks of the GRB are bound to the west by amphibolite facies tonalitic gneisses of the VRB, and to the east by greenschist facies granodiorites of the Abitibi belt (Figure 2-1). The GRB is separated from the CB by the northeast trending Wakusimi River Fault (WRF) and from the VRB by the Saganash Lake Fault (SLF) (Figure 1-2). The ILCZ, presumed to be the eastern boundary of the KSZ, is not positively identified in this block because of poor rock exposure. Outcrop indicates that the GRB contains a heterogeneous sequence of tonalitic gneiss, mafic gneiss and paragneiss in almost

equal proportions, characterized by a strong magnetic anomaly, but no gravity anomaly (Leclair and Nagerl, 1988).

3) Fraserdale-Moosonee Block (FMB)

The FMB is located 65 km northeast of the GRB (Figure 1-2), and is separated from it by tonalitic gneisses of the VRB. The high grade rocks that characterize the KSZ are not found in this 65 km gap (Percival, 1985). The FMB consists predominantly of granulite facies paragneiss, mafic gneiss and metasedimentary granulites with some tonalites. The high grade rocks of the FMB are in fault contact with biotite-bearing paragneiss and granite to the east (Percival and McGrath, 1986). Cataclastic zones, indicating faults, are also present on the western boundary (Percival, 1985). The high gravity and magnetic anomalies that characterize some blocks of the KSZ are observed over this block.

4) Val Rita Block (VRB)

The VRB is fault bounded to the west by the Lepage Fault (LF) and to the east by the Saganash Lake Fault (SLF) (Figure 1-2). It consists of amphibolite facies tonalitic gneiss, granite and minor occurrences of metasedimentary granulite which are limited to the western edge of the block and truncated by the LF (Percival and McGrath, 1986). Leclair and Nagerl (1988) recognize four major northeast trending units in the easternmost part of the VRB. These include the metavolcanic and associated metasedimentary rocks of the Saganash Lake metavolcanic belt (SLMV),

xenolithic hornblende-biotite tonalite gneiss with amphibolite and paragneiss enclaves, massive to weakly foliated granodiorite to granite, and porphyritic hornblende diorite. The metavolcanic and metasedimentary rocks of the SLMV represent the largest concentration of supracrustal rocks within the block (Leclair and Poirier, 1989).

The Abitibi Belt (AB) has characteristics similar to those of the Michipicoten belt. The rocks consist of mostly mafic metavolcanics, with minor metasedimentary and felsic and ultramafic metavolcanic rocks, metamorphosed from subgreenschist to amphibolite facies (Percival, 1986). Foliated to flaser gneissic tonalites are rare in this region (Percival and Krogh, 1983), but dome and basin structures similar to those in the MB are present in this belt (Percival and Card, 1983). Because of the lithological, structural and geochronological similarities between the MB and AB, Percival and Card (1983, 1985) suggest that they were once part of a continuous belt, now interrupted by the uplift of the Kapuskasing structure.

2.3 PREVIOUS GEOPHYSICAL WORK

Previous geophysical studies have identified the KSZ as an anomalous geophysical structure and have provided information on its deep crustal structure. These studies include gravity, magnetic, seismic refraction and seismic reflection surveys. The earliest gravity surveys within the KSZ were conducted by Garland (1950) and Innes (1960). Garland (1950) attributed the high gravity anomaly of this zone to thinning of the upper granitic layer, while Innes et al., (1968) suggested that the structure represented a deeply eroded rift. Subsequently, the zone was also

recognized as having a positive magnetic anomaly by Maclaren and Charbonneau (1968). Maclaren et al., (1968) conducted magnetic traverses across the region and identified several anomalies associated with rocks within the KSZ. However, the cause of these anomalies was only speculative. Gravity data within the central part of the uplift (in the GRB and VRB areas) was sparse (in most areas 5-10 km average station spacing). However, Percival and McGrath (1986), using these sparse data have modelled the geopotential anomalies over the different blocks of the KSZ and concluded that their geometries are similar to those of the basement uplifts of the Rocky Mountain Province (Figure 2-2). The CB (profile C-C') is interpreted as a tilted slab, similar in geometry to the Wind River Range (Hurich et al., 1982; profile WR-WR'); the GRB (profile V-V') and southern FMB (Profile F-F') are perched thrust tips which are similar in configuration to the Sangre de Cristo Range (profile S-S') and the northern FMB (profile M-M') has a pop-up geometry analogous to that of the Uinta Mountains (profile U-U'). However, because of the sparse gravity data and limited rock exposure certain structural problems within the central part of the uplift could not be resolved.

Before the Canadian LITHOPROBE seismic studies, very little was known about the deep crustal structure of the KSZ. Previous seismic experiments within the region were concentrated on the Lake Superior Basin 300 km to the southwest, the Ontario-Manitoba border area, 700 km to the west and the Grenville Front, 300 km to the southeast. Results from the Lake Superior experiment showed the crust to be

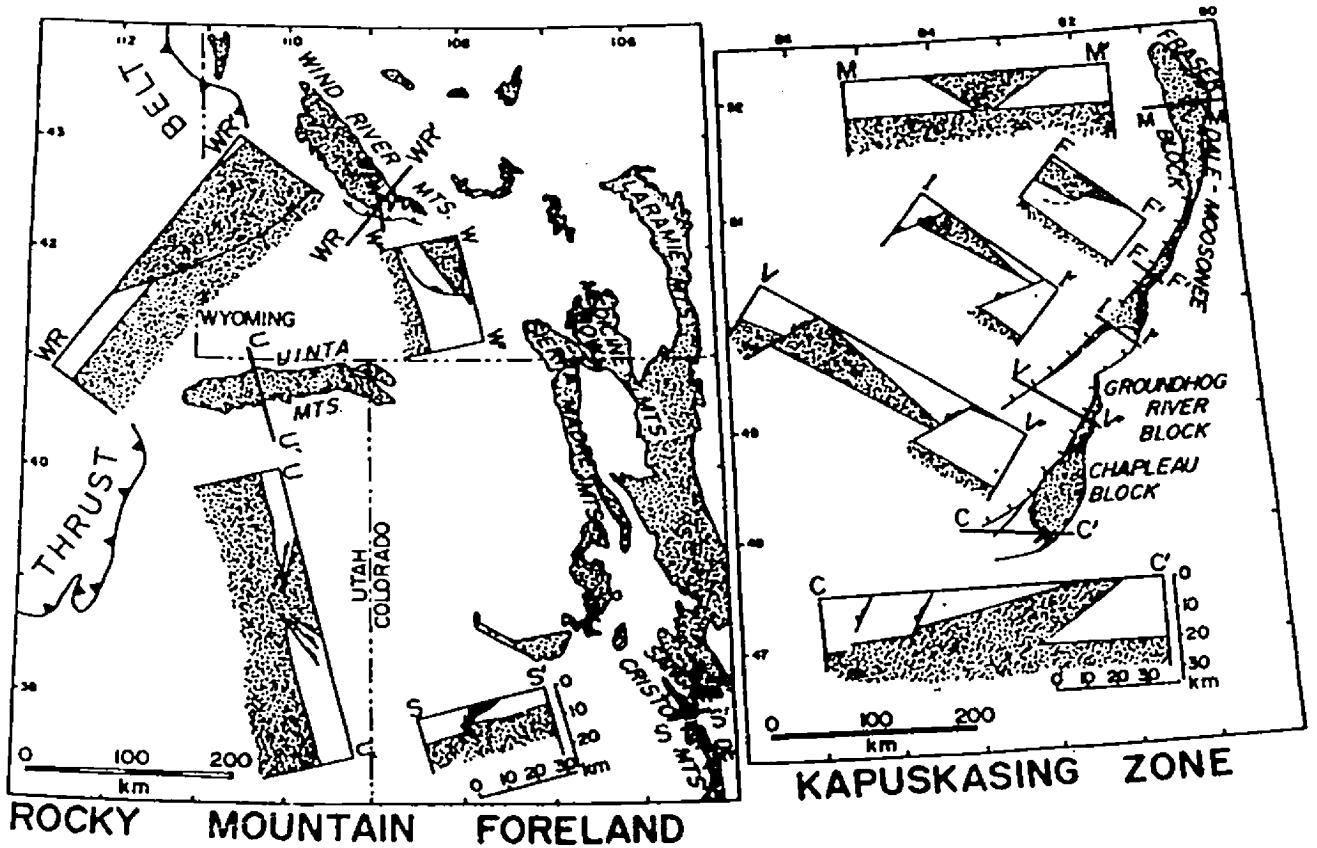

Figure 2-2. Maps and cross sections comparing the structural configuration of the different tectonic blocks of the KSZ and the basement uplifts of the Rocky Mountains. Stipples represent exposed Precambrian basement in Rocky Mountains and > 6 kbar granulites in the KSZ. Geometry of the Wind River Range (WR-WR'); southern Wind River Range (W-W'); Sangre de Cristo Range (S-S'); Uinta Mountains (U-U'); Chapleau Block (C-C'); Val Rita, Groundhog River and southern Fraserdale-Moosonee Blocks (V-V', I-I', F-F') (from Percival and McGrath, 1986).

50 km thick at the center of the basin, but shallowing towards the KSZ (Hall, 1982). The Ontario-Manitoba border region results suggested crustal thicknesses of 36-38 km (Green et al., 1979; Hall and Hajnal, 1973), while results from the Grenville Province suggested crustal thicknesses of 35-40 km with thickening under the Grenville Front (Mereu et al., 1986).

However, with the advent of the LITHOPROBE KSZ transect seismic studies, more light has been shed on the deep crustal structure of the zone. Several seismic refraction and reflection lines, including a pilot reflection survey have been shot within the region. The 10 km long pilot reflection survey shot along refraction line 5, (Figure 2-3) across the eastern boundary of the CB, has been interpreted by Cook (1985). The results indicate the presence of dipping reflectors related to the ILCZ. These events dip 40° to the west at depths of 6-12 km. Recently, five LITHOPROBE reversed refraction profiles with lengths of 360-450 km have been shot within the region (Figure 2-3). Three of these lines are parallel to the Kapuskasing structure (one within the WGT (Line 1), one along the KSZ (Line 2) and one within the AB (Line 3)) and two are in a cross strike direction (line 4 crosses the VRB and GRB and line 5 crosses the CB). The results from lines 4 and 5 (Figures 2-4a and b) indicate that rocks with high velocities (6.5-6.6 km/s) are uplifted from depths of 20 km beneath the WGT to near surface depths of 4-10 km beneath the CB (Northey and West, 1986; Boland and Ellis, 1988; Wu and Mereu, 1988). These results have been confirmed by the laboratory velocity results of Fountain et al., (1990). A crustal bulge is also detected underneath the CB and VRB, with Moho

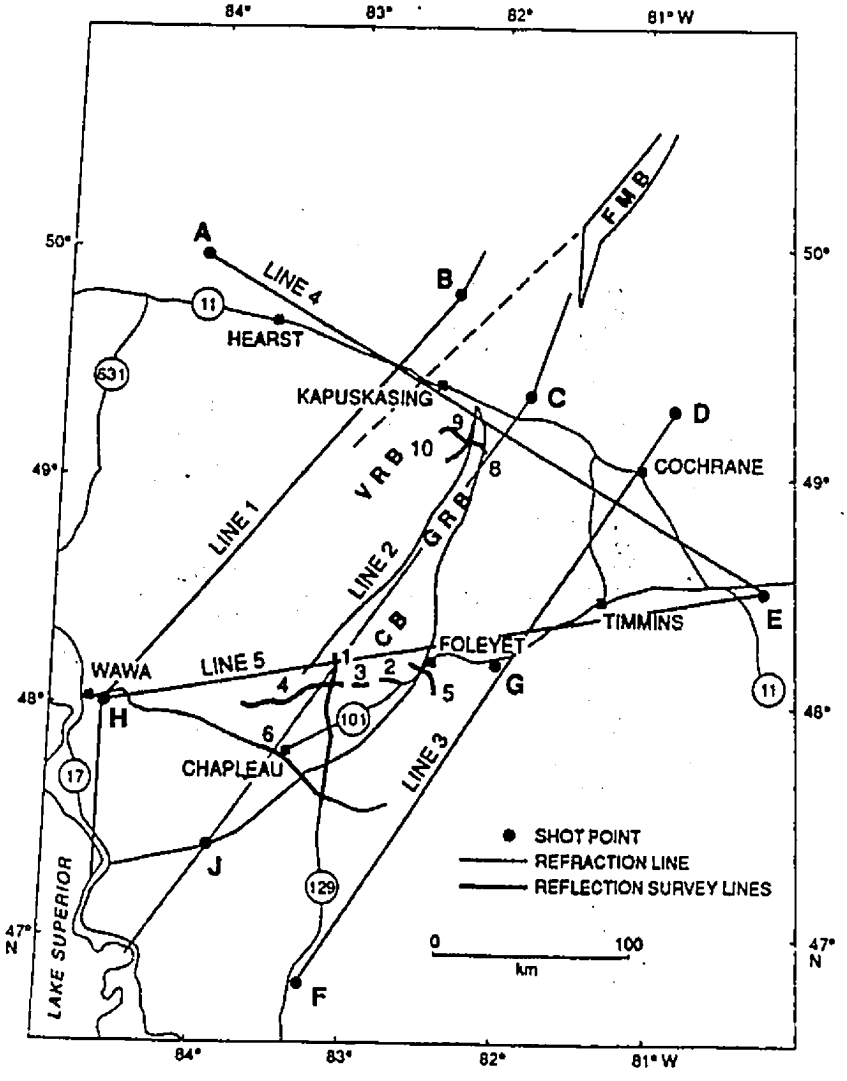

Figure 2-3. Location of Lithoprobe refraction and reflection lines. Numbers in circles are highway numbers.

a

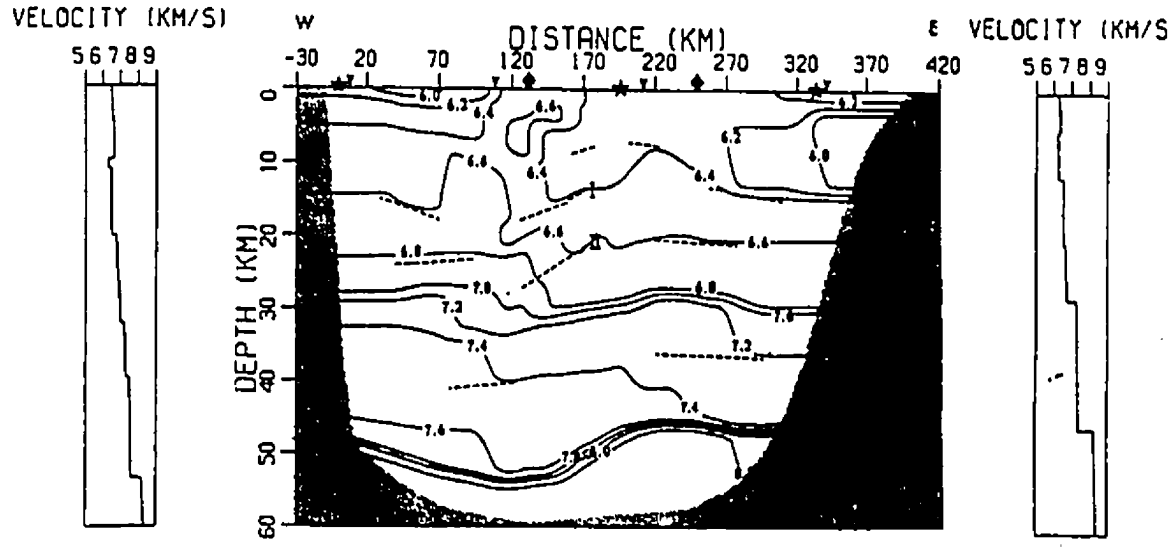

b

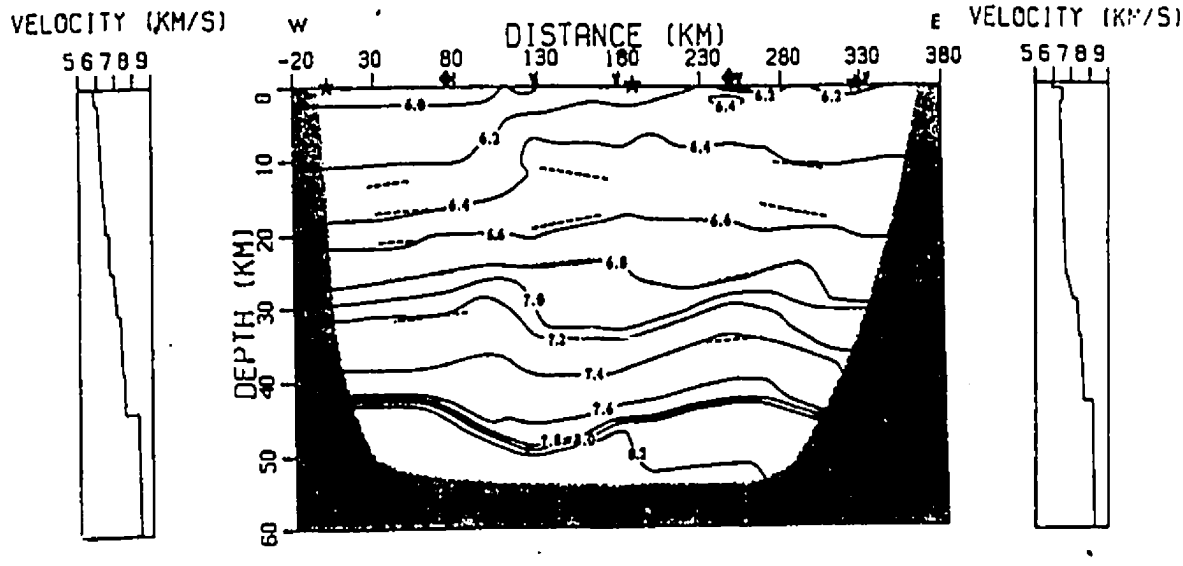

Figure 2-4a. Line 5 smoothed velocity structure and b: Line 4 smoothed velocity structure. The solid lines are the isovelocity contours, and the dashed lines are zones of reflectivity modelled by wide-angle reflections. The stippled region represents little or no ray coverage. The stars are the shot points, the arrows are locations of intersecting lines and the diamonds are the locations of the velocity depth profiles shown (from Boland and Ellis, 1988).

depths greater than 50 km compared to an average depth of 40-43 km beneath adjacent areas.

In addition, several seismic reflection lines totalling 300 km have been shot within the region (Figure 2-3). Lines 1-6 are within the CB and lines 8,9 and 10 are located in the northern part of the GRB and the eastern edge of the VRB. Results from the CB (Figure 2-5) show three major low angle thrust faults with 15-20° northwest dips associated with the ILCZ (Geiss et al., 1990). The interpretations of the lines within the GRB and VRB are still underway.

Other geophysical studies include heat flow measurements both in the northern part of the uplift along Highway 11 (Cermark and Jessop, 1971) and in the southern part of the uplift (Ashwald et al., 1987), and on-going paleomagnetic studies of the dykes and carbonatite intrusions to help determine the timing of tectonic activity associated with the uplift and evolution of the zone (Constanzo-Alvarez et al., 1988; Ernst et al., 1984). Knowledge on the deep crustal structure of the KSZ has been considerably increased as a consequence of the above mentioned geophysical studies. However, geophysical coverage within the central part of the uplift (VRB and GRB) is still reconnaissance in nature.

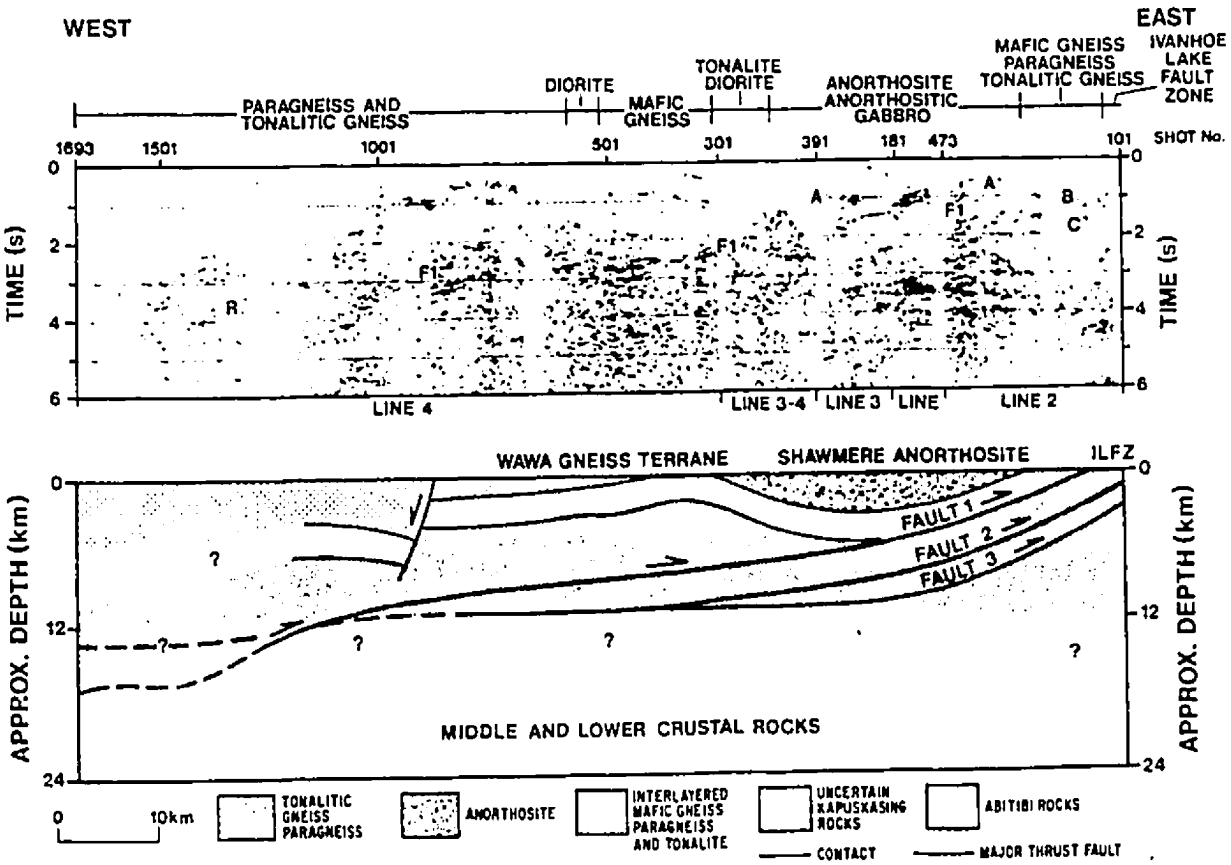

Figure 2-5. Regional seismic reflection data and interpretation across the CB. Three faults with ramp-flat geometry and a thin upper plate are interpreted (from Geis et al., 1990).

CHAPTER THREE: DATA ACQUISITION AND REDUCTION

3.1 INTRODUCTION

Two six-week field programs were carried out within the VRB, GRB and northern CB of the central Kapuskasing Uplift during the summers of 1987 and 1988, using the town of Kapuskasing as a base camp. Gravity, elevation and temperature data were collected along logging and winter roads and the Kapuskasing River using a four wheel drive truck and a single engine boat for transportation.

Other data for the study, not acquired in the field included magnetic, density and susceptibility data on rocks from the area..

3.2 FIELD PROCEDURES

3.2.1 Gravity Readings

Lateral variations in density exist from one location to another because of the heterogeneity of the earth's crust. These density variations cause gravity anomalies which can be measured with a gravity meter. After correction, the measured values are converted into a Bouguer anomaly map which may be used for the interpretation of geological features of interest, especially when used in conjunction with aeromagnetic data and laboratory data on the density, magnetic susceptibility and remanent magnetization of rocks from the area.

To augment existing gravity data for the central Kapuskasing Uplift, a total of 1380 gravity stations were occupied within the VRB, GRB northern CB between

Latitude 48.75 to 49.75°N and Longitude 81.8 to 83.5°W (Figure 3-1) over a period of three months during the summers of 1987 and 1988. In the first field season, 712 gravity measurements were made. During the second field season, a number of gravity stations from the previous field season were reoccupied to check for accuracy and an additional 572 gravity stations were occupied.

Gravity measurements were made at a spacing of 1 km parallel to the regional KSZ anomaly, and 0.5 km normal to the strike of the anomaly. Where possible, measurements were made along logging and winter roads and navigable rivers. Sparse data coverage in some areas of the survey (especially toward the west Figure 3-1) reflects poor accessibility.

A Lacoste and Romberg G112 gravity meter was used for the gravity measurements. A base station with known gravity and elevation (usually a bench mark, lake surface or road intersection) was created at the beginning of each traverse. The gravity meter was then moved from station to station, measuring the difference in gravity between the observation station and the base station. Repeat readings were obtained at the base station at regular intervals of at most 4 hours in order to correct for the drift of the instrument with time. The location of the gravity stations were determined from 1:10,000 aerial photographs and 1:50,000 NTS topographic maps.

Additional gravity data for the southern part of the uplift (e.g., southern CB) and the adjacent belts were provided from the Geological Survey of Canada, Geophysical Data Centre (Figure 3-2).

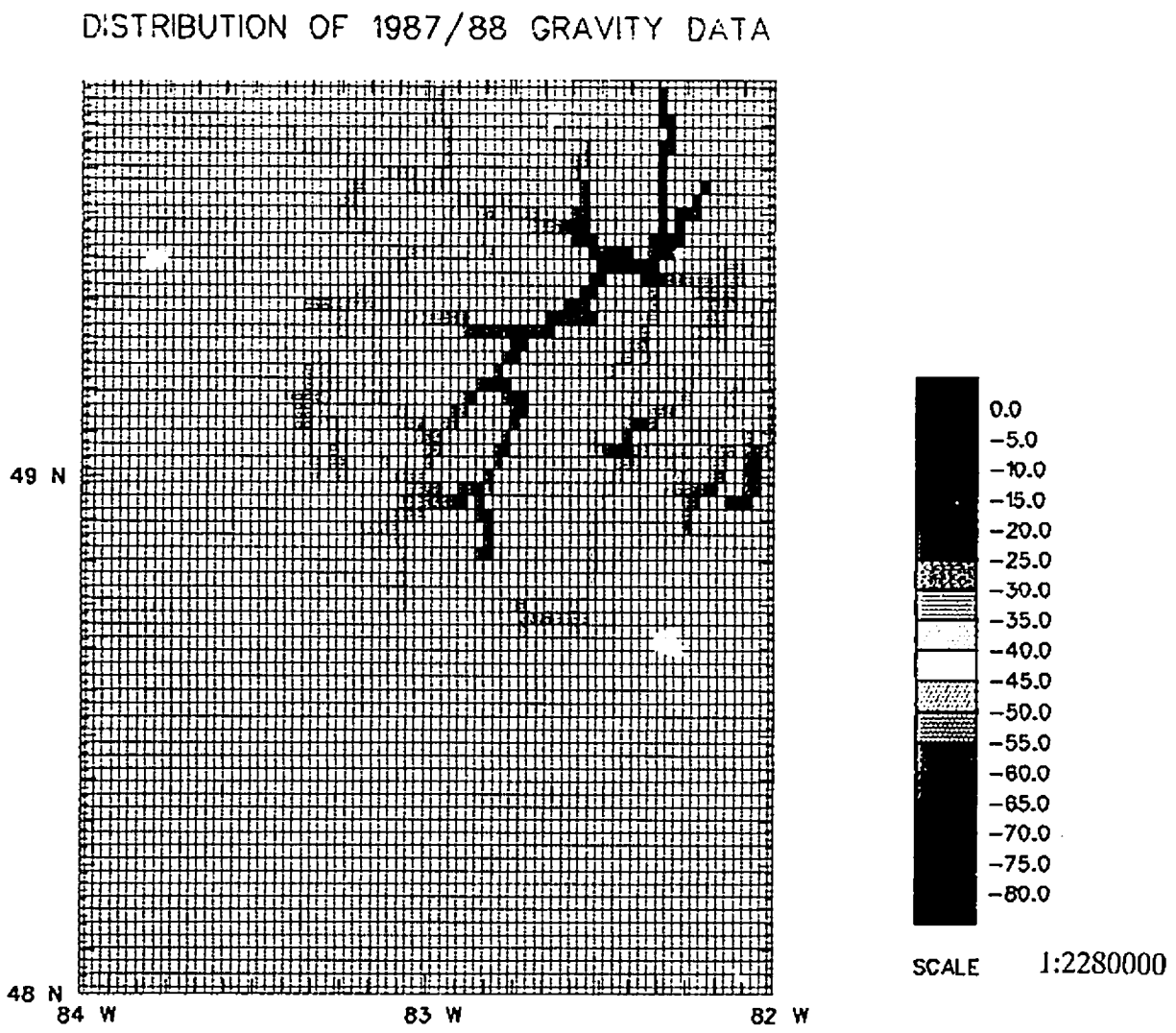

Figure 3-1. Gridded gravity data showing the distribution of the 1987/88 gravity stations. Color interval is 5 mGals.

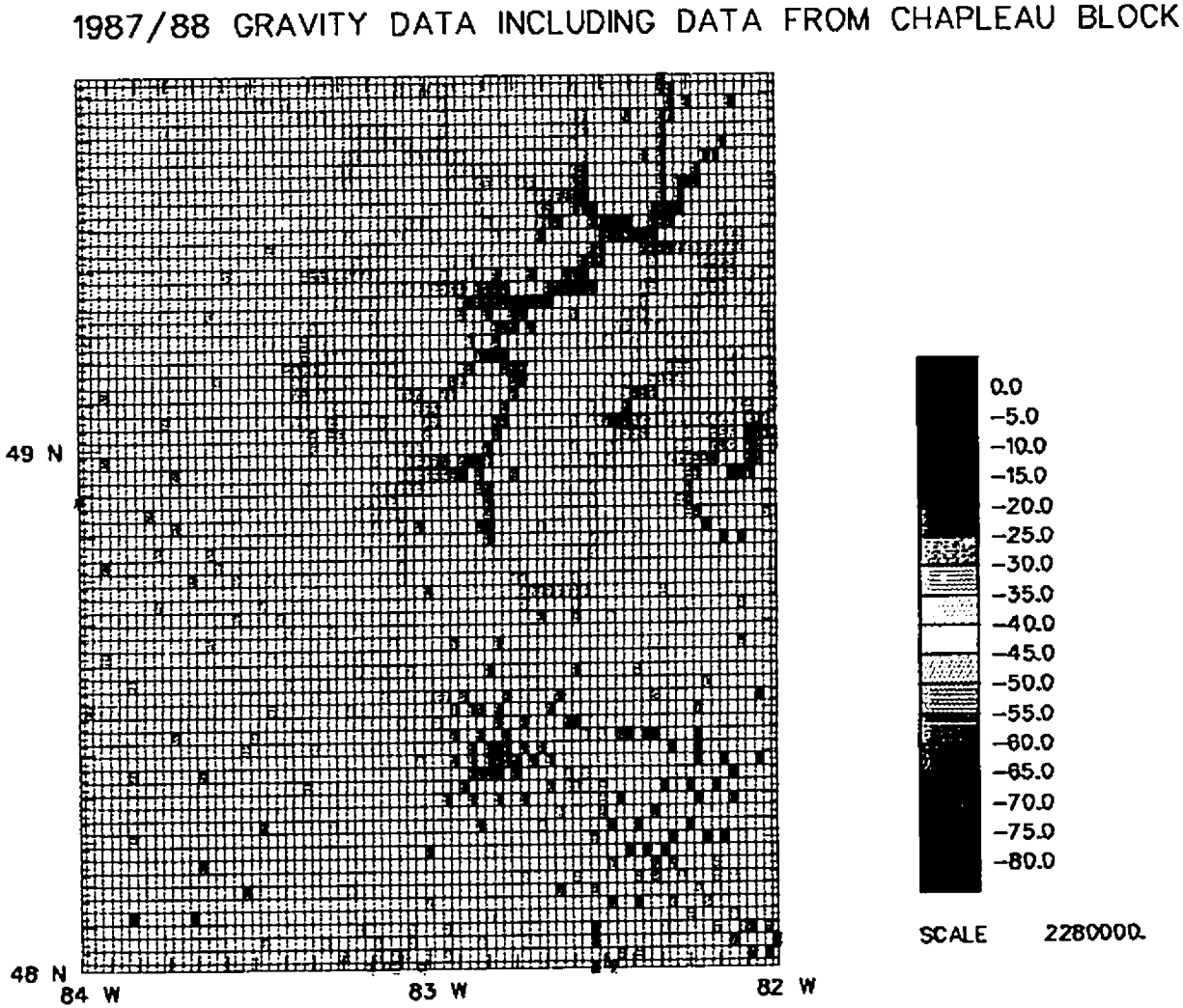

Figure 3-2. Gridded gravity data showing the distribution of the 1987/88 data with additional data from the CB. Color interval is 5 mGals.

3.2.2 Elevation Readings

Elevations for the traverse stations were determined using two F181A army type altimeters and a sling free psychrometer for wet and dry bulb temperature measurements. Two altimeter readings and a wet and dry bulb temperature measurement were recorded at each gravity station. As in the case of the gravity data, a base station for elevation was also created at the beginning of each traverse. A recording barometer was stationed at the base station to record the change in barometric pressure during the time of each traverse. Altimeter readings were taken at subsequent gravity stations using a modification of the single base method of observation.

When using this method, both altimeters were simultaneously set to the elevation of the base station and the temperature (wet and dry bulb), time, altimeter reading and weather conditions recorded. The recording barometer was left at the base station while the field altimeters were used at stations along the traverse. Readings of temperature, altitude and time were recorded at each station along the traverse and notes on wind direction and cloud cover were taken regularly to assess the quality of the data. The two altimeters were then returned to the base station at least once every hour, where another altimeter reading was taken. Any difference between the altimeter readings and their previous readings at the base station was considered to be due to barometric drift. All altimeters were then reset before a new traverse was begun.

3.3 DATA REDUCTION

3.3.1 Gravity Data

Gravity readings are influenced by factors such as instrument drift, variations in latitude, elevation and earth tides as well as rock density. Therefore at the end of each field day, the gravity and elevation readings were corrected for these factors using the standard reduction techniques outlined in Dobrin (1976) and Telford et al., (1976).

3.3.2 Sources of Error

The greatest source of error in gravity values results from errors in elevation because of the profound effect of elevation on gravity. The altimeters used for elevation control are sensitive to atmospheric conditions (wind, temperature inhomogeneity in the air column, and humidity) at the time a reading is taken. Temperature and humidity corrections were therefore applied to the altimeter readings using the procedures outlined in the Earth Physics Branch Field Procedures Manual (1984).

After the altimeter readings were corrected for temperature, the difference between the temperature-corrected altimeter reading at the base station and the actual elevation of the base station was assumed to represent the change in barometric pressure for the time of the traverse. Subsequent to temperature corrections the altimeter readings were corrected for barometric drift on the assumption that the drift is linear with time. The chart from the recording barometer

was used in determining both the barometric drift in the vicinity of the survey as well as in assessing the quality of the data. The altimeters had a precision of +/- 1.5 m which results in an error of +/- 0.3 mGals.

An additional source of error may have resulted from assumptions made in the Bouguer correction. The average density of the Bouguer slab was assumed to be 2.67 g/cm^3, whereas the average density of the rocks in this region are at least 2.73 g/cm^3, resulting in a difference of .004 mgals/m. This error is more profound in areas of high topography. For example, using the highest estimate of 300 m (generally, the topography in the study area did not exceed 300 m) obtained for the topography in the study area would have resulted in an error of +/- 1.2 mGals.

Another source of error could have resulted from the latitude correction, since the locations of the gravity stations were determined from aerial photographs and topographic maps. Error estimate due to location errors is about 0.08 mGals. The cumulative error estimate from all sources is approximately +/- 1.6 mGals.

3.3.3 Gridding Procedure

After all the corrections had been applied to the data, the Bouguer anomaly values were gridded using a geographical grid with a size of .025° in latitude and longitude (about 2.8 km in latitude and 1.9 km in longitude). In areas where the data distribution was sparse, a minimum curvature technique was applied (Briggs, 1974; Swain, 1976). In this technique, the observation values within the grid cell are "gridded" and an average value is obtained. This value is then assigned a specified

position (control point) in the centre of the concentration of the observation points. A minimum curvature or "numerical surface" that approaches the smoothest surface passing through the control points is then calculated (Swain, 1976). This gridding method works well with unevenly spaced data such as is the case with the data from this study. The resulting gridded data was then contoured to produce the Bouguer anomaly map of Figure 3-3, which will be used in subsequent chapters on the interpretation of anomalies. Principal facts on the gravity survey including station locations, elevation data and gravity data, can be obtained from the Geological Survey of Canada, Geophysical Data Centre.

3.4 MAGNETIC DATA

In order to constrain the gravity models, aeromagnetic data for the study area was obtained from the Geological Survey of Canada, Geophysical Data Centre. These data were obtained from airborne magnetometer surveys conducted during 1962 and 1963. The surveys were flown along north-south flight lines spaced 800m apart at a height of 305m above the ground surface. Differences in the levels of the total field data were adjusted by adding a constant value to parts of the data (Dods et al., 1985). This value was obtained by comparing the differences in the overlapping profiles at the borders of the surveyed areas (at longitude 83° W). The resulting magnetic anomaly map (Figure 3-4) shows no abnormal values at the borders between the two surveyed areas, indicating that the datum level was properly adjusted.

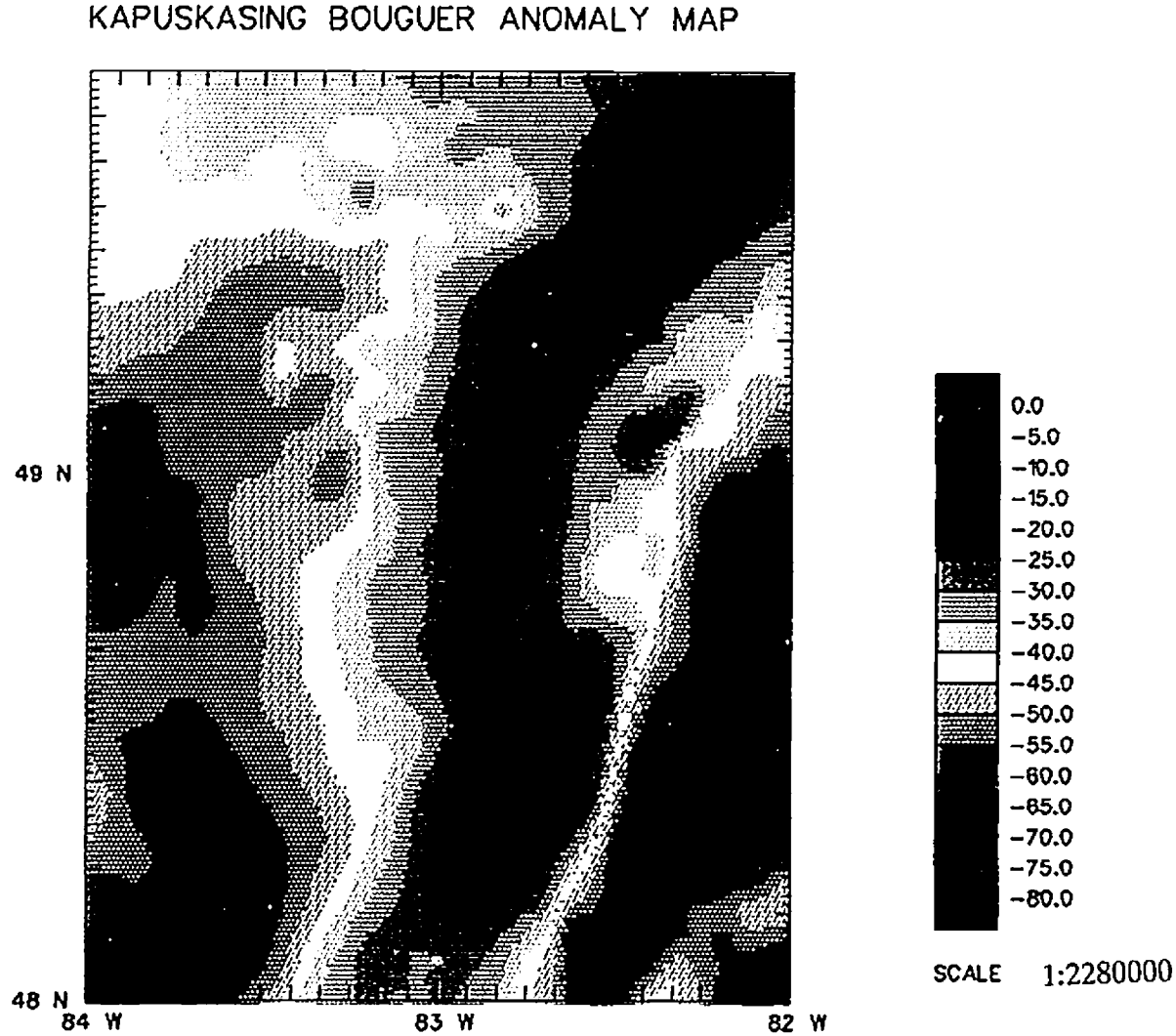

Figure 3-3. Bouguer anomaly map of the KSZ from data shown in Figure 3-2. Note the deviation of the anomaly from the CB into the VRB in the form of an arcuate anomaly. Contour interval is 5 mGals.

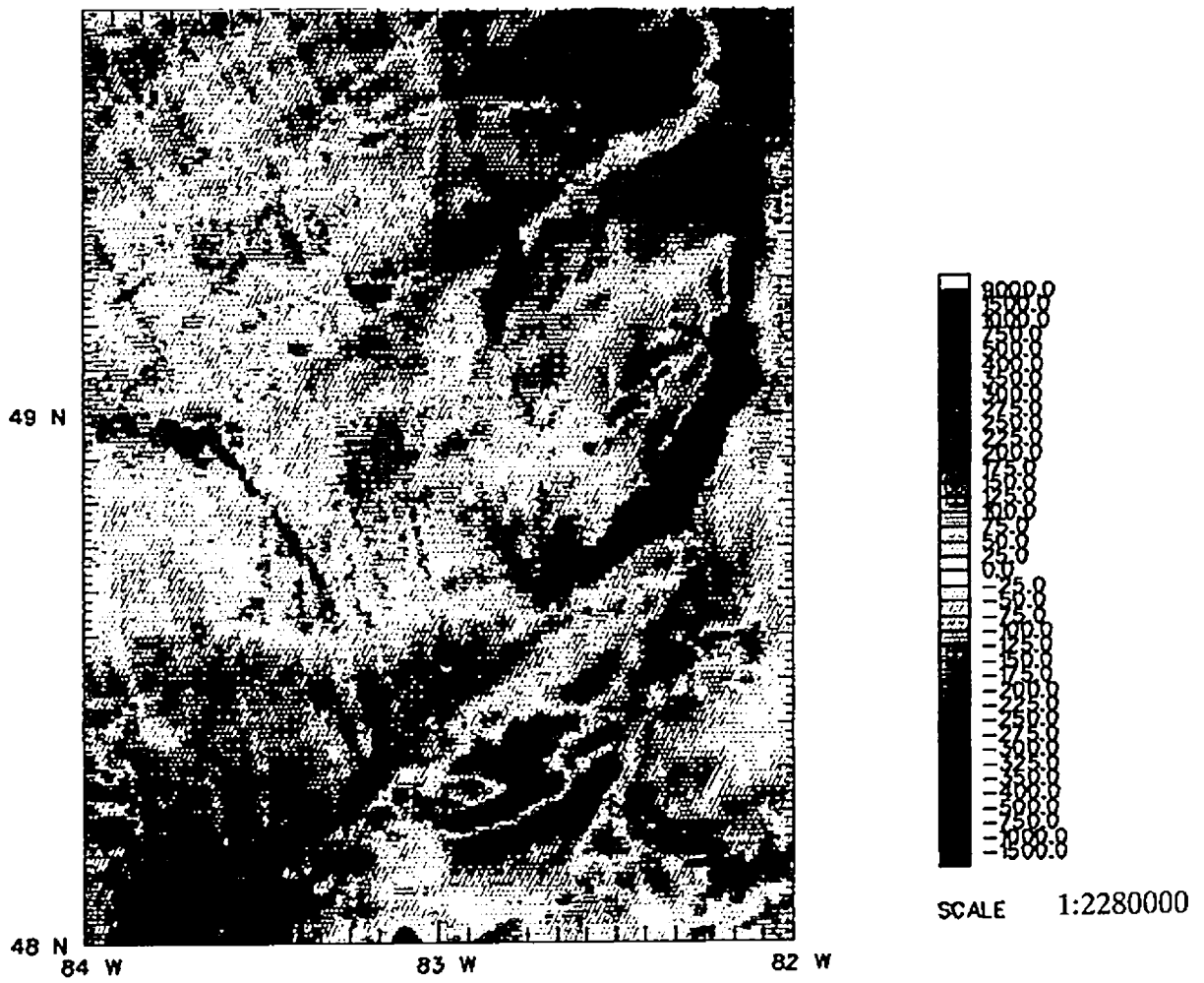

Figure 3-4. Aeromagnetic anomaly map of the KSZ. Magnetic anomaly in nT.

The data was then gridded by the same technique as that used for the gravity data with the same grid spacings of 2.8 km by 1.9 km. A regional trend defined by the International Geomagnetic Reference Field (IGRF) for 1963 was removed.

3.5 DENSITY DATA

Density data for rock samples collected within the area of a gravity survey provide excellent constraints in the modelling of gravity anomalies. To this end, density measurements were made on rock samples collected from the study area by A. Leclair. The density measurements were done at the Geological Survey of Canada in Ottawa using the wet-dry method (Feininger, 1986). Samples were weighed dry using an electronic beam balance. The samples were then reweighed while immersed in water after soaking in water overnight at room temperature to reduce the effect of gas bubbles which may introduce errors in the density measurements. Density measurements for the CB were kindly provided by T. Feininger and taken from Fountain et. al., (1990). A summary of the results from the density measurements is shown in Table 1 and the detailed data is provided in Appendix 1.

Sample locations were determined from 1: 50,000 topographic maps (Figure 3-5). Densities were assigned to geologic formations, and the resulting data were gridded (by the same techniques used for the gravity data) and plotted (Figure 3-6). For the density map of the Chapleau area, see Feininger (1986, p61).

Table 1. Summary of Density Data from the KSZ

Val Rita and Groundhog River Blocks

Rock Name	No. of Samples	Density in g/cm^3 Max	Min	Average	Standard Deviation
Amphibolite	20	3.17	2.79	2.98	.09
Anorthosite	6	2.79	2.71	2.74	.04
Metavolcanics	22	3.17	2.71	2.89	.10
Bi-Hn-Qz-Pl Gneiss	4	2.83	2.71	2.78	.04
Ga-Bi-Hn-Cpx Pl Gneiss	20	3.19	2.71	2.89	.15
Diorite	13	3.01	2.81	2.91	.08
Gabbro/Meta Gabbro	12	3.03	2.85	2.96	.07
Granite	41	2.76	2.63	2.67	.03
Granite Gneiss	16	2.77	2.63	2.69	.03
Granodiorite	50	2.76	2.65	2.71	.03
Mafic Tonalite	22	3.06	2.72	2.86	.08
Tonalite	36	2.78	2.66	2.71	.03
Diabase	11	3.10	2.84	3.03	.07
Tonalite-Granodiorite Gneiss	54	2.80	2.65	2.73	.04
Tonalite-Granodiorite	34	2.79	2.64	2.70	.04
Monzodiorite	8	2.79	2.74	2.77	.01
Mafic Gneiss	41	3.40	2.85	3.05	.10
Paragneiss	22	3.09	2.71	2.86	.11
Granulite	20	3.02	2.66	2.79	.09
Metagreywacke	12	2.80	2.68	2.74	.04
Metasedimentary Gneiss	53	3.01	2.68	2.80	.08

Chapleau Block (from Fountain et al., 1990)

Amphibolite	3.09
Metasedimentary Gneiss	2.80
Tonalite-granodiorite Gneiss	2.74
Anorthosite	2.82
Mafic Gneiss	3.05

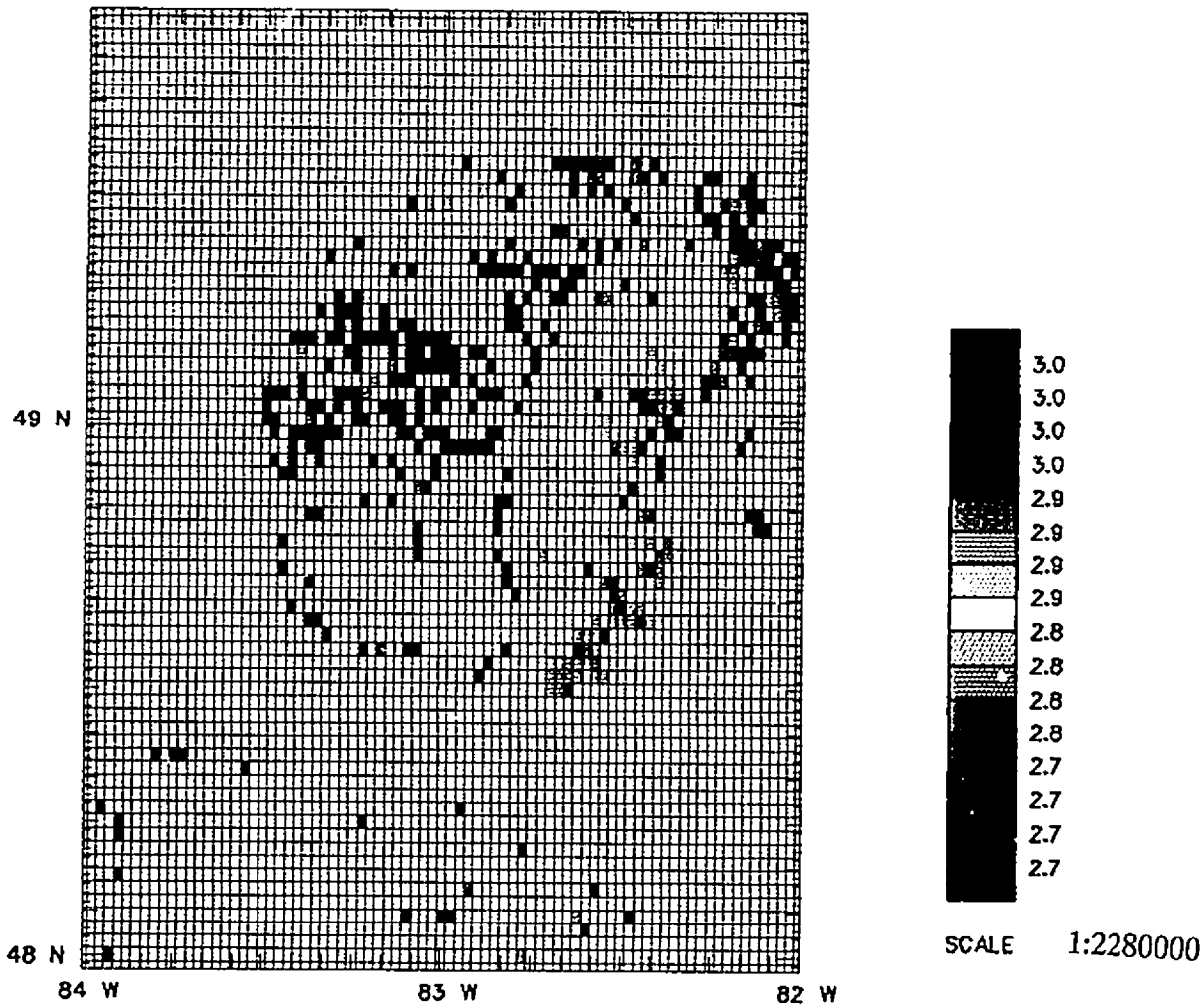

Figure 3-5. Gridded density data showing the distribution of the sample locations including data from the CB provided by Fountain et al., 1990. Color interval is .025 g/cm^3.

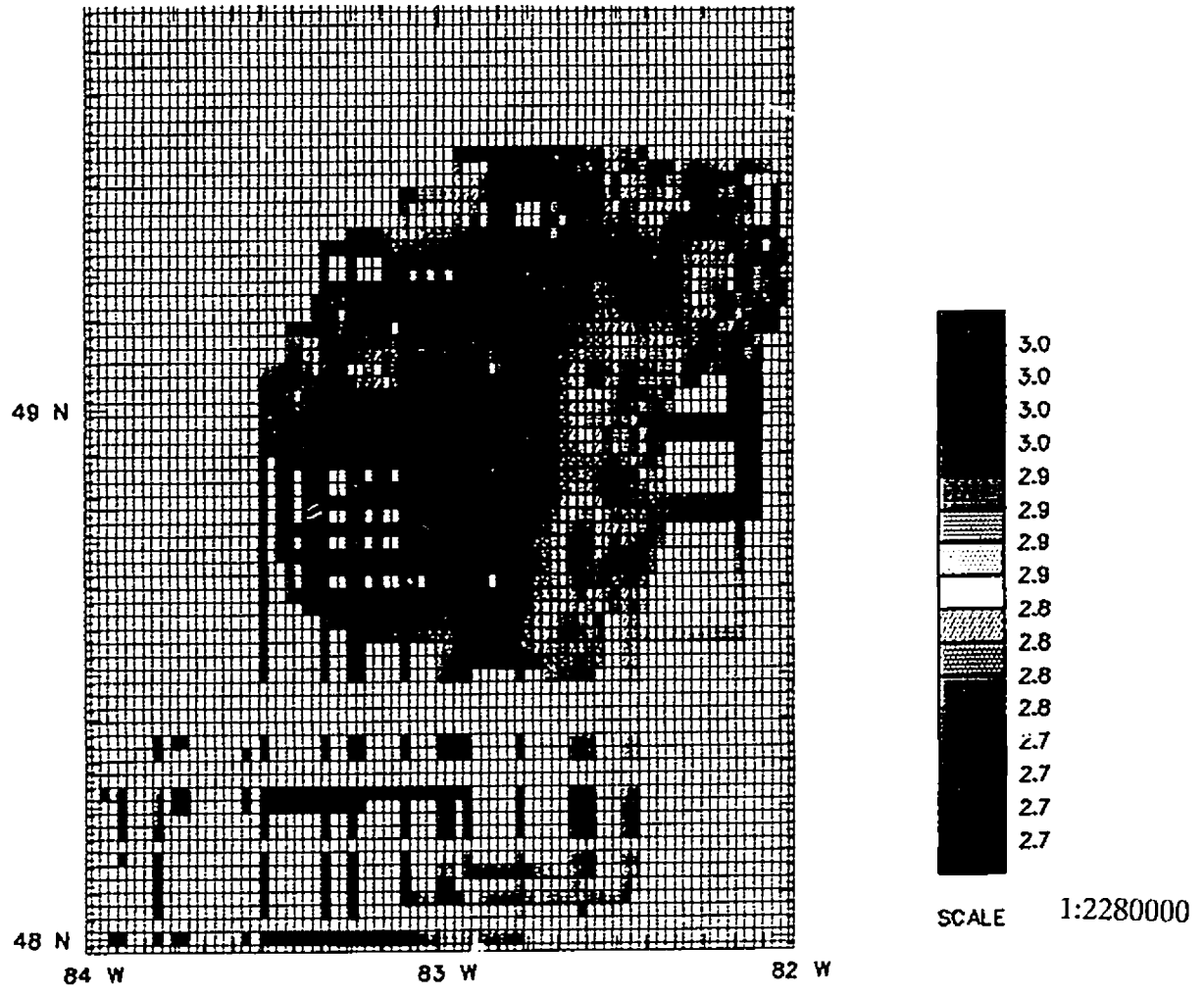

Figure 3-6. Density data filled with minimum curvature. Note the generally low values within the VRB and high values within the CB and GRB. Color interval is .025 g/cm^3.

3.6 REMANENT MAGNETIZATION AND MAGNETIC SUSCEPTIBILITY DATA

3.6.1 Introduction

The magnetization of a rock is usually composed of induced and remanent components which can be expressed as a vector sum. In the modelling of magnetic anomalies, however, it is generally assumed that the magnetization of a rock is dependent mainly upon the induced field and the magnetic mineral content. Thus, the effect of remanent magnetization on an anomaly is either assumed to be negligible or to lie in the direction of the induced component. However, this is not always true because the remanent magnetization may contribute significantly to the total magnetization vector.

In order to determine if the remanence was significant enough to be considered in the interpretation of the magnetic anomalies and to provide better constraints for modelling, it was necessary that both remanence and susceptibility measurements be obtained for rocks from the VRB, GRB and CB of the KSZ.

3.6.2 Remanent Magnetization

Remanent magnetization was measured on unoriented samples provided by A. Leclair, which had been collected for other purposes. Therefore, only the intensity of the remanent magnetization was measured in the laboratory. The stability of the remanence field was not investigated. A total of 12 samples from each

of the major lithologic units within the VRB, GRB and northern CB were analyzed. Results from the southern CB have been presented by Shive and Fountain (1988).

The measurements presented here were made using facilities at Dalhousie University. The intensity of the remanent component of magnetization was measured on 2.5 cm diameter cores drilled from the rock samples using a Schonstedt model DSM-2 Digital Spinner Magnetometer. Multiple cores from the same sample and duplicate measurements on the same samples showed virtually identical values. A summary of the results is given in Table 2.

3.6.3 Magnetic Susceptibility

The magnetic susceptibility is the principal variable in magnetics, which functions in the same way as density in the interpretation of gravity anomalies. It is a measure of the relative ease with which a material can be magnetized by induction and is dependent on the magnetic mineralogy and the grain shape and size of the magnetic minerals (McGrath, 1986).

Susceptibility measurements on cores from the rock samples were obtained using an MS-3 susceptibility bridge. During the measurements, the susceptibility bridge was first balanced without a sample in it, and the balance level recorded. The sample was then inserted into the sample holder and the bridge re-balanced and the new reading recorded. The two readings were then subtracted and using a calibration curve, the value obtained from subtracting the two readings (the apparent

Table 2. Magnetic Data

Sample	Lithology	$J_{NRM}x10^{-3}$	K,$x10^{-6}$	Q
	Groundhog River Block			
L1-2-87	Garnetiferous mafic gneiss	0.36	122	3.6
8-1-87	Paragneiss	5.57	10642	0.52
L152-1-87	2 pyroxene granulite	7.62	2881	2.64
N37-4-87	Tonalite-grano-diorite	3.29	3049	1.05
N122-1-87	Garnetiferous mafic gneiss	1.30	1548	0.84
	Val Rita Block			
L433-1-88	Paragneiss	0.08	130	0.61
L436-2-88	Mafic gneiss	0.36	642	0.57
L725-2-88	Tonalite gneiss	0.02	265	0.06
P59-1-88	Tonalite-grano-diorite	0.04	386	0.09
	Chapleau Block			
L183-2-87	Garnetiferous mafic gneiss	0.71	578	1.23
L256-1-87	Paragneiss	2.92	95	30.77
N210-1-87	Garnetiferous mafic gneiss	2.31	6004	0.39

J_{NRM}, Natural Remanent Magnetization; K, susceptibility in cgs units; Q, Koenigsberger ratio ($Q=J_{NRM}/KH$, where H=59500 nT)

susceptibility) was converted to magnetic susceptibility in cgs units per cm^3 using the following formula:

$$K = 106 \times (R_O - R_S)/V \times 10^{-6} \quad (3\text{-}1)$$

where R_O is the initial reading of the bridge without the sample, R_S is the reading with the sample, 106 is the calibration factor, and V is the volume of the sample. A calibration curve obtained with a standard provides a relationship between the measured susceptibility (K) and the change in inductance. To obtain the true susceptibility, correction for the varying length and diameter of the cores must be made by multiplying the apparent susceptibility by a known calibration factor. Results for the susceptibility measurements are presented in Table 2.

Following the remanent magnetization and susceptibility measurements, the Koenigsberger ratio (Q) was computed for the samples (Table 2). The data presented in Table 2 show that the susceptibility values are highly variable for the same rock types. For example, within the GRB, the garnetiferous mafic gneiss varies from 122 x 10^{-6} emu/cm^3 in sample L1-2-87 to 1549 x 10^{-6} emu/cm^3 in sample N122-1-87. Due to the limited number of samples used for this study, it becomes very difficult to determine the true susceptibility of the rock. Despite the variability in the data, Table 2 shows that the susceptibilities in the GRB are generally higher than those of the other blocks, except for sample N210-1-87 within the CB which has a susceptibility value comparable to those of the GRB. Although the data presented

in Table 2 may be biased because of the limited number of samples used in the analysis, previous susceptibility measurements of rock samples from the GRB, indicate values that are comparable to those obtained in this study (e.g., 1500×10^{-6} emu/cm^3 obtained by Maclaren et al., 1968; and 3409×10^{-6} emu/cm^3 obtained by McGrath, personal communication, 1990). The Q ratios also indicate that for some of the samples, the remanent magnetization contributes significantly to the magnetization of the rock, and its effects therefore cannot be ignored. Hence the common practice of ignoring the effect of the remanence in the interpretation of magnetic anomalies cannot be uniformly applied within this region. However, since no oriented samples were available, the effect of the remanent magnetization has not been taken into account.

CHAPTER FOUR: POTENTIAL FIELD MAPS

4.1 INTRODUCTION

Gravity maps reflect lateral variations in crustal and possibly mantle densities, while magnetic anomaly maps reflect variations in rock magnetization and susceptibility. Although correlations can often be made between potential field maps and geology, these correlations are not always straight forward because individual rock types may display a range of densities and susceptibilities and different rock types may display similar properties. However, when such correlations can be made, the potential field maps can be used to extrapolate the known geology to areas of poor rock exposure.

4.2 FILTERING OF GRAVITY AND MAGNETIC DATA

A regional field is usually present in potential field data, and may sometimes mask valuable information which may not be used effectively without the application of special filtering techniques (Broome, 1986). Application of such filters removes unwanted characteristics such as noise and enhances features related to the geology. It is often useful to separate the data into two wavelength components, in order to distinguish between anomalies due to near surface sources and those from deeper sources. Several filters have been applied to the potential field data in this study including reduction to the pole (magnetic data only), lowpass and highpass filters, continuation filters, vertical derivative filters and inversion filters (density and

magnetic susceptibility contrast). Filtering of the potential field data was done in the wave number domain. The resulting filtered maps can be readily compared with each other. For example, anomalies on magnetic maps can be easily compared with highpass filtered and vertical derivative gravity maps, which relate to near surface density contrasts. A brief discussion on the different filters used in this study is presented. Detailed theoretical discussion of the various filters can be obtained from Kanasewich (1975).

1) Reduction to the Pole

The inclination and declination of the earth's magnetic field varies at different locations on the earth's surface (Broome, 1986). Near the geomagnetic pole, the inclination is almost vertical, resulting in anomalies located directly over the causative bodies. However, as one moves away from the geomagnetic poles, the inclination becomes less vertical, causing the magnetic anomalies to become displaced with respect to their causative magnetic sources. Hence, any direct correlation of the magnetic anomalies with the geology may be misleading. A reduction to the pole removes the distortion caused by the earth's inclined magnetic field at that particular point, and presents the anomaly as it would appear at the geomagnetic pole (Baranov and Naudy, 1964). The resulting reduced to the pole map is shown in Figure (4-1). The other filter operators were then applied to the reduced to the pole map.

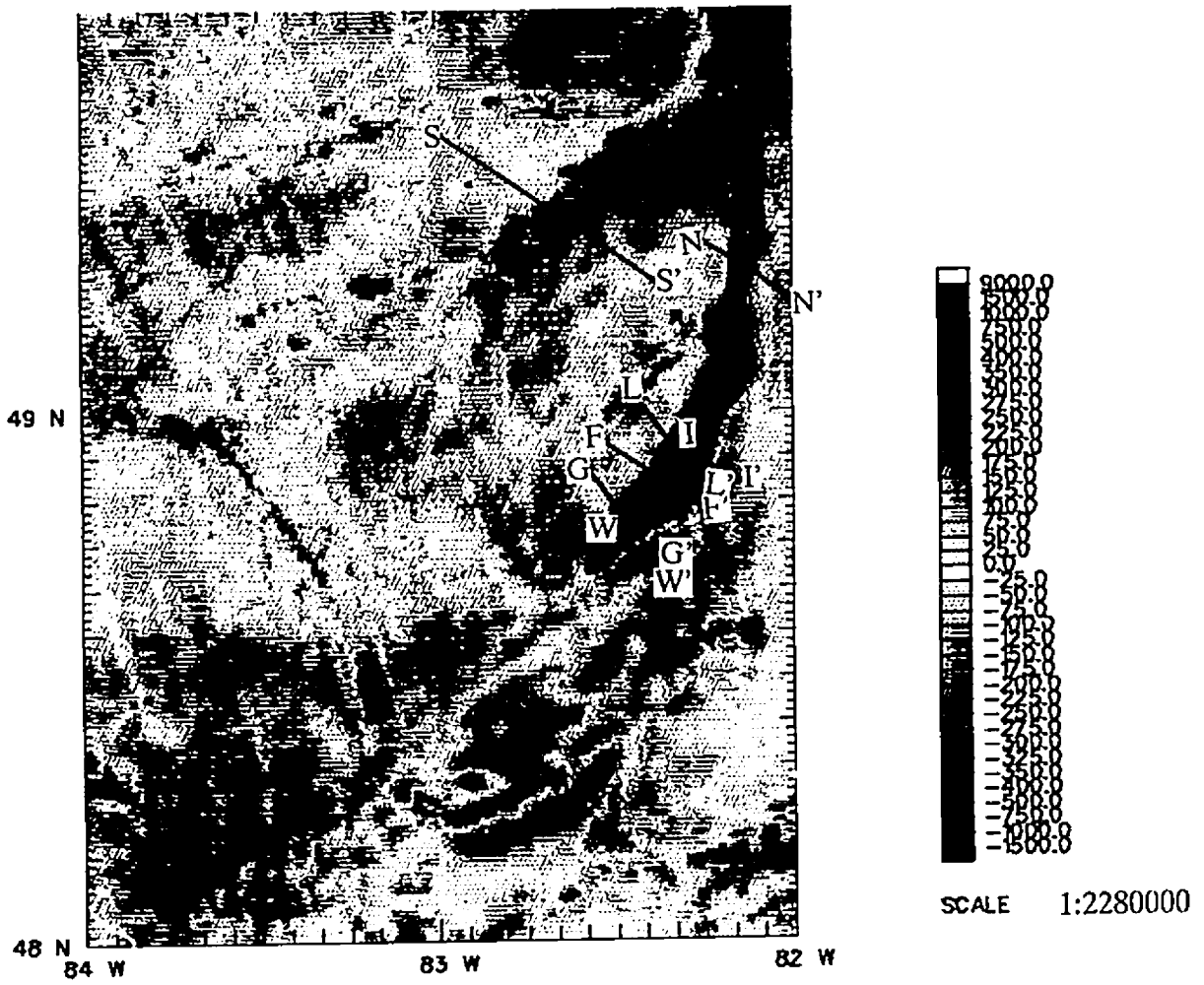

Figure 4-1. Reduced to the pole magnetic anomaly map of the KSZ with location of profiles used in modelling. A strong anomaly is associated with the GRB. Magnetic anomaly in nT.

2) Lowpass and Highpass Filters

Lowpass filters emphasize the long wavelength anomalies resulting from source bodies which are usually deep seated. By applying this operator to the data, the high wavenumber (short wavelength) information characteristic of near surface sources and also noise are attenuated. To produce the lowpass filtered maps (Figures 4-2 and 4-3) a two-dimensional Butterworth filter with a cut off wavelength of 50 km and a filter steepness of 12 dB/octave was used. An example of the frequency characteristic of a Butterworth lowpass filter is shown in Figure 4-4.

Conversely, the highpass filter accentuates the high wavenumber (short wavelength) information usually resulting from anomaly sources at or near the surface, while attenuating the low wavenumber (long wavelength) information. The resulting maps (Figures 4-5 and 4-6) may be more diagnostic of the local geology (Figure 4-7, transparency to overlay map is located in the back pocket) and emphasize the effects of density and susceptibility contrasts among the major rock types in the near surface geology. In the application of this filter, a cut off wavelength of 10 km was used (10 km was chosen because the average wavelength of the near surface sources is between 10-20 km) with a filter steepness of 12 dB/octave.

The filter steepness applied to the lowpass and highpass filters determines the range of wavelengths within the limit of the cut off wavelength to be passed. A filter steepness of 12 dB/octave was chosen because it provides a reasonable and smoother transition at the cutoff wavelength.

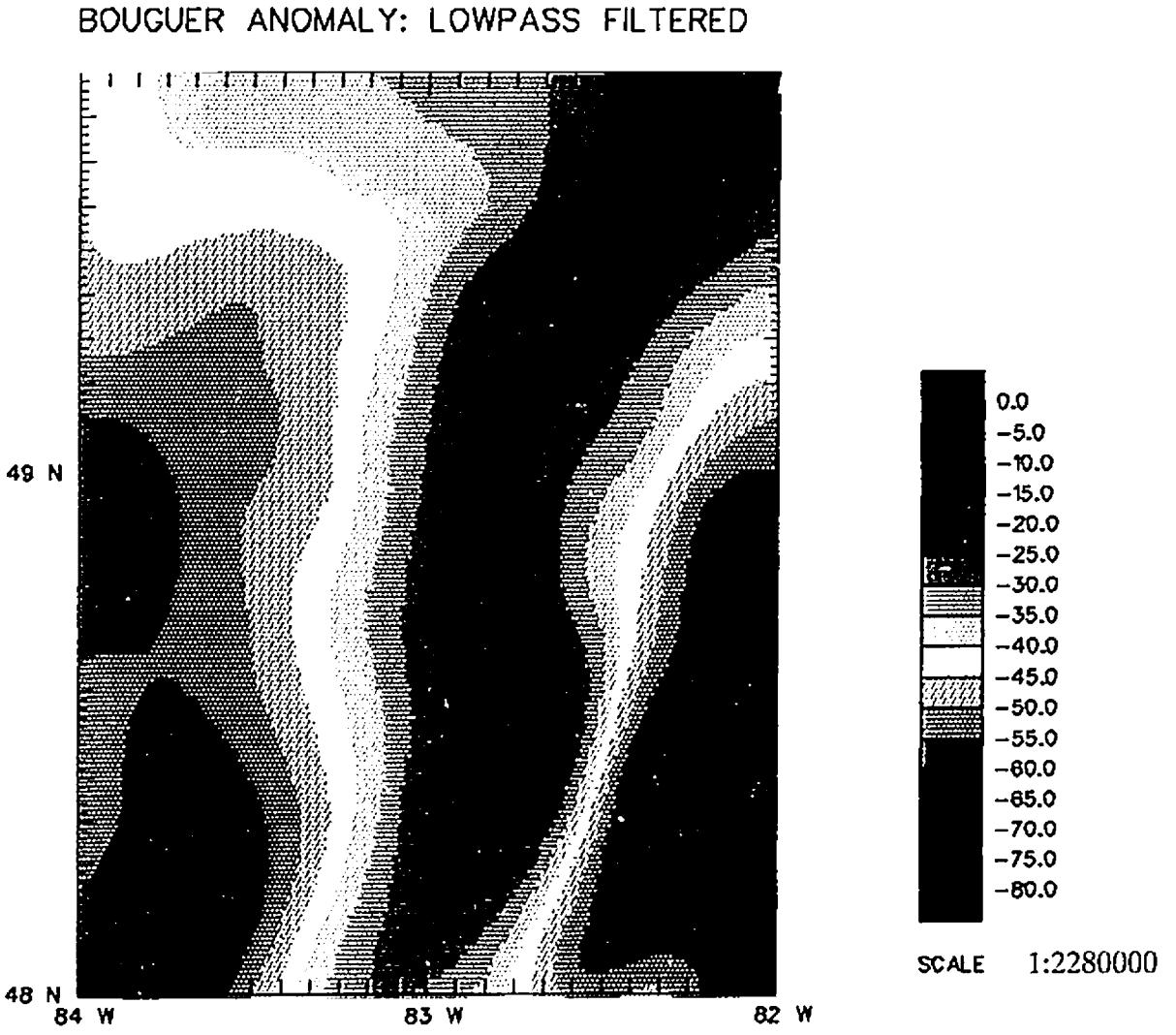

Figure 4-2. Lowpass filtered Bouguer anomaly map with cut off wavelength of 50 km and a filter steepness of 12 dB per octave. Gravity in mGals.

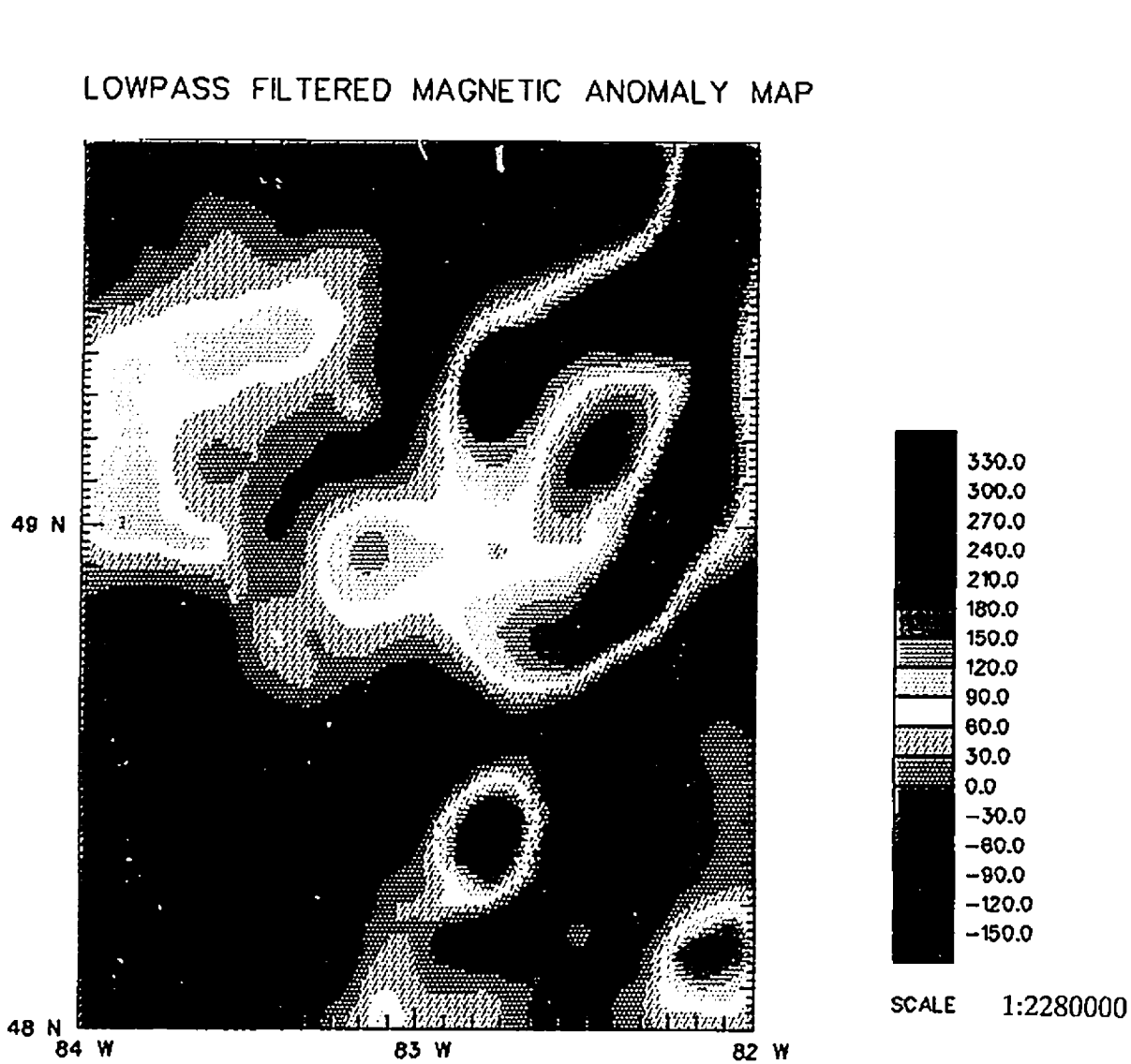

Figure 4-3. Lowpass filtered magnetic anomaly map with cut off wavelength of 50 km and filter steepness of 12 dB per octave. Magnetic anomaly in nT.

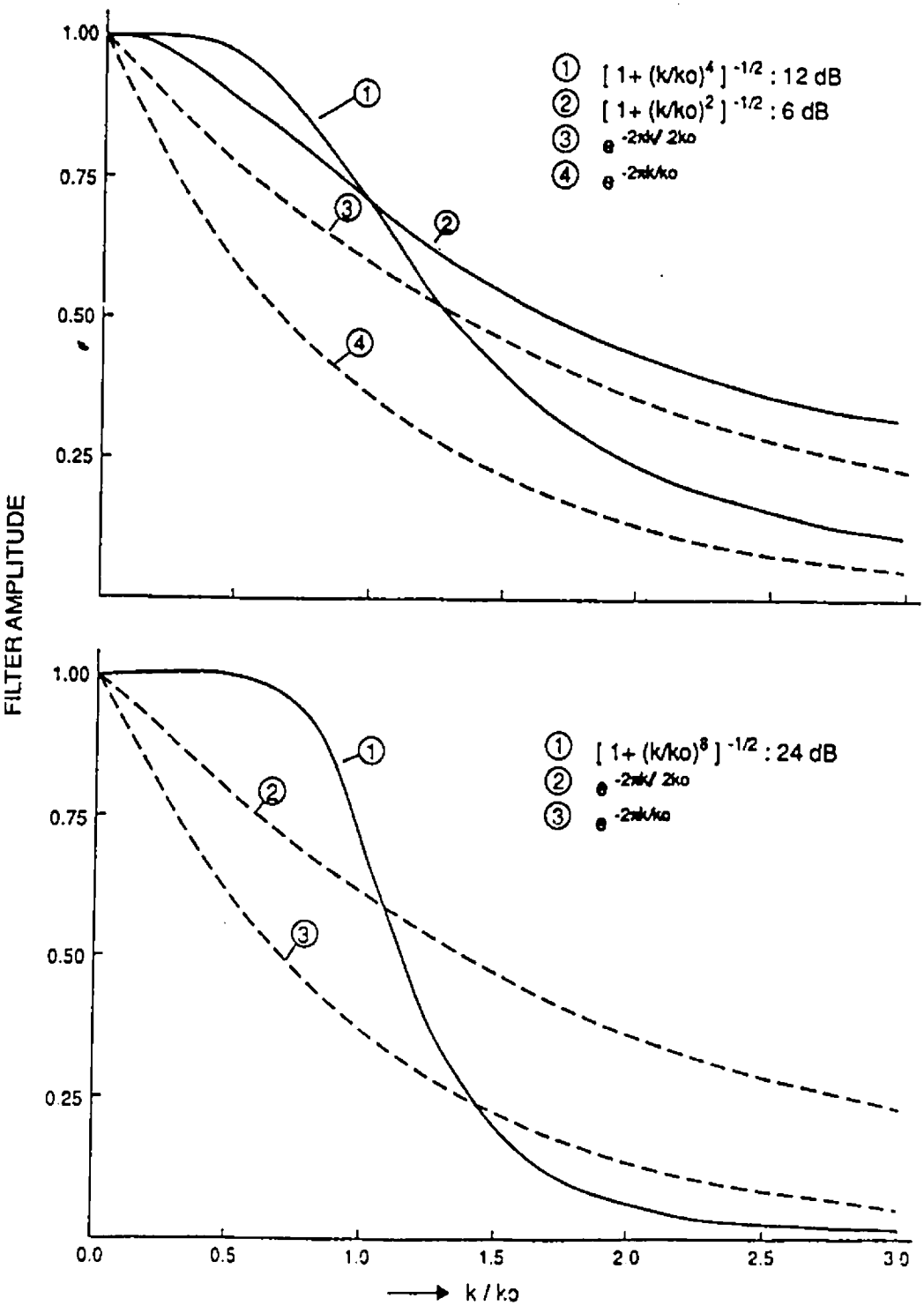

Figure 4-4. An example of a Butterworth filter with different filter steepness. The dashed lines are the upward continuation filters and the solid lines are the lowpass filters.

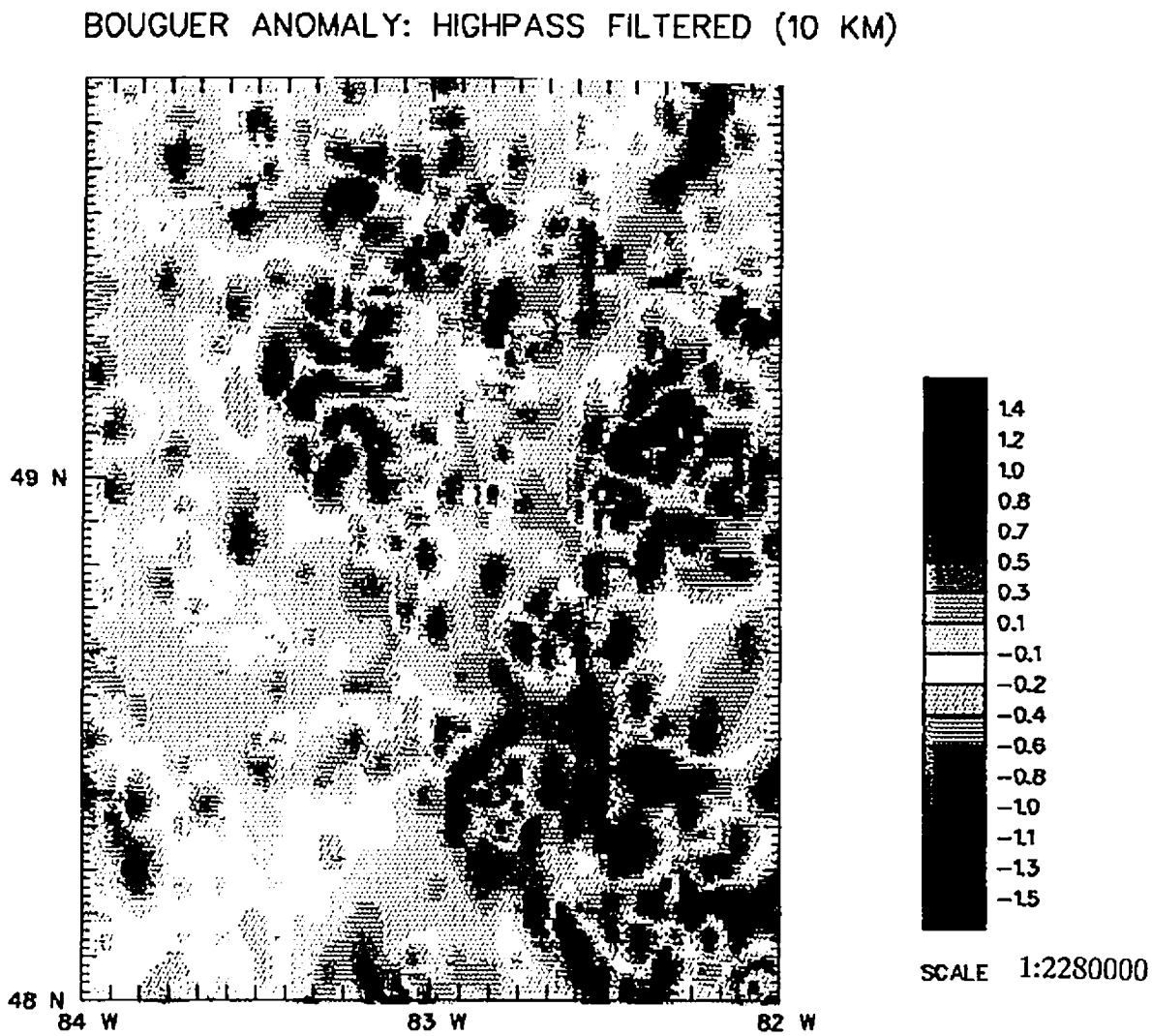

Figure 4-5. Highpass filtered Bouguer anomaly with a cut off wavelength of 10 km and filter steepness of 12 dB per octave. Anomalies from near surface sources are accentuated. Color interval is .02 mGals.

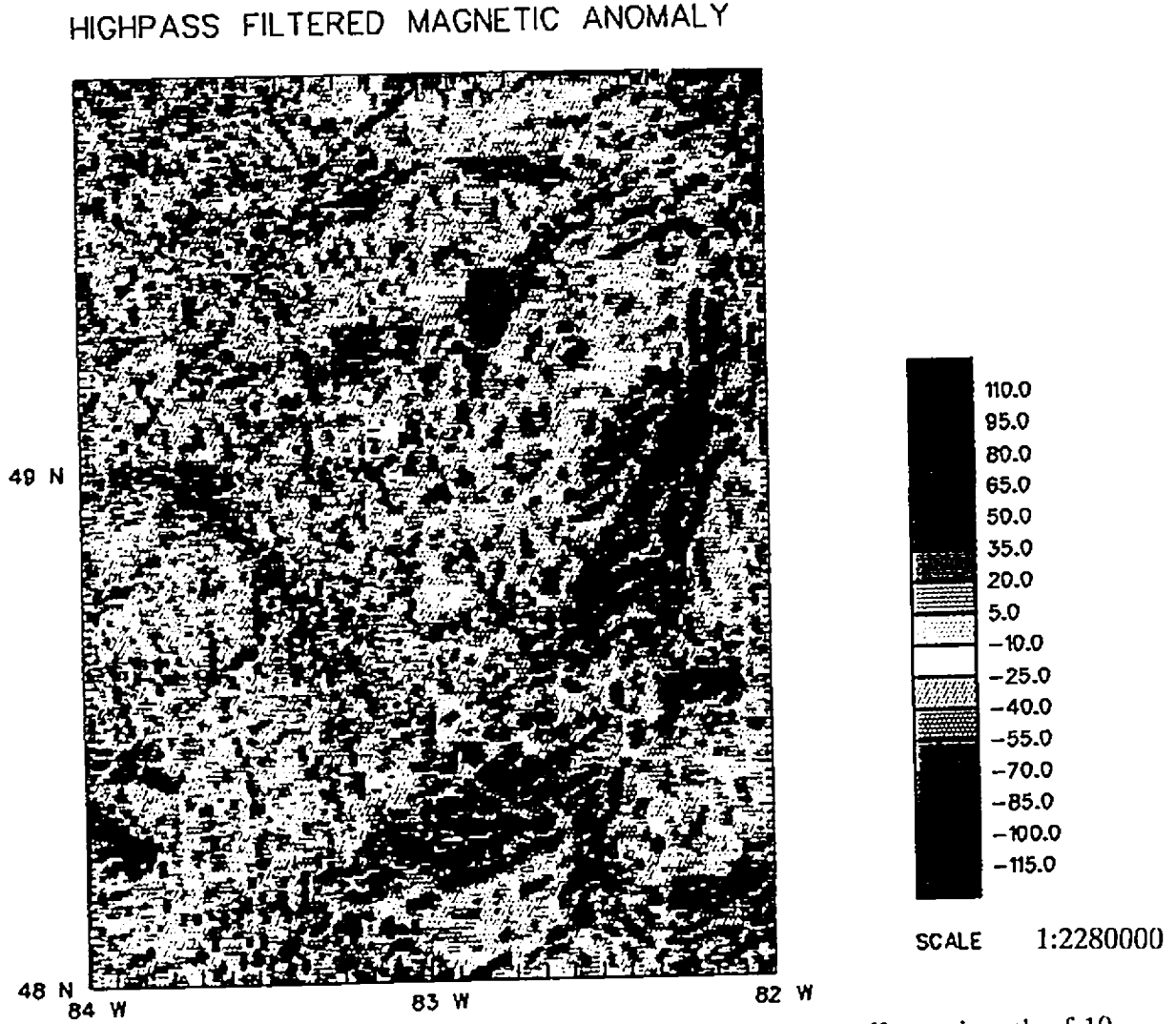

Figure 4-6. Highpass filtered magnetic anomaly map with a cut off wavelength of 10 km. Anomalies from near surface sources are accentuated. Magnetic anomaly in nT.

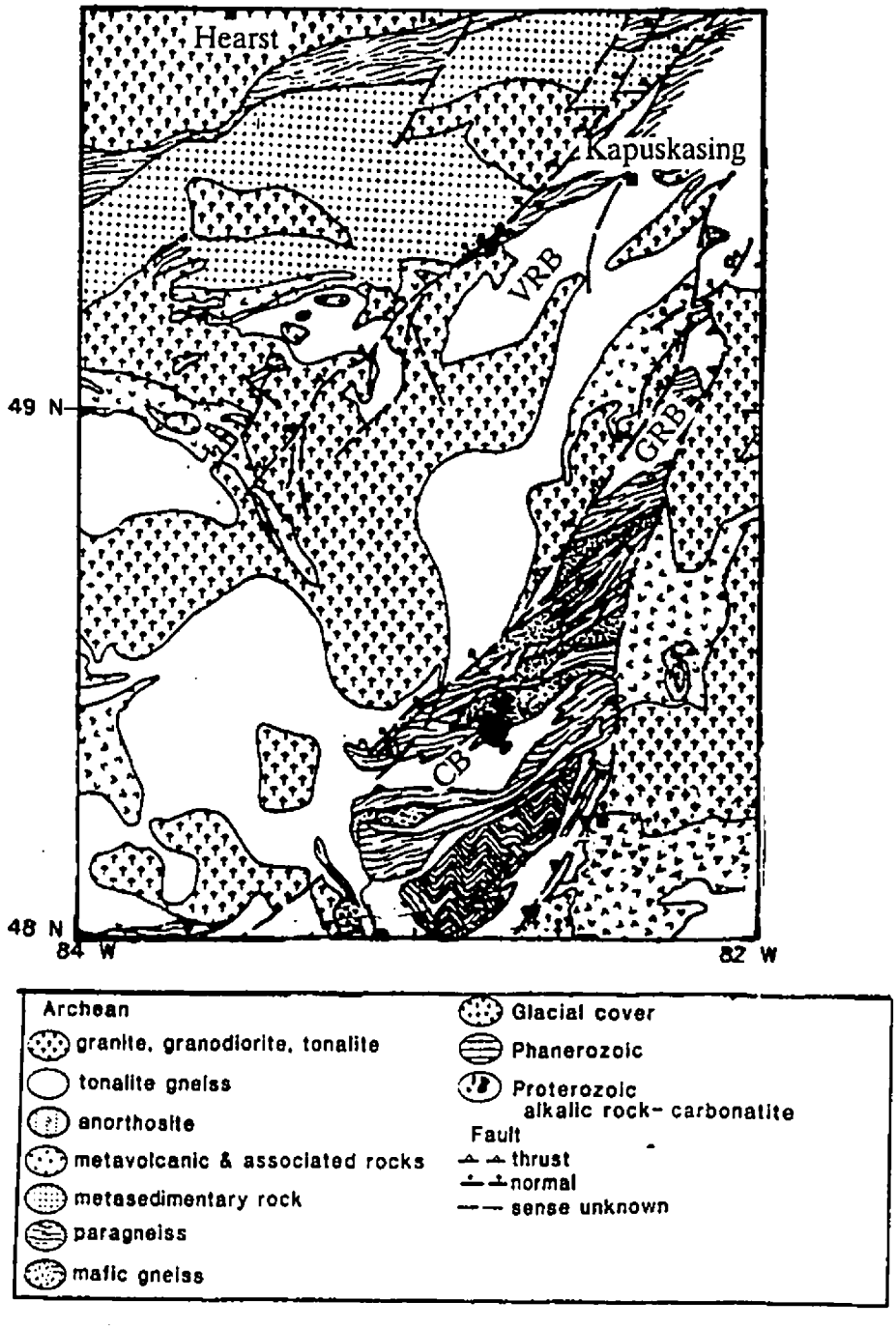

Figure 4-7. Geology map of the CB, GRB and VRB of the KSZ (adapted from Percival, 1990).

3) Continuation Filter

In applying continuation filters to the data sets, one is essentially obtaining the field at a level which is vertically displaced from the plane at which the observed data were collected (Telford et al., 1976; Dobrin and Savit 1988). The upward continuation filter transforms the potential field data measured on one surface to a higher surface and by so doing, suppresses the near surface anomalies and allows the regional field to be seen (Broome, 1986). In the resulting upward continued maps (Figures 4-8 and 4-9), anomalies with short wavelengths in the original data have been attenuated such that many of the remaining features are caused by sources from deeper levels. The upward continuation filter is thus comparable to the lowpass filter. As exemplified in Figure 4-4, the main difference between them results from the fact that for the same cut off wavelength, the lowpass filter contains more of the longer wavelength information and less short wavelength information than the upward continued filter.

4) Derivative Filters

Vertical derivative filters usually enhance local anomalies obscured by the broad regional anomalies. The first vertical derivative accentuates the high wavenumber component of the data by emphasizing gradients and in so doing accentuates the edges of anomalies. Because of noise amplification problems, results from the second vertical derivative filter are not presented. Figures 4-10 and 4-11 emphasize several local anomalies from dykes and intrusive bodies, that were otherwise obscured in the Bouguer anomaly map and the total field magnetic maps.

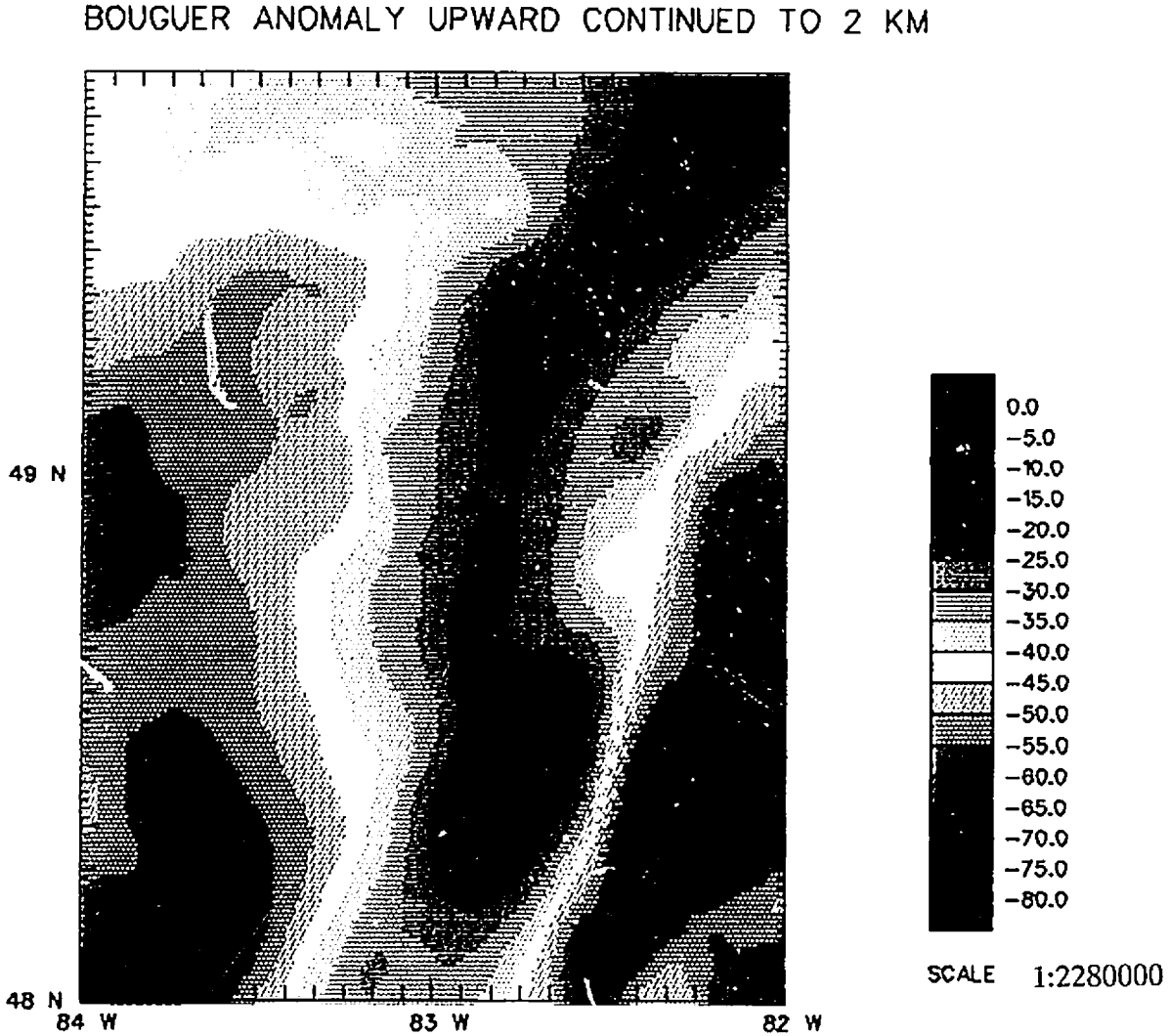

Figure 4-8. Bouguer anomaly map upward continued to 2 km. Gravity in mGals.

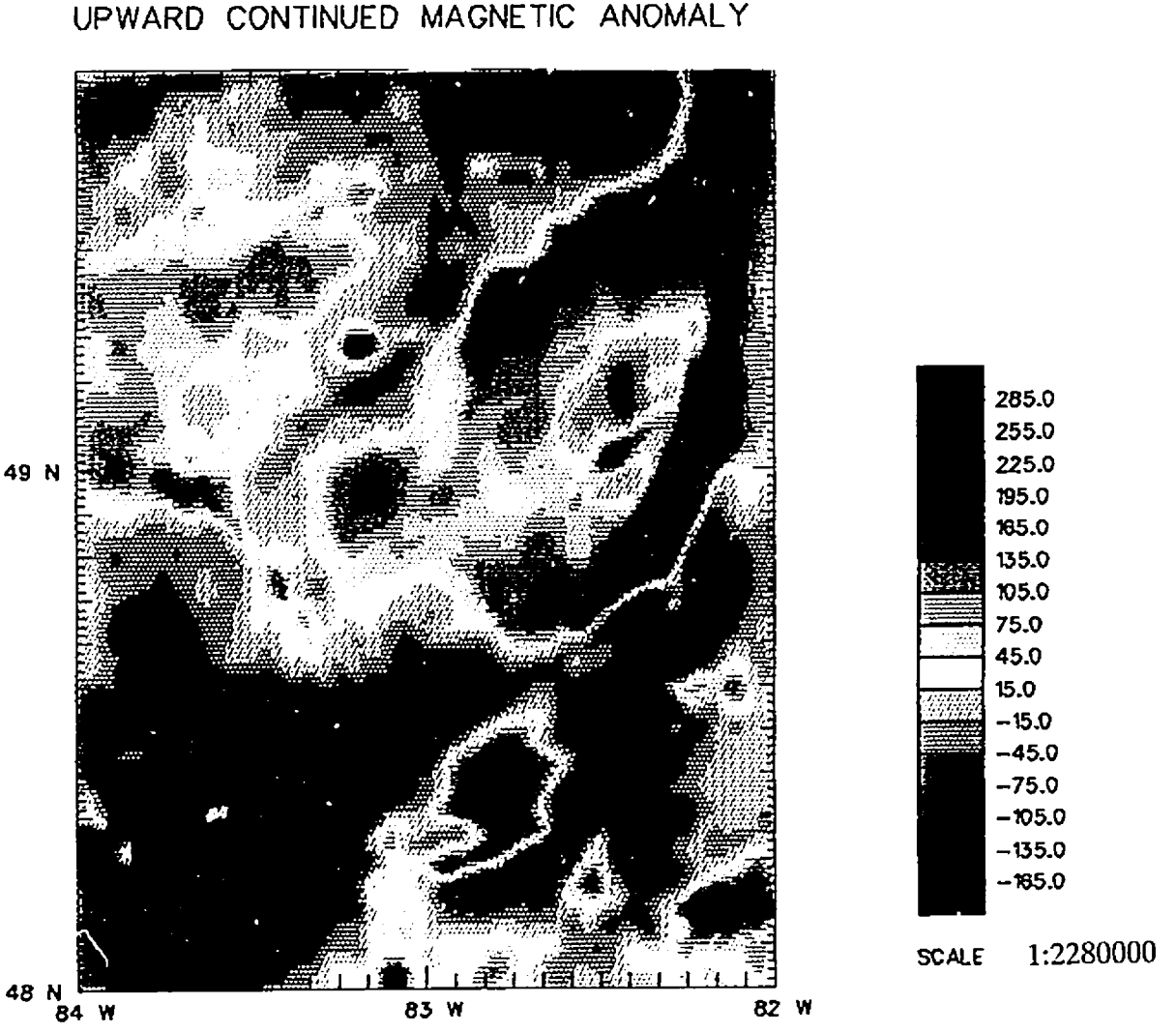

Figure 4-9. Magnetic anomaly map upward continued to 2 km. Magnetic anomaly in nT.

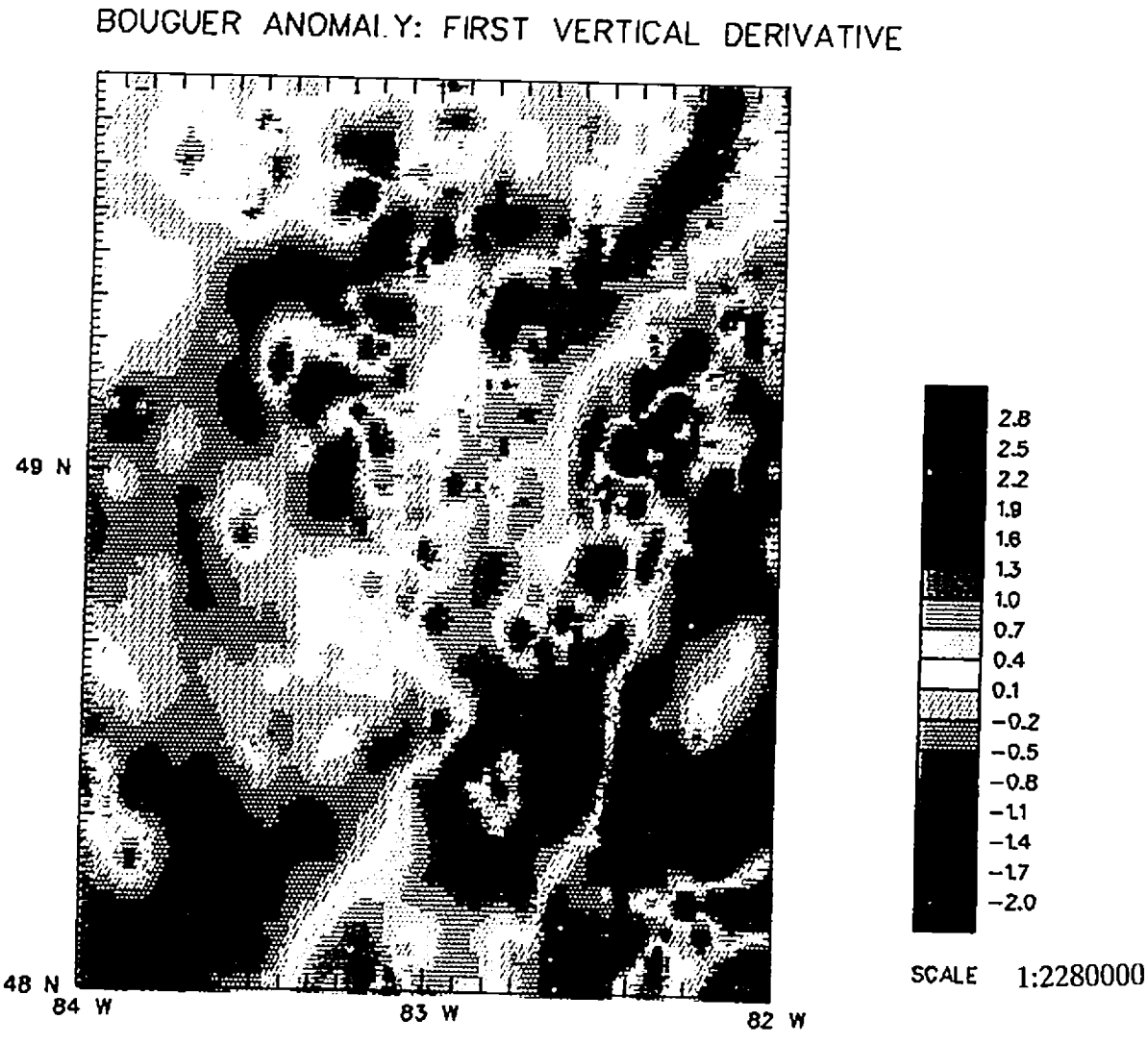

Figure 4-10. First vertical derivative of the Bouguer anomaly. Gravity in mGals/km.

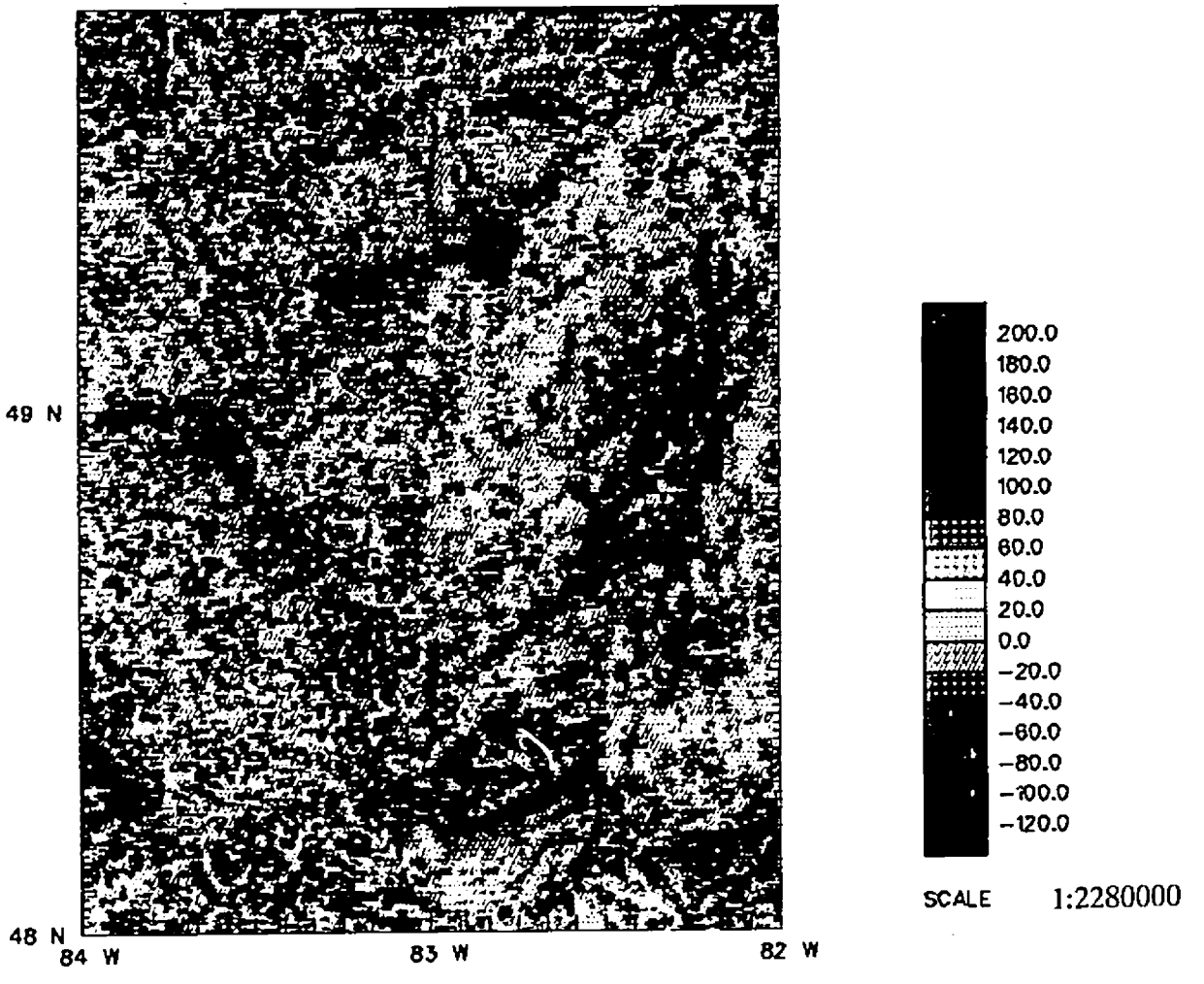

Figure 4-11. First vertical derivative of the magnetic anomaly. Magnetic anomaly in nT/km.

5) Inversion Filters

The density and magnetic susceptibility contrast mapping methods are inversion techniques which invert regional gravity and magnetic anomalies to lateral density and magnetic susceptibility contrasts in the crust (Grant, 1973; Letros, 1980; Letros et al., 1983; Urquhart et al., 1985; Yunsheng et al., 1985; Arkani-Hamed and Strangway, 1986; Arkani-Hamed and Verhoef, 1989). Both the density and magnetic susceptibility contrast maps (Figures 4-12 and 4-13) show better correlation with the geologic features (Figure 4-7) than the Bouguer anomaly (Figure 3-3) or total field magnetic anomaly maps (Figure 4-1). In the preparation of these maps, a regional field is usually removed and the data downward continued. However, to ensure stable downward continuation of the data, the data is first filtered using a bandpass filter.

The density contrast map (Figure 4-12) represents the lateral density variations in a layer between two flat surfaces (one at 0 km and the other at 6 km depth) that are needed to explain the observed anomalies. Six km was chosen as the depth extent of the major rock units observed in the surface geology. The density values obtained from this inversion are reasonable and are comparable to those obtained from laboratory measurements (Figure 3-5, Table 2). In the calculation of the magnetic susceptibility contrast map (Figure 4-13), it was assumed that the magnetization of the crust is parallel to the present geomagnetic field direction, that the bodies are vertical sided, and that the susceptibilities vary laterally but not vertically within the magnetic source layer. The resulting susceptibility contrast map

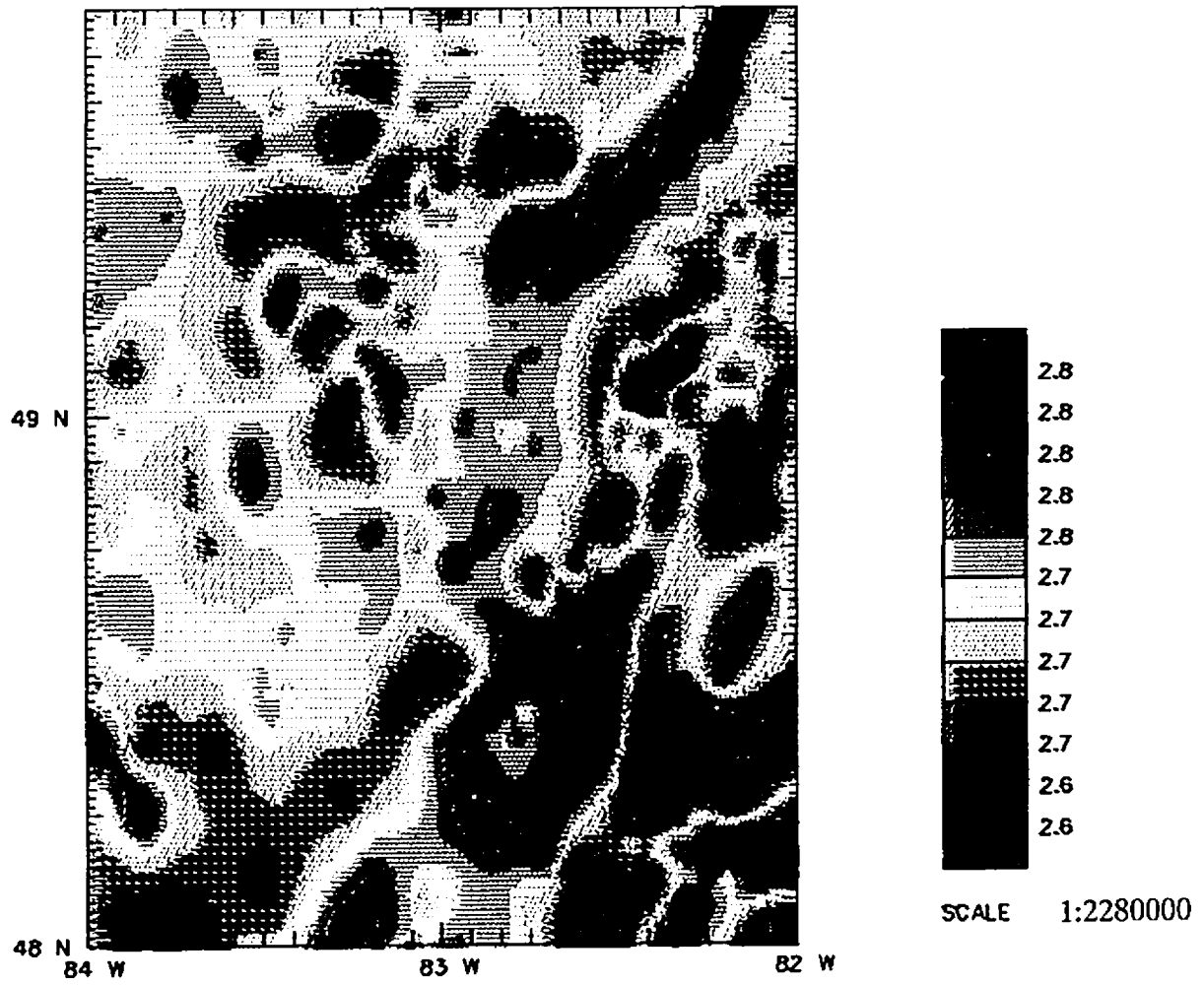

Figure 4-12. Density contrast map from inversion of gravity data. Color interval is .02g/cm^3.

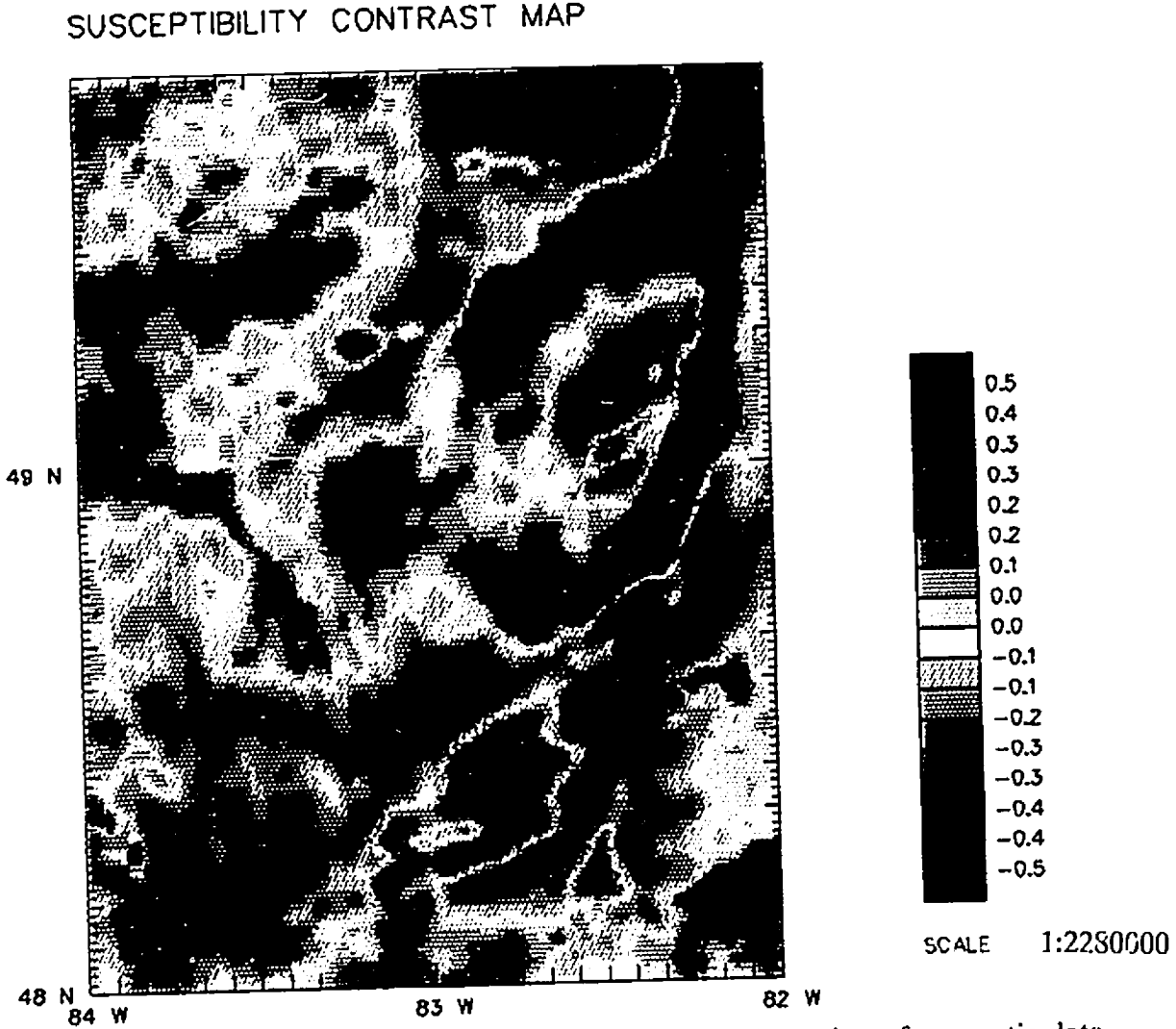

Figure 4-13. Magnetic susceptibility contrast map from inversion of magnetic data. Susceptibilities in SI units x 10^{-3}.

should be closely related to the geology. However, the danger of this method is that if the geology of the area does not fit the above assumptions, and if a significant remanent magnetization exist in the area, then the magnetic susceptibility values calculated may not correctly correlate with the geology.

4.3 DESCRIPTION OF GRAVITY AND MAGNETIC ANOMALY MAPS

4.3.1 Introduction

Many of the anomalies on the gravity and magnetic anomaly maps can be correlated with geologic features observed at the surface. However, there are others that do not correlate with surface geology and thus are due to sources deeper within the crust. Also apparent is the fact that some of the geologic features are associated with both a gravity and a magnetic signature. However, there are others that have a high gravity anomaly but subtle magnetic anomaly and vice versa. A quantitative correlation can be obtained using Poisson's relation, which relates the gravity anomaly of a body with a certain density to the magnetic anomaly caused by the same body with a certain susceptibility (c.f. Grant and West, 1965). This relation gives that the first vertical derivative of the gravity anomaly equates to the reduced to the pole magnetic anomaly (except for a constant). Therefore, a comparison of the Figures 4-10 with 4-1 will illustrate common sources for the gravity and magnetic anomalies.

To compare both maps quantitatively, a correlation map for the area was calculated (Figure 4-14) based on a quantitative technique developed by Arkani-Hamed and Strangway (1986) to identify features common between two maps. The

correlation coefficient η, which determines the degree of correlation between the vertical derivative of the gravity field and the magnetic anomaly was calculated by a modification of the formula from Arkani-Hamed and Strangway (1986) as follows:

$$\eta_{nm} = \frac{\sum\sum fg}{\left(\sum f^2 \sum g^2\right)^{1/2}} \qquad (4\text{-}1)$$

where $f(x,y)$ and $g(x,y)$ denote the magnetic and gravity anomalies, respectively, at a point with rectangular coordinates x and y, Σ denotes the summation of all the values within the window and *nm* denotes the position of the point in the window. The correlation map of Figure 4-14 was calculated by using the first vertical derivative map of Figure 4-10 and the reduced to the pole magnetic anomaly map of Figure 4-1 as input. For this, the correlation between both maps for each point is calculated inside a window around the point. The size of the window selected depends on the data distribution and the average wavelength of the anomalies of interest. With this in mind 5 km was selected as an appropriate size for the window. In the correlation map (Figure 4-14), areas with high correlation have a coefficient close to -1 or 1 and those with low correlation or no correlation have a coefficient equal or close to 0. A positive correlation suggests that the density and susceptibility of the source body are both "positive", while a negative correlation suggest that one of these properties is "negative". Figure 4-14 shows that the correlation coefficient of the entire study area is between 0.7 and -0.7, suggesting a common source for the gravity and magnetic anomalies.

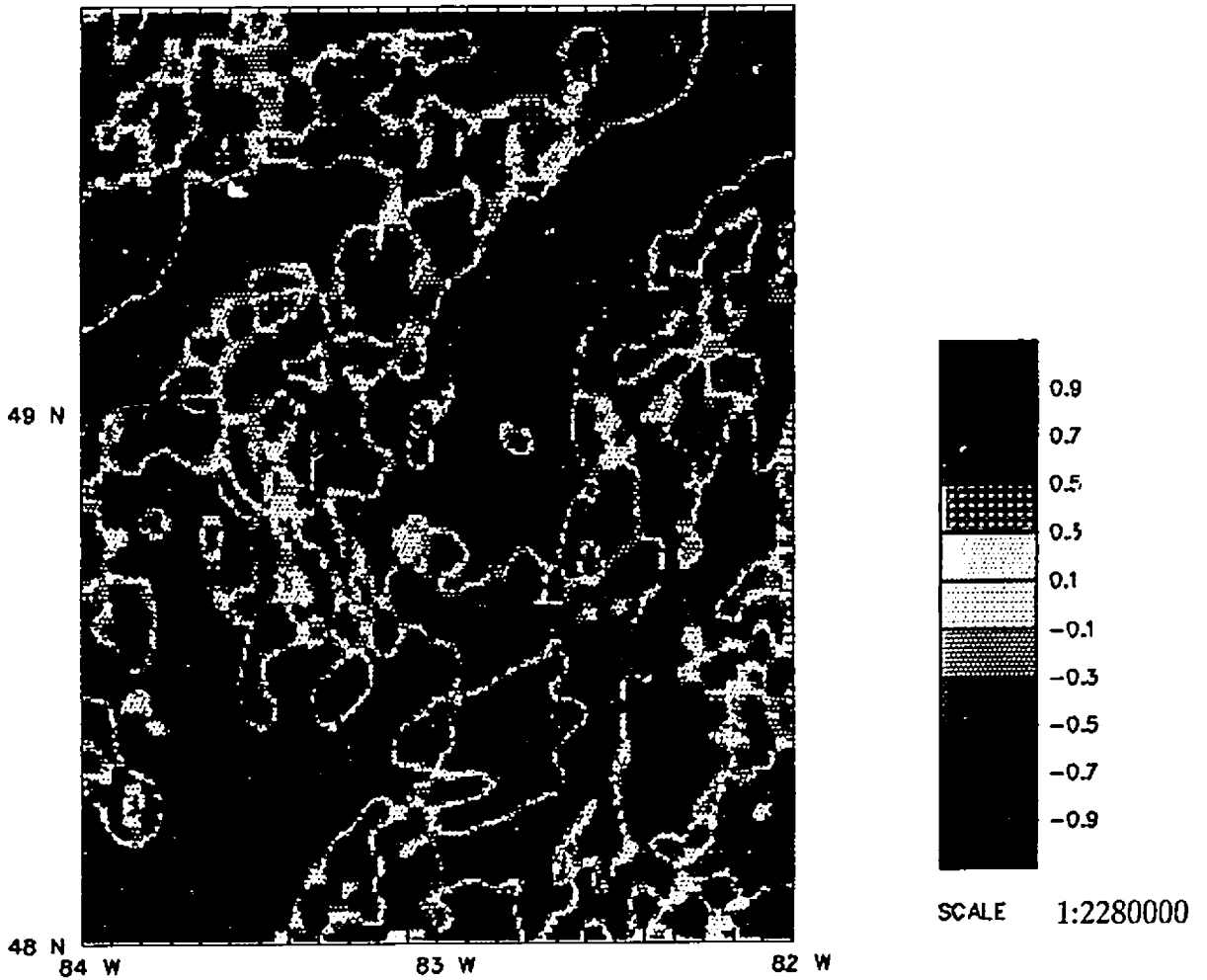

Figure 4-14. Correlation coefficient map.

4.3.2 Val Rita Block

Structural features within the VRB are more clearly defined on the magnetic anomaly maps than on the gravity anomaly maps. The most prominent feature within this block is the arcuate gravity anomaly (Figure 3-3) which also coincides with an arcuate magnetic anomaly (Figure 4-1). Although the arcuate magnetic anomaly is less pronounced on this latter figure, it is extremely striking in the susceptibility contrast map (Figure 4-13). A comparison of the Bouguer anomaly map (Figure 3-3) with the density map (Figure 3-6) and the geology map (Figure 4-7), shows that the arcuate VRB gravity anomaly is seemingly associated with lower density rocks (amphibolite facies tonalites and granodiorite gneisses with an average density of 2.73 g/cm^3) at the surface. This is well illustrated in Figure 4-15, where the high gravity anomaly of the VRB is associated with lower measured densities. The only high density rocks within this block are local occurrences of granulite facies paragneiss (with an average density of 2.86 g/cm^3) along the LF, just north of Highway 11 (Figure 4-7). The lack of correlation between the density and gravity profiles (Figure 4-15) suggests that the source of the gravity anomaly is buried.

Laboratory susceptibility measurements of rocks from this block (Table 2) show generally low values which may not be sufficient to explain the magnetic anomaly, also suggesting that the source bodies may be buried. The correlation map (Figure 4-14) shows high correlation coefficient values over the region of arcuate gravity anomaly, suggesting a common source for both gravity and magnetic anomalies. Therefore granulites similar to those exposed along the LF may underlie

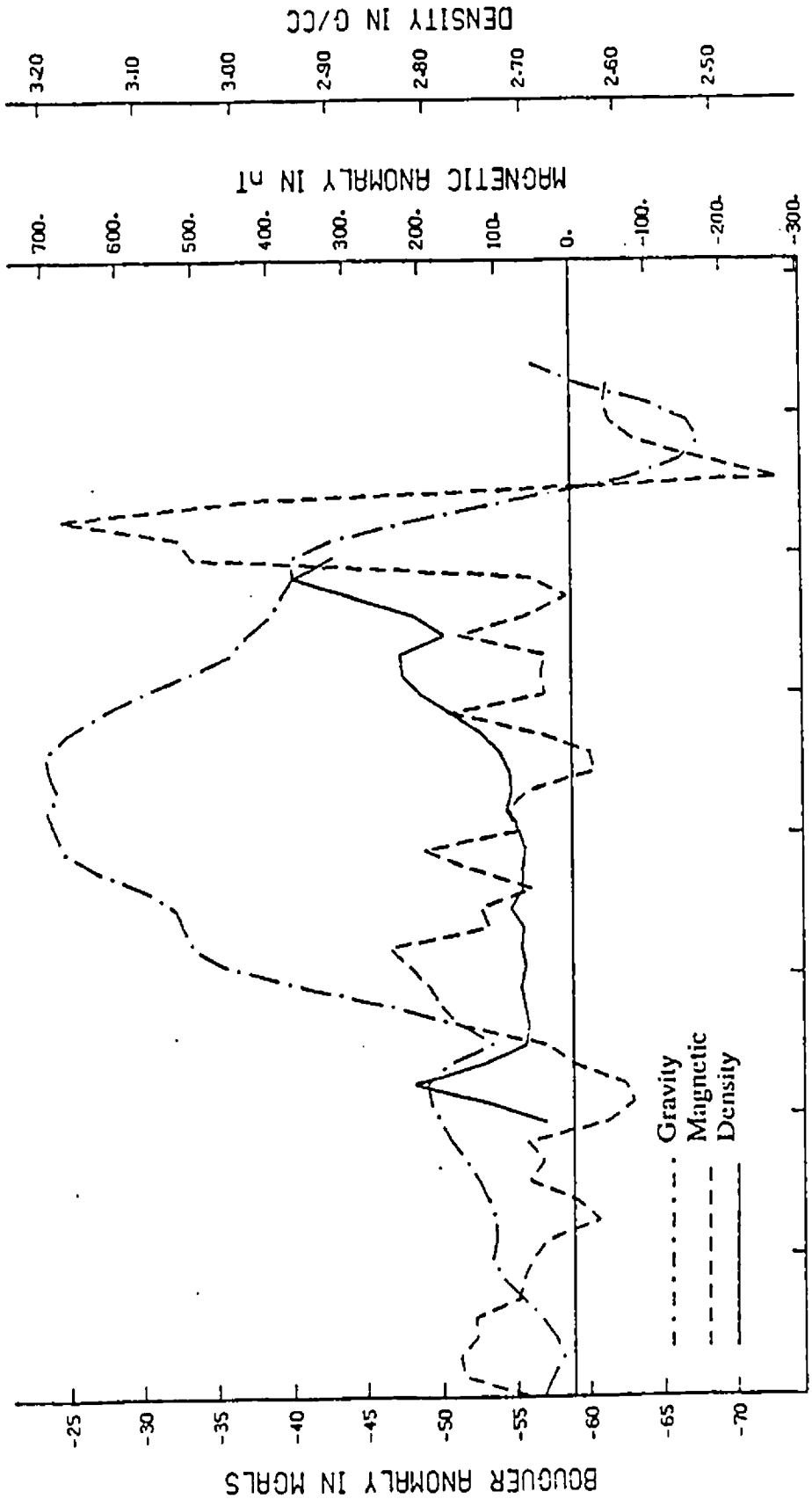

Figure 4-15. Comparison of gravity, magnetic and density (density from gridded data) data within the VRB and GRB (along Profile E-E', see Figure 5-1 for profile location).

the amphibolite facies gneisses of the VRB (Percival and McGrath, 1986; Nkwate and Salisbury, 1988) and may be responsible for both the gravity and magnetic anomalies of the VRB.

The amplitude of the arcuate gravity and magnetic anomaly of the VRB decreases southwards, which may relate to an increase in depth to the source bodies. The persistence of this feature in the lowpass (Figure 4-2) and upward-continued maps (Figure 4-8) as a strong feature suggests that these granulites may be fairly thick and extensive along strike. The long wavelength component of the magnetic anomaly map (Figures 4-3 and 4-9) reveals a doughnut-shaped structure underlying the VRB, with a magnetic low in the center and highs over the GRB and eastern VRB. This ring-shaped structure may correspond to an anticline (magnetic high) and syncline (magnetic low) at depth.

Several small gravity highs with corresponding magnetic highs are located along the axis of the regional gravity high and are correlated with carbonatite complexes on the geology map (Figure 4-7). These carbonatite complexes are particularly interesting because, like other carbonatite complexes in the region, their spatial occurrence is closely related to the axis of the KSZ gravity high. The structural significance of this relationship will be discussed later.

Density measurements of carbonatite samples from the Cargill complex gives values of 2.74g/cm^3, compared to 2.73 g/cm^3 for the surrounding amphibolite facies gneisses, which suggests that the carbonatites themselves are not responsible for the anomalies. Maclaren et al., (1968), Leclair and Poirier (1989) and Lewchuk and

Symons (1990) indicate that the carbonatite complexes are usually associated with other mafic intrusives such as pyroxenites and gabbros, which are quite dense (2.9-3.02 g/cm^3). It is thus probable that these mafic intrusives and not the carbonatite bodies are responsible for the anomalously high gravity anomalies observed over these complexes.

Magnetic anomaly values over these carbonatite complexes are as high as 9000 nT. Susceptibility values are not available for the carbonatites, but Maclaren et al., (1968) note that the alkali syenites of the Clay Howells carbonatite complex are rich in magnetite. Therefore, it is probable that the presence of substantial amounts of magnetite and other magnetic minerals within the carbonatite complexes may be largely responsible for their magnetic anomalies.

A strong magnetic gradient occurs at the western limit of the VRB and is correlated with the LF (Figures 4-1, 4-7). This gradient separates the generally low magnetic anomaly values to the west within the QB, from high values within the VRB. Anomalies within this block are at least 300nT higher than values within the QB. The gradient associated with the LF extends southwest in the WGT, terminating into a series of splays (Figures 4-1, 4-6 4-7 and 4-11).

Numerous north to northwest trending belts of linear magnetic anomalies are present in the QB and WGT, west of the VRB (Figures 4-1, 4-6, 4-11, 4-13). These anomalies, which correlate with the Hearst-Matachewan dyke swarms, are accentuated on the short wavelength maps (Figures 4-6 and 4-11) and attenuated on the long wavelength maps (Figures 4-3 and 4-9). Also present on these maps are

several northeast trending dykes which correlate with the Abitibi swarm and occasionally cut the northwest trending swarm. Unlike the magnetic anomaly maps, the gravity anomaly maps west of the VRB show no particular features of interest within the QB and WGT, (Figures 3-3, 4-5, 4-10 and 4-13). This may result from the sparse data coverage in this region of the study area (Figure 3-2). Correlations between the gravity and magnetic maps are also generally low within this region (Figure 4-14).

4.3.3 Groundhog River Block

As can be seen in Figure 3-3, the GRB (Figure 4-7) does not display a distinctive gravity anomaly. Profiles in the area show only a small (5 mGal) anomaly associated with the GRB, compared to a 25-35 mGal amplitude over the VRB. However, the small gravity anomaly coincides with a very strong magnetic anomaly (Figure 4-1), which is stronger than those of the other blocks in the region and displays values at least 500 nT above the regional background.

Recent geologic mapping within the GRB (Leclair and Nagerl, 1988; Figure 4-7), suggests that this block consists of upper amphibolite to granulite facies mafic gneiss, paragneiss and tonalite gneiss in almost equal proportions. Laboratory density measurements (Table 1) of rocks from this block and the resulting density map (Figures 3-5 and 3-6) give average density values of the paragneisses and mafic gneisses of 2.86g/cm^3 and 3.05 g/cm^3 respectively. Since the gravity and the density data for the GRB appear to be inconsistent (Figure 4-15), Percival and McGrath

(1986) suggested that the high density rocks are either not representative of the rocks in the block, or the GRB must be very thin. The additional gravity and density data obtained for this block and the separation of the Bouguer anomaly map into two wavelength components have provided additional insight into the nature of this block. Although Figure 3-3 does not show a distinctive gravity anomaly associated with the block, an anomaly is expressed in the high pass (Figure 4-5), first derivative (Figure 4-10) and density contrast (Figure 4-12) maps. Since these short wavelength maps presumably show anomalies from near surfaces sources, this implies that the source for the gravity anomaly within this block is found only in the shallow crust.

Susceptibilities of rocks from this block (Table 2) show values that are generally higher than those of the other blocks, the median value of 3.05×10^{-3} emu/cm^3 probably being sufficient to explain the magnetic anomaly. Previous studies of the GRB anomaly (Maclaren et al., 1968) and the Koenigsberger ratio calculated for the rock samples from this block (Table 2) suggest that the induced magnetization may be enhanced by a strong component of remanent magnetization. The correlation map shows high correlation with positive and negative coefficient values within this block. A comparison of this map with Figure 4-7 suggests that areas underlain by mafic gneisses coincide with a positive correlation coefficient value, while areas underlain by tonalites have a negative correlation coefficient value. Although this alternation from positive to negative correlation coefficient values may also imply a change in the polarity of the magnetization along the strike of this block, there is no evidence in this study to suggest that this is indeed the case.

The GRB is bounded to the west and separated from the VRB by the northeast trending belt of linear anomalies coincident with the SLF. Although its eastern boundary, defined geologically by the ILCZ (Figure 4-7) is not apparent on the Bouguer anomaly map of Figure 3-3, it can be traced on the short wavelength maps of Figures 4-5 and 4-10, and also on the magnetic anomaly and susceptibility contrast maps (Figure 4-1 and 4-13). In fact, the mere knowledge of its existence as the eastern boundary of this block is deduced from its aeromagnetic expression (Leclair and Poirier, 1988; Percival and McGrath, 1986).

The southern limit of the GRB is sharply defined by the northeast trending WRF (Figure 4-7). The strong magnetic anomaly of the GRB (Figure 4-1) is abruptly terminated against this fault. In Figure 3-3, this boundary is not clearly defined but corresponds to the deviation of the gravity anomaly from the CB into the VRB in Figures 4-2 and 4-8. However, in Figures 4-5, 4-10 and 4-13 no such discontinuity is associated with this fault; instead, the gravity anomaly from the CB extends uninterrupted into the GRB. It is not possible from the gravity maps to determine if the WRF terminates against the ILCZ or if it continues across it. Consequently, the relative ages of the faults cannot be determined. However, interruptions in the magnetic anomaly pattern (on the regional maps) within the AB, and along the strike of the northeasterly extension of this fault suggest that the WRF may extend far into the AB, implying that the fault is younger than the ILCZ.

The WRF also represents a major shift in the magnetic level from north to south, with higher levels within the GRB and VRB and lower levels in the CB and

WGT to the west. Changes in the geophysical characteristics across this fault have prompted some investigators (e.g., Leclair, 1990) to suggest that the GRB and CB are two geophysically distinct blocks. The WRF may therefore play an important role in the structural evolution of the KSZ.

The Abitibi belt to the east of the GRB is characterized by very low gravity values (Figure 3-3). An irregular, oval shaped anomaly is correlated with a granodiorite body (Figure 4-7).

4.3.4 Chapleau Block

In the Bouguer anomaly map (Figure 3-3), the CB is characterized by a gravity high flanked on either side by gravity lows forming a paired gravity anomaly, which is characteristic of the gravity anomalies across exposed continental crustal cross sections (Fountain and Salisbury, 1981). The high gravity anomaly within this block is correlated with dense granulite facies mafic gneiss, paragneiss and anorthosite (Figure 4-7). The carbonatite complexes (Figure 4-7) within this block are not associated with a distinct gravity high, and are expressed on the short wavelength maps (Figures 4-5 and 4-10) as gravity lows.

The pronounced gravity anomaly of the CB coincides with a generally more subtle magnetic anomaly, except for the areas surrounding the carbonatite complexes (Figure 4-7). However, several northeast trending belts of linear magnetic anomalies are apparent within this block and are attributed to northeast- striking units of mafic gneiss. The attenuation of these anomalies in Figures 4-3 and 4-10, suggests that the

magnetic source layers for these units are thin. Measured susceptibility values from this block (Table 2) are generally less than those of the GRB, except for one sample (N210-1-87), which has a high susceptibility (6×10^{-3} emu/cm^3). The correlation map (Figure 4-14) shows fairly low correlation coefficient values within this block, except for the region of mafic gneiss (Figure 4-7) surrounding the carbonatite complexes, and the area within the Shawmere anorthosite complex.

The CB is bounded to the west by the northeast striking SLF (Figure 4-7). Linear gravity anomalies associated with this fault (Figure 3-3) are well expressed within the CB and have a gentle gradient, such that the gravitational expression of the boundary between the CB and the WGT is gradual rather than abrupt. In Figures 3-3 and 4-10, northeast striking anomalies coincident with the ILCZ (Figure 4-7) characterize the eastern boundary of the CB. Unlike the western boundary, the ILCZ is characterized by steeper gradients, suggesting that the boundary between the CB and the AB is more abrupt.

The boundary zones of the CB are not as well defined on the magnetic anomaly map (Figure 4-1) as they are on the gravity anomaly map Figure (3-3). The SLF which forms the western boundary is characterized by a weak discontinuity (Figure 4-1) which separates the low magnetic anomalies of the WGT from the relatively moderate magnetic anomalies of the CB. Similarly, the eastern boundary of this block, which is defined by the ILCZ (Figure 4-7), is more complex than that along the GRB in that it displays two fault traces rather than one (Figures 4-1, 4-6, 4-10 and 4-13).

The AB to the east of the CB is characterized by a gravity low (Figure 3-3) which corresponds to a granodiorite body on the geology map (Figure 4-7). Several areas associated with metavolcanics, however (Figure 4-7), display moderate gravity anomalies (Figures 4-5, 4-10 and 4-12) with corresponding magnetic highs (Figures 4-1, 4-11 and 4-13). The attenuation of these anomalies in the lowpass (Figures 4-2 and 4-3) and upward continued maps (Figures 4-8 and 4-9) suggests that they may be limited to shallow levels of the crust. Figure 4-14 shows high correlation coefficients associated with these bodies, implying a common source for the gravity and magnetic anomalies.

4.4 CONCLUSIONS

Generally, there is a good correlation between the geology and the potential field maps and also between the different potential field maps. The correlation coefficient map enables the detection of those sources which may be responsible for both the gravity and magnetic anomalies. Tables 1 and 2 show that in most cases the density and susceptibility values are consistent with the anomalies observed over the different blocks and rock units of the KSZ. However, in certain areas the correlation between the geology and potential field maps is poor. For example, the strong gravity anomaly of the VRB is inconsistent with measured densities at the surface (Figure 4-15) and the relatively strong magnetic anomaly is also inconsistent with the low susceptibilities of the surface rocks. These observations suggest that the source for the dominant potential field anomalies in the VRB is buried. Furthermore, the

correlation map shows high correlation coefficient values over this block, suggesting a common source for the gravity and magnetic anomalies.

CHAPTER FIVE: POTENTIAL FIELD MODELS

5.1 INTRODUCTION

The interpretation of gravity and magnetic anomalies involves the construction of density and magnetization models that are consistent with the geology of the area. Synthetic anomalies are then calculated from these models and matched with the observed potential field anomalies until a fit is obtained.

The strong contrast in densities and susceptibilities between the Kapuskasing-related rocks and the adjacent areas gives rise to prominent gravity and magnetic anomalies (Figures 3-3 and 3-4) which can be modelled to obtain the structure of the KSZ at depth. In this chapter, several two-dimensional gravity and magnetic models will be developed to determine the crustal structure of the different tectonic blocks. A three-dimensional gravity model will also be constructed to determine the applicability of the two-dimensional models and to provide further insights to the structure of the KSZ.

5.1.1 Previous Potential Field Models

Percival and McGrath (1986) recently modelled potential field data from the various blocks of the KSZ assuming that the source bodies were restricted to the upper 25 km of the crust. On the basis of this modelling, they suggested that uplift of granulites along the Lepage Fault is responsible for the positive gravity anomaly within the VRB. Studies within the GRB, however, showed conflicting results

between the gravity and magnetic models. The gravity models suggested a thickness of less than 1 km for this block, while the magnetic models suggested that it was at least 5 km thick. They could not resolve the conflict between the two results in the absence of appropriate constraints (e.g., seismic, density, susceptibility, additional gravity data and geology). Furthermore, the deviation of the CB gravity anomaly into the VRB rather than the GRB (Figure 3-3) also raised questions concerning the relationship between these blocks that could not be resolved. Many of the interpretational problems faced by these authors resulted from the lack of suitable constraints available at the time of their investigation. This study seeks to provide solutions to some of these problems given new data and better constraints.

5.1.2 Constraints

Inherent in the interpretation of potential field anomalies is the problem of non-uniqueness, such that a model produced is usually not a unique solution to the problem, but is one of several possible solutions. However, when both gravity and magnetic models are obtained for the same area, they provide additional constraints on geologic models and reduce the problem of ambiguity.

Until recently, most geological studies within the KSZ (especially in the GRB and VRB areas) have been reconnaissance in nature. However, with the advent of the Canadian LITHOPROBE program, the region has received wide scientific attention. The result is a large geological and geophysical data base, which has provided many new constraints that may be used in modelling. The additional

constraints used for this study were: a) density and susceptibility measurements (Tables 2 and 3) obtained directly rock samples from the study area; b) seismic refraction results from Lithoprobe lines 2,4 and 5 (Boland and Ellis, 1989; Wu and Mereu, 1988; Northey and West, 1986); c) laboratory velocity measurements (Fountain et al., 1990); d) Lithoprobe reflection results for the CB (Cook, 1984; Geiss et al., 1990; Green et al., 1988); e) recent geologic mapping results of the GRB, VRB and northern CB (Leclair and Nagerl, 1988; Leclair and Poirier, 1989); and f) metamorphic geobarometry results (Leclair, 1990; Percival and McGrath, 1986;). The use of these constraints substantially reduces the problem of ambiguity normally associated with potential field modelling.

5.2 GRAVITY MODELS: TWO DIMENSIONAL

5.2.1 Introduction

The linearity of the KSZ makes it well-suited for two-dimensional gravity and magnetic modelling. In such a model, the shape of the model is allowed to vary in two dimensions, usually the x and z directions, while the body is thought to extend in the y direction to infinity.

The 2D algorithm used is based on the method of Talwani et al., (1959) and was kindly provided by Dr. Walter Roest (Geological Survey of Canada). In this method, an array of bodies with anomalous densities is approximated by n-sided polygons, the contribution of each body is calculated separately and the results are summed to provide the total gravity effect.

Several two-dimensional models were constructed by this means across the different blocks of the KSZ to interpret the gravity anomalies. The gravity profiles used in the modelling (Figure 5-1) were oriented perpendicular to the principal gravity trends and where possible, were positioned at or near refraction lines for easy correlation with the seismic results. The initial crustal models were based on the refraction results in order to determine if the seismic data provided suitable constraints for gravity modelling. After further refinements, the models so produced were then extrapolated to intervening areas with no refraction data.

5.2.2 Construction of Crustal Models

In order to construct the crustal models, the interpretation provided by Boland and Ellis (1989) for the refraction results for lines 4 and 5 was reviewed (Figure 2-4a and b). Figure 2-4a, which presents the results of refraction line 5 across the CB, shows a high velocity structure dipping to the west underneath the KSZ. This structure has a velocity of 6.6-6.8 km/s at a depth of 20 $\pm$ 5 km in the west and rises to the surface within the KSZ proper, where the velocity ranges from 6.3-6.5 km/s. There is also a progressive west to east increase in upper crustal velocities from 5.8 - 6.0 km/s over the greenstone belts to 6.1-6.3 km/s within the WGT and 6.5-6.7 km/s within the core of the KSZ. Laboratory velocity measurements by Fountain et al., (1990) also show a similar velocity structure for this region. In Figure 2-4b, which shows the results of line 4 across the VRB and GRB, surface velocities increase from 5.8-6.0 km/s in the Quetico belt to 6.0-6.2 km/s within the VRB and the GRB.

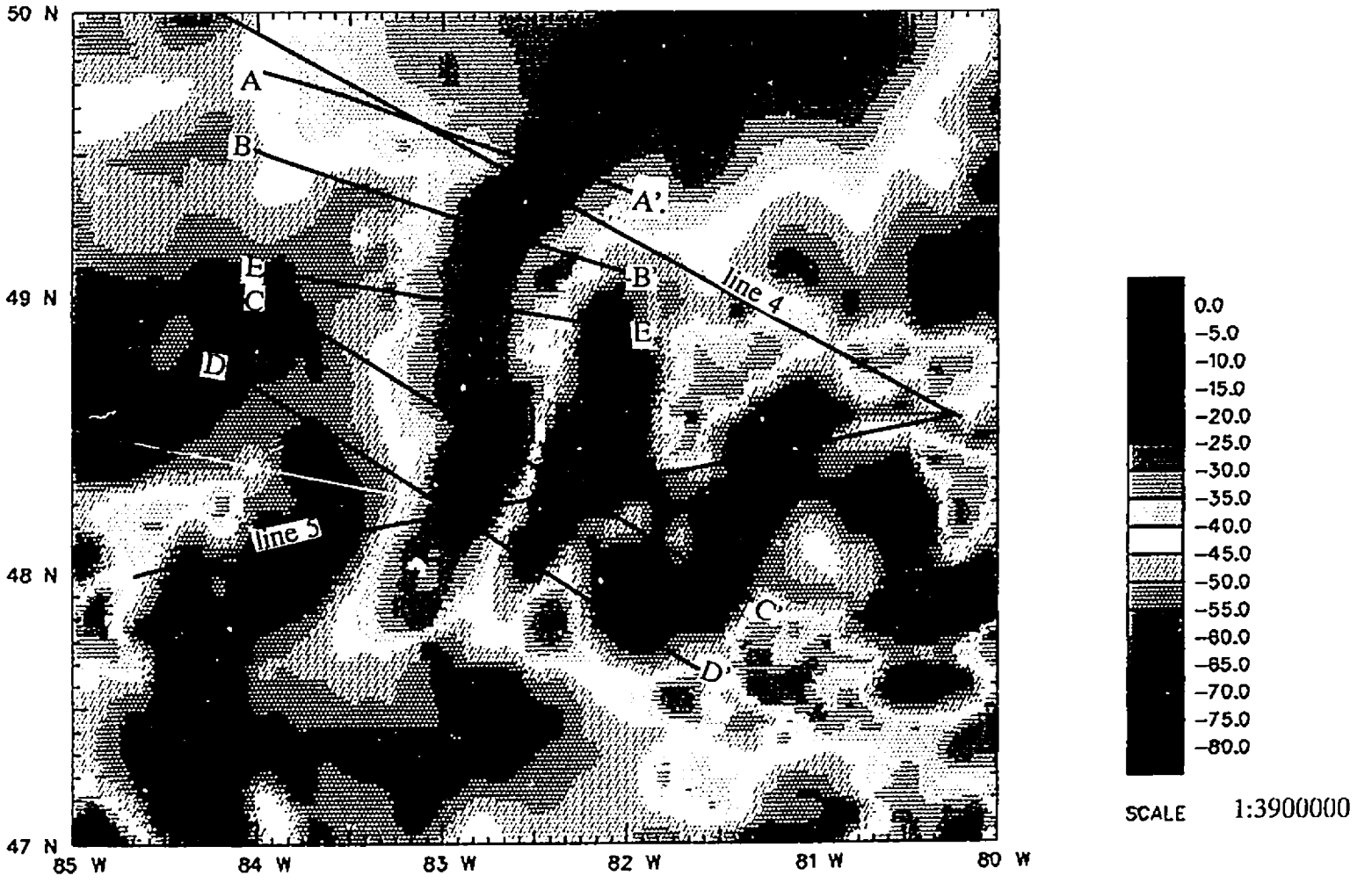

Figure 5-1. Gravity anomaly map with location of profiles and refraction lines used in modelling. Gravity in mGals.

In general, velocity contours are uplifted as the LF is approached from west to east. In Figure 2-4b , the 6.4 km/s velocity contour is at a depth of 20 km underneath the Quetico belt, but is uplifted to approximately 10 km underneath the VRB. Both figures show a maximum crustal thickness of 50-53 km underneath the CB and VRB compared to 43-46 km underneath adjacent areas. For details on the seismic experiment and results see Boland and Ellis (1989).

Based on the refraction results presented above, crustal models were constructed along lines 4 and 5. These lines were chosen because they are the only lines that cross the trend of the gravity anomalies. The velocity-depth contours shown in Figures 2-4a and 2-4b were digitized and used as input for the gravity models. Using the approach of Barton (1986), velocities from the refraction results were directly converted to densities using the Nafe and Drake relationship (Ludwig et al., 1971) between compressional wave velocities and densities (Table 3). If the refraction models are acceptable models for the KSZ, then their resulting calculated gravity anomalies should be similar to the observed gravity anomalies.

The results from the models based on refractions results (Figures 5-2a and 5-2b) are not in isostatic equilibrium and produce a smoother gravity profile. In fact, the amplitude of the observed gravity anomaly is not reflected by the calculated anomaly. To facilitate further modelling, the crustal velocity structure was simplified to a three-layer model. Three velocity discontinuities were selected from the refraction data: 1) a discontinuity at 15-20 km depth, coinciding with the 6.6 km/s velocity contour and rising toward the surface under the KSZ; 2) a discontinuity at

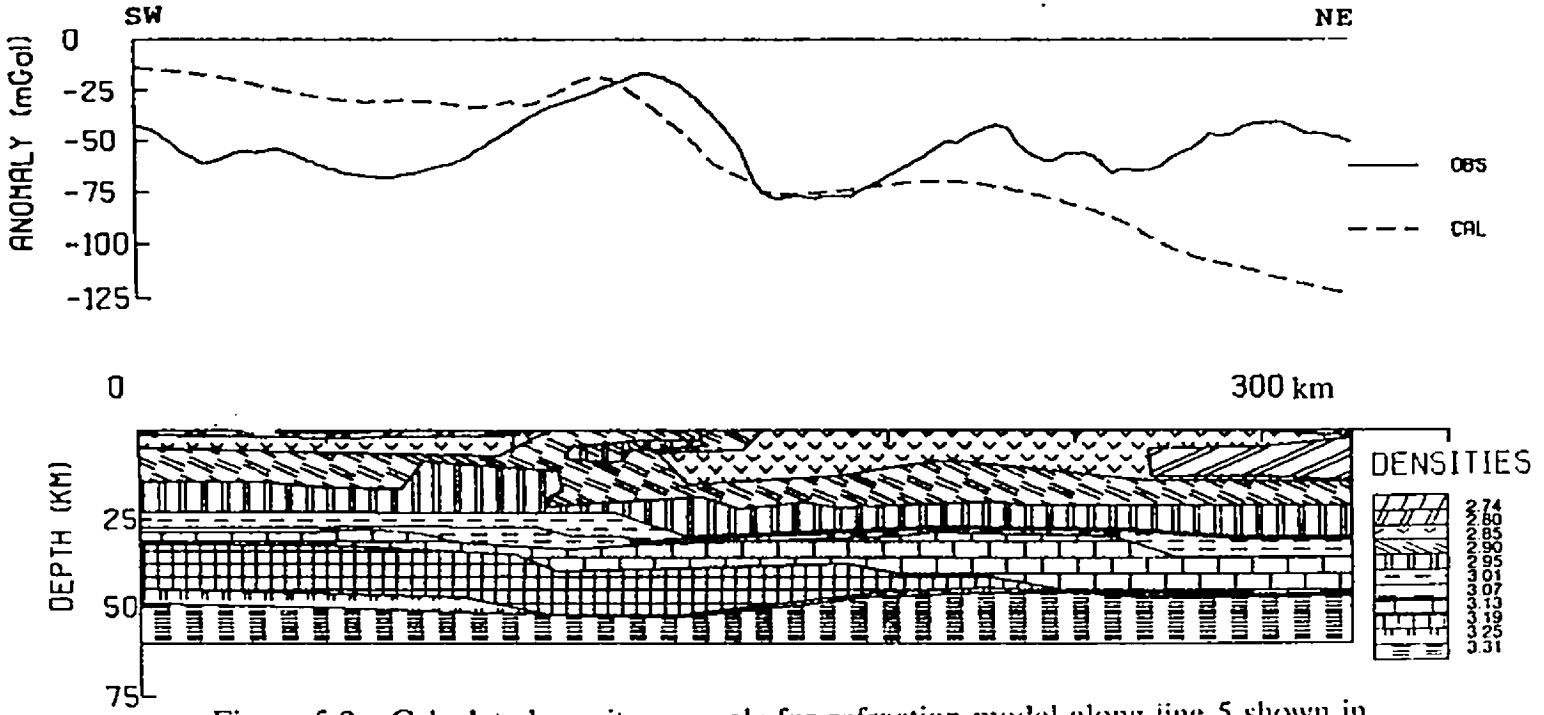

Figure 5-2a. Calculated gravity anomaly for refraction model along line 5 shown in Figure 2-4a. Densities in g/cm^3.

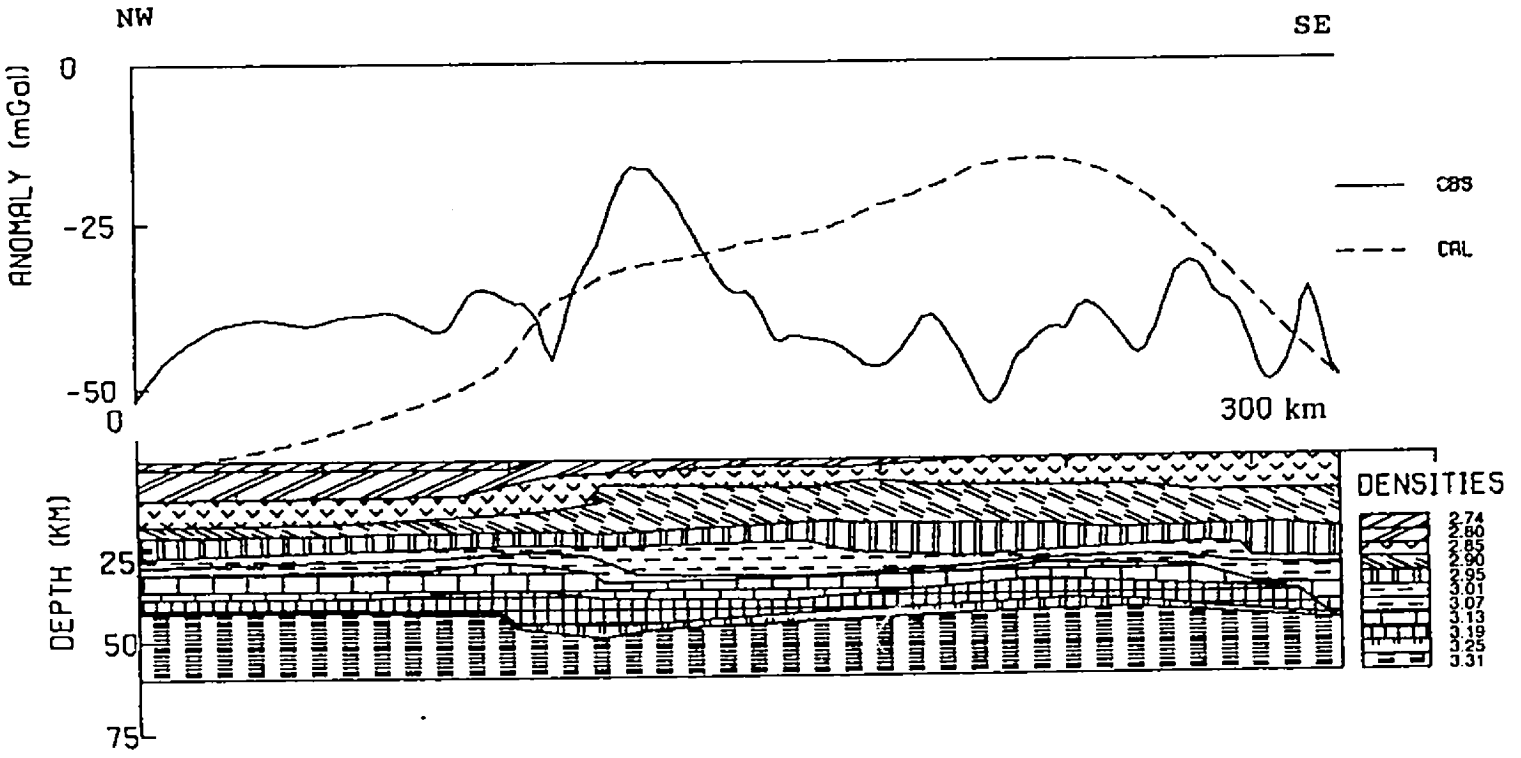

Figure 5-2b. Calculated gravity anomaly for refraction model along line 4 shown in Figure 2-4b. Densities in g/cm^3.

Table 3. Average Velocities and Densities from the Mean Nafe and Drake Curve

Velocities (km/s)	Densities (g/cm^3)
5.9	2.74
6.1	2.80
6.3	2.85
6.5	2.90
6.7	2.95
6.9	3.01
7.1	3.07
7.3	3.13
7.5	3.19
7.7	3.25
Moho	3.31

about 28 km representing the 7.0 km/s velocity contour; and 3) a discontinuity at about 48 km representing the Moho boundary. The velocities within each layer were then picked from the refraction results (Figures 2-4a and 2-4b) and averaged using a weighted mean technique to produce a single, average velocity for that layer. The result is the three layer crustal model shown in Table 4. Using this simplified three layer density model, the calculated gravity anomaly (Figure 5-3a) still shows a misfit between the calculated and observed gravity profiles. To obtain a better fit for line 5, a smooth, high density slab was introduced to the surface using the 6.6 km/s velocity contour, since interpretation of the laboratory velocity data (Fountain et al., 1990) shows that the velocities obtained for rocks within the KSZ correspond to those obtained by refraction at shallow to mid crustal levels. As can be seen in Figure 5-3b the resulting calculated anomaly shows a better fit to the observed profile than the previous model (Figure 5-3a). In Figure 5-4a, the densities have been further

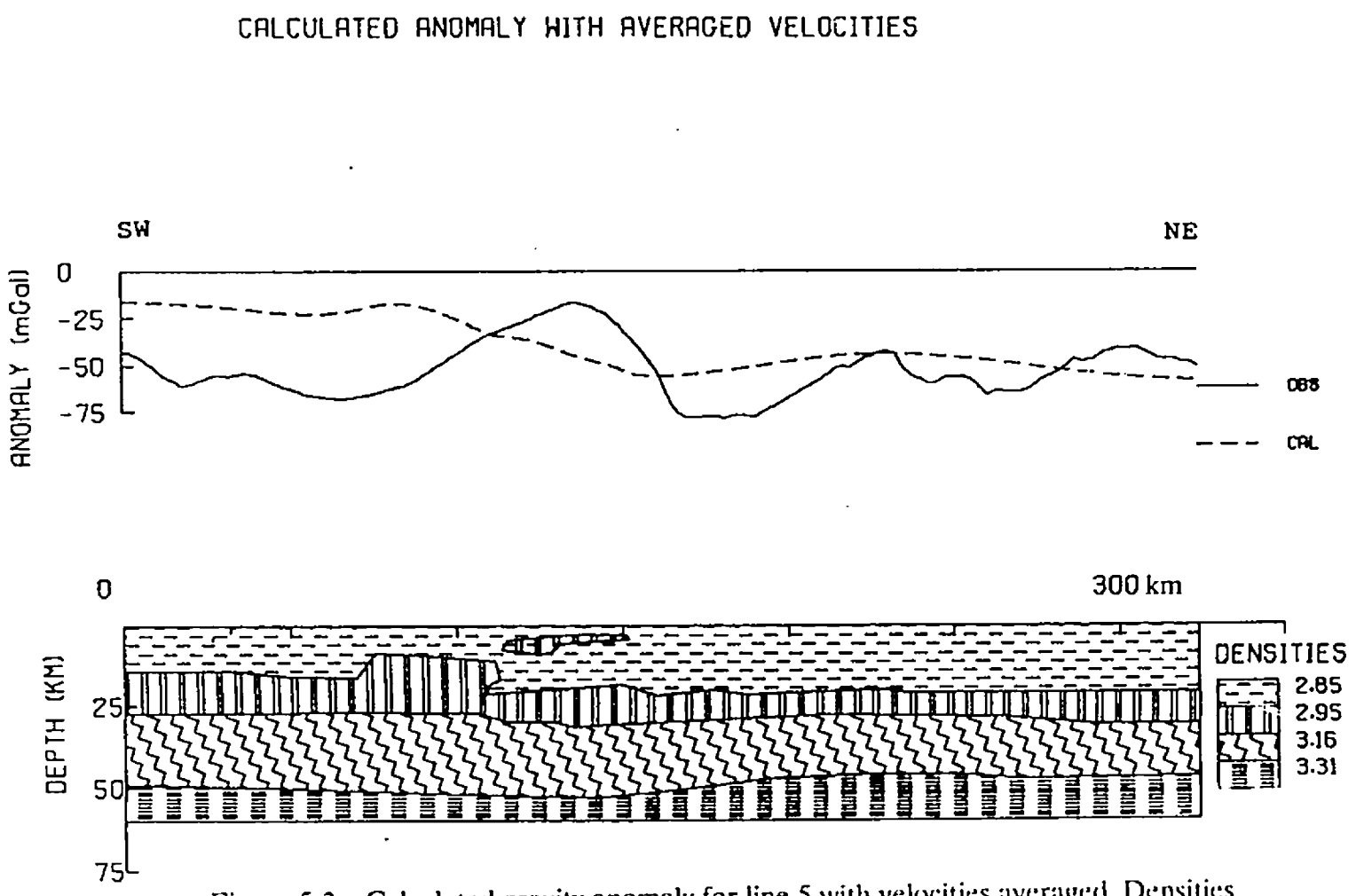

Figure 5-3a. Calculated gravity anomaly for line 5 with velocities averaged. Densities in g/cm^3.

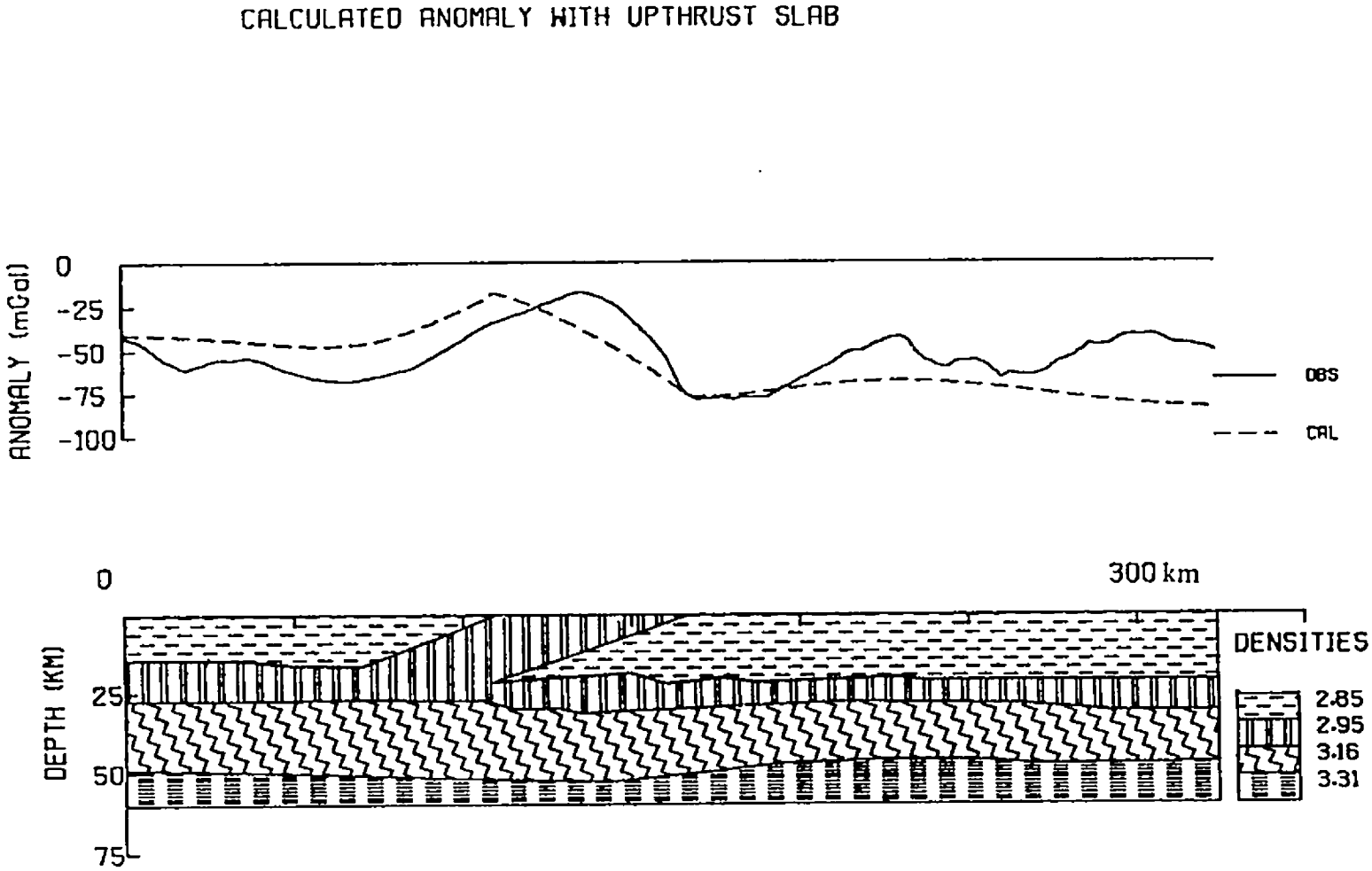

Figure 5-3b. Calculated gravity anomaly for line 5 with upthrust slab projected to depth. Densities in g/cm^3.

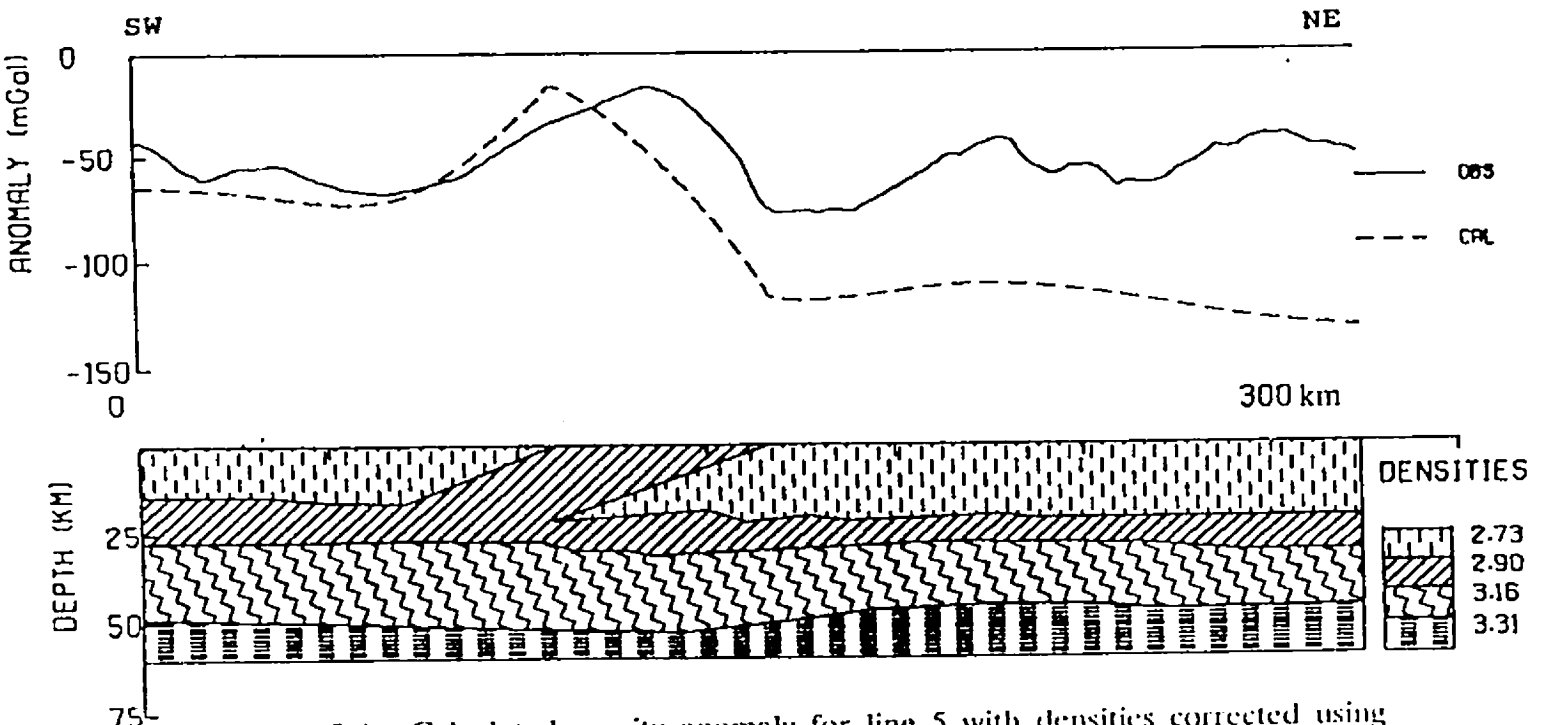

Figure 5-4a. Calculated gravity anomaly for line 5 with densities corrected using laboratory density measurements as constraints. Densities in g/cm^3.

Table 4. Summary of Crustal Layers used in Models

Layer	Depth	Velocity Range	Calculated Average Velocity	Mean Density (from Nafe & Drake curve)
Line 5				
1	0-15 km	6.0-6.6 km/s	6.3 km/s	2.85 g/cm^3
2	15-28 km	6.6-7.0 km/s	6.7 km/s	2.95 g/cm^3
3	30-48 km	7.0-8.0 km/s	7.4 km/s	3.16 g/cm^3
Moho				3.31 g/cm^3
Line 4				
1	0-18 km	6.0-6.4 km/s	6.2 km/s	2.83 g/cm^3
2	18-30 km	6.4-7.0 km/s	6.6 km/s	2.93 g/cm^3
3	30-43 km	7.0-8.0 km/s	7.4 km/s	3.16 g/cm^3
Moho				3.31 g/cm^3

readjusted using surface density measurements as constraints because the densities obtained from the Nafe and Drake curve are higher than the rock densities obtained from laboratory measurements. For depths greater than 30 km, the density of 3.16 g/cm^3 used was obtained from the average refraction velocity of 7.4 km/s using the Nafe and Drake curve. The 3.16 g/cm^3 density value used for the lower crustal rocks is comparable to that obtained by Christensen et al, (1975) for lower crustal granulites with similar velocities. This density may correspond to rocks that are more mafic than the Kapuskasing granulites. In fact, Fountain et al., (1990) suggest that the dominant lithologies below 20 km in the KSZ that have velocities in excess of 7.0 km/s are more mafic, more garnetiferous and could include some percentage of rocks such as peridotites, pyroxenites or eclogites. A summary of the corrected density

values used in the subsequent models is presented in Table 5. However, after these modifications the model is still not in isostatic equilibrium. A simple calculation for

Table 5. Corrected Surface Densities for lines 4 and 5

Layer	Density (g/cm^3)
1	2.73
2	2.90
3	3.16
Moho	3.31

isostatic equilibrium shows that the two ends of the model differed by about 1%, which corresponds to a difference of about 68 mGals. To correct for this, the 6.6 km/s contour was shifted by 6 km from a depth of 21 km to 15 km on the right hand side (Figure 5-4b). Final adjustments to the model were then made by matching short wavelength anomalies on the observed profiles with corresponding near surface anomaly sources using the surface geology as a constraint. The resulting model (Figure 5-4c) is in excellent agreement with the observed gravity profile. A similar exercise was done for Line 4 and the results are shown in Figures 5-5a, b, c and d. As was previously shown (Figures 5-2a and b), the initial refraction models of Boland and Ellis (1989) imply density models which are not in isostatic equilibrium. In addition, the above results suggest that densities may be more uniform in the crust than is suggested by the seismic results. Finally, the above results suggest that the velocity structure interpreted by Boland and Ellis (1989) may not be a unique model for the KSZ.

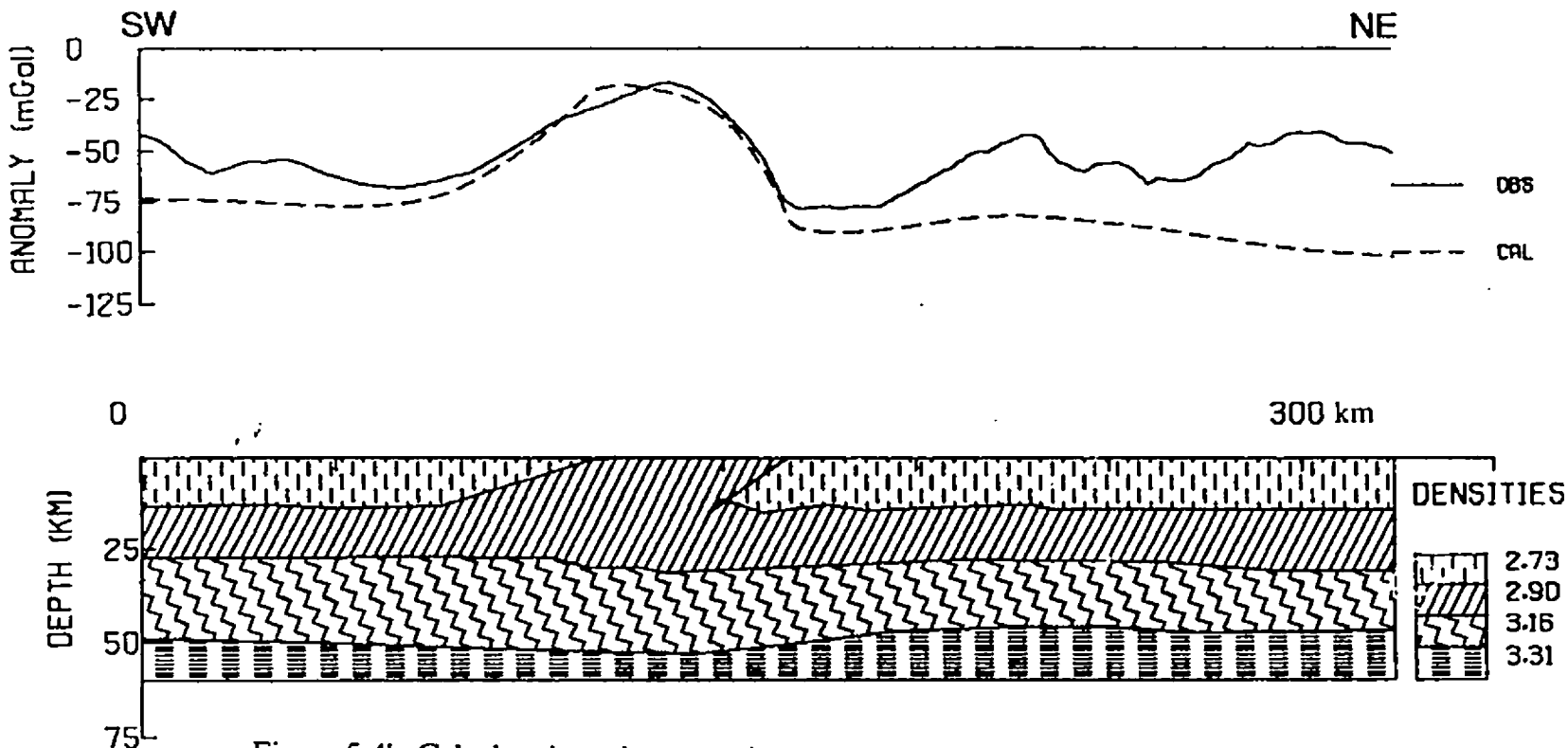

Figure 5-4b. Calculated gravity anomaly for line 5 with adjustments to obtain isostatic equilibrium.

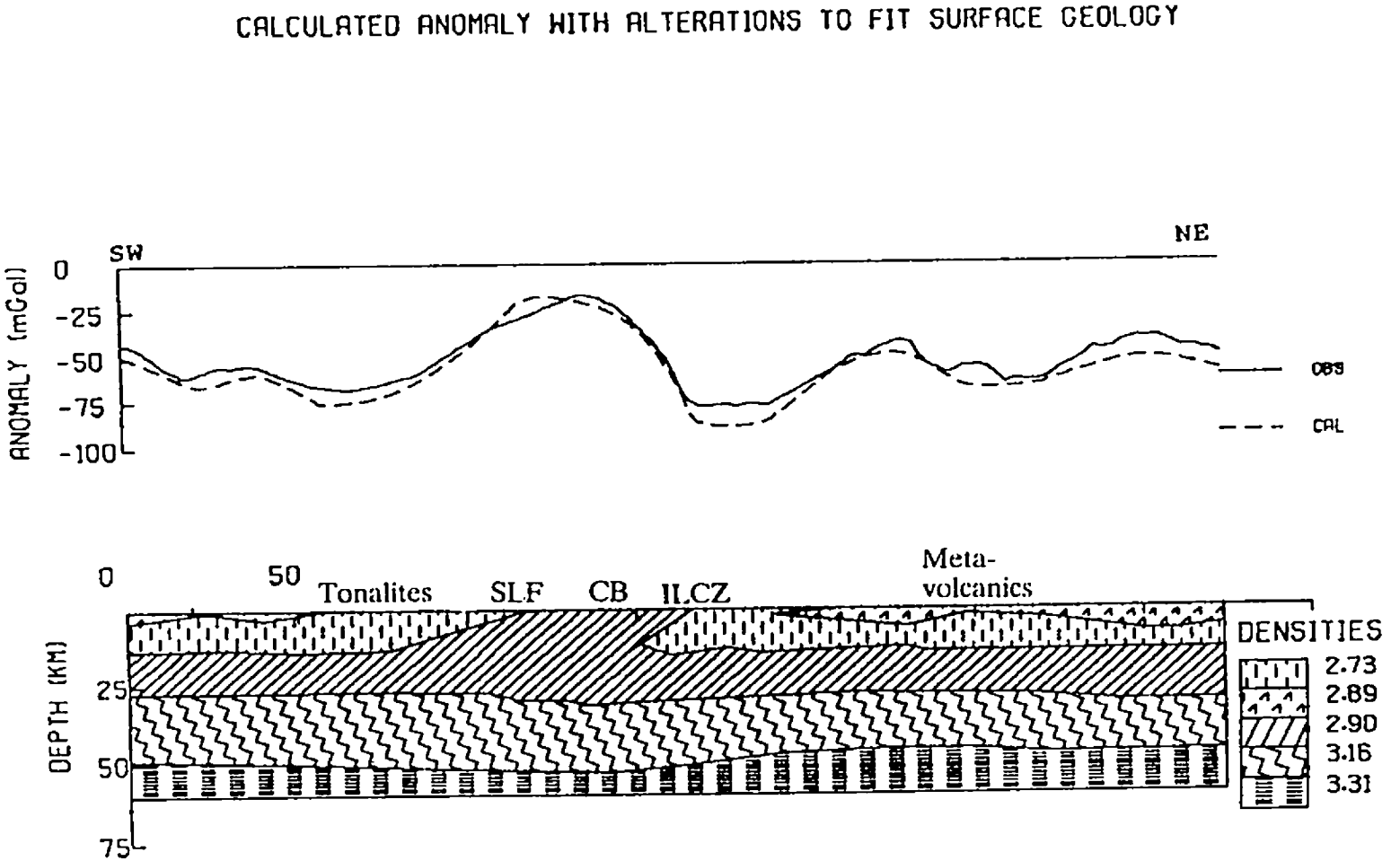

Figure 5-4c. Calculated gravity anomaly for line 5 with alterations using surface geology as constraint.

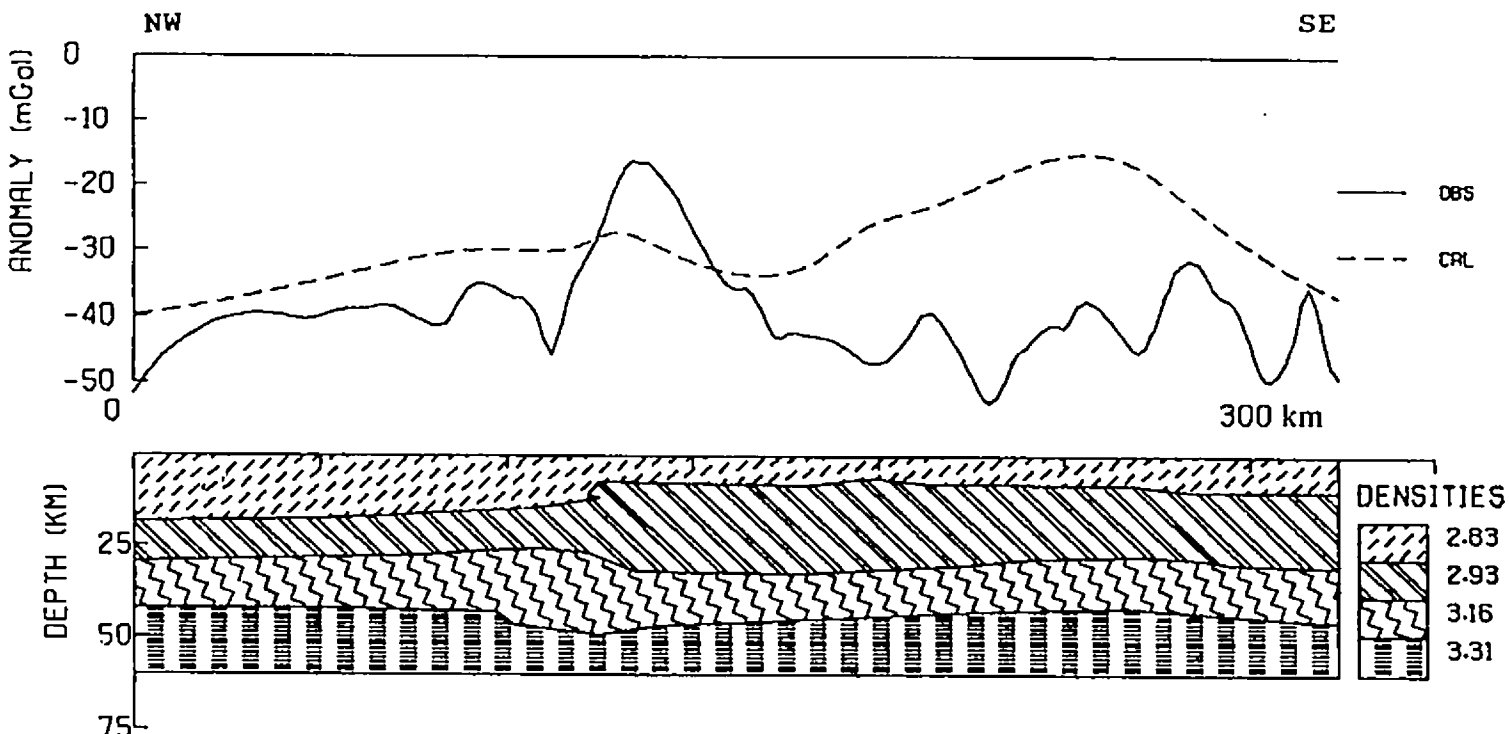

Figure 5-5a. Calculated gravity anomaly for line 4 with velocities averaged. Densities in g/cm^3.

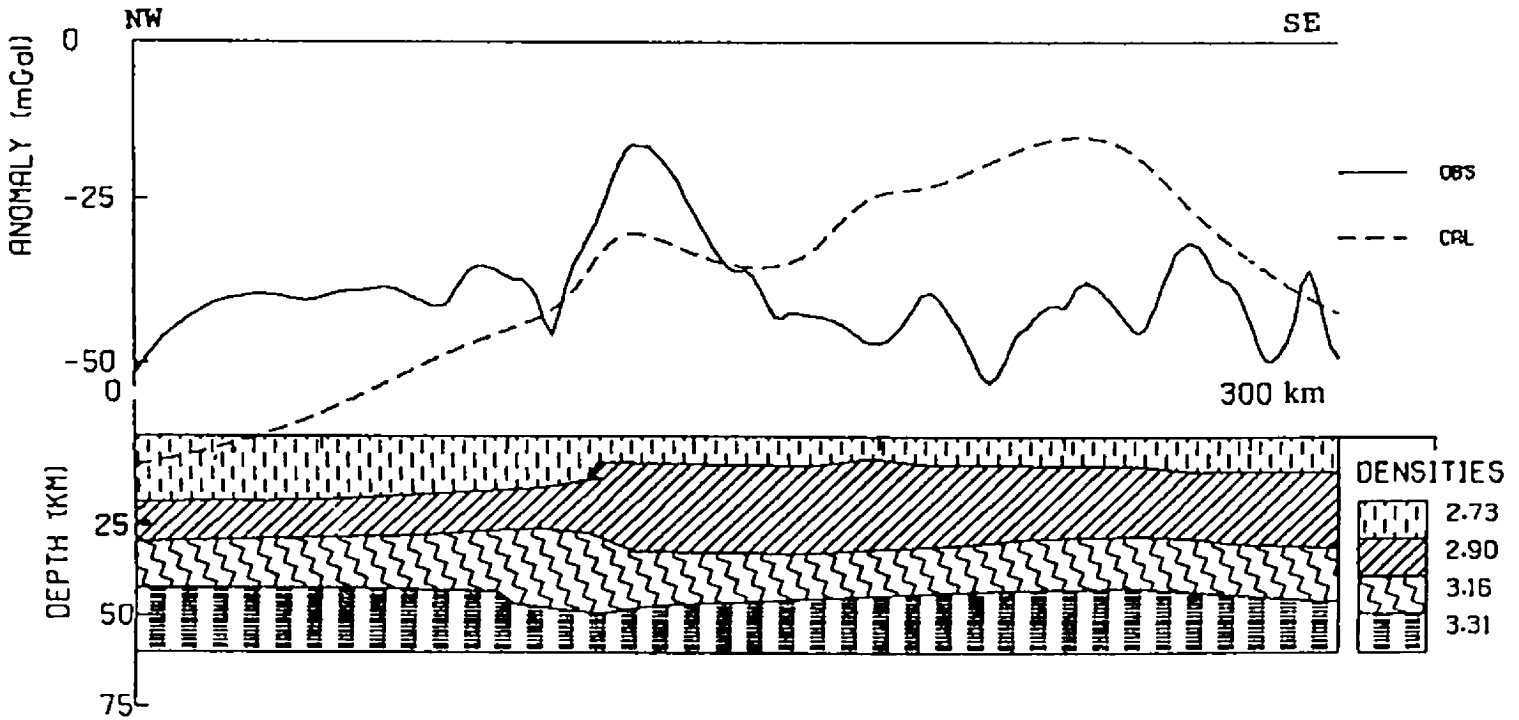

Figure 5-5b. Calculated gravity anomaly for line 4 with densities corrected using laboratory density measurements as constraints. Densities in g/cm^3.

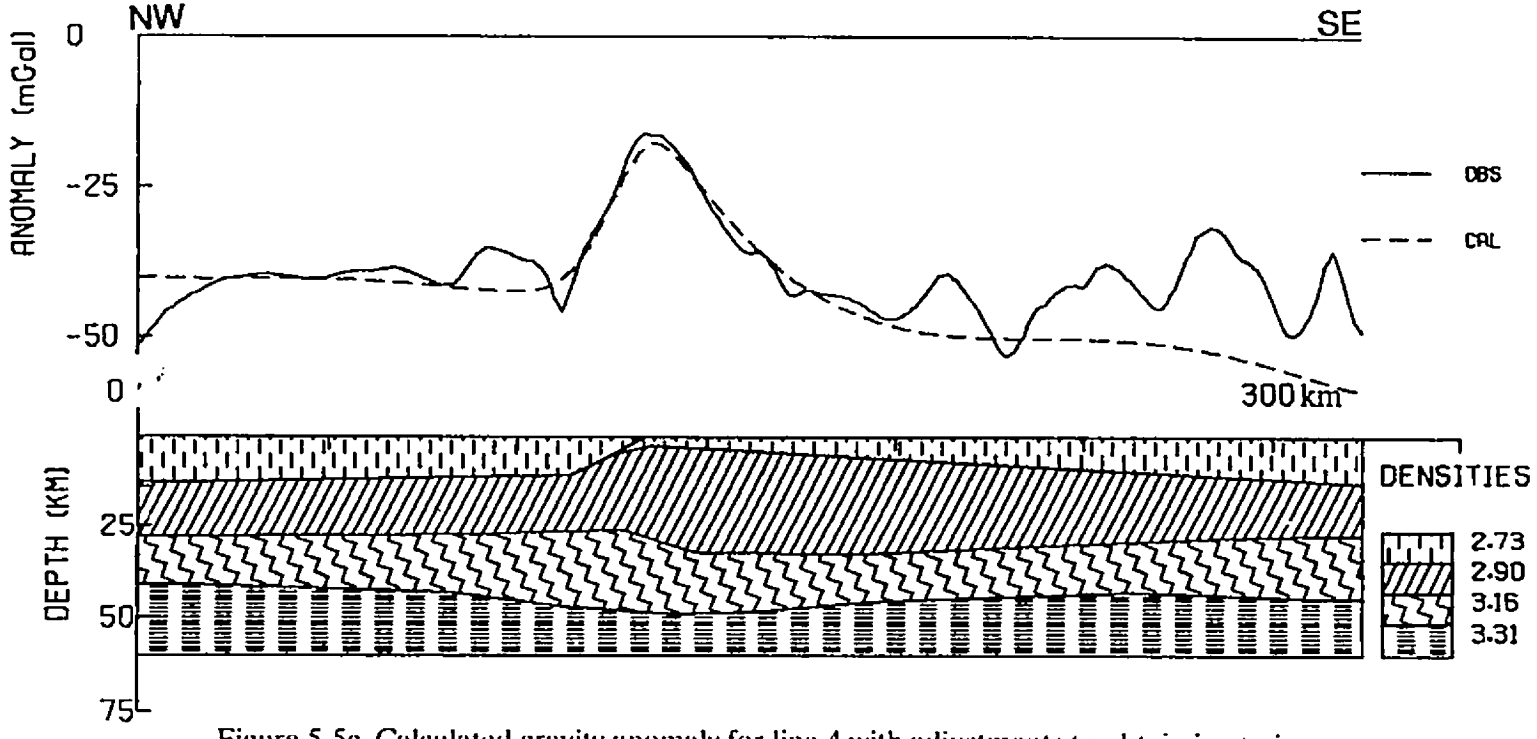

Figure 5-5c. Calculated gravity anomaly for line 4 with adjustments to obtain isostatic equilibrium.

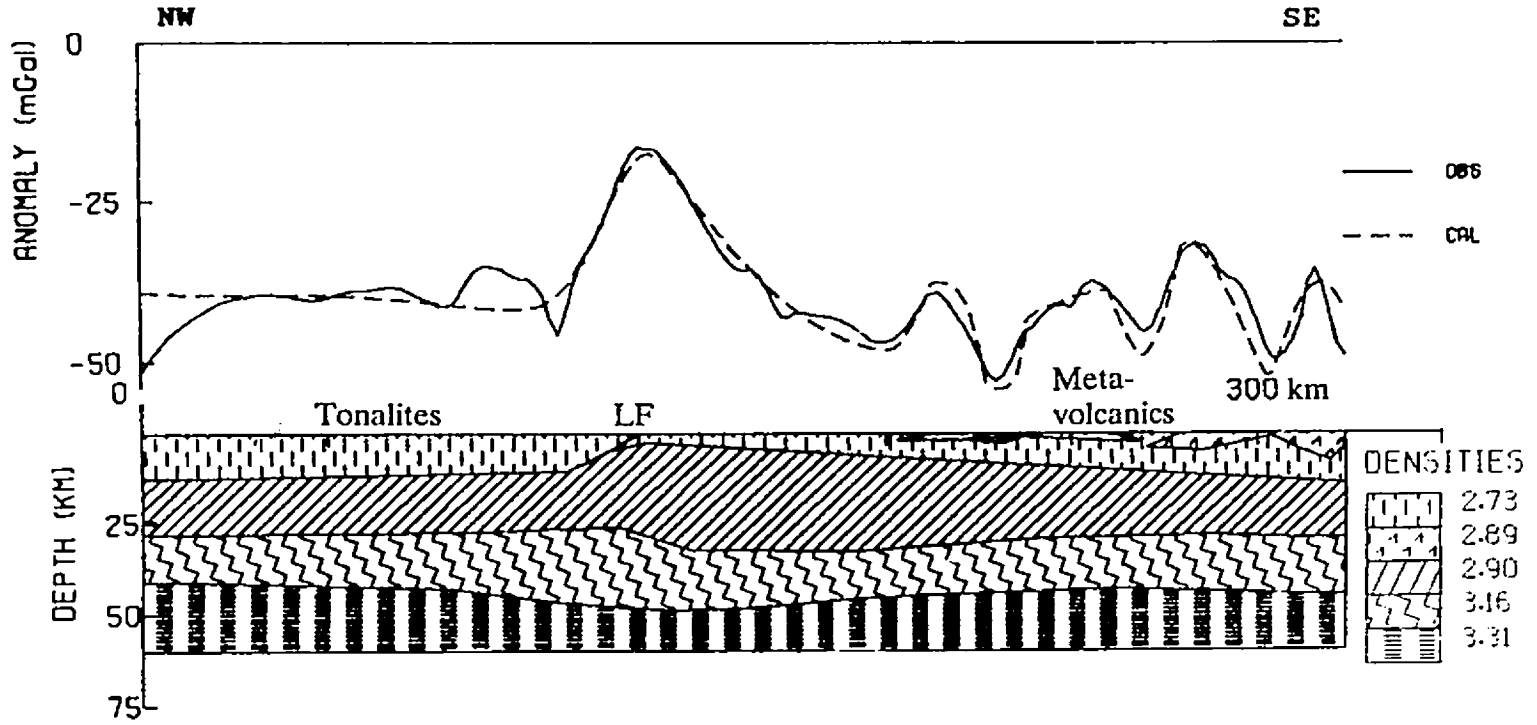

Figure 5-5d. Calculated gravity anomaly for line 4 with alterations using surface geology as constraint.

Because of additional velocity/density information available for the region, the general results using a simple 3 layer crustal model with average velocities and densities produced a better fit to the data than is usually achieved using the multi-layer model (e.g., Barton, 1986). The KSZ represents a classic example where mid-crustal rocks are exposed at the surface, which makes direct measurements of physical properties possible. Therefore, in this region we have the advantage that we not only know what the rock types are but we also know their velocities and corresponding densities. Consequently, the projection of these rocks to depth and the use of the laboratory velocity/density measurements provides additional constraints

in modelling the seismic refraction and gravity results.

5.2.3 Gravity Models Across the Different Tectonic Blocks

Insights into the structure of the crust in the areas between seismic lines 4 and 5 were gained by constructing gravity models across the different tectonic blocks of the region using the geometries suggested by the modified seismic refraction models (Figures 5-4c and 5-5d). No gravity models have been constructed for the Fraserdale-Moosonee Block (FMB) because of the lack of constraints for this block (e.g., density, seismic refraction and reflection).

5.2.3.1 Gravity Model: Val Rita Block

To explain the Bouguer anomaly within the VRB, several two-dimensional gravity models were constructed. The models were based primarily on the geometry proposed for the deep structure of this region shown in Figure 5-5d. A three layer crustal structure beneath the region is assumed with a homogeneous upper crust (2.73 g/cm^3), middle crust (2.90 g/cm^3) and lower crust (3.16 g/cm^3).

Profile A-A' is located along Hwy 11, while B-B' and E-E' are located south of refraction line 4 (Figure 5-1). These profiles show a general increase in gravity values from -55 mGals within the Quetico and Wawa belts to -5 mGals within the VRB and back to lower values of -60 mGals within the Abitibi belt.

In Figures 5-6, 5-7 and 5-8 the Lepage Fault (LF) is modelled as a high angle normal fault dipping 60-65° northwest, beneath the Quetico and Wawa belts. The density contrast across this fault is 0.17 g/cm^3, which is considerably higher than the 0.08 g/cm^3 suggested by previous gravity models (Percival and McGrath, 1986). The laboratory density measurements of the granulites exposed along this fault give values greater than 2.86 g/cm^3 compared to 2.73 g/cm^3 for the tonalites of the WGT or 2.70 g/cm^3 for the Quetico metasediments. Attempts were also made to model the LF as a southeast dipping reverse fault, with the VRB granulites thrusted to the northwest over the Quetico and Wawa belts. In order to fit the gravity data, however, the LF would have to be moved 10-15 km west of its surface expression, a result incompatible with the known geology (the results are not presented).

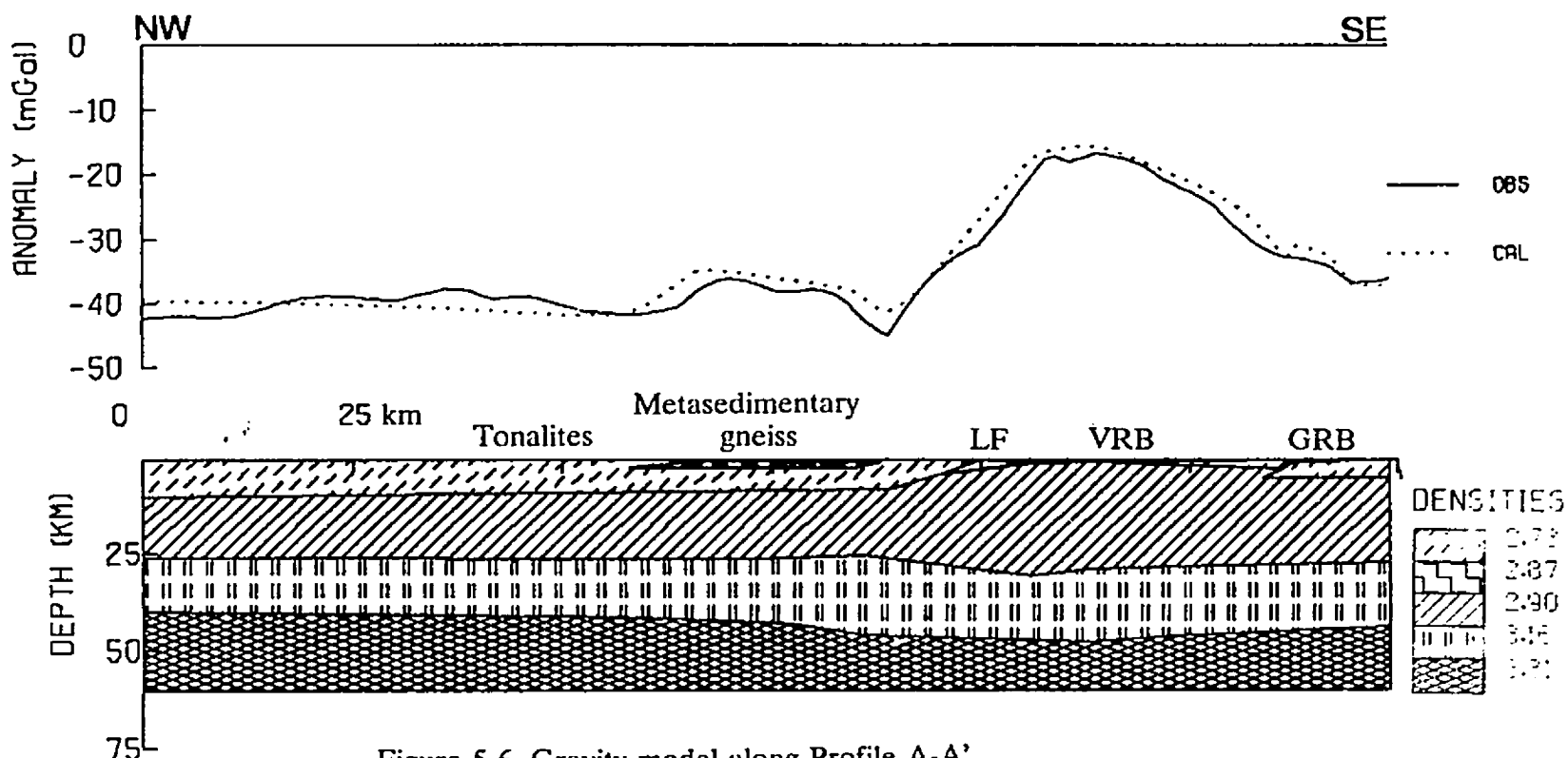

Figure 5-6. Gravity model along Profile A-A'.

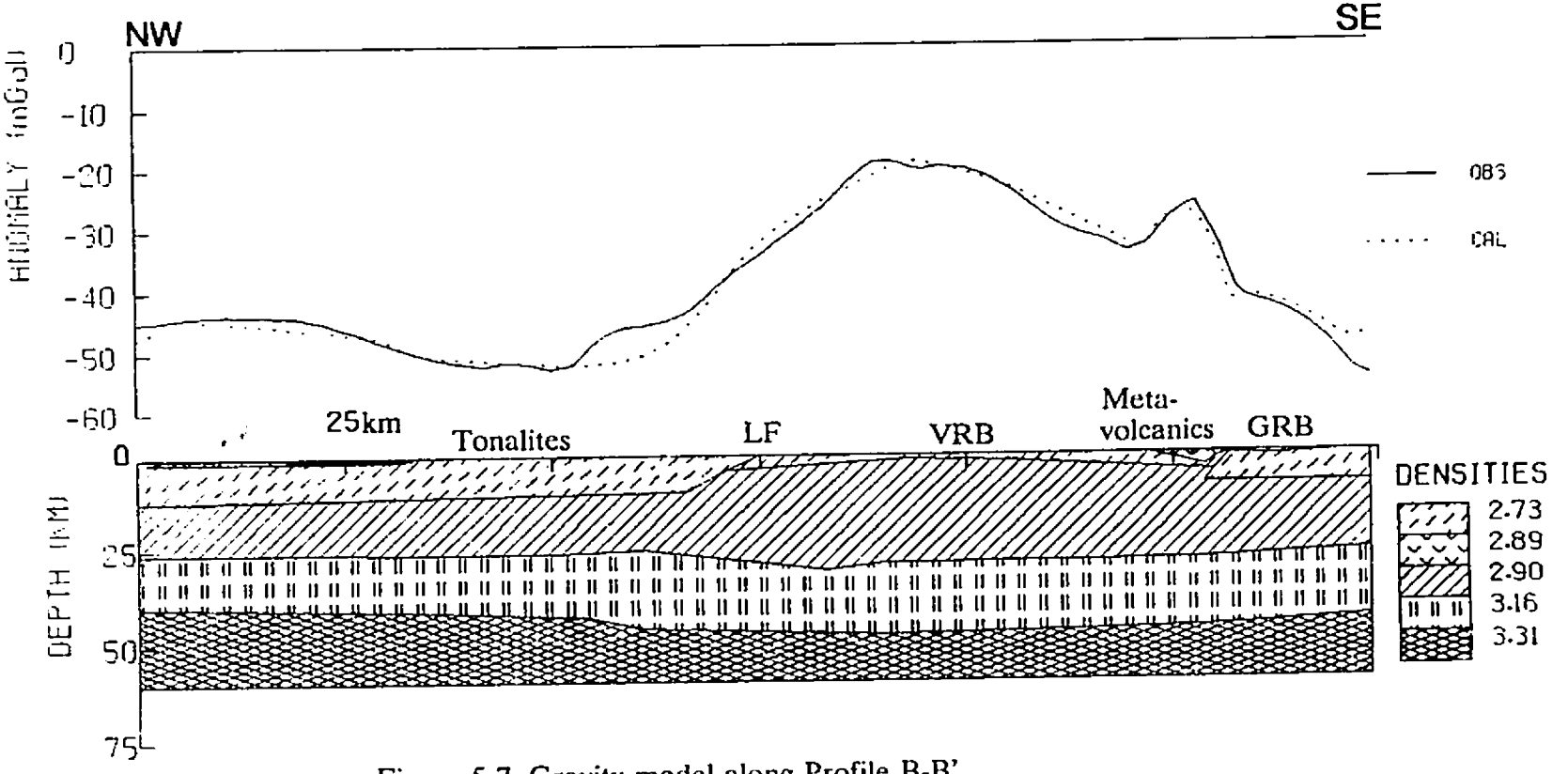

Figure 5-7. Gravity model along Profile B-B'.

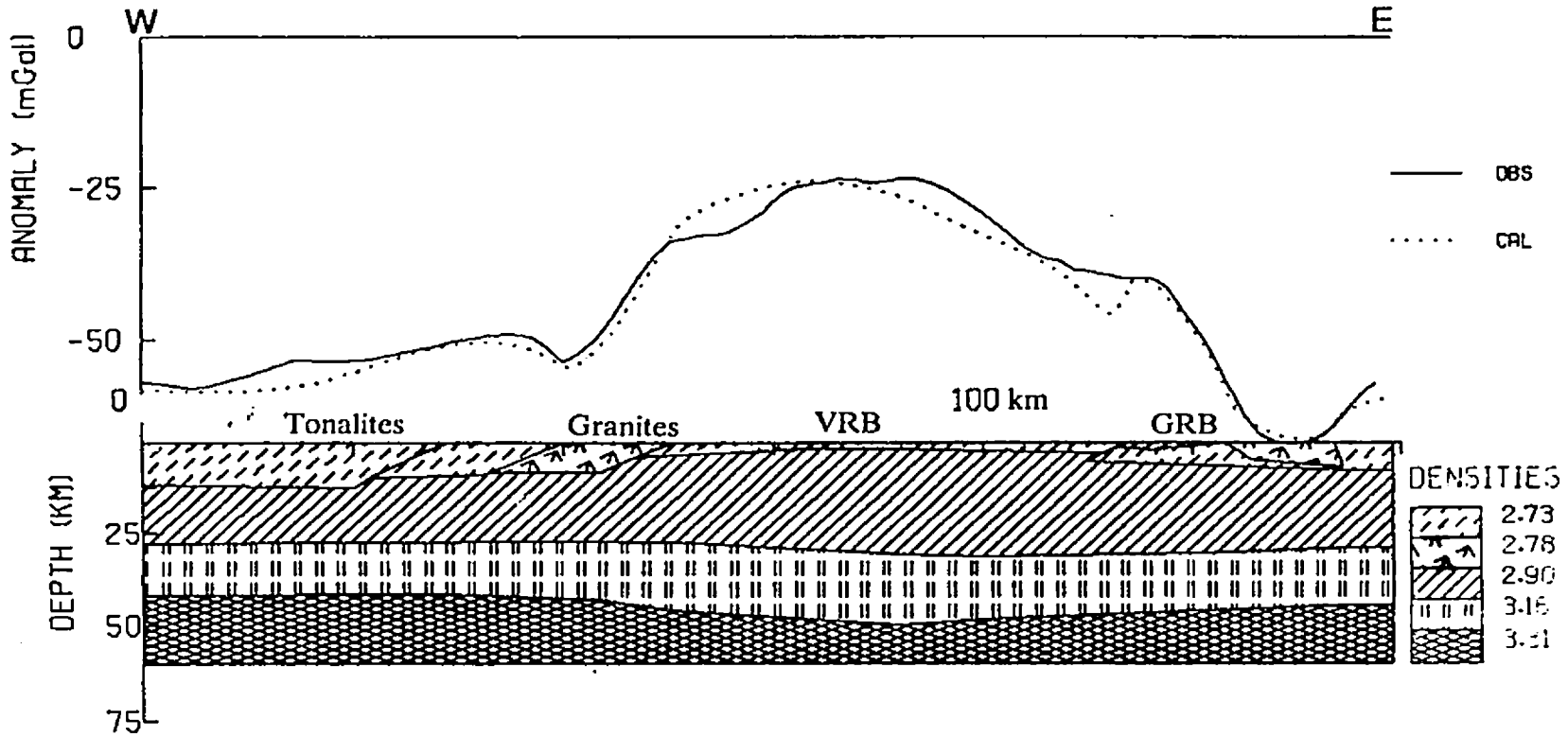

Figure 5-8. Gravity model along Profile E-E'.

Figures 5-6, 5-7 and 5-8 show the uplift of dense granulites east of the LF from depths of 15-25 km to shallow levels (0.5-3 km) with some exposures at the surface close to the fault (e.g., Figure 5-6). These uplifted, high density rocks coincide with the increase in velocities found east of the fault on refraction line 4 (Figure 2-4b) and are responsible for the anomaly observed over the VRB. The models suggest that the vertical extent of the LF is 10-13 km. The models presented in figures 5-6, 5-7 and 5-8 suggest that about 5-7 km of vertical displacement has taken place along the LF. The models show a progressive southward increase in depth to the top of the granulite source body (layer 2) from 0 km in Profile A-A' (Figure 5-6) to 1.5 km in Profile B-B'(Figure 5-7) and 2-3 km in Profile E-E' (Figure 5-8). To fit the gravity data for the block, the models require a west-dipping boundary between layers 1 and 2 at the western edge of this block, truncated by the LF. A southeast dipping boundary is compatible with the data on the east (Figures 5-6, 5-7 and 5-8). This discontinuity dips gently towards the Saganash Lake Fault (SLF) at an angle of 5-10°. Though not observed at the surface, the presence of this boundary within the VRB is consistent with surface geologic mapping which suggests a southeasterly regional dip for the region further to the east of the LF (Goodacre in Forsythe et al., 1983; Leclair and Poirier, 1989) and northwest-dipping foliations in the rocks along the western edge of the VRB near the LF (Leclair and Poirier, 1989). Percival and McGrath (1986) suggested that this boundary represents the contact between the lower Kapuskasing granulites and the upper low density amphibolite facies tonalitic gneisses of the VRB. The anticlinal structure suggested

by these models was not detected in the previous gravity models of Percival and McGrath (1986) because of the sparse gravity data coverage available for this block at the time of their study.

To fit the gravity data, the models require a thick crust underneath the region of high gravity. A thickness of about 49-50 km is obtained underneath this region compared to 43 km underneath adjacent areas, implying 6-7 km of crustal thickening. Attempts were also made to model the anomaly using a flat Moho. However, the results gave a calculated anomaly that was more positive than that observed. A good fit between the calculated and observed anomalies can be obtained by either reducing the densities of the uplifted granulites or by thickening the crust. A reduction in the density of the granulites is not compatible with the constraints provided by the laboratory measurements (Table 2). Therefore, a thickened crust constrained by the refraction results was used to model the gravity anomaly of this block. Finally, the short wavelength anomalies on each of the profiles were matched with corresponding near surface anomaly sources using the surface geology as a guide. Figures 5-6, 5-7 and 5-8 show that these bodies can be no more than 6-8 km thick. This is consistent with the low pass and upward continued maps (Figures 4-2 and 4-8) which show the attenuation of the anomalies associated with these bodies.

5.2.3.2 Gravity Model: Groundhog River Block

The amplitude of the gravity anomaly within the GRB is quite small (2-5 mGals) and is overwhelmed by the higher amplitude anomaly (25-30) mGal of the

VRB. Consequently, accurate modelling of the geometry of this block and its bounding faults is difficult. Nonetheless, the gravity models in Figures 5-6, 5-7 and 5-8 indicate that the GRB is very thin. The contribution of this unit to the total gravity anomaly in the region is almost negligible and is almost completely overshadowed by the greater contribution from the Saganash Lake Metavolcanics (SLMV, Figure 5-7) and the VRB. The models show a maximum thickness of 2-3 km for the granulites in the southern part of the GRB (Figure 5-8), and a thinning towards Highway 11 to the north (Figure 5-6), where thicknesses of less than 1 km are obtained.

The models suggest that the SLF is also a high angle normal fault with northwesterly dips having the same attitude as the LF. The total crustal extent of the SLF is at least 6 km. The amount of vertical displacement along this fault is estimated to be 4-5 km, smaller than the amount of displacement estimated for the LF. From the gravity observations, it is impossible to determine if the fault is listric at depth.

5.2.3.3 Gravity Model: Chapleau Block

Profiles C and D (Figure 5-1) were used to model the Bouguer gravity anomaly over the CB. These profiles (Figures 5-9 and 5-10) show the Bouguer gravity increasing from -50 mGals within the WGT to about 0 mGals within the CB and back to lower values of -75 mGals within the AB. The gravity profiles are slightly asymmetrical with a steeper slope near the Ivanhoe Lake Cataclastic Zone

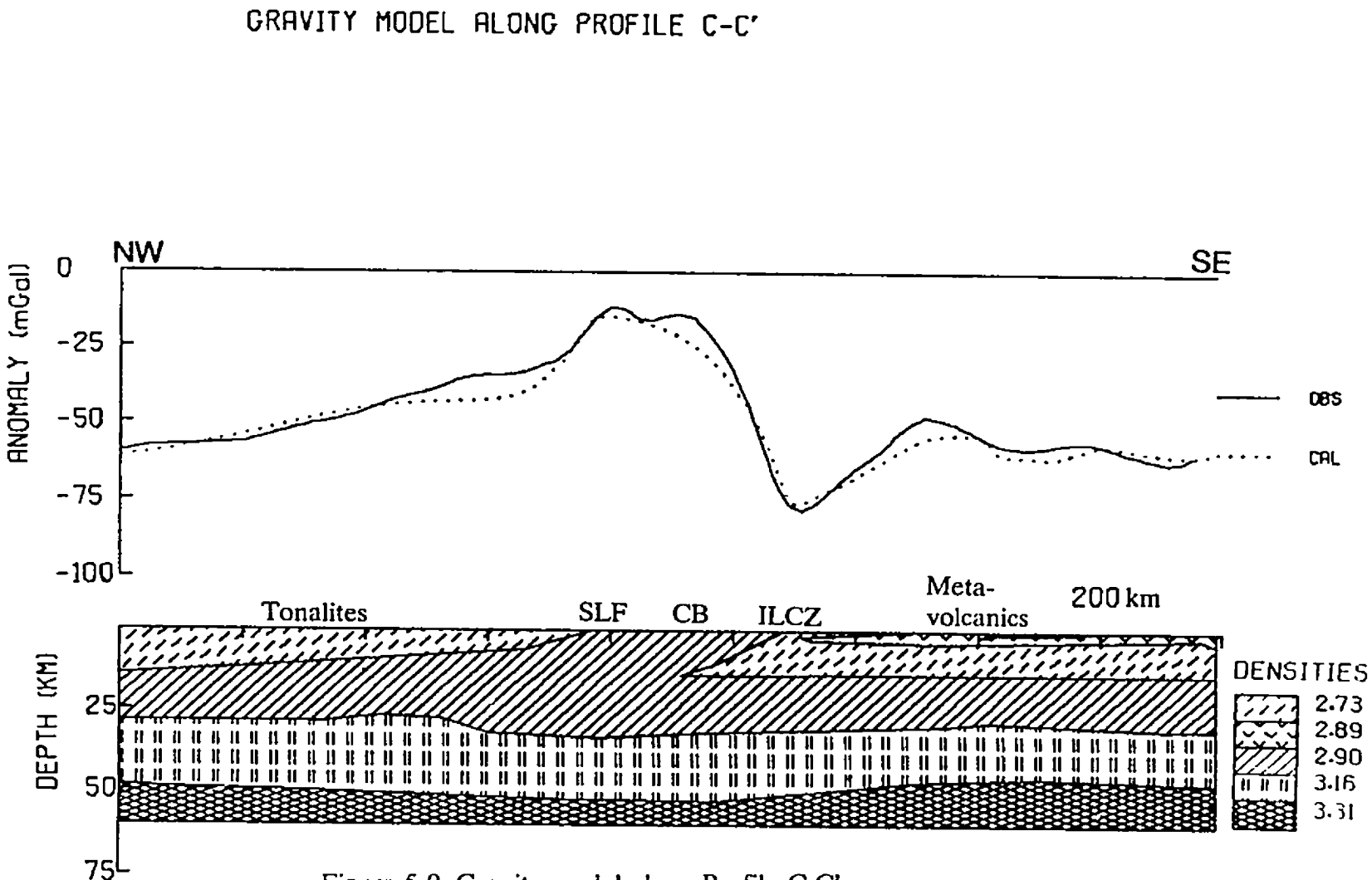

Figure 5-9. Gravity model along Profile C-C'.

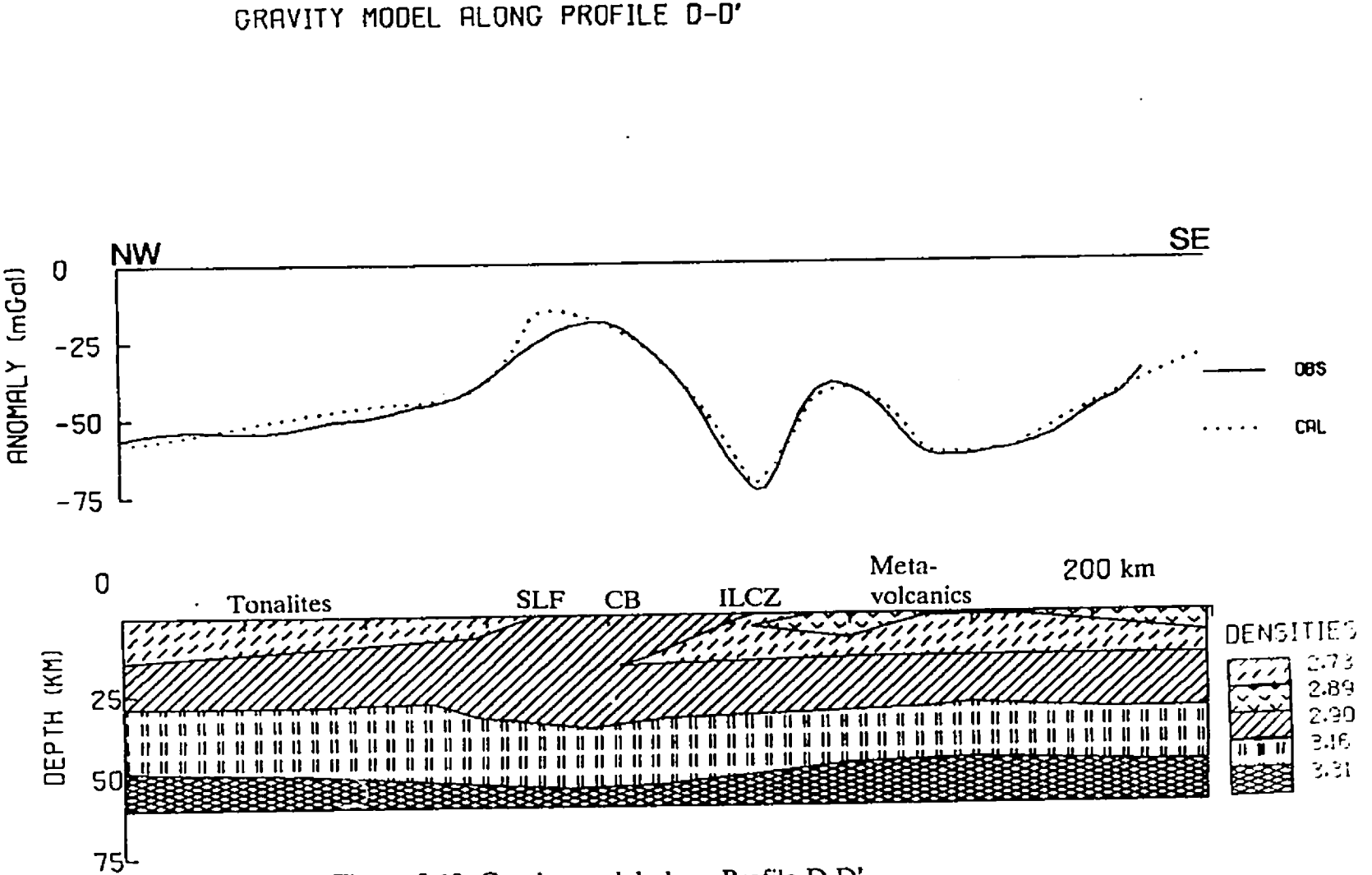

Figure 5-10. Gravity model along Profile D-D'.

(ILCZ) on the east than on the western boundary defined by the SLF. Most of the anomaly is caused by the effect of an uplifted slab of high density granulites from depths of 15-30 km juxtaposed against the lower density tonalites of the WGT and AB. This slab dips to the northwest underneath the WGT and coincides with the region of anomalously high velocities observed in the upper part of the crust in the refraction data (line 5, Figure 2-4a). Geobarometric results (Leclair, 1990) for granulites from the core of the CB indicate pressures of 7-8 kbar corresponding to depths of 25-30 km, supporting the above results.

The boundary faults along the CB are better defined than those of the GRB because of the greater amplitude of the anomaly (40-50 mGals) over this block. In Figures 5-9 and 5-10, the SLF is modelled as either a normal or a listric fault with northwesterly dips of 45-55° and a vertical crustal extent of 13-15 km. The ILCZ is modelled as a westerly dipping thrust fault with dips of about 30-35°. When a shallower dip of 15-20° (as suggested by the recent seismic reflection interpretation of Geiss et al., (1990), Figure 2-5) for the ILCZ is assumed, the fit between the calculated and observed anomalies within the CB is not as good (e.g., Figure 5-11).A better fit can only be obtained if the position of the thrust is moved further east, within the Abitibi belt. Such a position for the ILCZ does not agree with the surface trace of the fault, but may agree with the surface position suggested for Fault 3 in Figure 2-5. If the mapped position of the ILF is correct, however, then only the steep angle used above will fit the gravity data.

The ILCZ is estimated from gravity modelling to extend to an approximate

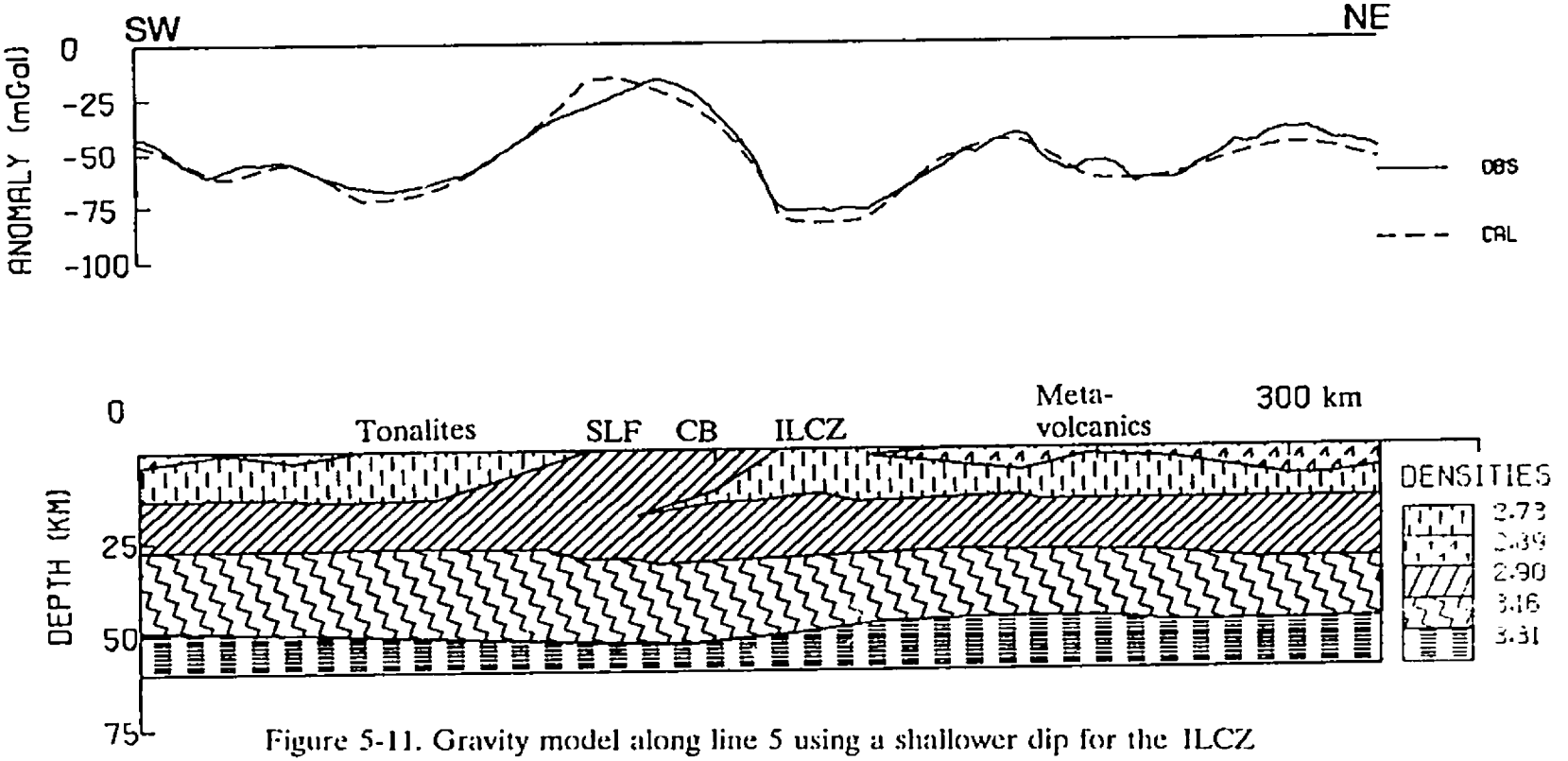

Figure 5-11. Gravity model along line 5 using a shallower dip for the ILCZ

crustal depth of 16-20 km, which is the depth estimated for this fault by refraction interpretation. In modelling the Moho, the gravity data requires a crust thickened by about 7 km over a width of 120 km underneath the region of high gravity anomaly. Maximum crustal depths of 52-53 km are obtained within this region and 45-48 km underneath adjacent areas. Attempts to model the gravity anomaly for this block using a flat Moho produced results similar those obtained for the VRB. Given the constraints provided by the refraction data (Figure 2-4a), a good fit between the observed and calculated anomalies is only obtained by using a thick crust underneath the CB.

Some of the short wavelength anomalies along Profiles C-C' and D-D' (Figures 5-9 and 5-10) have fairly high amplitudes (25-35 mGals). Figures 2-1 and 4-7 show that these anomalies are correlated with metavolcanics within the Wawa and Abitibi belts. As indicated in Figures 5-9 and 5-10, the metavolcanics used to model the short wavelengths of the observed anomalies are limited to the upper 6-7 km of the crust. Such shallow depths are compatible with the low pass (Figure 4-2) and upward continued (Figure 4-8) maps which show an attenuation of these anomalies.

5.3 GRAVITY MODEL: THREE-DIMENSIONAL

5.3.1 Introduction

Although the two-dimensional models discussed in the preceding sections have provided insight into the deep crustal structure of the different tectonic blocks of the KSZ, their value is limited because the models have made use of only single profiles.

Hence, much of the information present in the gravity field over the region has not been used. Three-dimensional modelling has an advantage over the two-dimensional method in that a theoretical gravity anomaly can be calculated over the entire area. The gridded gravity data available for the KSZ allows for the easy application of the three-dimensional method in the interpretation of the anomalies in the region. A three-dimensional model based on the best fitting two-dimensional models was constructed over the study area. The purpose of the three-dimensional modelling was two-fold: 1) to provide insight into the three-dimensional geometry of the KSZ and 2) to verify the validity of the two-dimensional models already discussed.

The algorithm for the modelling was provided by Dr. Jacob Verhoef (GSC) based on the method of Cordell et al., (1968). In this method, the gravity anomaly caused by a 3D body is calculated by applying a 2D Fourier transform to the horizontal directions (x and y) of the source geometry and approximating the integral over the z-extension of the body by a summation of thin layers.

5.3.2 Procedure

The 3D gravity modelling technique used makes several simple assumptions including the following: 1) the causative bodies have a uniform density within each layer (i.e., homogeneous layers); 2) a density variation occurs across an analytical surface; and 3) the density contrast and the position of a plane delineating either the top or bottom of the source body is specified. Using the gridded gravity values and

the above assumptions, a 3D structural model is calculated directly from the gravity anomaly data.

The slab of mid crustal rocks thrust to the surface within the KSZ and the shallow source bodies responsible for the short wavelength anomalies suggested by the 2D models represent a deviation from a homogeneous crust. Therefore, in order to assume homogeneity, and to calculate the anomaly caused by deeper layers including the Moho, the Bouguer anomaly is corrected for the effect of the upthrust slab and the near surface sources. To do this, the 3D gravity effect of the upthrust slab defined by the depth to the top of layer 2 (Figure 5-12) obtained from the 2D models discussed in the preceding section was calculated and subtracted from the observed Bouguer anomaly map of Figure 5-1, while the near surface sources can be largely eliminated by filtering. Following the removal of the gravity effect of the upthrust slab, the resulting anomaly map (Figure 5-13) shows a low gravity anomaly replacing the positive anomaly of the KSZ, partly because the density of the granulites (2.9 g/cm^3) is now replaced by the density of the tonalites (2.73 g/cm^3) and partly because of the thick crust underneath this region.

5.3.3 Depth to Moho

After correcting for the upthrust slab it can be assumed that the resulting gravity anomaly (Figure 5-13) is caused by depth variations of the lower boundaries of layers 2 and 3 as shown in Figure 5-14. The Moho surface can be calculated from the Bouguer anomaly map of Figure 5-13 by inversion following the method of

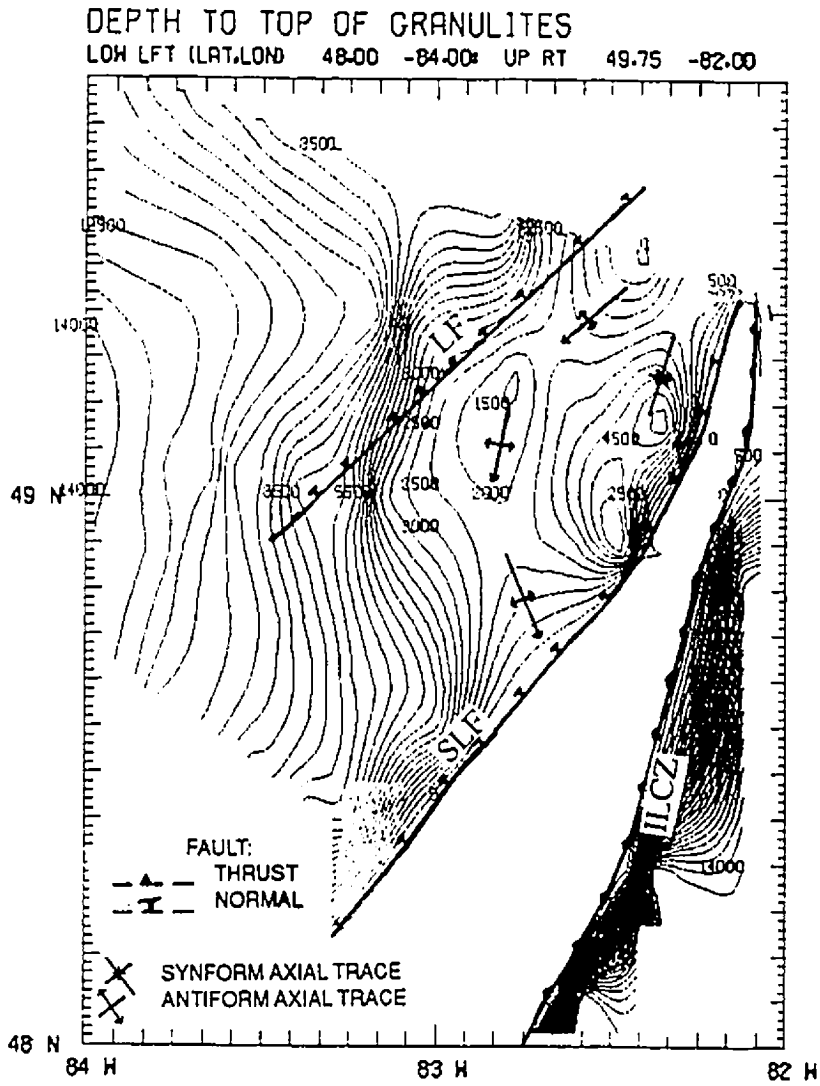

Figure 5-12. Depth to top of granulite layer (layer 2). Depth is in meters and contour interval is 500m.

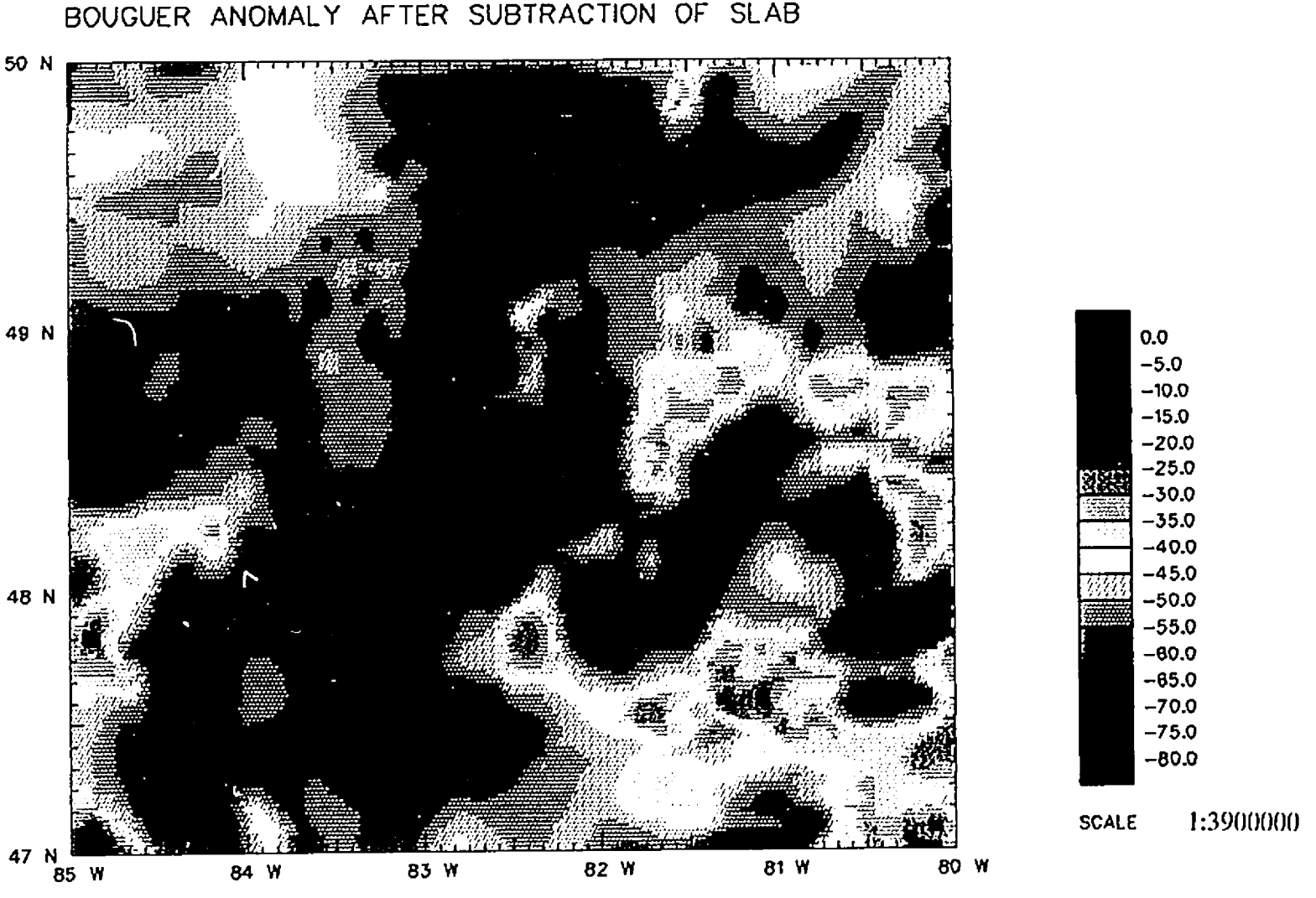

Figure 5-13. Gravity anomaly map after subtraction of upthrust slab. Gravity in mGals.

Marillier and Verhoef (1988) using Parker's formula (Parker, 1972). The Bouguer anomaly map of Figure 5-13 still contains short wavelength anomalies. In the inversion process, these wavelengths will be greatly amplified. Therefore, if it can be assumed that these short wavelengths are not caused by variations of the crust-mantle boundary, they can be eliminated by filtering. Using this argument, the power in the shortest wavelengths in Figure 5-13 was reduced with a two-dimensional lowpass Butterworth filter with a cutoff wavelength of 50 km and a filter steepness of 12dB/octave (50 km was selected as an appropriate cutoff wavelength based on an evaluation of the power spectrum of the anomalies). The resulting map (Figure 5-15) therefore contains the long wavelength information assumed to be from deeper sources.

Figure 5-15 was then used as input for the depth to Moho calculation. The model used for the inversion (Figure 5-14) was based on assumptions derived from the 2D models and refraction data: a) the crust is made up of three layers; b) after

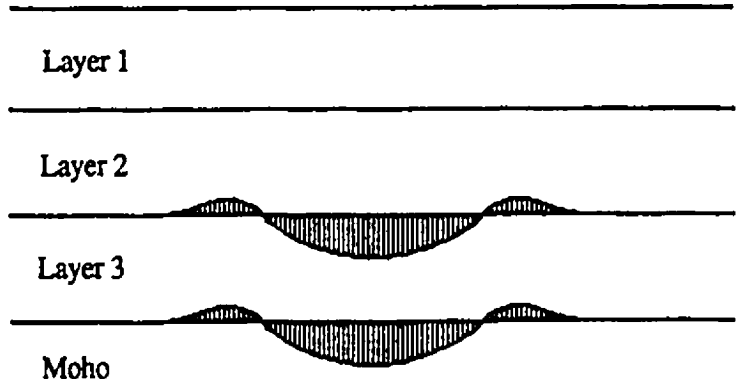

Figure 5-14. Illustration of layers used for the depth to moho inversion after subtracting the upthrust slab. The shaded area is the topography which is the deviation from an average depth.

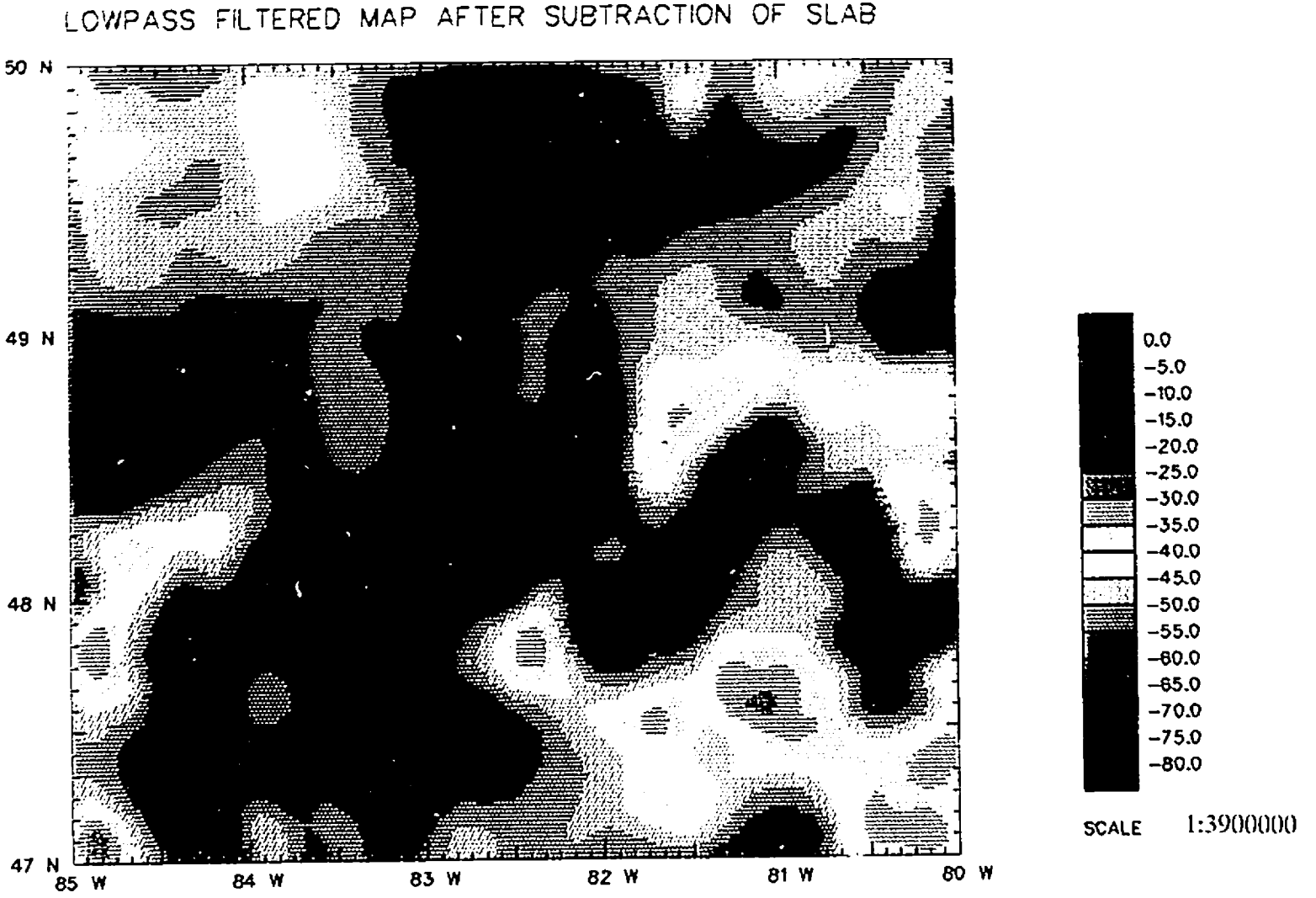

Figure 5-15. Lowpass filtered map of Figure 5-13 with cut off wavelength of 50 km. Gravity in mGals.

correcting for the upthrust slab and shallow features, the interface between layers 1 and 2 is flat, while the interfaces between layers 2 and 3 and layer 3 and the Moho have topography and are parallel (the 2D models show that these two interfaces are roughly parallel).

For the inversion, the average depth to the first interface was specified as 14 km and the density contrast across it as 0.17g/cm^3, the average depth to the second interface as 28 km and the density contrast across it as 0.26g/cm^3, while the average depth to the third interface (the crust-mantle boundary) was fixed as 47 km and the density contrast across it as 0.15 g/cm^3. The formula for the inversion had to be modified by altering Parker's formula for a single layer (Parker, 1972) to include several layers as follows (Figure 5-16a):

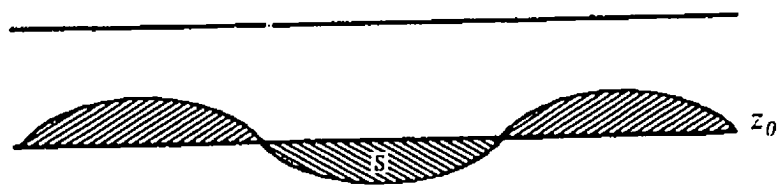

Figure 5-16a. An example of a single layer model used in Parker's inversion formula. The shaded area is the topography, defined as s and is the deviation from $z = z_0$.

Consider a topographic surface with an amplitude $s(x)$, around an average level at $z=z_0$ The fourier transform of the gravity anomaly caused by this surface is given by:

$$F=2\pi G\Delta\rho e^{-kz_0}\left[\sum_{n=1}^{\infty}\frac{k^{n-1}}{n!}(S)^n\right] \qquad (5\text{-}1)$$

where G is the gravitational constant, k is the wave number, $\Delta\rho$ is the density contrast, s is the amplitude of the deviation of the topography from $z=z_0$ and S is the Fourier transform of s. If s is assumed to be small, then equation 5-1 becomes:

$$F=2\pi G\Delta\rho e^{-kz_0}\,[S] \qquad (5\text{-}2)$$

The extension to include several layers can be obtained as follows:

Suppose two layers (Figure 5-16b), one as above but with a density contrast $\Delta\rho_1$ at its base, and a second layer with a base at $z = z_o + d$ and a deviation of topography with amplitude r and density contrast $\Delta\rho_2$ at its base,

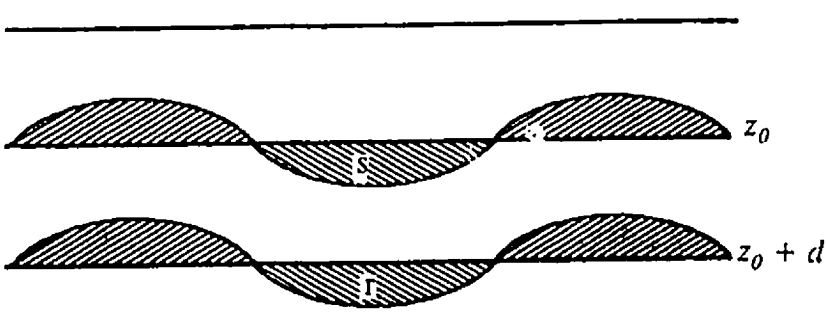

Figure 5-16b. An example of a two layer model used in the modification of Parker's inversion formula. The shaded area is the topography, defined as s and r and is the deviation from $z = z_0$ and $z_0 + d$ respectively.

then equation 5-2 becomes:

$$F=2\pi G\Delta\rho_1 e^{-kz_0}(S)+2\pi G\Delta\rho_2 e^{-k(z_0+d)}(R) \qquad (5\text{-}3)$$

where R is the Fourier transform of r. Since equation (5-3) contains two unknowns S and R, we cannot obtain them from the gravity anomaly. Therefore, the simplification of $S=R$ can be made (because it was assumed that both layers are parallel), which gives:

$$F=2\pi G e^{-kz_0}\ [S(\Delta\rho_1+\Delta\rho_2 e^{-kd})] \qquad (5\text{-}4)$$

Equation 5-4 can now be solved for S

$$S=\frac{Fe^{kz_0}}{2\pi G(\Delta\rho_1+\Delta\rho_2 e^{kd})} \qquad (5\text{-}5)$$

The inversion to the three layers was calculated and results after inverse Fourier transformation are in values for s. From this a depth to Moho is obtained by adding an average level of 28 km (to obtain the depth to the 28 km interface) to the s values and then 19 km to obtain the depth to the Moho (Figure 5-17). This map shows that a general thickening of the crust (52 km) occurs underneath the CB, extending to the southeast and also northwesterly into the VRB but thinning towards Lake Superior.

Although the thinning of the crust towards Lake Superior appears to be inconsistent with previous refraction results (Halls, 1982), it can be explained by the fact that this thinning may coincide with the shallowest parts of the Lake Superior basin (Halls, 1982 suggests that the crust is thickest at the centre of the basin and thins towards the KSZ). In the present circumstances, it is not possible to determine whether the above explanation is correct, because the portion of the lake shown is at the edge of the map. Furthermore, the depth to Moho map shows some relatively short wavelength features which may be explained by lateral density variations in the lower crust. Finally, the depth to Moho map (Figure 5-17) also suggests that the crust is shallowest underneath the adjacent areas, where the Moho rises to an average depth of less than 46 km.

5.3.4 Comparison of Depth to Moho with Refraction Results

To compare the above results (Figure 5-17) with the depth to Moho obtained from the refraction results of Northey and West (1986), profiles along seismic refraction lines 2, 4 and 5 of Boland and Ellis (1989) were selected, (see Figure 2-3 for location of profiles). It would have been more useful to compare the depths to the Moho obtained from the gravity inversion with the depths obtained from refraction results. Unfortunately, such data were not available. Instead, the depth to Moho contours from the results of Northey and West were digitized (Figure 5-18) and used for the comparison.

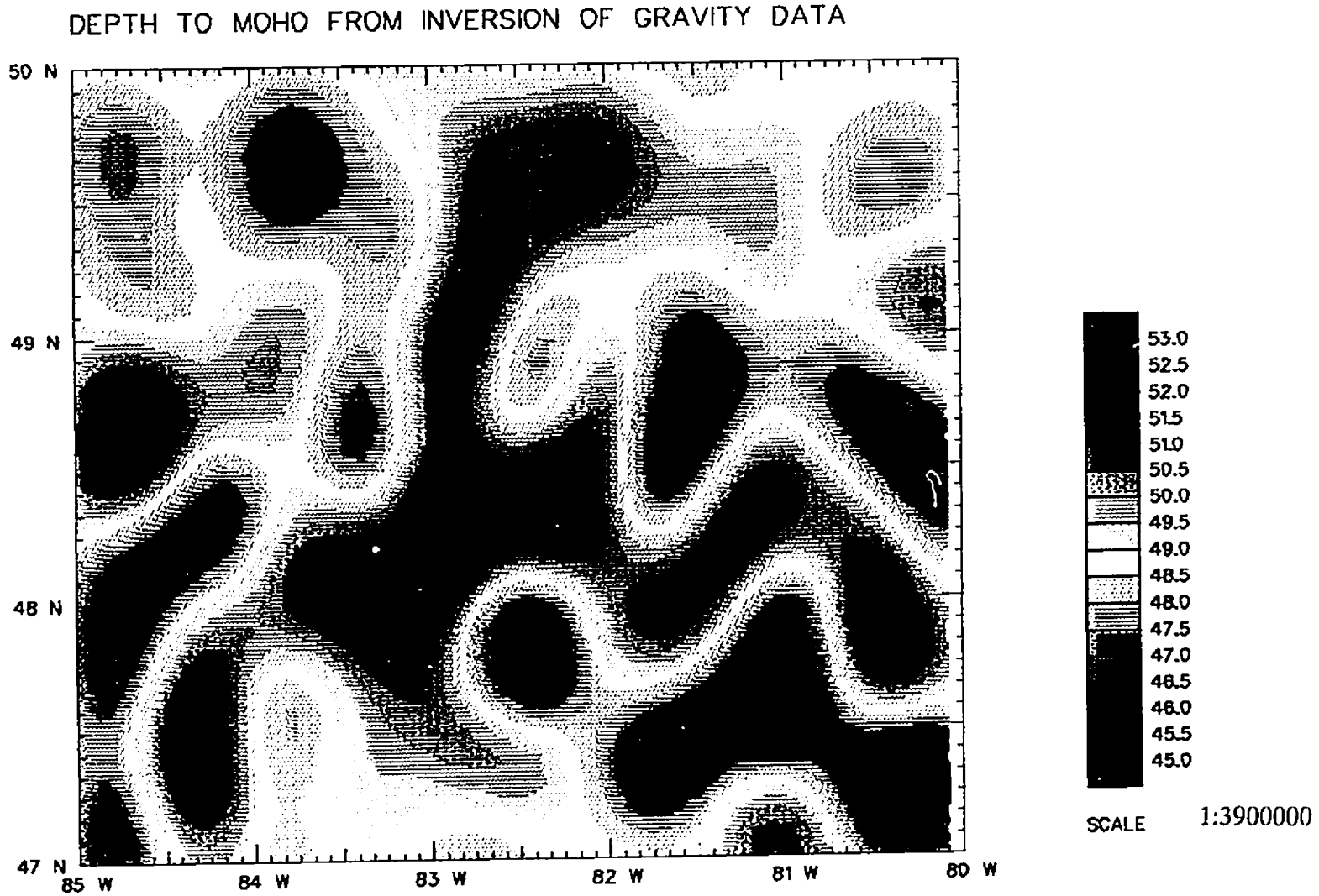

Figure 5-17. Calculated depth to Moho map from inversion of gravity data. Depth in km.

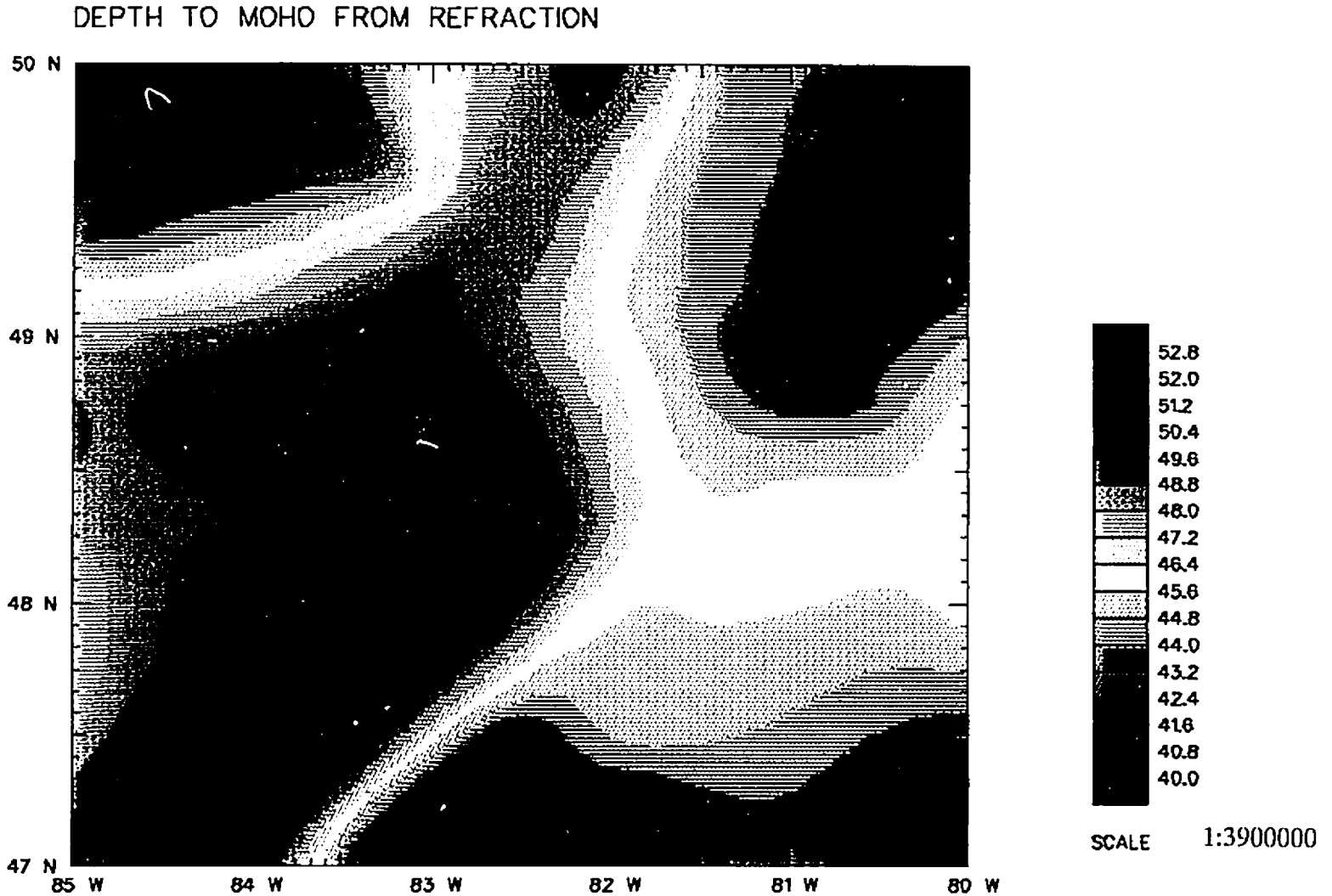

Figure 5-18. Depth to Moho map from refraction results of Northey and West (1986). Depth in km.

Along line 2 (Figure 5-19), which lies along the axis of the CB, the fit is generally good (within 1-2 km) except for the deviation observed at 180-260 km, where the calculated Moho appears deeper than the refraction Moho. The apparent difference may be explained by the fact that the refraction data lacks the details observed in the gravity data. Generally, both results show a deepening of the Moho from north to south with the thickest part of the crust underlying the CB.

Along line 5 (Figure 5-20) which cuts across the CB, the fit is generally good up to 140 km. Beyond this point, the Moho calculated from gravity appears deeper to the east with undulations. However, the general shape of the Moho topography between the two profiles is similar. Furthermore, as in Figure 5-18, both profiles show that the crust is thickest beneath the CB. The undulations to the east in the calculated profile may be explained by density variations in the crust that are not resolved in the refraction data.

Line 4 (Figure 5-21) which cuts across the VRB and GRB, shows good agreements in the shape of the Moho topography between the two results. The gravity profile shows undulations which may be attributed to lateral density variations within the crust that are not evident on the refraction profile. The crust is significantly thicker within the VRB. However, there is an approximately 2-3 km shift in level between the two results, with the Moho calculated from gravity deeper than the refraction Moho. Such a discrepancy between the two results could be possible if a slightly higher density contrast was used for the granulites within the VRB during the inversion. Furthermore, this discrepancy may possibly have resulted from the

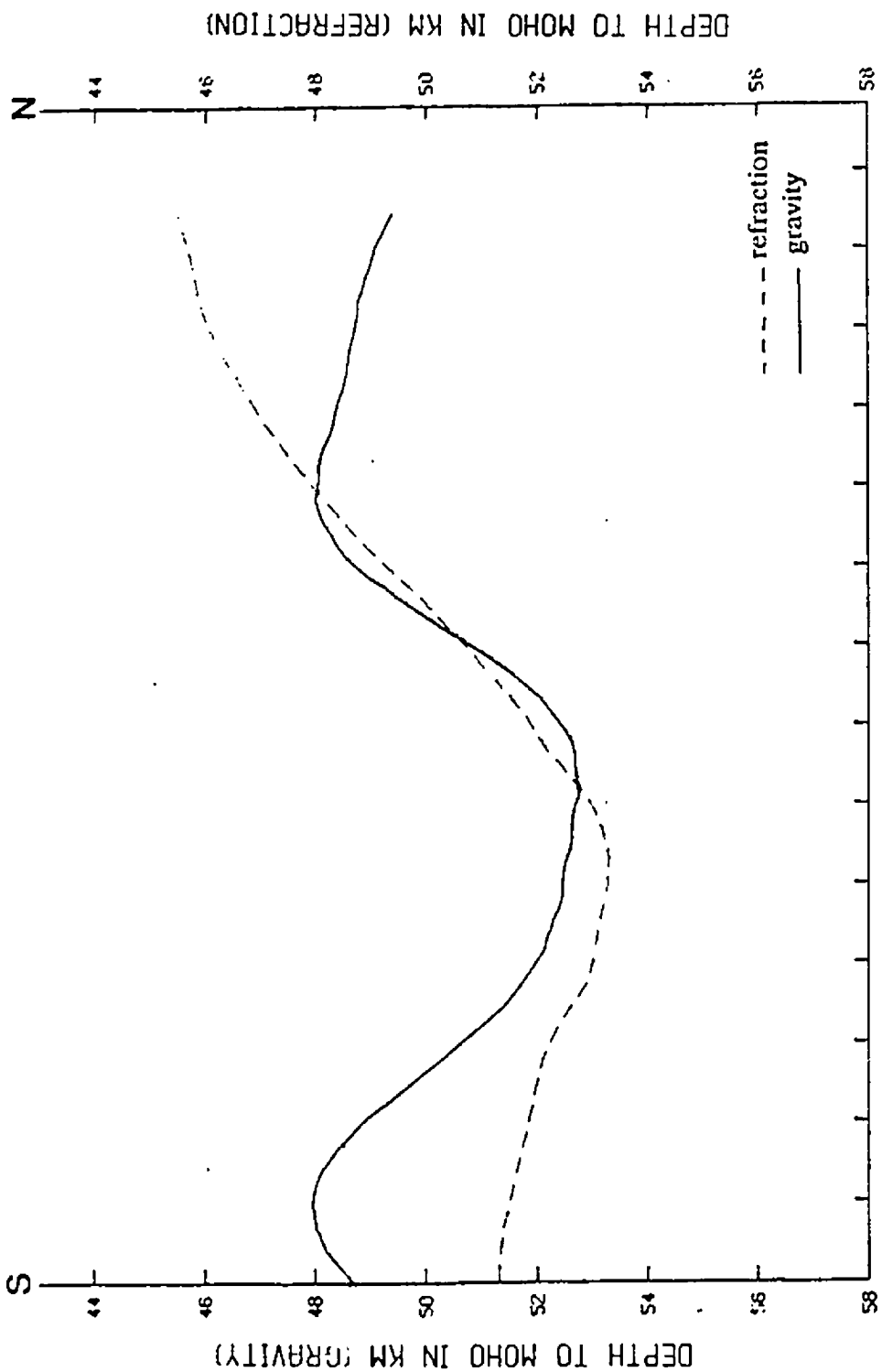

Figure 5-19. Comparison of depth to Moho from refraction and gravity data along line 2 (see Figure 2-3 for location of profile).

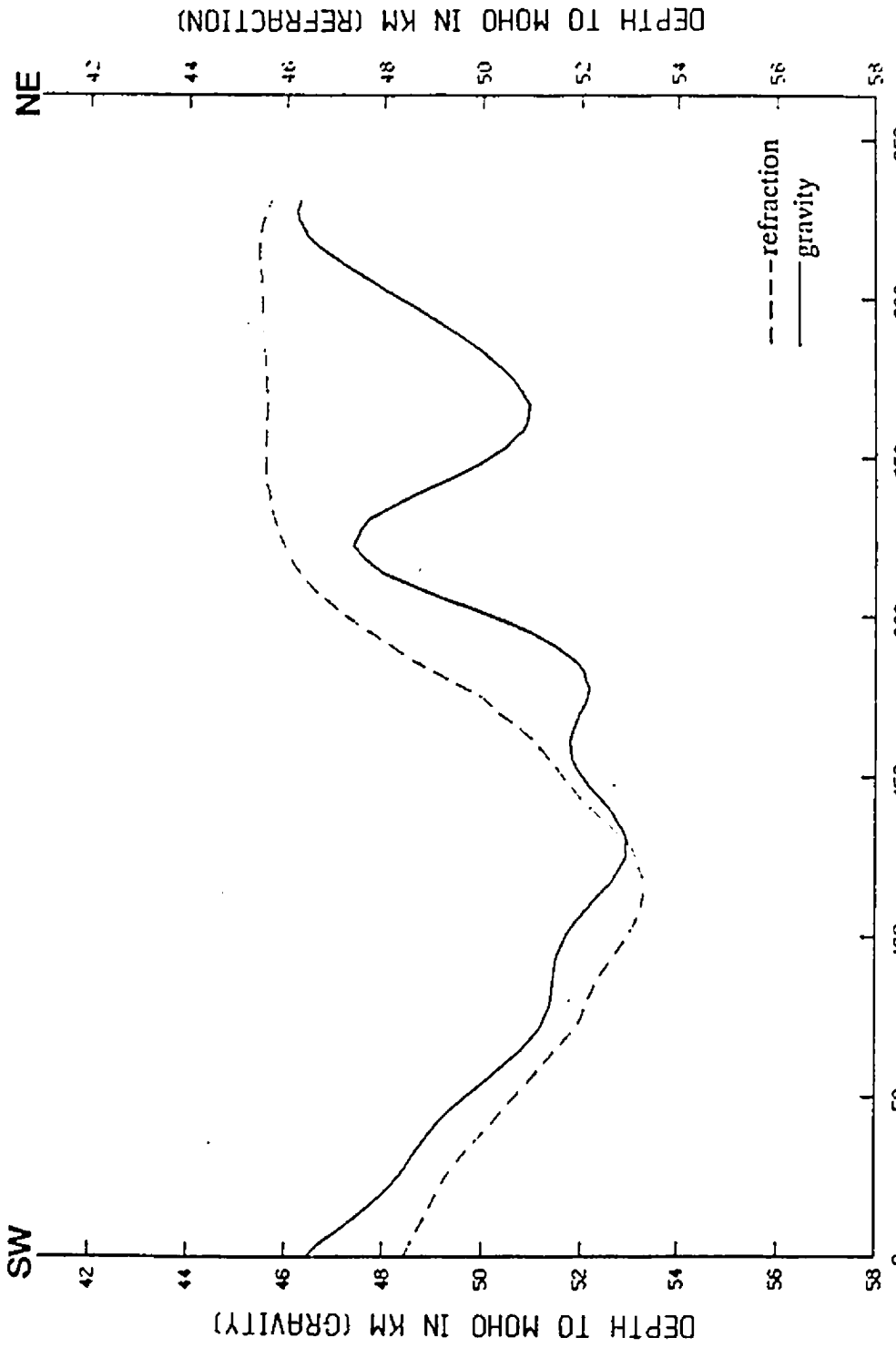

Figure 5-20. Comparison of depth to Moho along line 5 (see Figure 2-3 for location of profile).

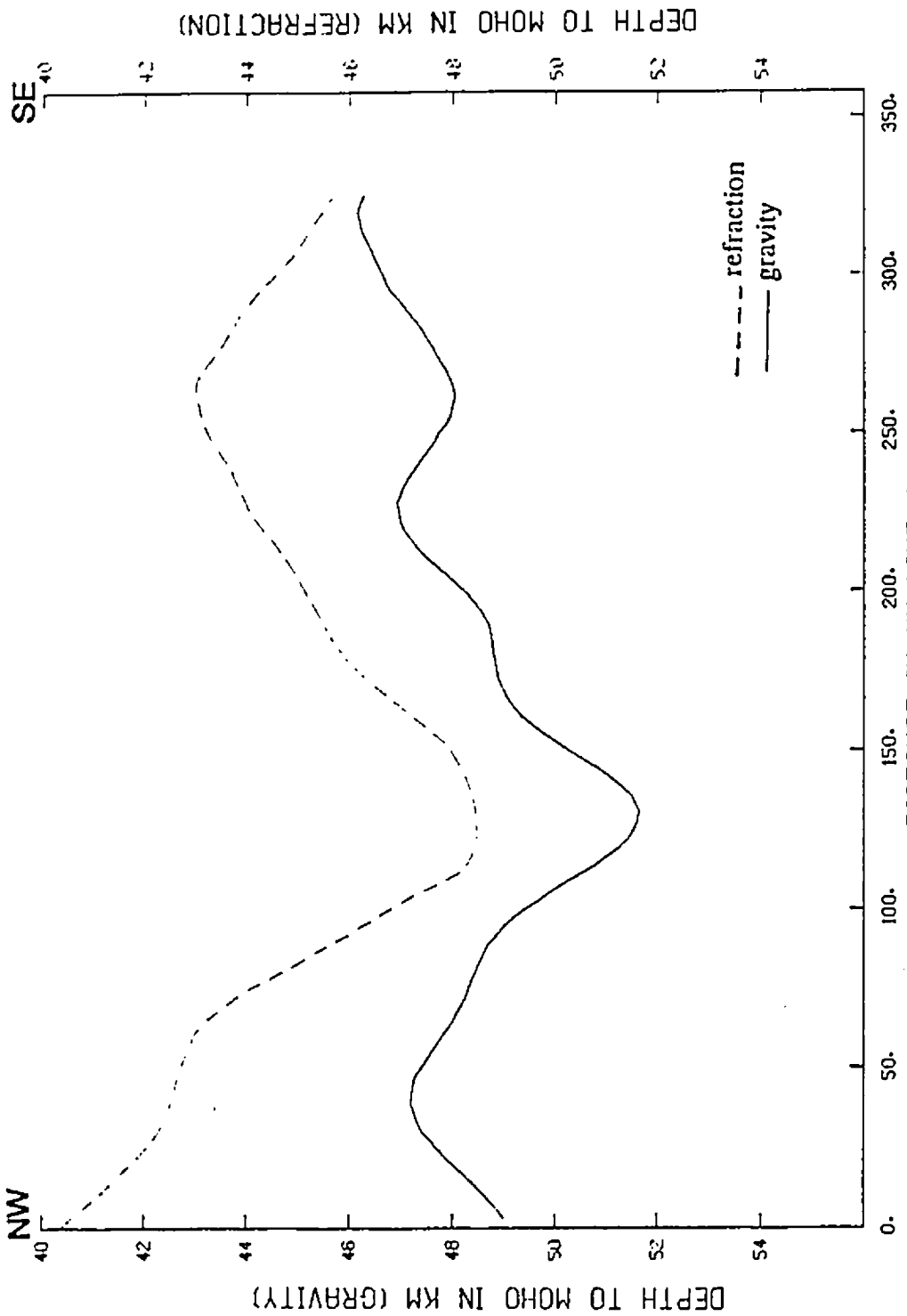

Figure 5-21. Comparison of depth to Moho along line 4 (see Figure 2-4 for profile location).

average depth to Moho of 47 km which was used in the original inversion process. Such a depth is about 2 km deeper than the average depth of about 45 km obtained for this part of the KSZ (see Figure 2-4b).

5.3.5 Calculation of Residual Gravity Anomalies

So far, the 3D gravity calculations have dealt with the longer wavelength component of the gravity anomaly resulting from deeper sources. The final step in the gravity analysis was to derive the residual anomaly associated with near surface sources. To do this, the 3D gravity anomaly caused by the relief and density variations at the top of layer 3 and the Moho were computed. The computed anomaly, which contains only the longer wavelength information was then added to the gravity anomaly of the upthrust slab that was initially isolated. The resulting map (Figure 5-22) can be compared with the observed Bouguer anomaly map (Figure 5-1). Lines 4 and 5 (Figure 5-1) were used for this purpose. The results (Figures 5-23a and b) show a good fit between the calculated and the observed gravity values. Next the calculated 3D gravity anomaly was then subtracted from the original Bouguer anomaly map of Figure 5-1 to obtain the residual map (Figure 5-24). The residual gravity anomaly map (Figure 5-24) contains mostly the short-wavelength information which can be attributed to lateral density variations in the upper part of the crust. On the basis of the previous 2D models and the surface geology map (Figure 2-1), these short-wavelength anomalies can be correlated with mafic metavolcanic rocks, granite, granodiorite and ultramafic plutons in the adjacent Wawa and Abitibi belts.

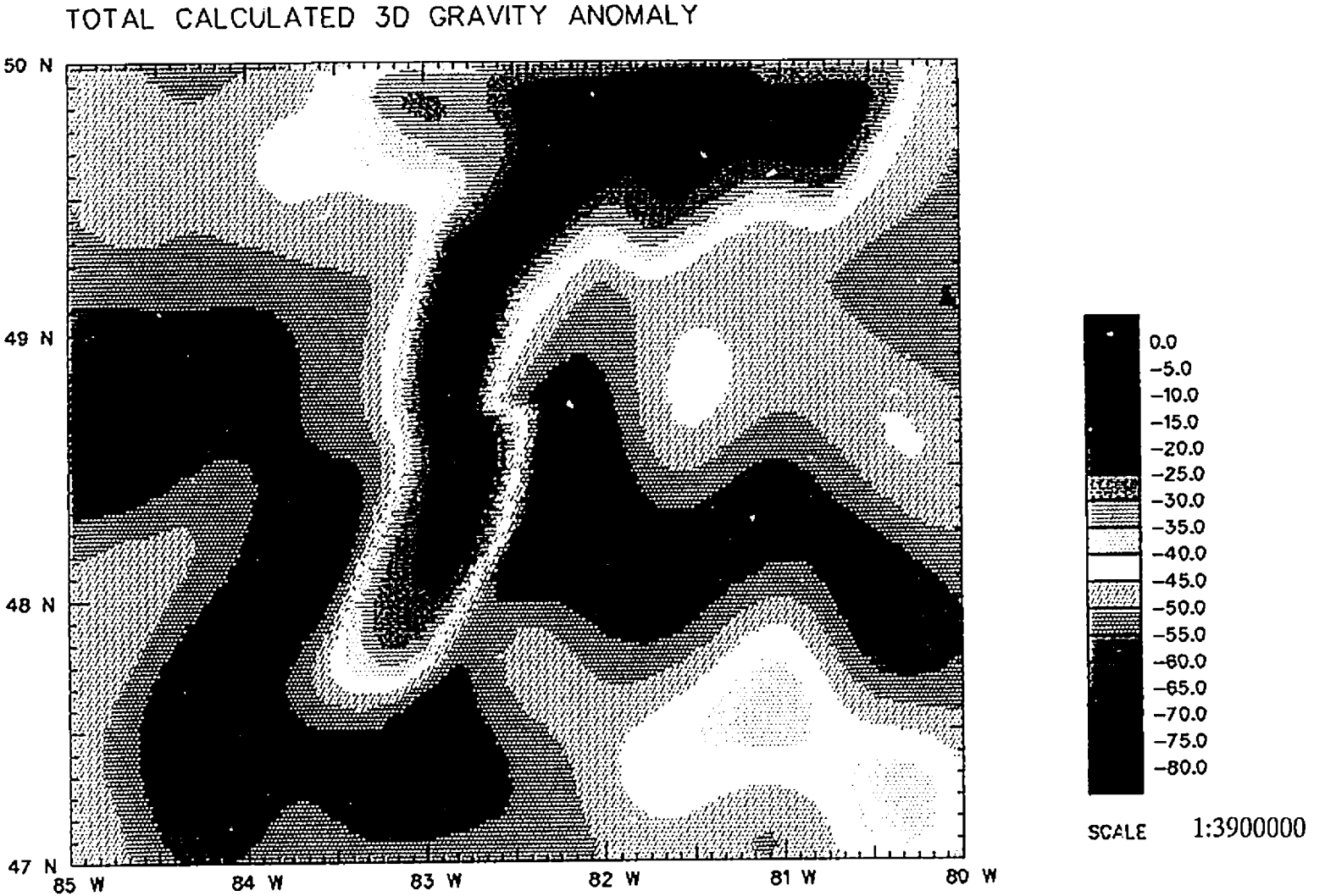

Figure 5-22. Calculated 3D gravity anomaly from the upthrust slab and the remaining deep layers as shown in Figure 5-14. Gravity in mGals.

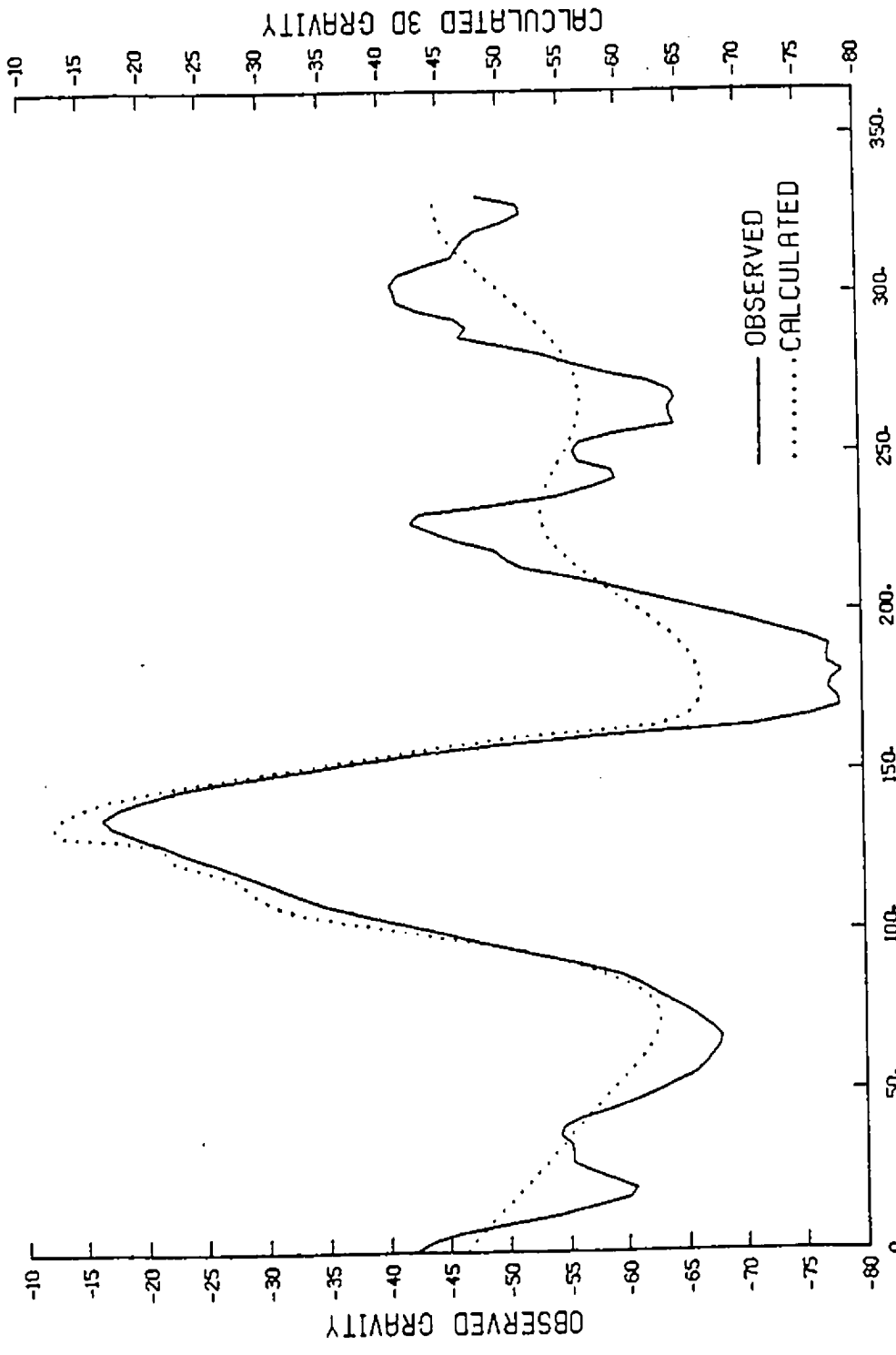

Figure 5-23a. Comparison of the calculated 3D gravity anomaly with the observed anomaly along line 5.

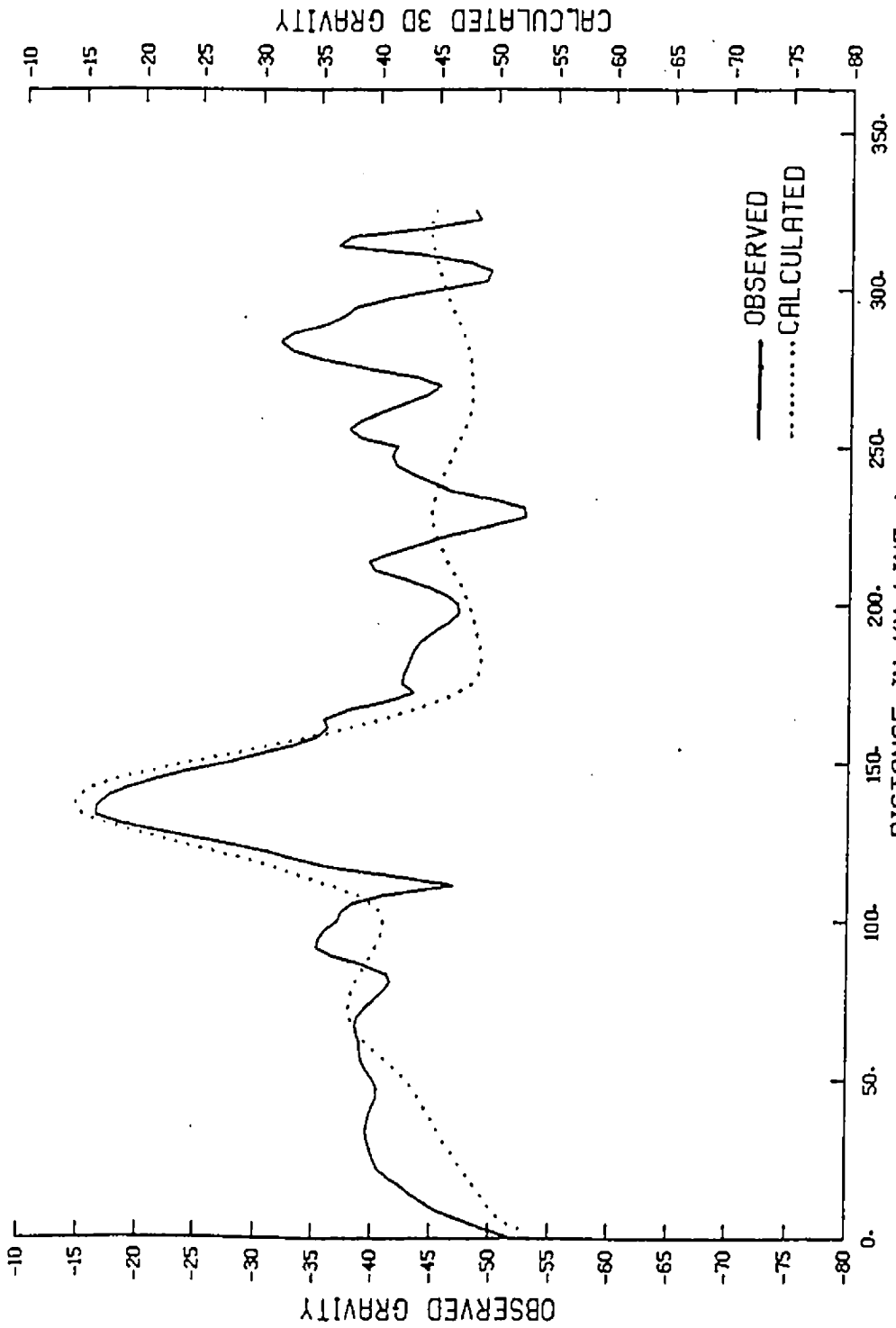

Figure 5-23b. Comparison of the calculated 3D gravity anomaly with the observed anomaly along line 4.

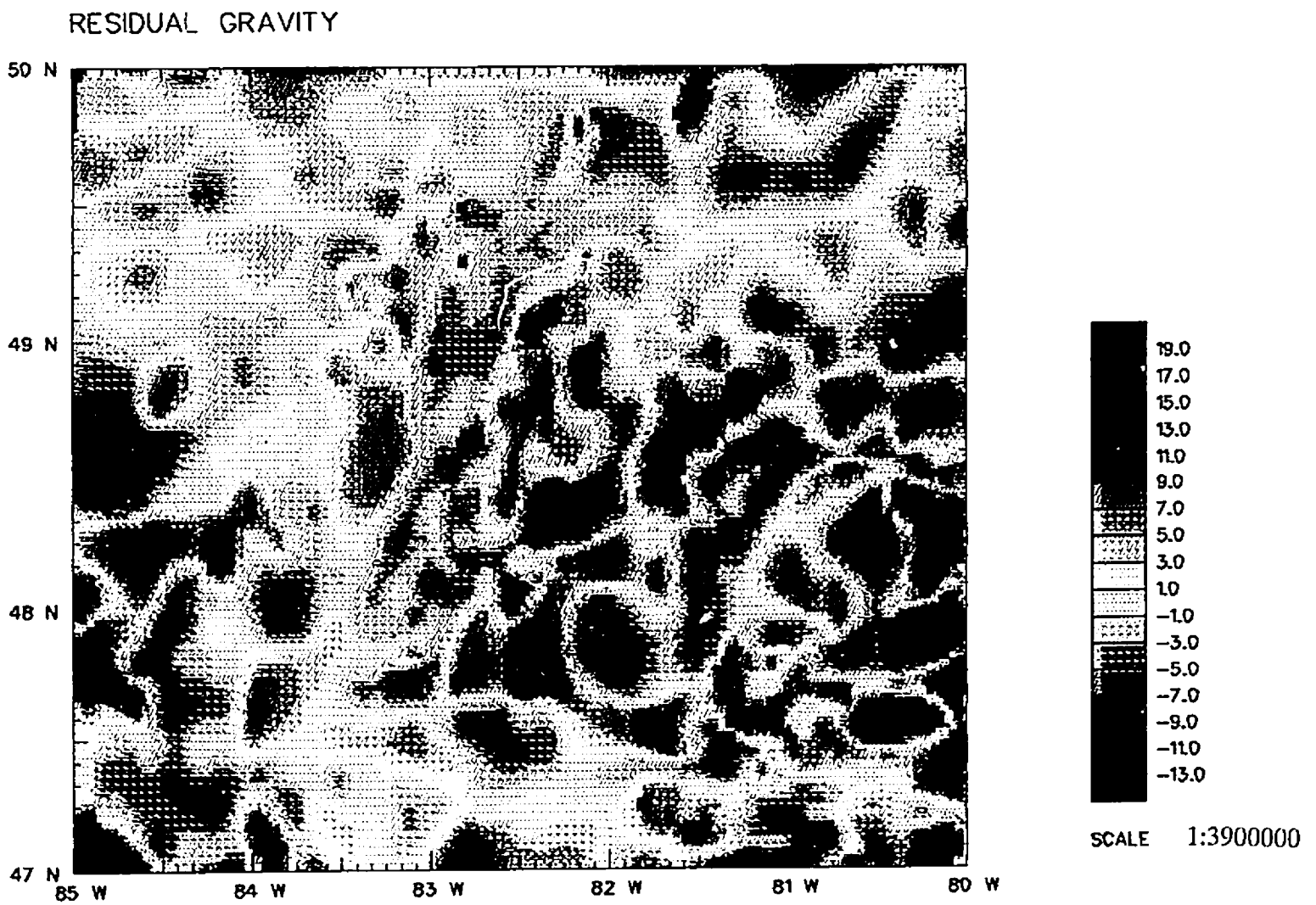

Figure 5-24. Residual gravity anomaly from subtracting Figure 5-22 from the observed gravity anomaly (Figure 5-1). Gravity in mGals.

The short wavelength filtered maps (Figures 4-5 and 4-9) suggest that these density variations are found within the shallow levels of the crust, which is consistent with the depths (6-8 km) obtained from 2D gravity models for these near surface sources.

5.4 MAGNETIC MODELS

5.4.1 Introduction

The techniques employed in the interpretation of the magnetic data are similar to those used for the gravity data. However, the magnetic method is more complicated than the gravity method because susceptibility variations can be more pronounced than density variations for a given rock type and also because the magnetic field is dipolar. The main objectives of the magnetic modelling were to provide additional constraints for the gravity models and to determine the attitude of some of the faults that could not be accurately determined from the gravity data (especially within the GRB). Variations in the magnetic anomalies are interpreted in terms of differences in magnetization. The algorithm used in the interpretation is similar to that used for the gravity anomalies except that the calculation uses a magnetic scalar potential (Talwani et al, 1964).

Magnetic coverage for the area is excellent (Figure 4-1). Most of the modelling is concentrated within the VRB and GRB. No magnetic models have been produced for the CB because the magnetic anomalies within this block are subtle, and are limited to narrow strips of granulites and areas of carbonatite intrusion. The susceptibility values used for the modelling are from Table 2. To facilitate the

modelling process, the high frequency anomalies have been filtered out by upward continuation to 2 km. The danger of upward continuing the data is that the anomalies become broader and a change in the slope of the anomalies occur. For example, a fault will have a shallower dip than is actually observed if modelled with data that are upward continued. Therefore, to counteract the uncertainties in the slopes of the anomalies which may be introduced in upward continuing the data to 2km, the magnetic anomalies have been modelled at 2 km depths. In the modelling, it is assumed that the anomalies caused by the bodies are induced from the Earth's field with an inclination of 78° and a declination of -7°. Although the remanent magnetization may contribute significantly to the magnetic anomaly (especially for the GRB as shown in Table 2), its contribution was not taken into account during the modelling because of the lack of good constraints for its direction and intensity.

5.4.2 Magnetic Model: Val Rita Block

The magnetic anomaly within the VRB indicates a change of about 300 nT across the LF from west to east (Figure 4-1). In order to fit the magnetic data, the granulites within this block have been modelled with susceptibility values comparable to those of the GRB (Table 2). The magnetic model (Figures 5-25) requires that the magnetic source body must have an upper surface which dips gently to the southeast at an angle of 12 degrees. This result is in agreement with the gravity modelling results for this block (Figures 5-6, 5-7 and 5-8). In fact, using the gravity models shown in Figures 5-6 and 5-8 as inputs for the magnetic models, the calculated

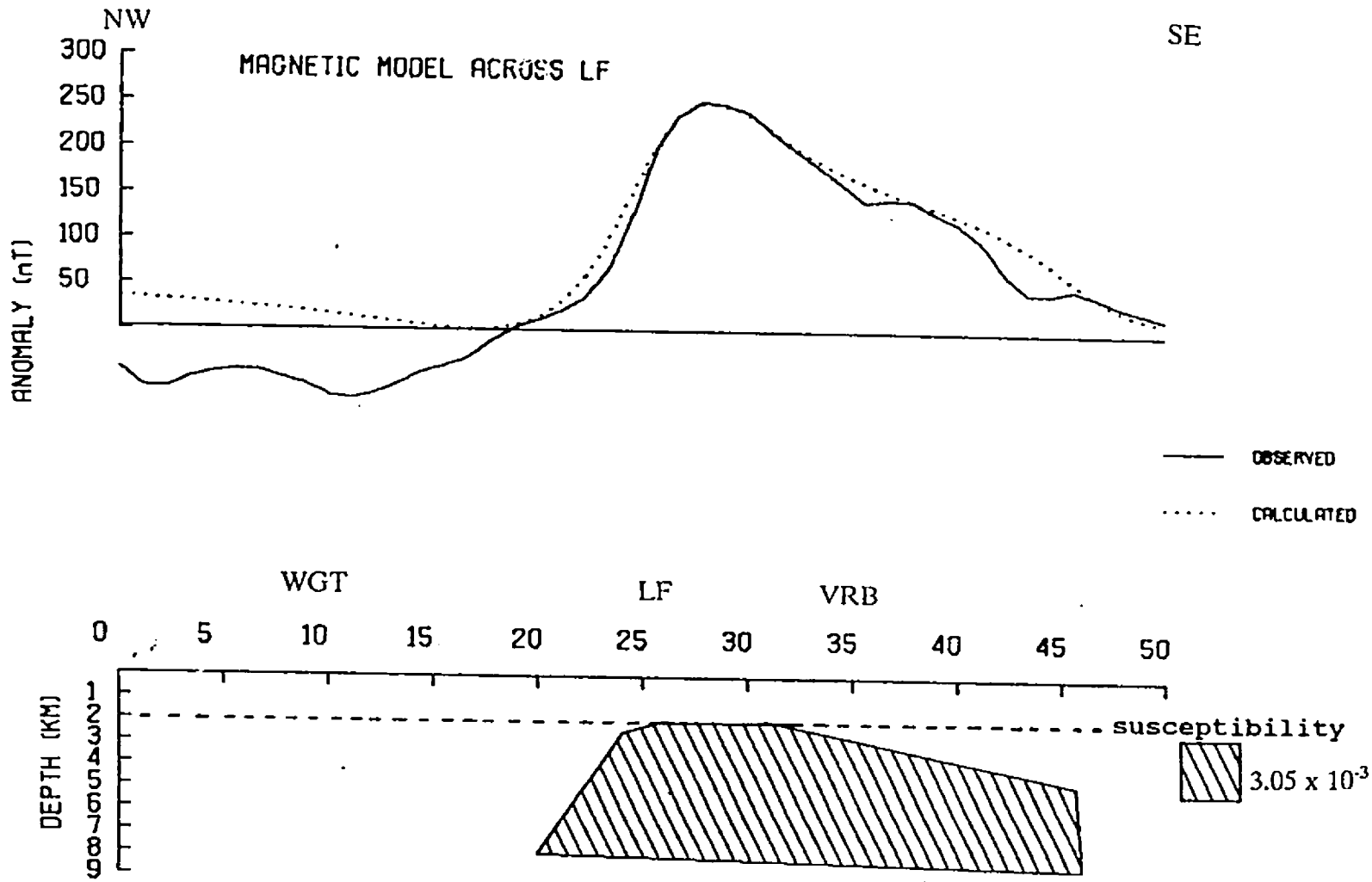

Figure 5-25. Magnetic model along the profile S-S' (see Figure 4-1 for profile location). Susceptibilities in emu/cm^3. The dashed line is the 2 km depth used for the modelling.

anomalies (Figure 5-26a and b) agree with the corresponding observed magnetic anomalies. In these models only the granulites (layer 2) have been specified as a magnetic unit (with a susceptibility of 3.05 x 10^{-3} emu/cm^3) because of the lack of constraints for the susceptibility of the lower layers. The results also show that the source body is not exposed at the surface, except for minor exposures along the LF, but is buried at shallow crustal depths of about 1-2 km. It is therefore probable that the high density granulites responsible for the gravity anomaly within the VRB are also responsible for the magnetic anomaly observed over this block (In fact, the correlation map, Figure 4-14 suggests that this may indeed be the case). In Figures 5-25, 5-26a and b, the LF is modelled as a normal fault dipping 60° to the northwest, underneath the Quetico belt.

5.4.3 Magnetic Model: Groundhog River Block

A very strong magnetic anomaly with an amplitude of 500nT which is not over-shadowed by the anomaly from the VRB characterizes the GRB, and allows for detailed study of the faults bounding the block. Table 2 shows that susceptibility values within this block are quite variable, ranging from 0.0012 x 10^{-3} emu/cm^3 to 10.64 x 10^{-3} emu/cm^3, with a mean around 3.05 x 10^{-3} emu/cm^3. In modelling the magnetic anomaly within this block several susceptibility values from Table 2 were used. When a value of 1.55 x 10^{-3} emu/cm^3 was used, a thickness of about 5 km was obtained for the granulites. However, when the average value for the block (3.05 x 10^{-3} emu/cm^3) based on the data in Table 2 was used, a thickness of about

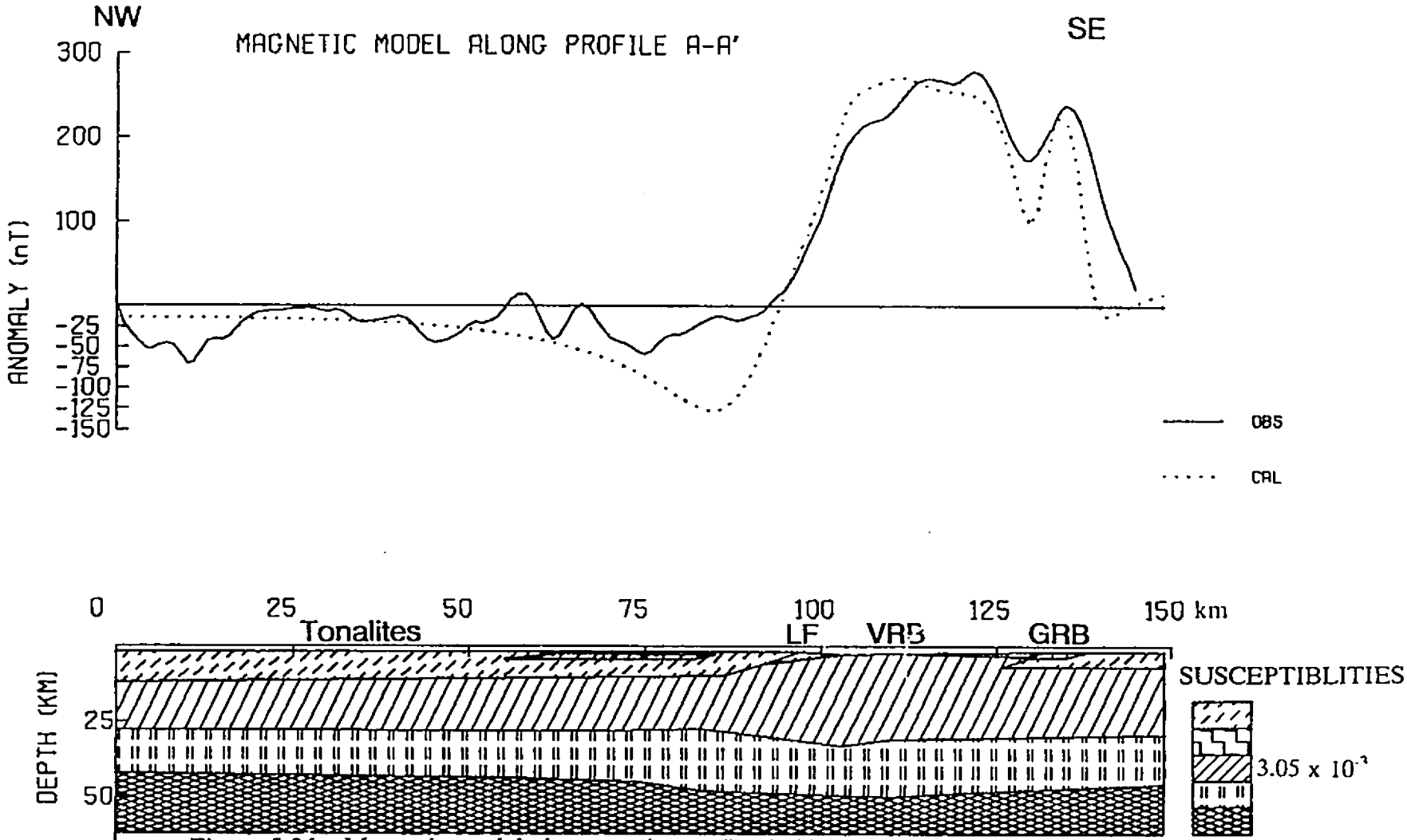

Figure 5-26a. Magnetic model along gravity profile A-A' (see Figure 5-1 for profile location). The susceptibilities of all layers except the granulite layer is set to zero. Susceptibilities in emu/cm^3.

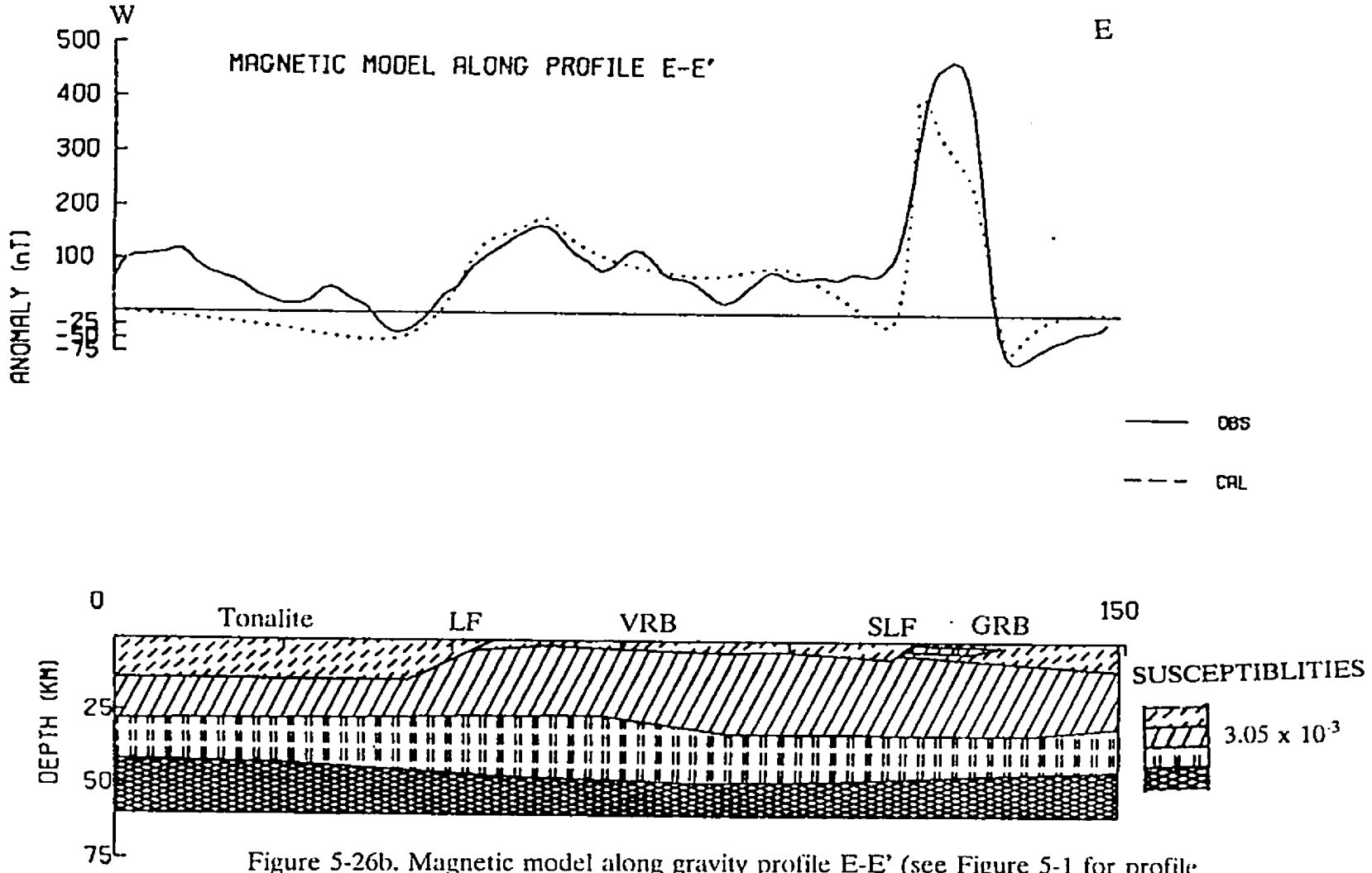

Figure 5-26b. Magnetic model along gravity profile E-E' (see Figure 5-1 for profile location). The susceptibilities of all layers except the granulite layer is set to zero. Susceptibilities in emu/cm^3.

3 km was obtained (Figure 5-27a). Furthermore, when the highest susceptibility of 10.64 x 10^{-3}emu/cm^3 was used, a thickness of about 1 km is obtained (Figure 5-27b). Using a susceptibility of 3.05 x 10^{-3} emu/cm^3, Figures 5-28a and b show that the thickness of the GRB varies from north to south. The thickest part of the block (4 km) is to the south (Figure 5-28b), and the thinnest is to the north (Figure 5-28a) where a thickness of about 1.5 km is obtained. Therefore, within the limits of the susceptibility data available, the same block model can satisfy both the gravity and magnetic data. However, because of the wide variability in the measured susceptibility values, the lack of appropriate information on the remanent magnetization and because of the limited data available, the thickness cannot be further constrained. Most of the models, (especially Figures 5-27a and b) show a poor fit to the southeast. This may be attributed to the fact that the susceptibilities within the AB may be much lower than those in the VRB, or it could also suggest some remanence in the GRB (as can be seen by the asymmetry of the profiles).

Several profiles (Figure 4-1) have been used to model the faults bounding the GRB and the results are shown in Figures 5-29a, b and c. Using the average susceptibility of 3.05 x 10^{-3}, the WRF is modelled as a normal fault (Figure 5-29a) dipping about 65° to the northwest underneath the GRB. In Figure 5-29b, the SLF is also modelled as a northwest dipping fault, with dips of about 48°. Finally the ILCZ (Figure 5-29c) is modelled with a dip of about 45-50° to the northwest.

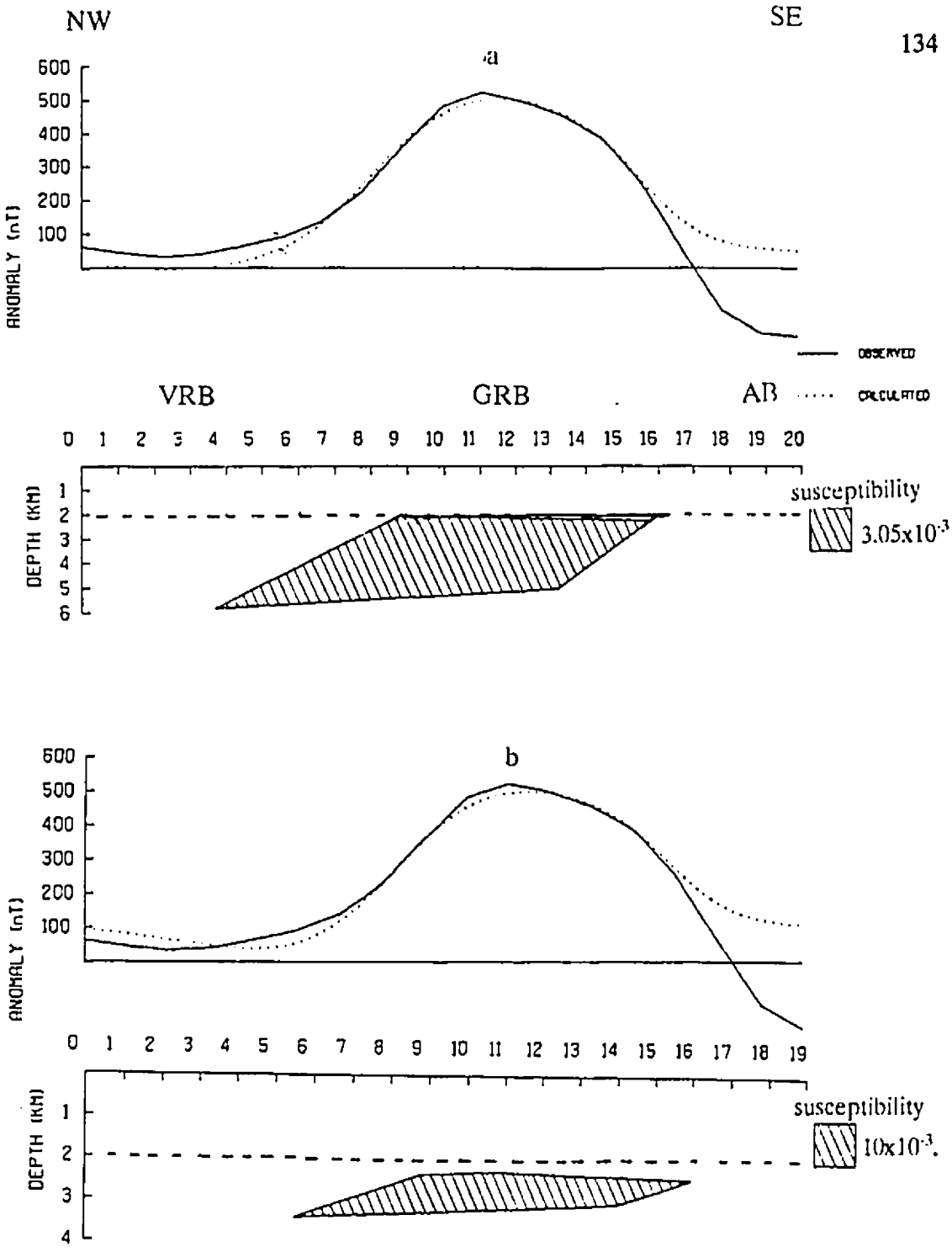

Figure 5-27 a: Magnetic model along profile G-G' showing a 3 km thick GRB using a susceptibility of 3.05 x 10^{-3}. b: Magnetic model along profile G-G' showing a 1 km thick GRB using the highest susceptibility value of 10 x 10^{-3} (see Figure 4-1 for profile location). Susceptibilities in emu/cm^3. The dashed line is the 2 km depth used for the modelling.

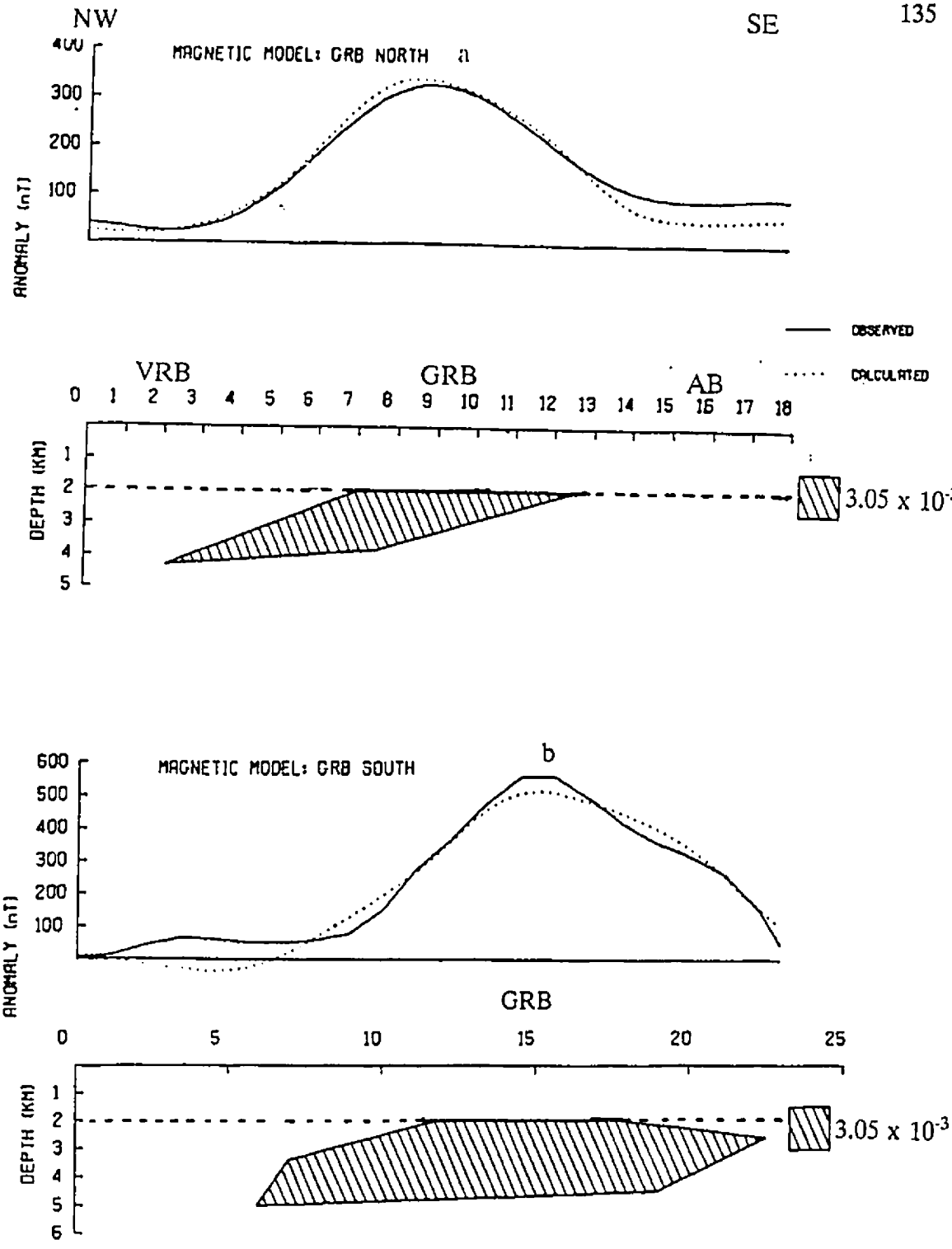

Figure 5-28 a: Magnetic model along profile N-N' north of the GRB block. The block is about 1.5 km thick in the north. b: Magnetic model along profile F-F'. The block is about 4 km thick in the south (see Figure 4-1 for profiles' location). Susceptibilities in emu/cm^3. The dashed line is the 2 km depth used for the modelling.

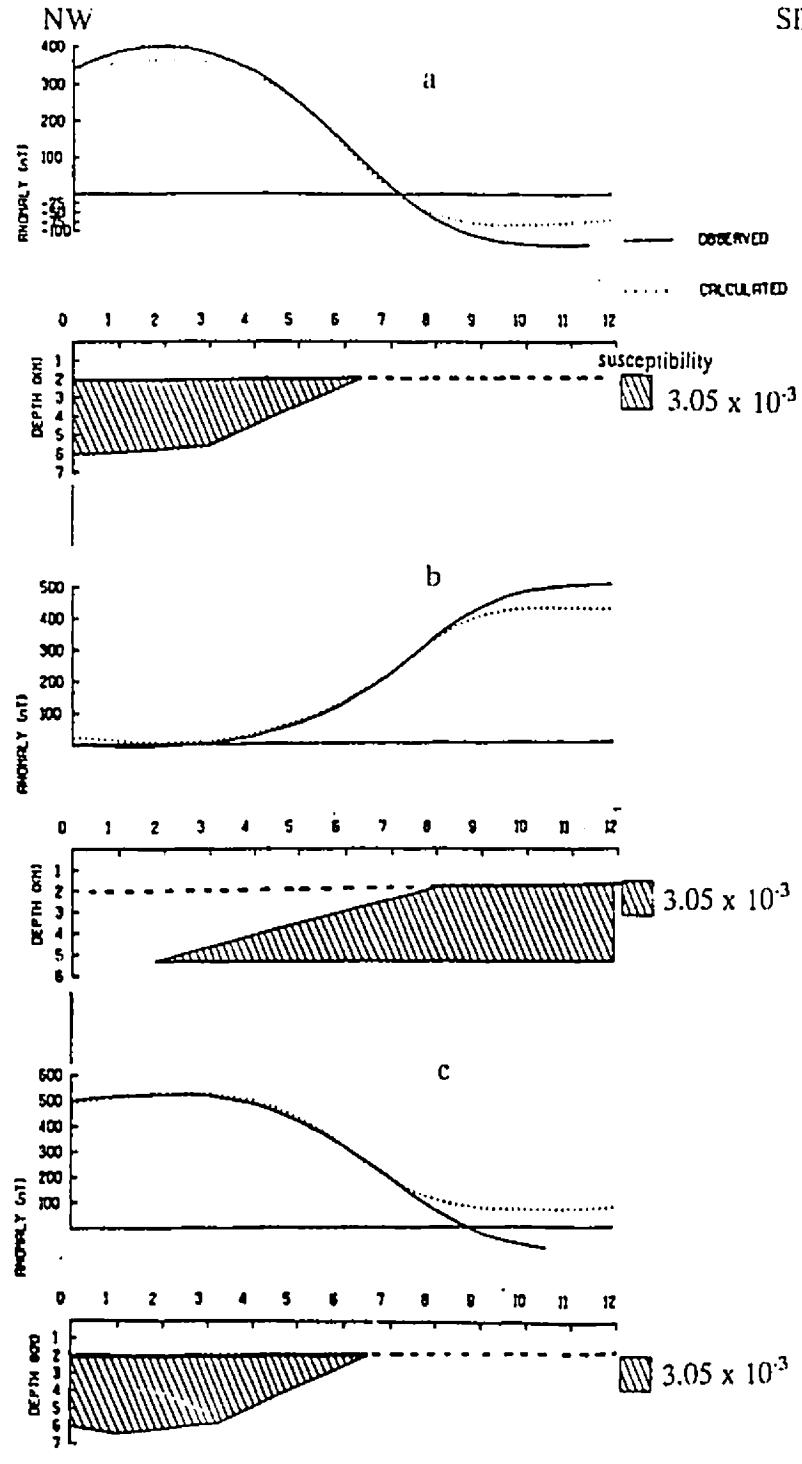

Figure 5-29 a: Magnetic model across the WRF (profile W-W', Figure 4-1); b: Magnetic model across the SLF (profile L-L'); c: Magnetic model across the ILCZ (profile I-I') (see Figure 4-1 for profiles' location). Susceptibilities in emu/cm^3. The dashed line is the 2 km depth used for the modelling.

5.5 CONCLUSION

Several profiles have been modelled using 2D and 3D algorithms to interpret the potential field anomalies across the different tectonic blocks of the KSZ. The models, which have been well constrained by other data sets, show a good fit between the observed and calculated anomalies. In addition, the models show that simple density and magnetization assumptions can be used to explain the observed potential field anomalies. In the CB, dense granulites from deeper levels have been uplifted to the surface and are responsible for the anomaly observed over it. Although the geology does not correlate with the potential field anomalies over the VRB, the model results show that uplift of granulites from deeper levels of the crust to shallower levels is responsible for the anomalies observed over the block. On the other hand, granulites present in the GRB do not show a corresponding gravity anomaly because of their limited depth extent. An inversion to the Moho produced results that are in general agreement with depths obtained from refraction results. The crust is considerably thickened underneath the CB and VRB and thins underneath the adjacent regions. Several high angle normal faults have been modelled from the potential field data and are seen as discontinuities or breaks on the gravity and magnetic maps.

CHAPTER SIX: RESULTS AND INTERPRETATION

6.1 INTRODUCTION

One of the objectives of this study has been to provide an interpretation of the deep crustal structure of the KSZ by integrating results from potential field data with other available data. In the previous chapter, several models were constructed to explain the potential field anomalies over the different blocks of the KSZ. The purpose of the present chapter is to review the structures suggested by these models, to integrate them with the results from other studies and provide a structural interpretation of the different tectonic blocks. The cross-sections from the potential field models will be balanced, in order to determine their validity. Furthermore, the relationship between the different blocks will be examined as a means of explaining the geophysical disparities observed among them and a comparison between the Kapuskasing uplift and other structures will be made. Finally, the structural evolution of the KSZ will be discussed from insights gained from this study, and the implications of the interpreted structures will be examined.

6.2 RESTORABLE CROSS-SECTIONS OF THE 2D GRAVITY MODELS

6.2.1 Introduction

The 2D cross-sections constructed from the gravity models can be balanced in order to determine the validity of the sections. It is suggested that if the cross-sections can be restored to their original un-deformed state, then they can be considered viable (Elliott, 1983). A balanced section occurs when the bed-lengths,

or cross section areas, are equal in both the deformed and un-deformed state (Woodard et al, 1985).

Although balanced cross-sections are predominantly used in fold and thrust belts, Percival (1988) has demonstrated that this technique can also be applied in the KSZ. In fact, the structures modelled in the KSZ are similar to those in the fold and thrust belts. Therefore, the application of this technique to the KSZ is a worthwhile effort and may be important in determining the amount of shortening that has occurred in this region.

The 2D cross sections can be balanced given the following constraints based on gravity models and existing geological and geophysical data: 1) rocks from 15-30 km (8-9 Kbars) depth are exposed within the KSZ; 2) the ILCZ was the thrust surface responsible for uplifting these rocks to the surface; 3) the ILCZ has a dip of 25-30° and 4) about 10 km of crustal thickening has occurred underneath the KSZ.

6.2.2 Restorable section of the CB along profile C-C'

The cross-section along profile C-C' (Figure 6-1a) can be balanced for shortening using the following assumptions: 1) a ramp antiform geometry during the uplift; 2) no movement of material away from the plane of the section; 3) the granulites were cool at the time of the uplift; 4) the average crustal thickness is between 43-47 km; and 5) the direction of transport is to the southeast (direction of transport is perpendicular to the direction of the regional structural trend). Using the above assumptions, the restorable section (Figure 6-1b) suggests that 65 km of crustal

shortening has taken place within this block. It is interesting to note that Percival (1988) suggests about 70 km of crustal shortening within the KSZ.

6.2.3 Restorable sections of the VRB and GRB along Profile B-B'

Using a similar approach, the cross section along the profile B-B' within the VRB and GRB can also be restored. However, the excellent constraints for the depth to the decollement provided by the reflection data for the CB are not available for this region. Hence, balancing can only be done in a cursory fashion. In balancing the sections along B-B' additional assumptions to those listed in 6.2.2 include: 1) the thrust plane can be represented by either a single or a double ramp; 2) the VRB and GRB are part of continuous thrust sheet (following restoration after normal faulting).

Using the above assumptions, Figure 6-2a and b suggest that approximately 35-40 km of shortening has occurred within the VRB and GRB. Results from both profiles (C-C' and B-B') suggest that shortening above the decollement is balanced by thickening of the crust below the decollement. These results are consistent with results obtained by Percival (1990) and imply the following: 1) deformation in the detached plate above the decollement may have been brittle, and could only have happened if the Kapuskasing rocks were cool (in fact, Percival, 1990 suggests that these rocks had cooled to below the 300°C isotherm); 2) the thickening beneath the KSZ can be seen as a direct response to shortening in the upper plate and can be possible if the rocks beneath the decollement exhibited a ductile behavior (Percival

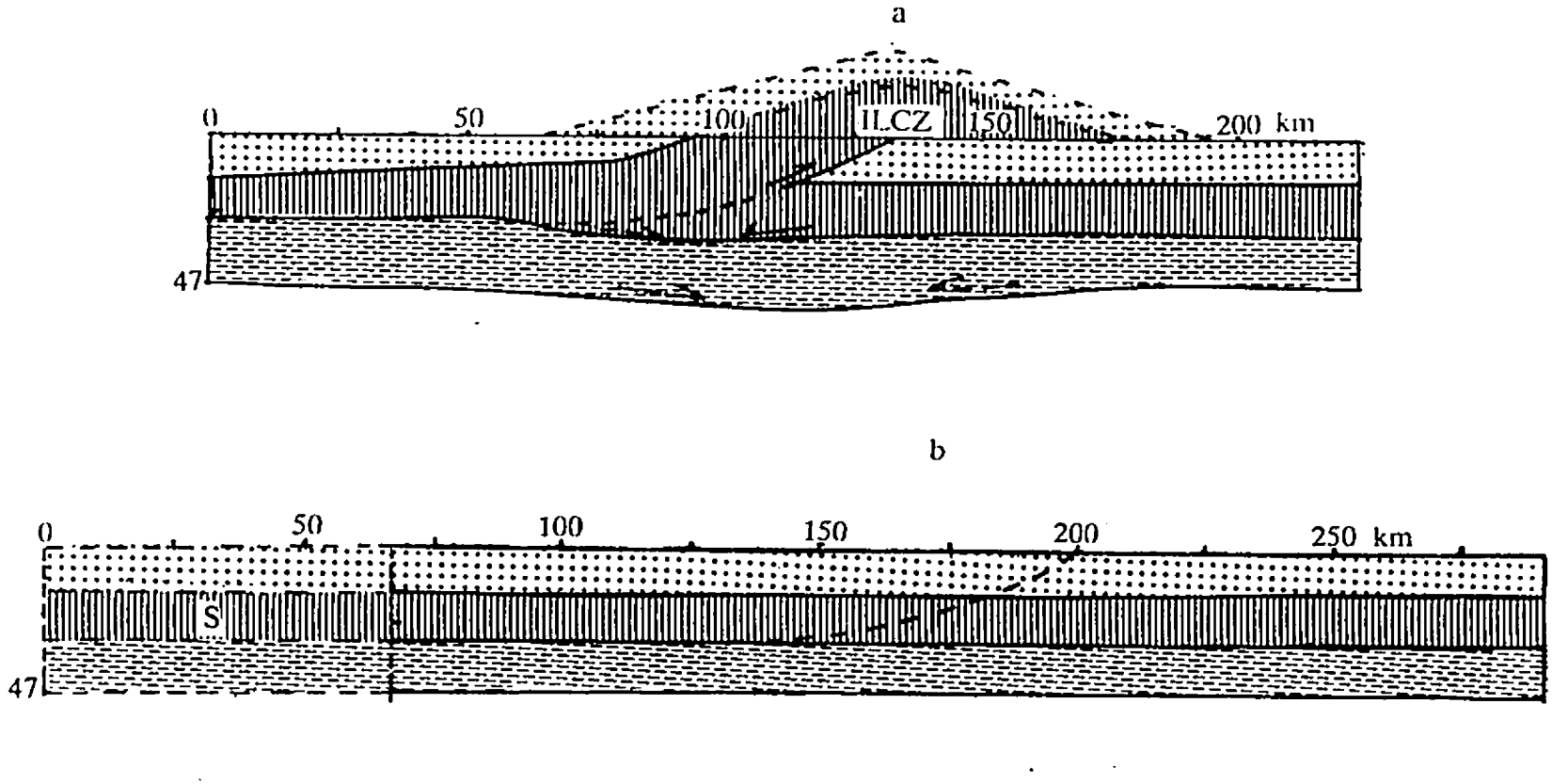

Figure 6-1a: Present day configuration (deformed) of the crustal section along profile C-C' assuming an initial ramp antiform geometry for the uplift. Broken arrows indicate ductile deformation, while solid arrows indicate brittle deformation; b: restored section along profile C-C' indicating 65 km of shortening (see Figure 5-1 for profile location). S indicates the amount of shortening.

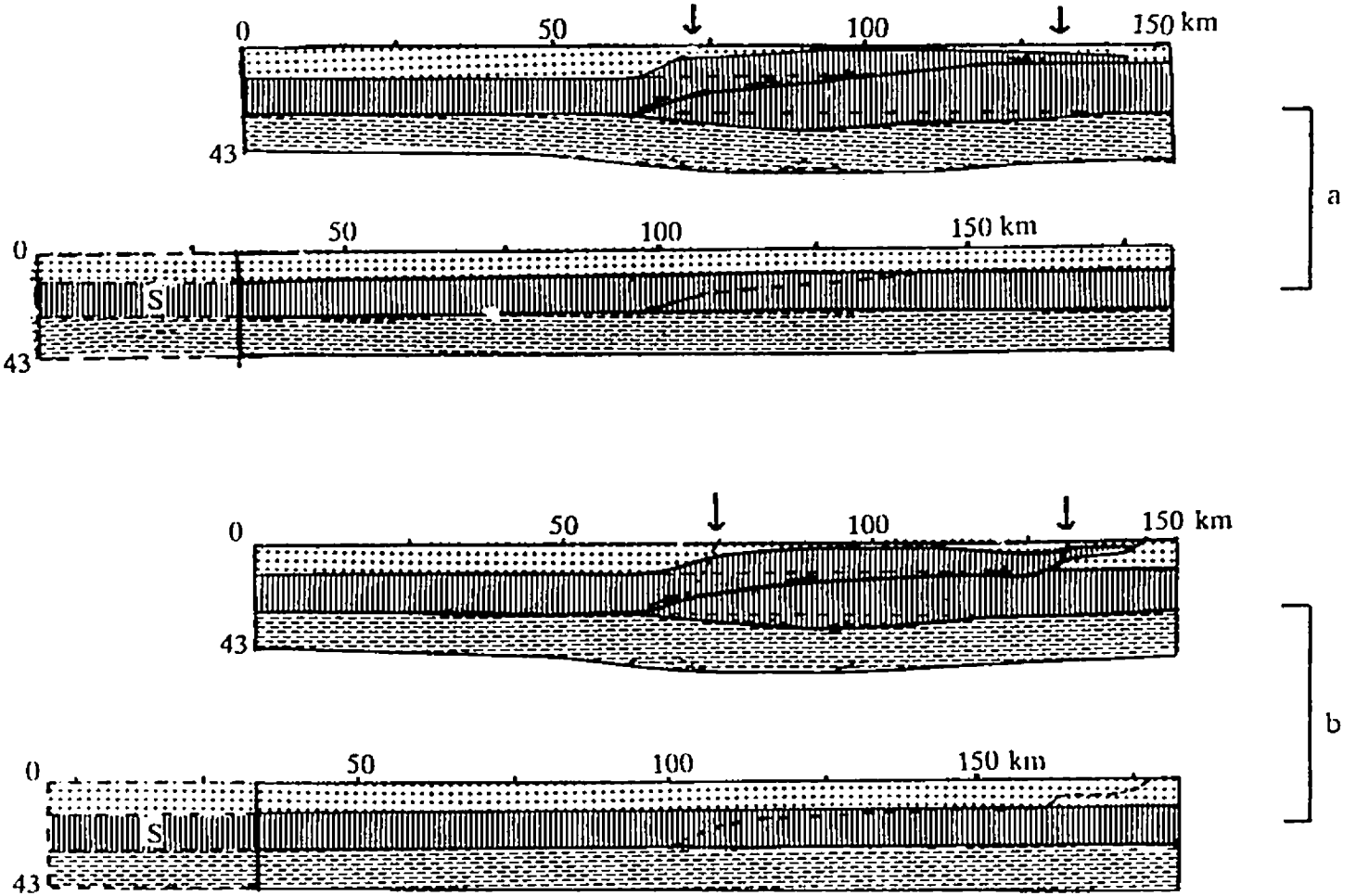

Figure 6-2a: (upper) Deformed geometry of the crustal section along profile B-B' assuming a single ramp; (lower) restored section indicating 32 km of shortening; b: (upper) Deformed geometry of the crustal section along profile B-B' assuming a double ramp; (lower) restored section indicating 35 km of shortening. S indicates the amount shortening, and arrows indicate locations of later normal faults.

and Green, 1988); and 3) maximum vertical and horizontal displacement (accompanied by 65 km of shortening) occurred within the CB and that displacement decreased northwards towards the VRB and GRB (35 km shortening). If more displacement occurred within the CB, this can explain why the granulites within the VRB are buried but exposed within the CB (i.e., the ramp antiform must have been removed by erosion. This can also explain why the crust under the CB is thicker (52-53 km) than that under the VRB (48-50 km).

6.3 STRUCTURAL INTERPRETATION OF THE TECTONIC BLOCKS

6.3.1 Previous Interpretations

Several interpretations have been postulated for the KSZ including : a thinning of the granitic layer (Garland, 1950), a deeply eroded rift (Innes , 1960; Innes et al., 1967), an upwarp of the Conrad discontinuity (Wilson and Brisbin, 1965), an uplifted Archean or Proterozoic horst (Bennet et al., 1967; McGlynn, 1970), a suture (Wilson, 1968; Gibb and Walcot, 1971), a failed arm of a plume-generated triple junction (Burke and Dewey, 1973), a broad zone of sinistral transcurrent fault movement (Watson, 1980) and recently, an upthrust lower crustal slab (Percival and Card; 1983, 1985, and subsequent references). This latter interpretation has gained support from recent reflection and refraction results, as well as laboratory velocity measurements. The results presented in this study support the above interpretation of an upthrust lower crustal slab.

The fault bounded blocks of the KSZ exhibit differences in their lithology, metamorphic assemblages and deep crustal structure, resulting in the geophysical disparities among them. These disparities have been explained by variations in subsurface geometry among the different blocks, resulting from the dissection of an originally coherent thrust sheet by post thrust normal faults (Percival and McGrath, 1986), and by the exposure of different lithostructural levels of the crust, juxtaposed together by displacements along several northeast trending normal faults (e.g., Leclair, 1990). Hence, the CB is interpreted as a tilted slab and the GRB as a perched thrust tip. No interpretations were provided for the subsurface structure of the VRB. This study differs from previous interpretations in that it combines the results from potential field modelling with the results from other geophysical studies (seismic reflection and refraction) to provide interpretations for the upper and deeper crustal structures of the VRB, GRB and CB of the KSZ.

6.3.2 Val Rita Block

In the absence of any reflection data, insights into the deep crustal structure of the VRB are provided by the potential field models, refraction data, subsurface mapping and geobarometric results. The deep crustal structure of the VRB has been considered enigmatic because the CB gravity anomaly is seen to diverge into this block, in the form of an arcuate anomaly (Figure 3-3), and the anomaly appears to be inconsistent with the surface geology (Figures 2-1 and 4-7), which includes amphibolite facies tonalitic gneiss and granodiorites of the WGT with lower densities

(2.73 g/cm^3 and 2.69 g/cm^3, respectively (Table 1)) than those of the other blocks. This implies that the causative bodies must be buried at depth.

Gravity and magnetic models across the VRB show that uplift of granulites from 10-25 km depth to shallow levels of the crust is responsible for the gravity anomaly within this block. The refraction results of Boland and Ellis (1989) presented in Figure 2-4b show an increase in near surface velocities on the eastern side of the LF, coinciding with the presence of uplifted granulites. As the gravity models show, these granulites are not exposed but are buried under a thin layer of tonalites with variable thickness. The exposure of these granulites north of Highway 11 (Figures 4-7, 5-6 and 5-12) and their absence in the south towards the CB could suggests a south plunging structure at depth and that maximum displacement along the LF is presumably is to the north, and that the displacement progressively decreases southwards. This southerly tilt may correspond to the southerly decrease in metamorphic pressure evident on the geobarometry map (Leclair, 1990). Furthermore, the southerly increase in depth to the top of the granulites (layer 2) (Figures 5-12 and 6-3) is compatible with such an interpretation.

Until now, the mechanism for the uplift of the granulites within the VRB has remained unknown largely because the geometry of the uplift was uncertain. Uplift by listric faulting on the SLF has been suggested (Percival and McGrath, 1986; Leclair and Poirier, 1989), but other mechanisms are possible, including: 1) thrusting along a reverse LF (a high angle southeast-dipping thrust); 2) horst block rotation; 3) arching and folding of the granulites; and 4) formation of a crustal duplex or ramp

VAL RITA AND GROUNDHOG RIVER BLOCKS

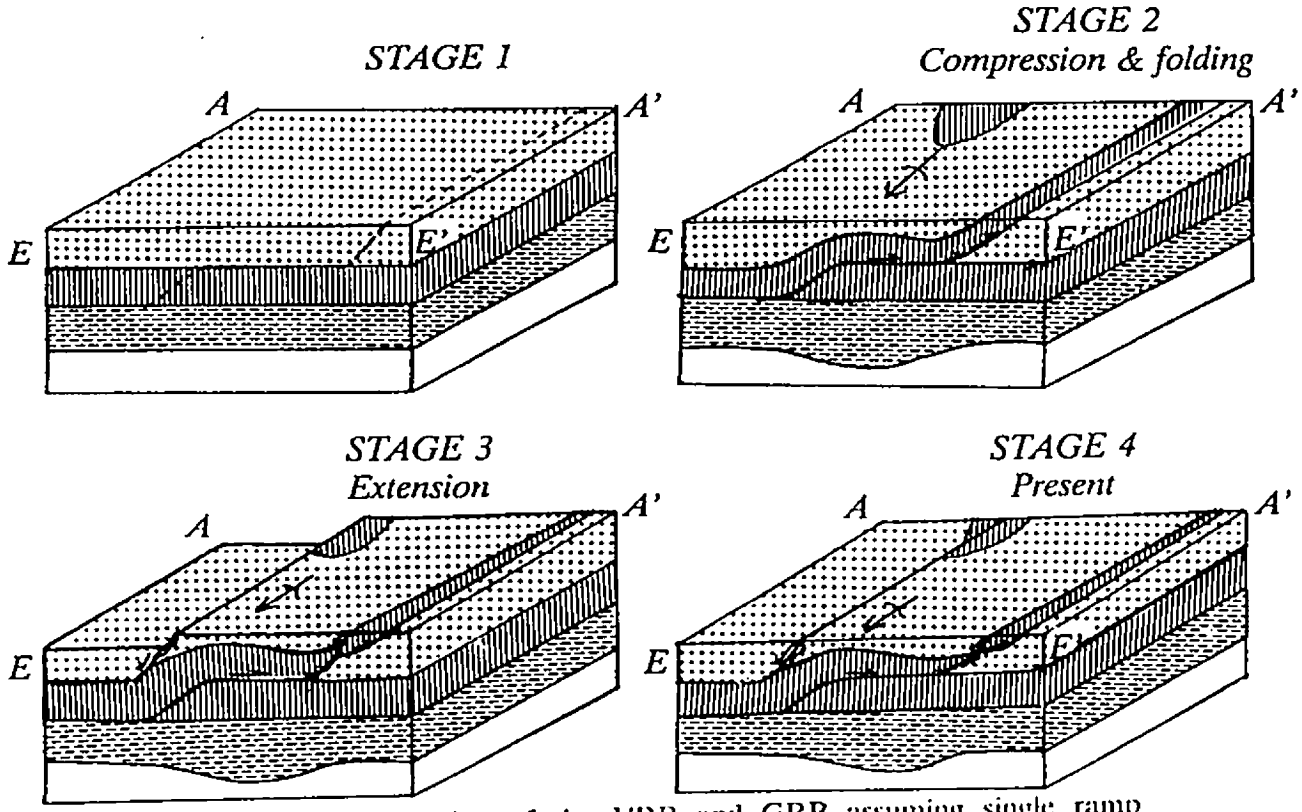

Figure 6-3. Structural evolution of the VRB and GRB assuming single ramp geometry; stage 1: pre-deformation, including the location of the future ramp. An additional ramp is shown which will bring the GRB granulites to the surface; stage 2: thrusting produces arching in granulites over ramp-flat thrust plane; stage 3: normal faulting caused by extension following thrusting (pre-erosion) stage 4: present configuration after erosion.

anticline. The potential field models presented here cannot confirm or disprove a listric faulting on the SLF or horst block rotation but they appear to be inconsistent with reverse faulting on the LF. Similarly, arching and folding could produce the upper surface observed for the granulites but fail to explain the thickening observed for this layer in both the gravity models and the velocity structure along Line 4. While listric faulting and horst block rotation remain feasible, this study suggests that arching and folding by a crustal duplex or ramp anticline similar to what is observed in fold and thrust belts is the most likely mechanism for uplift of granulites within the VRB. It is difficult to differentiate between uplift by a crustal duplex and uplift by a ramp anticline because the thickening shown on the model cross-sections can equally be explained by both mechanisms. One possible way of discriminating between the two is in their geometrical thickness, where the overall thickness may be greater for a duplex than for a ramp anticline. Furthermore, a crustal duplex should show metamorphic stacking which is not common in ramp anticlines and should also show several faults defining the individual horses. However, because the cause of the potential field anomalies within the VRB is buried, and because of the absence of several faults in the geology map (Figure 4-7) that may suggest duplexing, uplift by a ramp anticline (Figure 6-3) may be a more acceptable and plausible model for the VRB. In fact, Wilson and Stearns (1958) have demonstrated that successive anticlines within the Cumberland Plateau overthrust of east Tennessee were related to ramps in the underlying thrust surface, even when no thrust was exposed locally. It is possible that this may be the case in the VRB.

As noted previously, the potential field models reveal the presence of a northwest-dipping surface marking the top of the granulites (layer 2) close to the LF, which rolls over and dips to the southeast towards the SLF, while the refraction data along line 4 shows that layer 2 thickens under the VRB. The geometry suggested by these results is compatible with that of a ramp anticline produced during the compressional event that resulted in the thrusting of granulites within the GRB and CB. Further support for this interpretation is provided by the Lithoprobe seismic reflection lines to the south which show a ramp structure in the thrust slab under the KSZ (Figure 2-5). If a ramp anticline developed within the VRB, then it is suggested that vertical displacement along the LF and SLF could not have been the primary mechanism for uplift within this block (as initially suggested by previous investigators, e.g., Percival and McGrath (1986); Leclair, personal communication (1989). The LF is seen as a later feature which resulted in the truncation and further exposure of the granulites (Figure 6-3) by subsequent erosion. In fact, the Bouguer anomaly map (Figure 3-3) shows that the anomaly within the VRB does not lie parallel to the strike of the LF (Figure 1-2), but appears to be truncated by it north of latitude 49°, implying that the LF must postdate the uplift of the granulites. Furthermore, if the VRB anomaly is caused by a ramp anticline, then the SLF does not have to be listric to produce the southeast-dipping discontinuity as was previously suggested by Percival and McGrath (1986).

6.3.3 Groundhog River Block

The GRB is unusual in that it displays a small gravity anomaly even though geologic mapping (Figure 4-7) indicates that it consists largely of high density granulites (3.19 g/cm^3, Table 1 Figure 4-15). At the same time, this block is characterized by a much stronger magnetic anomaly than is observed over the other blocks. This seeming inconsistency between the magnetic and gravity signatures and the geology has made it difficult to resolve the deep crustal structure of the block. However, the additional gravity, density and susceptibility data collected during the course of this study and the diverse filtering techniques applied to the gravity and magnetic data have shed considerable light on the problem.

Based on the results of the potential field modelling, the GRB is interpreted as a very thin flat sheet of high density and strongly magnetized granulites. This interpretation is consistent with both the gravity and magnetic models which suggest a flat base for the granulites of the GRB. The implications for such an interpretation is that both the granulites of the VRB and GRB must come from the same depth (Figure 6-3). This idea is supported by similar metamorphic pressures for the granulites exposed along the LF (8 kbars) and those of the GRB (Leclair, 1990). If the GRB and VRB came from the same depth, then it can explain the differences in the magnetic anomaly of the GRB and CB, and the similarities of the GRB magnetic anomaly to that of the VRB. Contrary to the results of Percival and McGrath (1986), who obtained different thicknesses for the block from gravity (<1 km) and magnetic (5 km) modelling, this study demonstrates that the potential

field results are consistent with each other, and that the thickness of the block is dependent on where the profile is located. For example, the southern part has a thickness of up to 4 km, and the northern part has a thickness of less than 1 km (Figures 5-6, 5-8, 5-26a and b). However, it is suggested that the magnetization of the GRB may be influenced by a strong component of remanent magnetization supporting earlier observations by Percival and McGrath (1986). It is evident that a dense but strongly magnetized body of limited depth extent can satisfactorily explain the character of the potential field anomalies observed over the block. The convergence of the SLF with the ILCZ toward Highway 11 results in the northward thinning of the block and is reflected in the potential field models by the differences in the thickness of the block from north to south. Support for a thin GRB is also provided by the seismic refraction results along line 4 (Figure 2-4b) which crosses the northern tip of the GRB where it is thinnest. No noticeable increase in velocities is associated with the dense granulites of the GRB, suggesting that the body is too thin or too small to be resolved by the seismic refraction techniques employed.

6.3.4 Chapleau Block

The CB is the best understood and least complex block of the KSZ. The existence of several reflection and refraction profiles has allowed us to image its deep crustal structure and a wealth of geologic data has provided good constraints on its structural interpretation. The interpretation for this block is consistent with the prevailing geologic model of a slab thrust to the surface from mid crustal depths of

15-30 km along the ILCZ (Figure 6-4), which is consistent with geobarometric results for granulites from the core of the CB which indicate pressures of 7-8 kbar corresponding to depths of 25-30 km (Leclair, 1990). As suggested by the balanced sections (Figures 6-1a and b) the CB formed as a ramp antiform and that maximum uplift and erosion has taken place within this block such that the ramp antiform has been subdued and its rocks represent the deepest parts of the crust exposed in the KSZ (Percival and McGrath, 1986, Leclair, 1990). The Ivanhoe Lake Cataclastic Zone, which is well expressed along the eastern boundary of this block, is modelled with only one fault with dips of 30-35°. Although this dip is consistent with previous gravity models (Percival and Card, 1983) and the results of the pilot reflection survey (Cook, 1985), it differs significantly from the recent Lithoprobe reflection interpretation (Geis et al., 1990), which suggests three faults with shallower dips (15-20°). Although the gravity data is not sensitive enough to resolve the presence of three faults within this zone, the modelling results indicate that the gravity data is best modelled with a 30-35° dip for the ILCZ (as shown in Figure 5-11). However, the possibility that the ILCZ may decrease in dip with depth and extend further to the west underneath the WGT cannot be ruled out.

The gravity models and the inversion of the gravity data show that crustal thickening (8-10 km) has taken place underneath the high gravity anomaly regions within the VRB and the CB. Such a bulge in the crust could have developed as a response to the emplacement of a load introduced by thrusting on a rigid lithosphere (Gianna Bassi, personal communication (1990)). The wavelength (at least 100 km)

CHAPLEAU BLOCK

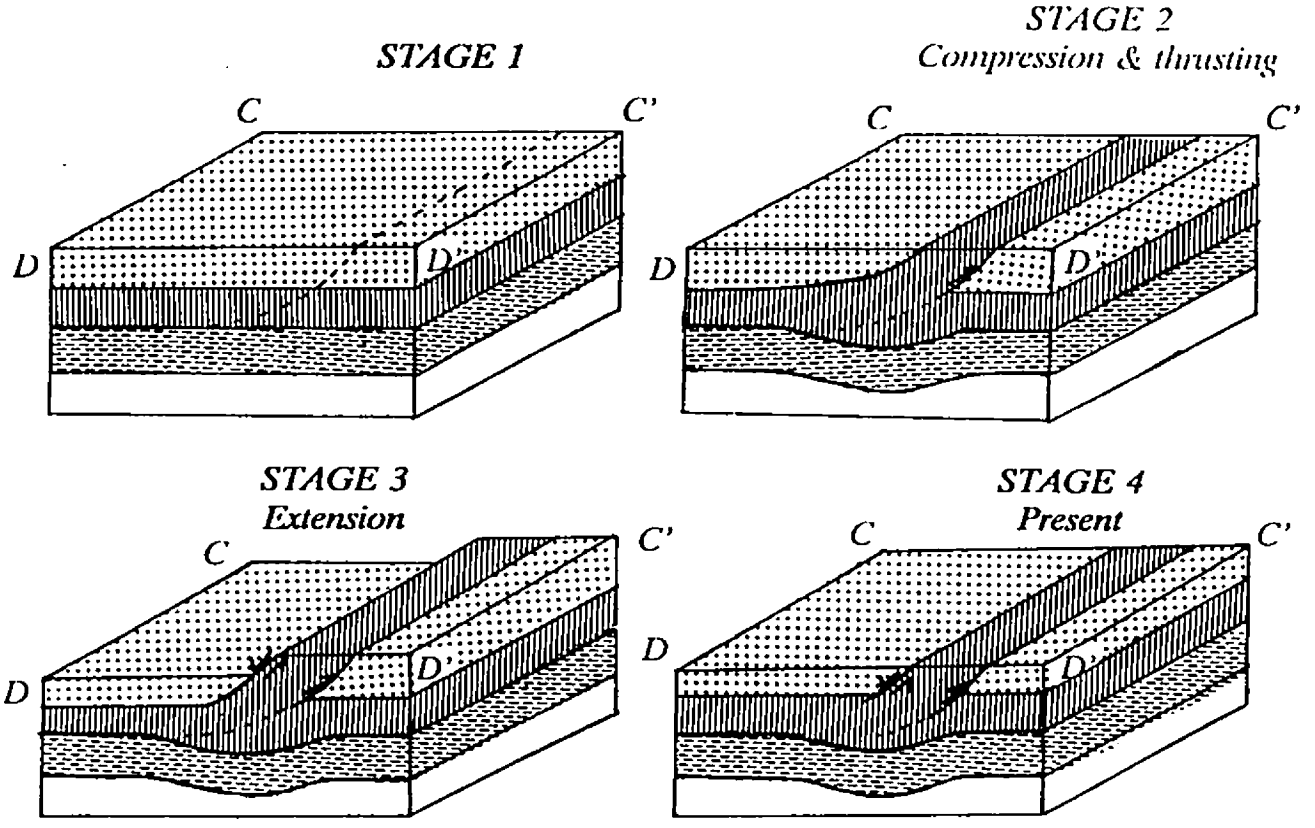

Figure 6-4. Structural evolution of the CB; stage 1: pre-deformation, including location of the future thrust; stage 2: thrusting of the Kapuskasing granulites over the AB during compression; stage 3: post thrust normal faulting caused by extension following the compression (pre-erosion); stage 4: present day configuration after erosion.

and amplitude of the bulge (~8-10 km) suggest that the load is regionally compensated. Alternatively, the bulge could have developed to accommodate the crustal shortening in the upper part of the crust.

6.4 RELATIONSHIP BETWEEN THE BLOCKS

The deviation of the CB gravity anomaly into the VRB and the differences in the geophysical anomalies among the different tectonic blocks of the KSZ raise questions concerning the structural relationship of the VRB and GRB to the CB. A review of some of the characteristics displayed by these blocks (Appendix 2) suggests that several structural relationships are possible. These relationships are discussed below.

1) The GRB is the northern continuation of the CB

The GRB could be considered as the northern continuation of the CB, and the varying character of the potential field anomalies along the strike of the KSZ explained by the progressive thinning of the granulites resulting from the northward convergence of the SLF and ILF (Figures 6-3 and 6-5). The apparent lateral continuity of the geology across the WRF (the WRF merely juxtaposes garnetiferous mafic gneiss of the GRB against garnet-biotite metasedimentary gneiss of the CB (Leclair and Nagerl, 1988)) and the similarity in metamorphic pressures (7-9 kbar) between the two blocks provide support for such a relationship. Further support for this interpretation is provided by the short wavelength filtered maps (Figures 4-5, 4-10

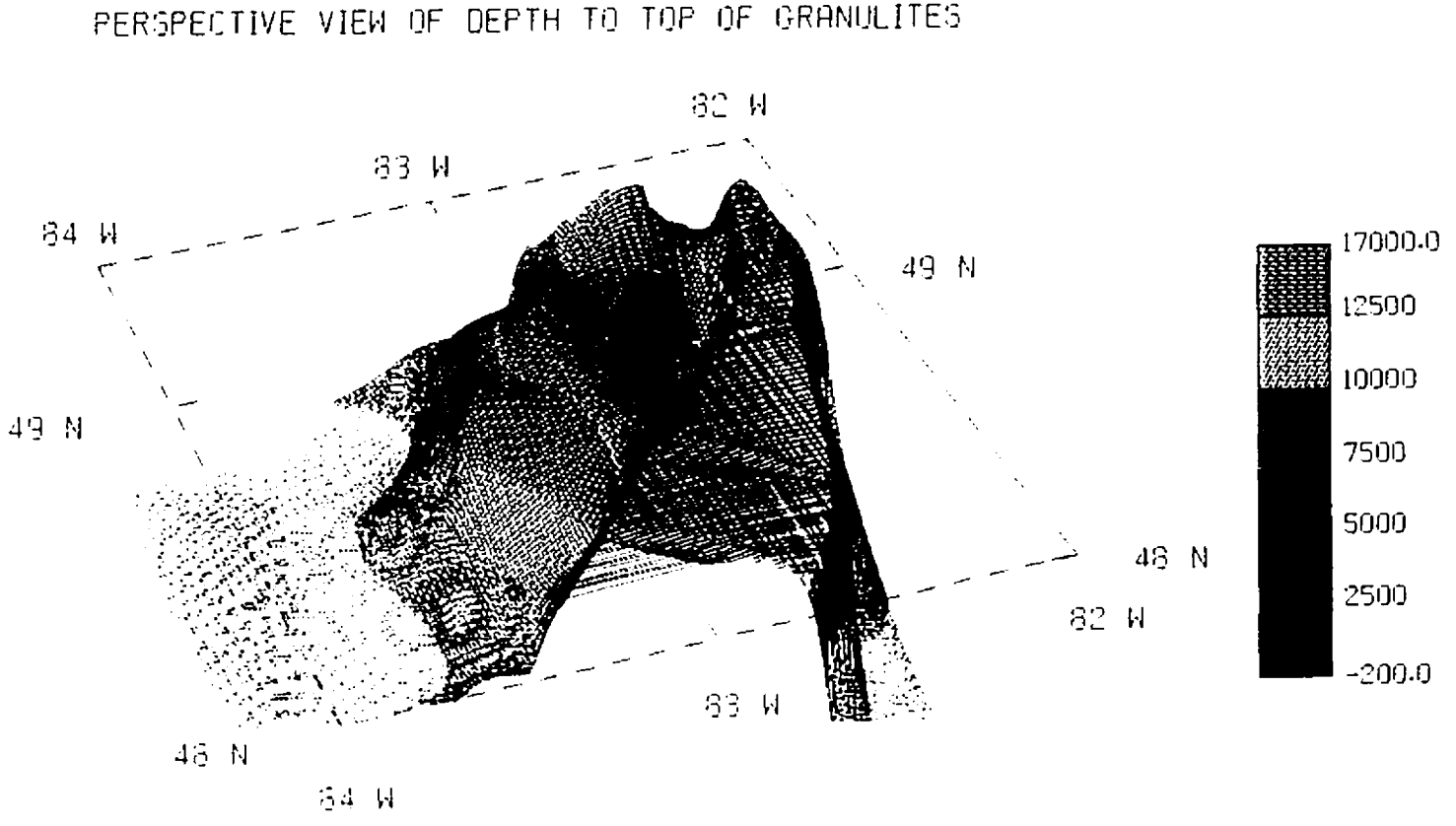

Figure 6-5. Perspective view of the depth to the top of the granulites (layer 2). Depth in meters.

and 4-12), which show the continuity of the CB gravity anomaly into the GRB without any interruptions across the WRF. However, the distinct contrast in the magnetic signatures of the two blocks, and its abrupt termination across the WRF (Figure 4-1), raises questions about the validity of such relationship.

2) The GRB and the CB are two originally distinct granulite terranes

Because of the disparities in the geophysical characteristics between the CB and GRB (Appendix 2), it is possible that the GRB and the CB may represent two originally separate and distinct rock assemblages that have been juxtaposed by the northeast trending WRF. The distinct differences in their magnetic signatures support this idea and this interpretation is favoured by some investigators (e.g., Leclair, 1990; Leclair and Nagerl, 1988). The unique characteristics exhibited by the GRB (Leclair and Nagerl, 1988) which include: 1) the absence of a gravity anomaly associated with the dense granulites; 2) the presence of northerly trending dykes of the Matachewan swarm and their absence in the CB; 3) the much stronger magnetic anomaly within this block; and 4) the lack of anorthosite-suite rocks and centers of carbonatite magmatism, which are present within the CB, favour the interpretation that these two blocks may have been originally different.

3) The VRB is a northerly continuation of the CB

The deviation of the CB gravity anomaly into the VRB and its continuation within this block suggests that the VRB may be a continuation of the CB. Support for the

hypothesis that the VRB and CB anomalies are closely related is provided by the similarities displayed by the two blocks (Appendix 2). For example, both blocks exhibit an anomalous velocity structure (Figure 2-4a and b) characterized by the presence of high velocities within the upper parts of the crust. Furthermore, the two blocks have a similar lower crustal structure characterized by a thickened crust underneath the high gravity anomaly region. In addition, both blocks are characterized by the presence of carbonatite intrusive centers along the axes of their gravity anomalies. These similarities suggest that the tectonic development of the VRB was closely related to the evolution of the CB.

4) The VRB, GRB and CB were all part of a once northerly continuous thrust sheet.

This next hypothesis is the preferred relationship and proposes that the potential field anomalies within the different blocks of the KSZ result from the uplift of an originally coherent sheet of granulites from a common apparent depth of 15-30 km to the surface. However, lateral variations in thrust plane geometry, normal faulting, tilting, differential uplift and erosion (Figures 6-3 and 6-4) have resulted in the different geological and geophysical features now observed. Hence, in the VRB and GRB, uplift of the granulites is associated with the development of a ramp anticline and the granulites are covered by a thin veneer of lower density tonalite gneiss (Figure 6-3), while in the CB and GRB, uplift is by simple thrusting and the granulites are exposed because of greater amounts of uplift and erosion (Figures 6-3 and 6-4).

Support for this hypothesis is provided by the highpass and first vertical derivative maps (Figures 4-5, 4-10), which show the continuation of the CB gravity anomaly into the VRB and GRB without any interruptions.

6.5 DISCUSSION AND IMPLICATIONS

6.5.1 Discussion

The interpretation provided for the KSZ suggests that differential uplift of granulites from mid-crustal depths of 15-30 km by thrusting, possible folding and normal faulting is responsible for the potential field anomalies observed over the KSZ. Although sparse exposures and inadequate seismic coverage in the northern and central part of the uplift (in the GRB and VRB area) have made interpretation difficult, most of the geophysical anomalies can be adequately explained by structural features at depth. Figures 6-3, 6-4 and 6-5 summarize the interpretations suggested for the different blocks and include:

1) The CB is a west-dipping slab of granulites from depths of 15-30 km consistent with previous interpretations (Percival and Card, 1983; Cook, 1985; Percival and McGrath, 1986). The CB represents the region of maximum uplift and erosion and thus exposes the deepest parts of the crust in this region.

2) The GRB gravity anomaly is caused by a thin flat sheet of granulites resulting from the progressive convergence of the ILCZ with the normal SLF such that its dense granulites are cut off from the main sheet of granulites of the VRB by normal west side down movement along the SLF.

3) A southerly plunging antiform underneath a thin veneer of tonalites best describes the upper surface of the granulites beneath the VRB. This most likely represents the top of a ramp anticline developed during the thrusting over a ramp-flat thrust plane. 4) Initial uplift of the granulites by thrusting and folding within the VRB did not expose them, however post-thrust faulting along the LF and SLF and subsequent erosion has resulted in their exposure in areas within the northern part of the block (Figures 5-12 and 6-3).

The coincidence of the arcuate gravity anomaly and the arcuate magnetic anomaly within the VRB suggests that the granulites are also responsible for the broad magnetic anomaly patterns observed over the different blocks of the KSZ. In fact, the correlation coefficient map (Figure 4-14) suggest that this may in deed by the case. Recent magnetotelluric (MT) results over the GRB have postulated that the presence of oxide facies iron formation, and not granulites is in large part responsible for the magnetic anomalies over the GRB (M. Mareschal, personal communication, 1990). However, the present study disagrees with these results and contends that although the iron formations may contribute to the magnetic anomaly of this block, the granulites are the main source of the anomalies. The models presented in this study show that the susceptibilities (Table 2) of the granulites in the region are high enough to explain the VRB and GRB magnetic anomalies. In addition, the strong component of remanent magnetization measured on rocks from the area may contribute significantly to the observed anomalies. The existence of highly magnetic layers within the lower crust is not uncommon. Wasilewski et al.

(1988), working in the Ivrea Zone, have found mafic-ultramafic lithologies within the amphibolite-granulite facies transition that exhibit high values of initial susceptibility. In fact, the change in magnetic signature along the strike of the Kapuskasing Uplift can be easily explained by differences in the erosional level and depth of burial of the granulites (Figure 5-12). Therefore, the magnetic anomaly within the GRB is stronger than that in the other blocks because the source body has a very high susceptibility and is very close to the surface, while the change in magnetic anomaly strength and character across the WRF into the CB can be explained by assuming that relative northwest side down movement along the WRF has resulted in more erosion within the CB to a different compositional level from that of the GRB.

Furthermore, because the granulites within the VRB are generally not exposed, the anomaly appears more subtle than that of the GRB. This implies that where these granulites are exposed, they should have a correspondingly stronger signature similar to that of the GRB. The geology maps (Figure 4-7), the magnetic anomaly maps (Figure 4-1) and the model results show that this is indeed the case. The magnetic anomaly over the VRB becomes increasingly strong north of Highway 11 where granulites are exposed and decreases to the south, where they are buried.

Finally, the arcuate shape of the gravity anomaly within the KSZ is very similar to that of the Mid Continent Rift system, parts of the East African Rift system and some of the basement uplifts of the Wyoming province of the Rocky Mountain forelands (e.g., the Bighorn Range). The arcuate shape of the gravity anomalies

within these zones has been explained by the reversal of assymetries along the main boundary faults across accommodation zones or transfer faults (Bosworth, 1985; Bosworth et al., 1986; Chandler et al., 1989). In fact, Sales (1968) experimentally produced structures of two orientations oblique to each other from one deformational event in laboratory models to explain some of the structures of the Wyoming province. He suggested that the application of a sinistral shear couple superimposed on tangential compression could produce such an arcuate structure. Cook et al., (1983) used the same explanation but with dextral shear to explain some of the structures in the Franklin Mountains of the Northwest Territories. By analogy, the application of Sales' approach to the KSZ, but with sinistral movements, could provide an explanation for the arcuate shape of the gravity anomaly within this region. In fact, a reversal in the sense of thrusting between the CB and VRB is suggested by the schematic cross section of Leclair and Poirier (1989). However, the absence of a fault analogous to a main boundary fault (ie, a northwest-verging thrust along the western edge of the VRB parallel to the strike of the gravity anomaly) and evidence of dextral, rather than sinistral motion on the SLF (e.g., Figure 2.1-7, page 2-13 in LITHOPROBE Phase III proposal) rules this out as a possibility. Therefore, it is proposed here that whereas the CB came to the surface as a simple thrust (Figure 6-4), the thrust within the VRB and GRB was folded over a ramp-flat thrust surface and then both were later on cut by normal faults (Figure 6-3). Thus, the arcuate nature of the KSZ gravity anomaly is caused by a north-south change in thrust plane topography and differential amounts of shortening and uplift.

6.5.2 Implications

6.5.2.1 Structural Evolution

The present interpretation of the anomalous potential field data over the KSZ leads to several implications related to the structural evolution of the region. The structural development of the KSZ involved several phases of tectonic activity which are summarized in Table 6 and Figures 6-1a and b, 6-2a and b, 6-3 and 6-4 and are discussed below.

Geochronological studies (U-Pb on zircon and sphene; K-Ar and $^{40}Ar/^{39}Ar$ on hornblende, biotite, and Rb-Sr on biotite) suggest that the Kapuskasing granulites cooled at depth at about 2696 Ma (Stage 1; Percival et al., 1988) until they were uplifted by thrusting. From the age of the Hearst-Matachewan dyke swarms (2454 Ma (Heaman, 1988)), it is clear that these dykes were emplaced before the thrusting although magmatism spanned a period of about 1230 Ma and was active during the entire evolution of the KSZ.

Following this magmatic phase, east-west compression probably related to distant orogenic events within the Churchill Province such as the Trans-Hudsonian orogeny (Hoffman, 1988; Percival and Mcgrath, 1986) or to orogenic events within the Grenville Province (Percival and McGrath, 1986), resulted in the uplift of the Kapuskasing granulites along the ILCZ (Stage 2, Figures 6-3 and 6-4). During this stage, tectonic thickening and folding within the VRB (Figure 6-1) and other parts of the WGT is suggested to have been coeval and linked with the southeasterly thrusting of granulites within the other blocks of the KSZ. Crustal shortening on the

Table 6. Summary of Proterozoic Tectonic Activity in the KSZ

STAGE	AGE (Ma)	TECTONIC ACTIVITY
4	1000-1050	Lamprophyres and final carbonatite activity in the KSZ.
	1240	Further dyke activity with emplacement of the Sudbury dyke swarm.
	1888	Beginning of carbonatite activity within the KSZ (emplacement of the Cargill carbonatite complex)
3	1950-1900	Normal faulting with possible exposure of granulites in the VRB. Segmentation of KSZ into different tectonic blocks.
2	2140 1900	East-west compression, resulting in tilting, folding, thrusting and uplift of granulites within the CB, GRB and VRB.
	2000-2050	Emplacement of Kapuskasing dykes.
	2140	Emplacement of Preissac dyke swarm.
1	2454	Emplacement of Hearst-Matachewan dyke swarm.
	2696-2519	Cooling of Kapuskasing granulites at depth, and formation of Shawmere anorthosite complex.
Archean	2750-2696	Development of the Michipicoten, Wawa and Abitibi belts.

order of about 65 km within the CB and 35 km within the VRB and GRB was presumably an important component of the deformation during this time. The shortening in the upper crust was probably accommodated by ductile flow and thickening in the lower crust. Although the age of the uplift is debatable, Percival et al., (1988) suggest that uplift may have occurred between 2000-1900 Ma. However, other results (LeQuentrec et al., 1989) suggest that uplift may have occurred in two stages at about 2475 Ma and later.

Relaxation of the crust immediately following the compressional event resulted in an extensional phase of deformation. This is reflected in the presence of numerous post thrust, high angle normal faults (Stages 3 and 4, Figures 6-3 and 6-4) and carbonatite magmatism in the area.

A close relationship between extensional faulting and crustal shortening has been suggested by Armstrong (1982) for the metamorphic core complexes of the North American Cordillera, by Burchfiel and Royden (1985) for the Himalayas of southern Tibet and by Brown and Journeay (1987) for the Shuswap metamorphic terrane of southeastern British Columbia. The presence of normal and thrust faulting within the KSZ similar to what is observed in the above metamorphic terranes suggests that the normal faulting within the KSZ may have also been a delayed response to the crustal shortening and tectonic thickening that occurred during the previous compressive phase. Further exposure of the granulites was provided by movement along these normal faults. For example, normal movement along the LF (Stage 3, Figure 6-3) and subsequent erosion (Stage 4, Figure 6-3) may have resulted

in the exposure of granulites within the VRB. This faulting was also responsible for segmenting the Kapuskasing Uplift into the different tectonic blocks observed today (e.g., the WRF separating the CB and GRB).

The last phase, which may have also exhibited extension, was marked by alkaline and carbonatite magmatism spanning a period of about 840 Ma. Uplift and tilting must have ceased by this time, as these events are not recorded in the various carbonatite complexes in the region (Lewchuk and Symons, 1990). The close association of the centers of carbonatite activity to the KSZ gravity high has been noted by various authors (e.g., Gittins et al., 1967; Innes, 1960; Innes et al., 1967; and Watson, 1980) but their relationship to the structure has not been determined. Since the carbonatite complexes are spatially associated with faults and major fractures within the region, it is probable that the latter acted as conduits for carbonatite emplacement in the upper crust.

6.5.2.2 Implications of Structures within the KSZ

The KSZ exhibits characteristics that may have important implications. The tectonic style of folding and thrusting suggested by the models presented here is commonly observed in orogenic belts, such as the fold and thrusts belts and metamorphic core complexes. Geis et al. (1990) note, for example, that the geometry of the faults interpreted from the Lithoprobe reflection lines within the CB is similar to that seen in the fold and thrust belts. In fact, their profile (Figure 2-5) shows a ramp in the thrust plane and possible imbrication of the main thrust sheet.

Such structures are very typical of many fold and thrust belts. The KSZ has been described as a "distal basement uplift" within a craton, far from a collision (Percival, 1990). Why then should the KSZ exhibit structures commonly formed at continent-continent collision belts? This can only be possible if the Kapuskasing rocks exhibit behaviour that is typical of cover rocks. Therefore, it is possible that the style of uplift may have important implications or provide additional constraints on the time of uplift. For example, the deformational style of antiformal folding above a ramp-flat thrust plane and subsequent normal faulting may suggest that the Kapuskasing granulites were cool at the time of their uplift. If this assumption is correct, then it will imply that the 1950-1905 Ma date for uplift (Percival et al, 1988) is a more likely age (as the rocks would have been cool by this time), rather than the 2475 Ma date (Le Quentrec et al., 1989). In fact, at 2475 Ma the Kapuskasing rocks would have been warm and deformation would probably have been more ductile than brittle. Therefore, it is proposed that the Kapuskasing rocks behaved like cover rocks because at the time of their uplift, they were cool.

6.6 COMPARISON OF THE KSZ WITH OTHER STRUCTURES

6.6.1 Introduction

Structural analogies between the KSZ and Rocky Mountain structures have been made by Percival and McGrath (1986). The results from this study present no conflicting evidence to question such a comparison. However, further comparisons will be made between the KSZ and other structures

6.6.2 Comparisons with the Boothia Uplift (BU)

Similarities in the high grade of metamorphism between the KSZ and the Boothia Uplift (BU) were originally noted by Berkhout (1973) and Innes et al., (1967). Further comparisons between the KSZ and the Boothia Uplift (BU) of the Canadian Arctic can now be made using the new results obtained from the KSZ.

Kerr (1977) describes the BU as a strongly positive tectonic feature at least 1110 km long, extending from the Boothia Peninsula to Grinnell Peninsula (Figure 6-6). It consists of three parts: 1) the Boothia Horst, an exposure of Precambrian crystalline basement which is an extension of the Churchill Province and plunges north beneath the other two parts; 2) the Cornwallis Fold Belt, a north-plunging, strongly-folded anticlinorium; and 3) the mildly deformed sedimentary units of the Sverdrup Basin. Kerr (1977) and Okulitch et al., (1986) suggest that these different parts of the BU correspond to different structural levels, with the crystalline basement being the lowest structural level, the Cornwallis Fold Belt representing an intermediate level and the sedimentary suprastructure of the Sverdrup basin being the highest structural level. Similarly, Leclair (1990) suggests that the different tectonic blocks of the KSZ reflect different lithostructural levels, with the CB representing the lowest level, the GRB an intermediate level and the VRB the highest structural level of the crust.

The mechanism of uplift for the KSZ and the BU are also comparable. Both structures represent Archean tectonic features produced by east-west compressive stresses that have resulted in the folding and thrusting of high grade metamorphic

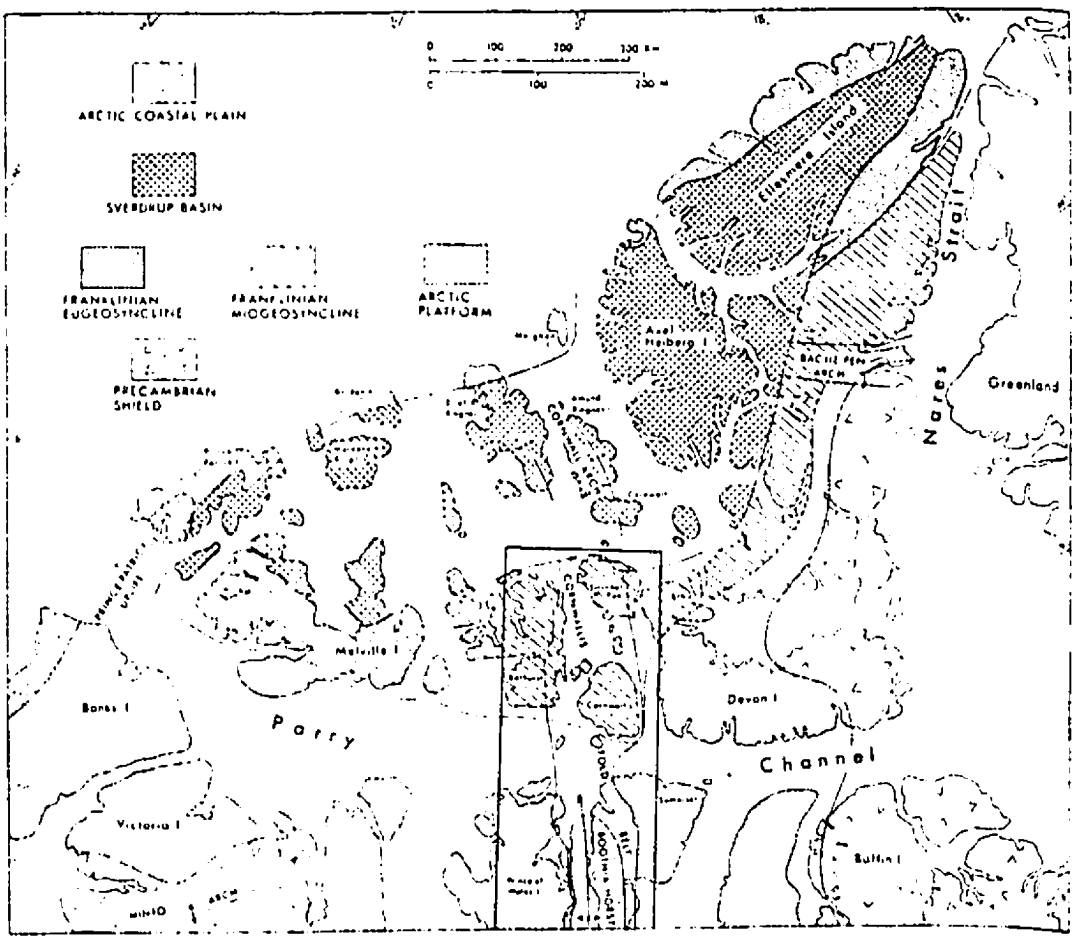

Figure 6-6. Location map of the Boothia Uplift (from Kerr, 1977).

rocks from lower levels of the crust to the surface. This has resulted in the characteristic gravity high observed over both uplifts. Uplift within the KSZ is bracketed between 1950 Ma and 1900 Ma, and is suggested to have developed from compressive stresses generated by the distant Trans-Hudson orogeny (Hoffman, 1988; Percival and McGrath, 1986). Okulitch et al., (1986) suggest that uplift of the Boothia Horst resulted from west-directed compressive stresses associated with the late stages of the Caledonian orogeny.

The crystalline basement of the BU (the Boothia Horst) is an asymmetric block, bounded on the west by steeply to moderately east-dipping reverse faults and on the east by normal and reverse faults (Stewart and Kerr, 1984) and segmented by northeast- to northwest-trending normal and reverse faults (Figure 6-7). The predominant structural trends are north-south, changing to northeast-southwest at the southern end of the Boothia Peninsula (Figure 6-7). Although the gravity maps of the region do not reflect an arcuate pattern (gravity data is available for the southern region), it is likely that the offset in exposed basement between latitude 71 and 72° N (Figure 6-7) by later reverse faults may result in an arcuate gravity anomaly similar to that over the CB and VRB.

Gravity models (Berkhout, 1973) across the Boothia Horst of the BU suggest that uplift of the high grade rocks occurred along an east-dipping thrust fault with dips of 5-15° (Figure 6-8). Using these dips, it is estimated that about 30 km of crustal shortening took place (Miall, 1983; Okulitch et al., 1986). Similarly, gravity models from the present study (Figures 5-10 and 5-11) suggest that uplift of the

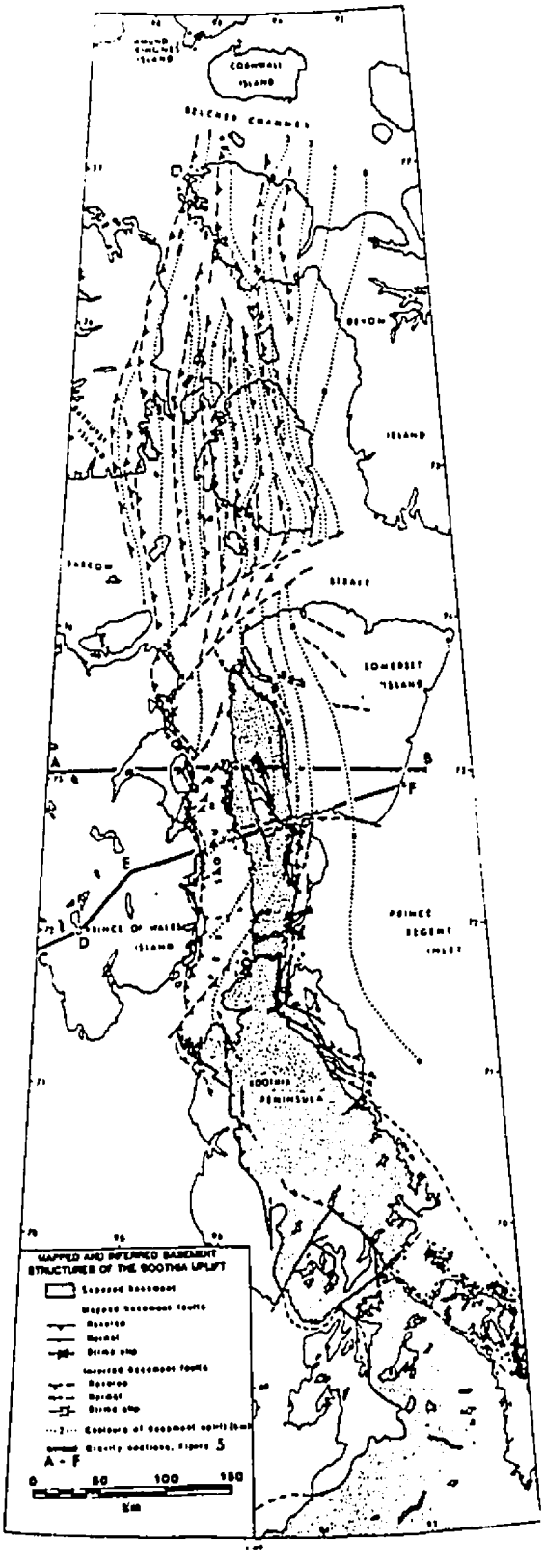

Figure 6-7. Structural map of the Boothia Uplift (from Okulitch et al., 1986).

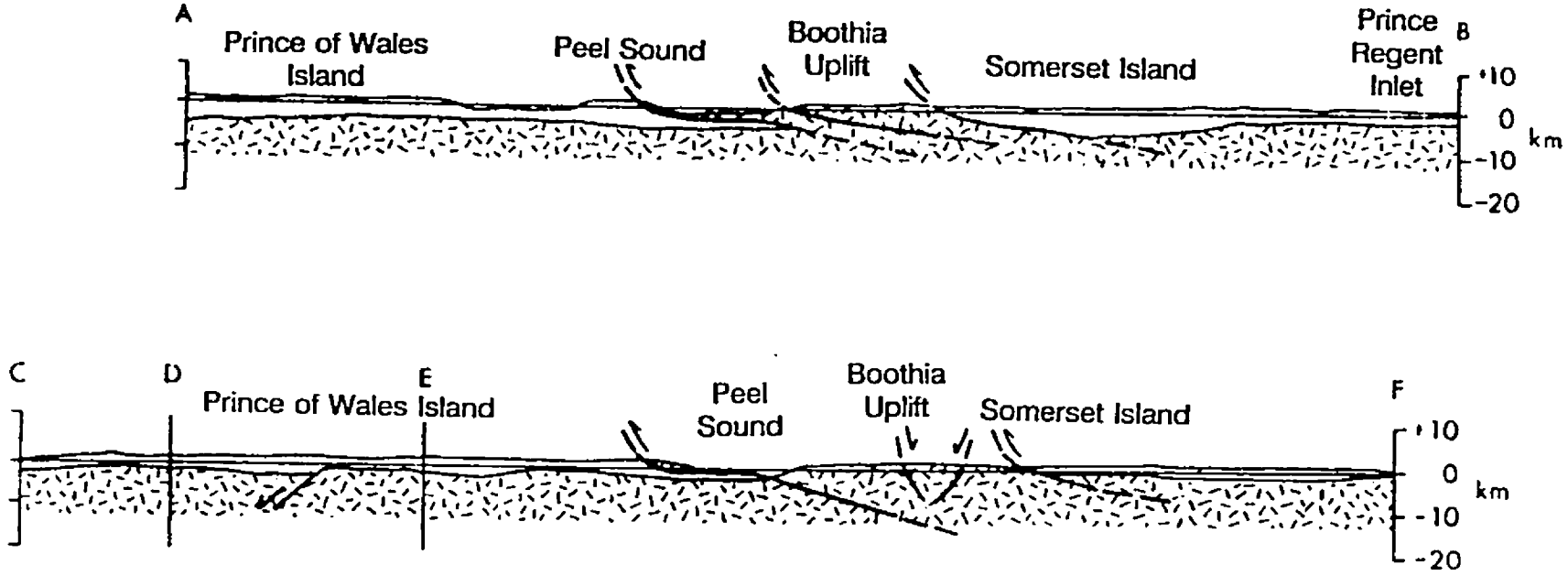

Figure 6-8. Cross-sections of the Boothia Uplift on Somerset and Prince of Wales Islands based on gravity data and models of Berkhout (1973). Locations of profiles are shown in Figure 6-7.

granulites within the KSZ occurred along a west-dipping boundary fault (the ILCZ), with a dip of 30-35°, translating to 65 km of crustal shortening. Crustal tilting and normal and reverse faulting are common features of the deformation in both areas.

The lack of extensive geophysical coverage for the BU (R. Jackson, personal communication (1990) suggests that any comparisons made between the geometry of the deep crustal structure of the BU and that of the KSZ must be regarded as preliminary. However, current knowledge on the deep crustal structure of the KSZ gained from the available geophysical data may have important implications for understanding the deep crustal structure of the BU.

6.6.3 Comparisons with the Limpopo Belt (LB)

In light of the new interpretations provided for the different blocks of the KSZ, a comparison of the structural configuration and scale of deformation between the VRB and GRB and the Limpopo Belt (LB) in southern Africa can be made. The LB is similar to the KSZ in that both areas reveal sections of the lower crust that have been uplifted by crustal scale thrust faulting and erosion (Fountain and Salisbury, 1981). As previously discussed, model results from the VRB and GRB suggest folding and thrusting of granulites within the central portion of the Kapuskasing Uplift. A similar configuration is seen in the gravity model (Coward and Fairhead, 1988) and schematic section across the LB (Coward, 1984). In these sections (Figure 6-9), uplift of lower crustal rocks from depths of 10-40 km to the surface has occurred by anticlinal folding and thrusting above a ramp, comparable to

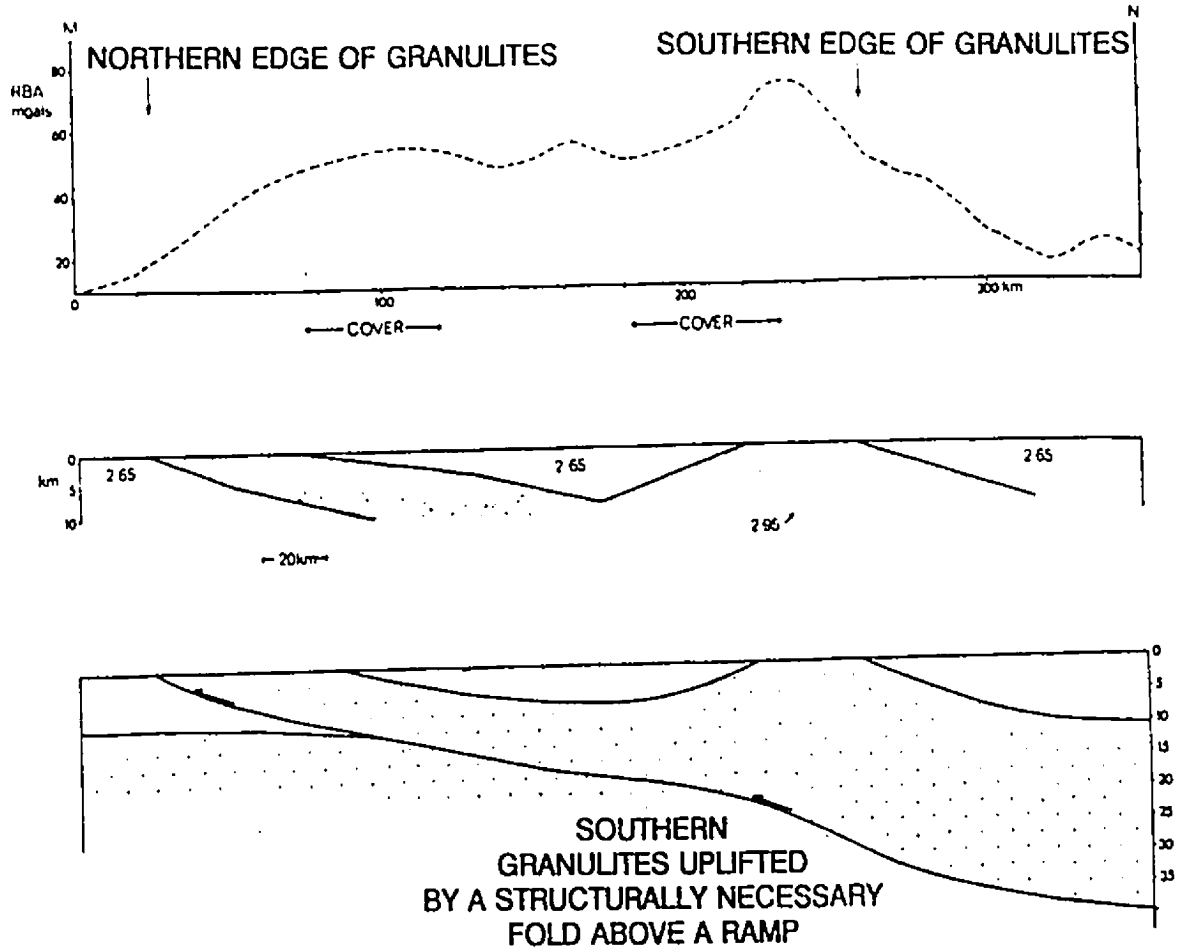

Figure 6-9. Gravity model and schematic cross section of the Limpopo belt (from Coward, 1984).

what has been interpreted for the VRB and GRB. It is also interesting to note that the scale of crustal deformation is comparable in both areas (i.e., single fold and thrust sheet). However, the areas differ in that post thrust normal faulting, which has truncated the granulites of the VRB and GRB, is not present within the LB. The lack of other geophysical information on the deep crustal structure of the LB prevents further comparisons between the two areas. However, knowledge gained from the deep structure of the VRB and GRB may provide insights into the deep crustal structure of the LB.

CHAPTER SEVEN: SUMMARY AND CONCLUSIONS

7.1 CONCLUSIONS

This study was undertaken with the primary purpose of providing an interpretation of the deep crustal structure of the Val Rita, Groundhog River, and Chapleau Blocks of the Kapuskasing Structural Zone by modelling the potential field anomalies observed over them. The collection of new gravity, density and susceptibility data within the central part of the zone (Val Rita, Groundhog River and northern Chapleau Blocks), coupled with the modelling of the potential field anomalies (with good constraints provided by recent seismic refraction and reflection data) have provided important information on the structure of the crust beneath the KSZ. The conclusions generated from this study include the following:

1) A simple three layer crustal model based on the Nafe and Drake curve, but modified in light of the physical properties of rocks from the area, can be used to explain the gravity field over the KSZ. Density models derived from this crustal model support earlier interpretations (e.g., Percival and Card, 1983) that the KSZ gravity high is caused by the presence of high density rocks from mid-crustal levels (15-30 km) at or near the surface.

2) 2D models and the inversion of the gravity data suggest that the thickness of the crust varies within the region. The depth to the Moho varies from 43-47 km underneath the WGT and AB to 50-53 km underneath the CB and VRB. The thickened crust underneath the CB and VRB coincides with the high gravity anomaly zones. These results suggest that the thick crust underneath the gravity high may

have developed in order to compensate the dense load in the upper parts of the crust or alternatively, the thick crust may have developed in response to the shortening in the upper parts of the crust.

3) The short wavelength, high amplitude Bouguer anomalies in the region can be explained by density variations in the upper 6 km of the crust and are attributed to the presence of mafic metavolcanics, ultramafics and granitoid plutons in the WGT and AB and to carbonatite complexes in the CB and VRB.

4) A plunging fold or arch in the granulites at depth best describes the geometry of the Val Rita Block. It is proposed that this arch is a ramp anticline which developed over a thrust plane with ramp-flat geometry when thrusting of the granulites was occurring within the other blocks of the KSZ. This mechanism is different from the uplift by rotation along a listric SLF proposed by Percival and McGrath (1986). The exposure of the granulites in some localities, however, may have been aided by the plunge of the fold and by normal west side down movement and subsequent erosion along the 60° northwest dipping LF and by listric motion on the SLF after thrusting ceased. It is proposed that about 35 km of crustal shortening accompanied the uplift in this block.

5) A thin flat sheet best describes the geometry of the GRB. Such a thin structure is consistent with both the gravity and magnetic models. In fact, magnetic models based on granulite susceptibilities suggest that the thickness of the block varies from 1 km in the north to 4 km in the south. This change in thickness of the GRB along strike is a result of the convergence of the SLF with the ILCZ.

6) The Chapleau Block is best modelled as a relatively simple west-dipping thrust sheet. Thrusting of the granulites occurred along a west dipping ILCZ with 30-35° dips and a vertical crustal extent of 15-20 km. This dip is consistent with that obtained from previous gravity modelling (Percival and Card, 1983) and from the Lithoprobe pilot reflection survey (Cook, 1985), but differs from that obtained from the Lithoprobe seismic reflection interpretation (Geiss et al., 1990). It is estimated that about 65 km of crustal shortening accompanied the uplift.

7) The structural evolution of the KSZ involved both a compressional and an extensional phase. The various northeast-trending, high angle normal faults within the zone developed after folding and thrusting, as a response to the relaxation of the crust after compression.

8) The geophysical characteristics displayed by the different tectonic blocks of the KSZ suggest that several structural relationships are possible between the blocks, including: 1) the GRB is a northern continuation of the CB; 2) the GRB and CB are two originally distinct granulite terranes juxtaposed by the WRF; 3) the VRB is a continuation of the CB and 4) the VRB and GRB are both northerly continuations of the CB The fourth relationship is the most probable and suggests that the different tectonic blocks of the KSZ resulted from the differential uplift of an originally coherent thrust sheet by folding and thrusting. Subsequent normal faulting and erosion resulted in the segmentation of this once continuous thrust sheet into the discrete blocks with varying geophysical signatures observed today.

9) Similarities exist in the deformational style (folding, thrusting and normal faulting) of the KSZ and the Phanerozoic fold and thrust belts suggest that the Kapuskasing rocks must have been cool at the time of their uplift.

10) Similar geometries are interpreted for the CB and the Basement Horst of the BU, and the style of deformation within the VRB and GRB prior to normal faulting is analogous to that of the LB in southern Africa.

7.2 SUGGESTIONS FOR FURTHER STUDY

1) Given the uncertainties involved in the construction of the magnetic models due to a limited data set, it is suggest that a systematic study of more oriented samples for susceptibilities and remanent magnetization for the KSZ may be quite profitable.

2) A follow-up seismic reflection survey over the VRB and GRB would be useful in substantiating the results of this study.

APPENDIX 1: Density Data from the Val Rita and Groundhog River Blocks

LITHOLOGY	LATITUDE	LONGITUDE	DENSITY
Amphibolite	49° 19.89'N	82° 10.96'W	3.01 g/cm^3
Hn-Cpx-Gt Amphibolite gneiss	49 03.38	82 26.29	3.10
Amphibolite	49 03.38	82 26.29	2.93
Gt-Amphibolite	49 02.32	82 28.21	3.05
Metagraywacke	49 02.32	82 28.21	2.68
Hn-Bt Tonalite	49 18.11	82 09.63	2.71
Px-Bt Granulite gneiss	49 04.38	82 13.83	2.79
Cpx-Bt-Opx Granulite gneiss	49 04.19	82 13.38	2.77
Bt-Ep Granodiorite	49 03.78	82 15.54	2.67
Granodiorite to granite	49 04.76	82 17.00	2.69
Granodiorite	49 04.76	82 17.00	2.68
Metavolcanic	49 01.27	82 24.17	2.83
Gabbro	49 02.00	82 24.25	3.03
Metavolcanic	49 02.11	82 24.17	2.88
Gt-Hn-Bt Amphibolite	49 02.11	82 24.17	2.95
Gt-Hn-Bt Amphibolite	49 02.11	82 24.17	2.90
Metavolcanic	48 59.32	82 24.38	3.01
Metavolcanic	48 59.62	82 24.25	2.79
Gt Amphibolite	49 03.03	82 24.21	3.11
Metavolcanic	49 03.03	82 24.21	2.89
Metavolcanic	49 03.41	82 26.13	2.99
Metavolcanic	49 02.95	82 24.96	2.93
Metavolcanic	49 02.68	82 22.75	2.99
Bt-Ep-Hn Granite	48 50.68	82 30.38	2.67
Granite	48 52.51	82 28.92	2.67
Metagabbro	49 07.30	82 06.90	2.97
Gabbro	48 54.38	82 24.50	2.98
Hn-Bt Tonalite	48 54.86	82 24.25	2.76
Cpx-Bt Gneiss	48 55.05	82 23.71	2.78
Tonalite gneiss	48 54.86	82 24.04	2.79
Granite gneiss	48 54.86	82 24.04	2.63
Tonalite to granite gneiss	48 54.86	82 24.04	2.74

Hn-Bt-Ep-Pl Granite	48 58.43	82 21.38	2.66
Gabbro	48 59.49	82 23.98	2.93
Amphibolite	49 00.30	82 22.06	3.17
Metagabbro	49 12.03	82 12.08	3.02
Metagabbro	49 10.82	82 09.42	2.85
Metagabbro	49 10.43	82 09.58	3.07
Tonalite	49 10.34	82 09.58	2.67
Metagabbro	49 07.30	82 06.90	2.99
Hn Granite	49 09.81	82 07.50	2.76
Bt-Ep-Mt Granite	49 10.92	82 05.40	2.67
Granite	49 08.49	82 08.71	2.71
Hn-Cpx-Pl gneiss	49 09.46	82 11.79	2.90
Granite	49 08.38	82 13.25	2.68
Mafic gneiss	49 10.65	82 09.95	2.98
Mafic gneiss	49 10.65	82 09.95	2.99
Bt-Hn Granodiorite	49 09.81	82 07.88	2.69
Granodiorite to tonalite gneiss	49 09.97	82 07.44	2.71
Bt-Hn Granodiorite	49 11.41	82 07.17	2.67
Mafic gneiss	49 10.14	82 07.88	2.98
Bt-Hn Tonalite	49 10.22	82 07.27	2.68
Bt Granodiorite	49 14.11	82 06.21	2.68
Hn Granodiorite	49 13.89	82 07.25	2.76
Tonalite gneiss	49 17.27	82 07.21	2.72
Mafic gneiss	49 16.54	82 06.42	3.03
Hn Granite	49 16.86	82 06.94	2.75
Tonalite gneiss	49 16.97	82 07.13	2.65
Granite gneiss	49 16.32	82 04.21	2.77
Hn-Ep-Bt Granite to granodiorite	49 16.97	82 04.63	2.81
Hn Granite gneiss	49 17.65	82 04.58	2.75
Granite to tonalite	49 19.16	82 04.67	2.67
Granite gneiss	49 17.88	82 01.92	2.66
Bt Granite	49 17.84	82 03.71	2.68
Hn-Mt Granite	49 17.84	82 03.71	2.66
Bt-Mt Granite	49 17.84	82 03.71	2.68

Metasedimentary schist	49 15.11	82 03.17	2.74
Hn-Bt-Ep-Sph-Mt Granodiorite	49 11.22	82 03.52	2.71
Hn-Bt-Ep Granite	49 11.64	82 02.95	2.69
Hn-Bt-Ep Granodiorite	49 12.03	82 02.73	2.69
Hn-Bt Granodiorite	49 12.54	82 02.54	2.74
Hn-Bt Granodiorite	49 13.78	82 02.99	2.74
Bt Granite	49 14.65	82 03.66	2.66
Bt-Pl-Qz Metasedimentary gneiss	49 17.35	82 04.71	2.73
Bt-Pl-Qz Metasedimentary gneiss	49 17.35	82 04.71	2.92
Mafic gneiss	49 17.97	82 05.21	2.98
Hn-Bt Tonalite to diorite	49 17.92	82 07.92	2.86
Hn-Bt Tonalite gneiss	49 17.86	82 08.46	2.71
Hn-Bt Tonalite gneiss	49 17.86	82 08.46	2.69
Bt-Hn Tonalite gneiss	49 17.86	82 08.46	2.72
Hn-Bt Tonalite gneiss	49 17.86	82 09.13	2.68
Bt-Hn Tonalite	49 24.29	82 07.92	2.69
Bt-Hn Tonalite gneiss	49 26.16	82 08.94	2.68
Meta3gabbro	49 24.41	82 11.38	2.96
Hn Tonalite gneiss	49 24.51	82 11.69	2.57
Hn Granite	49 25.65	82 10.50	2.66
Bt-Hn Granite	49 23.14	82 12.29	2.67
Mafic gneiss	49 19.59	82 11.00	3.08
Mafic gneiss	49 19.59	82 11.00	2.75
Gt-Bt-Qz Paragneiss	49 19.19	82 08.98	2.86
Qz Paragneiss	49 19.19	82 08.98	2.77
Qz Paragneiss	49 19.19	82 08.98	2.73
Hn-Pl Mafic gneiss	49 19.15	82 07.54	2.99

Gt-Hn-Pl Mafic gneiss	49 19.15	82 07.54	3.05
Hn-Cpx-Pl-Qz Mafic gneiss	49 19.15	82 07.54	3.03
Bt-Hn Tonalite gneiss	49 19.32	82 06.92	2.77
Bt Tonalite gneiss	49 19.32	82 06.92	2.77
Granodiorite	49 19.19	82 06.08	2.52
Bt Granodiorite	49 19.17	82 04.68	2.69
Bt-Mt-Sph Granodiorite	49 01.73	82 20.92	2.70
Bt Granodiorite	49 19.57	82 06.58	2.66
Hn-Bt Granite	49 19.57	82 06.58	2.68
Hn-Bt Metasedimentary gneiss	49 19.57	82 06.58	2.76
Bt Granite	49 19.81	82 06.30	2.65
Bt-Qz-Pl Metasedimentary gneiss	49 20.11	82 06.27	2.77
Bt-Hn Metasedimentary gneiss	49 20.11	82 06.27	2.94
Hn-Pl Mafic gneiss	49 18.86	82 07.06	2.95
Bt-Hn granodiorite to tonalite	49 20.49	82 12.13	2.69
Bt-Hn Tonalite gneiss	49 19.27	82 11.96	2.72
Hn-Pl Mafic gneiss	49 17.81	82 10.13	3.02
Gt-Cpx-Hn-Pl Mafic gneiss	49 17.81	82 10.13	2.98
Hn-Gt-Pl-Qz Mafic gneiss	49 18.92	82 09.88	3.12
Bt-Hn Granodiorite	49 23.16	82 09.71	2.68
Hn-Bt-Pl-Qz Metasedimentary gneiss	49 24.73	82 08.38	2.80
Bt-Mt Granite	49 26.16	82 09.63	2.66
Bt-Hn Granite gneiss	49 25.78	82 11.00	2.66
Bt-Hn Granite gneiss	49 25.78	82 11.00	2.67
Hn-Bt Tonalite	49 25.78	82 11.00	2.73
Bt granite	49 25.68	82 09.75	2.66
Hn Granite	49 24.36	82 09.75	2.67
Hn-Bt Granite	49 24.81	82 10.42	2.69

Gt-Cpx-Hn-Pl Gneiss	49 23.65	82 09.92	3.00
Gt-Cpx-Hn-Pl Gneiss	49 23.65	82 09.92	3.08
Bt-Hn Granodiorite	49 16.68	82 13.29	2.70
Gt Amphibolite	49 17.05	82 12.83	2.94
Hn granite	49 20.05	82 11.71	2.66
Hn-Bt Metasedimentary gneiss	49 20.10	82 11.96	2.92
Hn-Bt Metasedimentary gneiss	49 20.27	82 12.46	2.96
Hn-Bt-Ep Granodiorite	49 21.72	82 14.92	2.66
Gt-Opx-Pl Gneiss	48 42.95	82 35.63	3.07
Gt-Opx-Pl Gneiss	48 42.95	82 35.63	3.18
Gt-Cpx-Pl-Qz Gneiss	48 42.95	82 35.63	3.12
Bt Metasedimentary gneiss	48 45.22	82 43.38	2.69
Hn-Bt Metasedimentary gneiss	48 45.22	82 43.38	2.98
Hn-Bt Paragneiss	48 45.22	82 43.38	2.80
Bt Granite	48 45.35	82 43.92	2.65
Px-Hn Granulite	48 42.10	82 32.75	2.76
Px-Hn Granulite	48 42.10	82 32.75	2.79
Hn Granulite	48 42.10	82 32.75	2.66
Gt-Bt Granulite	48 41.85	82 31.67	2.98
Gt-Bt Granulite	48 41.85	82 31.67	2.88
Gt-Bt Granulite	48 41.36	82 32.08	2.77
Qz rich 2Px Granulite	48 49.30	82 26.21	2.70
Granulite	48 49.30	82 26.21	2.73
Granulite	48 49.68	82 27.71	2.77
Granulite	48 49.68	82 27.71	2.76
Granulite	48 49.68	82 27.71	2.81
Hn-Bt-Ep Granite	49 02.42	82 34.17	2.68
Hn-Bt-Ep Granite	49 02.42	82 34.17	2.68
Hn-Bt Granite	49 02.42	82 34.17	2.67

Bt-Hn-Ep Granite	49 02.62	82 34.21	2.65
Bt-Mt-Ep Granite	49 02.82	82 34.13	2.67
Bt-Hn Paragneiss	49 02.28	82 35.63	2.72
Hn-Bt Metasedimentary gneiss	49 02.28	82 35.63	3.01
Bt-Ep Paragneiss	49 02.01	82 34.46	2.71
Bt Granite	49 02.01	82 34.46	2.65
Bt Granite	49 00.29	82 34.58	2.67
Metavolcanic	49 00.00	82 33.83	2.96
Metavolcanic	49 00.00	82 33.83	3.17
Mafic tuff	48 59.46	82 33.58	3.01
Bt Paragneiss	49 00.45	82 33.88	2.93
Qz-Pl Paragneiss	49 00.45	82 33.88	2.98
Serpentinic Paragneiss	49 01.35	82 33.67	3.05
Gt-Bt-Qz Paragneiss	49 01.35	82 33.67	2.75
Bt-Qz Paragneiss	49 01.35	82 33.67	2.80
Metavolcanic	49 15.19	82 12.67	2.86
Bt-Hn Tonalite	49 23.00	82 44.79	2.68
Hn-Bt Tonalite gneiss	49 24.40	82 07.00	2.75
Hn-Bt Tonalite gneiss	49 24.40	82 07.00	2.77
Paragneiss	49 26.49	82 03.67	3.03
Hn-Bt Tonalite gneiss	49 24.30	82 12.79	2.68
Bt-Hn Tonalite	49 24.32	82 13.38	2.66
Bt-Cpx Granite	49 05.08	82 09.67	2.66
Bt Tonalite	49 18.54	82 06.46	2.69
Bt-Hn Tonalite	49 18.54	82 06.46	2.67
Gt-Bt Metasedimentary gneiss	49 19.68	82 09.65	2.72
Gt-Cpx-Hn-Pl Mafic gneiss	49 19.68	82 09.65	3.09
Gt-Cpx-Hn-Pl Mafic gneiss	49 19.68	82 09.65	3.12
Hn Granite	49 20.46	82 10.13	2.68
Hn Granite	49 20.46	82 10.13	2.69
Gt-Cpx-Hn-Pl Mafic gneiss	48 31.25	82 39.04	3.40
hn-Bt Granodiorite	48 31.00	82 39.44	2.73

Hn-Bt Granodiorite	48 31.00	82 39.44	2.74
Gt Mafic gneiss	48 30.50	82 39.48	3.09
Gt Mafic gneiss	48 30.50	82 39.48	3.15
Bt Metasedimentary gneiss	48 32.10	82 40.17	2.83
Hn Mafic gneiss	48 32.10	82 40.17	3.06
Metasedimentary gneiss	48 32.10	82 40.17	2.76
Metasedimentary gneiss	48 32.15	82 39.38	2.83
Mafic gneiss	48 32.30	82 38.67	2.87
Mafic gneiss	48 31.53	82 37.75	3.08
Mafic gneiss	48 31.35	82 38.17	3.20
Hn-Bt Metasedimentary gneiss	48 31.50	82 38.58	2.82
Metasedimentary gneiss	48 32.35	82 38.04	2.87
Semi-pelitic schist	48 32.35	82 37.60	2.71
Metasedimentary gneiss	48 32.62	82 38.00	2.75
Metasedimentary gneiss	48 33.07	82 37.96	2.68
Gt Metasedimentary gneiss	48 32.85	82 37.96	2.85
Gt-Bt Metasedimentary gneiss	48 31.45	82 41.67	2.83
Gt-Cpx-Bt Meta-sedimentary gneiss	48 31.05	82 42.69	2.69
Amphibolite	48 30.64	82 42.46	2.86
Gt-Hn-Bt Metasedimentary gneiss	48 30.45	82 41.13	2.78
Hn-Bt Metasedimentary gneiss	48 30.45	82 41.13	2.79
Hn-Bt Metasedimentary gneiss	48 30.55	82 41.63	2.76
Gt-Hn-Qz-Pl Gneiss	48 32.75	82 40.25	2.98
Gt-Hn-Bt-Qz Gneiss	48 32.54	82 41.35	2.71
Gt-Bt Metasedimentary gneiss	48 04.43	82 37.46	2.78

Gt-Bt Metasedimentary gneiss	48 04.69	82 38.08	2.74
Semi-pelitic gneiss	48 40.27	82 30.50	2.78
Pelitic gneiss	48 39.75	82 30.50	2.78
Pelitic gneiss	48 39.55	82 31.13	2.78
Gt-Bt-Hn Metasedimentary gneiss	48 32.14	82 41.00	2.74
Gt-Bt-Hn Metasedimentary gneiss	48 32.14	82 41.00	2.82
Gt-Bt-Hn Metasedimentary gneiss	48 32.14	82 41.00	2.72
Bt Granite	48 31.10	82 37.42	2.64
Bt Granite	48 39.68	82 30.00	2.67
Mafic gneiss	48 35.90	82 37.63	2.93
Mafic gneiss	48 35.90	82 37.63	2.95
Mafic gneiss	48 35.63	82 35.21	3.02
Gt-Bt Semi-pelitic gneiss	48 35.35	82 35.21	2.88
Gt-Hn Gneiss	48 35.25	82 36.19	2.77
Bt-Hn-Qz-Pl Gneiss	48 35.50	82 36.19	2.75
Gt-Bt-Opx Gneiss	48 40.00	82 30.75	2.81
Mafic gneiss	48 40.27	82 30.92	3.09
Gt Mafic gneiss	48 40.00	82 31.29	3.19
Bt-Hn-Opx Metasedimentary gneiss	48 36.00	82 35.39	3.01
Gt-Hn-Bt Gneiss	48 36.00	82 35.39	2.81
Bt-hn-opx Gneiss	48 36.00	82 35.39	2.97
Gt-Opx-Bt Metasedimentary gneiss	48 36.58	82 34.58	2.75
Bt-Hn-Qz-Pl Gneiss	48 36.09	82 36.38	2.77
Gt-Bt Metasedimentary gneiss	48 34.93	82 37.13	2.73
Gt-Bt Gneiss	48 35.05	82 35.21	2.79
Mafic gneiss	48 35.25	82 36.19	3.09
Gt-Bt Mafic gneiss	48 35.28	82 37.79	2.95

Qz-Cpx-Opx Granulite	48 44.25	82 24.95	2.71
Granite	48 46.27	82 23.33	2.70
Cpx-Opx-Bt Gneiss	48 46.27	82 22.52	2.83
Gt-Cpx-Hn-Pl-QZ Mafic gneiss	48 39.25	82 27.86	3.15
Cpx-Opx-Bt-Hn Granulite	48 43.78	82 26.65	2.89
Bt Metasedimentary gneiss	48 46.27	82 22.52	2.83
Qz-Cpx-Opx Metasedimentary gneiss	48 46.27	82 22.52	2.71
Gt-Cpx-Hn Gneiss	48 37.90	82 26.36	2.95
Gt-Cpx-Opx Gneiss	48 37.90	82 26.36	2.86
Gt-Bt-Opx Gneiss	48 38.19	82 27.86	3.19
Gt-Bt-Opx Gneiss	48 38.19	82 27.86	3.17
Hn Anorthosite	48 38.04	82 27.95	2.79
Hn-Bt Anorthosite	48 38.04	82 27.95	2.70
Gt Amphibolite	48 38.43	82 27.40	3.02
Gt-Bt-Opx-Cpx Metasedimentary gneiss	48 38.17	82 25.67	2.90
Tonalite gneiss	49 14.19	82 25.58	2.72
Metavolcanic	49 00.83	82 24.58	2.91
Amphibolite	49 01.08	82 26.33	3.02
Amphibolite	48 56.84	82 29.67	3.07
Meta-diorite	49 03.24	82 23.00	2.89
Diorite	48 56.48	82 28.67	2.92
Granodiorite	49 01.68	82 20.92	2.70
Metavolcanic	49 02.16	82 22.23	2.77
Metavolcanic	49 01.68	82 22.04	3.00
Metavolcanic	49 03.49	82 21.46	2.94
Granodiorite	49 05.68	82 14.27	2.70
Tonalite gneiss	49 06.75	82 11.15	2.70
Hn-Bt Tonalite	49 07.19	82 10.42	2.70
Metasedimentary gneiss	49 03.00	82 05.17	2.73
Bt Tonalite	49 07.54	82 08.96	2.68

Metasedimentary gneiss	49 12.15	82 04.38	2.74
Hn-Bt Granite	49 17.48	82 09.57	2.67
Hn-Bt Tonalite	49 18.18	82 02.51	2.71
Granodiorite gneiss	49 15.58	82 01.55	2.72
Tonalite	48 49.05	82 07.50	2.71
Tonalite	48 48.97	82 09.17	2.73
Granite	49 14.28	82 04.33	2.68
Metasedimentary gneiss	49 12.27	82 03.92	2.81
Hn Tonalite granodiorite	49 12.50	82 01.17	2.72
Metagabbro	49 07.02	82 06.94	2.95
Mafic orthogneiss	49 14.16	82 05.13	2.95
Hn Tonalite granodiorite	49 15.27	82 04.44	2.77
Mafic gneiss	49 13.08	82 01.92	3.00
Mafic gneiss	49 13.08	82 01.92	2.96
Diabase	49 12.08	82 01.21	3.05
Bt-Hn Tonalite gneiss	49 17.73	82 02.17	2.80
Bt-Qz-Pl-Px Metasedimentary gneiss	49 23.06	82 07.93	2.72
Paragneiss	49 21.82	82 08.73	2.82
Hn-Bt Granodiorite	49 09.43	82 02.63	2.69
Gt-Bt Diorite	48 35.20	82 09.21	2.99
Bt-Px Diorite	48 35.20	82 09.21	2.78
Tonalite	48 48.19	82 06.63	2.69
Bt-Ep Tonalite	48 48.64	82 07.42	2.71
Bt-Hn Tonalite	49 23.35	82 09.55	2.69
Bt Granodiorite	49 26.25	82 08.93	2.69
Qz-Ks-Bt-Hn Metasedimentary gneiss	49 26.15	82 08.62	2.77
Hn-Bt Granodiorite orthogneiss	49 27.20	82 08.93	2.71
Hn-Bt Granodiorite orthogneiss	49 27.20	82 08.93	2.71
Hn-Bt Paragneiss gneiss	49 27.60	82 09.40	2.96
Bt Paragneiss	49 27.60	82 09.40	2.72
Bt-Hn-Cpx Orthogneiss	49 27.30	82 10.60	2.79
Paragneiss	49 26.45	82 10.75	2.85

Paragneiss	49 19.75	82 06.58	2.76
Granodiorite	49 16.46	82 11.37	2.69
Granite	48 47.78	82 35.46	2.65
Gt-Cpx Paragneiss	49 06.73	82 14.46	2.99
gneiss			
2Px Granulite	49 07.32	82 12.42	3.00
gneiss			
Bt Tonalite	49 22.72	82 16.42	2.66
Bt Granite	48 57.51	82 09.80	2.63
Bt Granite	48 57.95	82 09.35	2.70
gneiss			
Gt- Cpx Mafic gneiss	48 33.03	82 35.58	3.17
gneiss			
Gt-Bt Paragneiss	48 33.38	82 35.83	2.86
Cpx Tonalite	48 33.62	82 36.06	2.80
gneiss			
Gt Tonalite	48 32.85	82 36.15	2.77
gneiss			
Tonalite	48 32.63	82 36.15	2.72
gneiss			
Tonalite	48 32.29	82 36.25	2.74
gneiss			
Metasedimentary	48 34.19	82 35.55	2.79
gneiss			
Tonalite	48 33.21	82 35.25	2.69
gneiss			
Tonalite	48 32.15	82 32.95	2.70
gneiss			
Gt-Cpx-Opx	48 32.25	82 33.25	2.81
Metasedimentary gneiss			
Gt-Bt Metasedimentary	48 37.51	82 30.00	2.82
gneiss			
Hn Tonalite	49 06.89	82 13.83	2.71
Mafic Tonalite	49 02.00	83 09.06	2.87
gneiss			
Hn-Bt-Ep	49 01.86	83 10.02	2.74
Tonalite			
Tonalite	49 01.19	83 09.13	2.71
gneiss			
Tonalite	49 00.17	83 08.10	2.75
gneiss			
Tonalite	49 00.89	83 08.33	2.74
gneiss			

Mafic Tonalite gneiss	49 03.84	83 09.42	2.81
Mafic Tonalite gneiss	49 00.34	83 08.54	2.84
Mafic Tonalite gneiss	49 04.68	83 10.00	2.83
Mafic Tonalite gneiss	49 04.78	83 10.25	2.93
Mafic Tonalite gneiss	49 05.83	83 09.00	2.81
Bt-Ep Tonalite gneiss	49 06.24	83 09.00	2.71
Hn-Bt Tonalite gneiss	49 04.27	83 09.06	2.72
Pyroxenite	49 06.08	83 08.13	2.98
Qz Diorite	49 04.80	83 11.96	2.81
Qz Diorite	49 04.74	83 11.54	2.84
Bt-Ep Tonalite gneiss	49 00.70	83 13.38	2.74
Bt-Ep Granodiorite	49 00.05	83 13.71	2.69
Mafic Tonalite gneiss	49 04.96	83 11.04	2.91
Bt-Ep Tonalite gneiss	49 01.83	83 07.63	2.74
Mafic Tonalite gneiss	49 04.03	83 07.35	2.86
Mafic Tonalite gneiss	49 04,82	83 14.63	2.85
Hn-Bt-Ep Tonalite gneiss	49 06.28	83 14.79	2.71
Qz Diorite	49 06.53	83 14.79	2.79
Tonalite-granodiorite	49 11.97	83 17.67	2.69
Tonalite	49 11.04	83 17.42	2.73
Granodiorite to tonalite	49 09.75	83 18.46	2.74
Bt Granodiorite to tonalite	49 11.04	83 17.42	2.65
Metagraywacke	49 12.81	83 18.15	2.73
Diorite	49 11.58	83 21.54	3.01
Hn-Bt Tonalite	49 11.58	83 21.54	2.76
Bt-Ep Tonalite	49 02.27	83 28.85	2.71
Paragneiss	49 02.81	83 29.75	2.85
Amphibolite	49 02.95	83 29.50	3.07

Amphibolite paragneiss	49 02.95	83 29.50	2.93
Bt Tonalite	49 00.75	83 29.33	2.74
Mafic Tonalite gneiss	49 03.11	83 08.54	2.95
Mafic tonalite gneiss	49 04.00	83 14.63	2.86
Bt Granodiorite	49 27.41	82 16.95	2.68
Bt Granodiorite to tonalite	49 26.85	82 14.75	2.69
Bt Tonalite gneiss	49 23.60	82 18.42	2.70
Bt-Hn Tonalite	49 14.86	82 30.00	2.75
Hn Tonalite	49 13.50	82 32.29	2.73
Mafic Tonalite gneiss	49 13.50	82 32.29	3.06
Meta-Gabbro	49 13.50	82 32.29	3.11
Bt Granodiorite	49 13.17	82 33.67	2.67
Hn-Bt Tonalite to granodiorite	49 19.32	82 26.63	2.67
Bt-Ep Granodiorite	49 00.19	83 19.50	2.71
Bt-Ep Granodiorite	48 59.74	83 19.25	2.69
Bt-Ep Granodiorite	48 57.80	83 18.60	2.70
Bt-Ep Granodiorite	48 58.00	83 18.08	2.69
Bt-Ep Tonalite gneiss	49 08.50	83 24.58	2.69
Metagraywacke	49 09.50	83 21.88	2.74
Metagraywacke	49 09.50	83 21.88	2.78
Diorite	49 06.85	83 24.13	2.97
Granite	49 12.95	82 34.00	2.64
Mafic tonalite gneiss	49 20.00	82 26.92	2.81
Granulite gneiss	49 28.70	82 28.51	2.73
Mafic gneiss	49 26.88	82 26.75	2.98
Mafic gneiss	49 26.88	82 26.75	3.10
Mafic tonalite gneiss	49 27.25	82 17.10	2.92
Mafic tonalite gneiss	49 29.58	82 31.24	2.79
Granulite gneiss	49 27.62	82 28.69	2.78
Metasedimentary gneiss	49 27.35	82 33.85	2.78

Hn-Bt Tonalite	49 25.05	82 35.71	2.69
granodiorite gneiss			
Hn-Bt Granodiorite	49 29.15	82 33.74	2.68
gneiss			
Granodiorite	49 28.00	82 36.76	2.68
Tonalite	49 28.83	82 41.75	2.72
gneiss			
Metasedimentary	49 27.65	82 34.95	2.82
gneiss			
Metasedimentary	49 27.65	82 34.95	2.80
gneiss			
Diorite	49 26.00	82 38.13	2.77
Bt Granodiorite	49 16.38	82 47.62	2.65
gneiss			
Bt-Ep-Mt Granodiorite	49 27.78	82 36.25	2.67
to tonalite			
Bt-Ep-Mt Granodiorite	49 14.59	82 40.71	2.79
to tonalite			
Mafic tonalite	49 14.59	82 40.71	2.79
gneiss			
Mafic gneiss	49 15.16	82 40.65	3.06
Granodiorite	49 15.46	82 40.35	2.70
gneiss			
Orthogneiss	49 15.65	82 40.45	2.75
Granodiorite	49 16.02	82 39.45	2.68
to granite gneiss			
Bt-Hn Granodiorite	49 16.02	82 39.45	2.71
gneiss			
Bt Granodiorite	49 15.70	82 39.05	2.67
gneiss			
Bt Granodiorite	49 16.41	82 37.73	2.69
to granite gneiss			
Hn-Bt Granodiorite	49 17.54	82 34.30	2.69
to tonalite gneiss			
Mafic gneiss	49 24.35	82 30.40	3.05
Mafic gneiss	49 24.35	82 30.40	3.13
Bt Granite	49 26.00	82 33.65	2.63
Metagraywacke	49 24.56	82 49.00	2.73
Metagraywacke	49 26.14	82 53.43	2.73
Bt Granite	49 16.19	82 52.89	2.69
Diabase	49 00.75	83 06.71	3.03
Pyroxenite	49 00.75	83 06.71	3.22
Pyroxenite	49 00.70	83 06.43	3.11
Bt-Ep Granodiorite	49 01.59	83 01.08	2.70

Hn-Bt Granodiorite to tonalite	49 00.47	83 04.69	2.76
Tonalite gneiss	49 05.46	82 59.29	2.68
Tonalite gneiss	48 55.70	83 01.94	2.70
Hn-Bt-Ep Granodiorite	48 58.97	83 02.10	2.76
Hn-Bt Granite	49 05.12	82 51.10	2.68
Mafic gneiss	49 04.37	82 50.83	3.04
Bt-Ep Granodiorite	48 51.65	83 09.46	2.67
Bt Granite granodiorite	49 02.75	82 50.92	2.68
Hn-Bt-Ep Granodiorite	49 04.30	82 55.51	2.72
Granodiorite	49 02.58	82 52.88	2.68
Bt Granodiorite to granite	49 02.77	82 53.29	2.70
Granodiorite	49 02.77	82 53.29	2.70
Granodiorite	49 02.58	82 52.88	2.71
Tonalite gneiss	49 12.30	82 47.54	2.72
Tonalite gneiss	49 05.25	83 01.21	2.75
Granodiorite to tonalite	49 12.16	82 50.06	2.69
Bt-Hn-Ep Granodiorite	48 45.76	83 04.50	2.71
Bt-Ep Granodiorite	48 51.94	83 04.92	2.73
Bt-Ep Granodiorite	49 02.58	83 01.71	2.72
Bt-Ep Granodiorite	48 57.23	82 55.85	2.69
Granodiorite gneiss	49 13.26	82 49.58	2.73
Granodiorite gneiss	49 13.26	82 49.58	2.67
Granodiorite gneiss	49 05.16	82 58.04	2.66
Hn-Bt Tonalite gneiss	49 05.25	83 01.24	2.76
Granodiorite gneiss	49 12.25	82 48.92	2.70
Hn-Bt Granodiorite	49 03.74	82 54.63	2.70
Hn-Bt Granodiorite	49 03.74	82 54.63	2.71
Bt-Ep Granodiorite	49 02.62	82 59.50	2.69
Bt-Ep Granodiorite	49 03.65	82 59.50	2.70
Bt Granite	49 05.81	82 57.90	2.67

Qz Diorite	49 05.25	83 02.25	2.81
Bt-Ep Granodiorite	49 05.55	83 01.13	2.69
Bt-Ep Granodiorite to tonalite	49 07.27	83 05.35	2.71
Qz Diorite	49 05.25	83 02.25	2.81
Bt-Ep Granodiorite to tonalite	49 06.24	83 03.50	2.70
Qz Diorite	49 05.85	83 02.75	2.79
Hn-Bt Tonalite gneiss	49 07.20	83 09.50	2.69
Bt-Ep Tonalite	49 04.70	83 06.88	2.64
Hn-Bt-Ep Tonalite gneiss	49 05.82	83 06.17	2.83
Qz Diorite	49 05.62	83 02.75	2.78
Bt-Ep Tonalite to granodiorite	49 07.93	83 06.71	2.71
Bt-Ep Tonalite to granodiorite	49 06.10	83 06.00	2.77
Bt-Ep Tonalite to granodiorite	49 06.23	83 05.67	2.74
Bt-Ep Tonalite to granodiorite	49 06.85	83 04.92	2.70
Bt Tonalite	49 09.20	83 10.00	2.68
Bt Tonalite	49 10.36	83 03.88	2.65
Bt-Ep Tonalite to granodiorite	49 08.55	83 05.42	2.69
Bt Granodiorite	49 11.07	83 10.04	2.67
Monzodiorite	49 12.00	83 10.79	2.78
Bt-Ep Granodiorite to tonalite	49 09.63	83 05.33	2.68
Bt-Ep Tonalite to granodiorite	49 06.95	83 05.13	2.70
Bt-Ep Granodiorite	49 09.60	83 05.21	2.68
Hn-Ep Granodiorite	49 08.92	83 03.13	2.75
Bt-Ep Tonalite	49 08.78	83 03.38	2.71
Bt-Ep Tonalite to granodiorite	49 28.30	82 41.10	2.65
Bt-Ep Tonalite gneiss	49 06.55	83 04.54	2.72
Bt-Ep Granodiorite to tonalite	49 08.22	83 06.54	2.71
Bt-Hn Tonalite	48 49.62	83 21.81	2.71
Diorite	48 49.55	83 21.96	3.02

Bt-Hn Tonalite gneiss	48 43.81	83 27.29	2.71
Mafic Tonalite gneiss	48 41.58	83 21.90	2.77
Orthogneiss	49 04.84	82 14.23	2.78

Abbreviations: 2Px, two pyroxene; Bt, biotite; Cpx, clinopyroxene; Ep, epidote; Gt, garnet; Hn, hornblende; Ks, potassium feldspar; Mt, magnetite; Opx, orthopyroxene; Pl, plagioclase; Px, pyroxene; Qz, quartz; Sph, sphene.

APPENDIX 2: Characteristics of the Different Tectonic Blocks of the KSZ

CHARACTERISTICS	GRB	VRB	CB
Lithology	Main assemblages include mafic gneiss, paragneiss and tonalite gneiss, metamorphosed to granulite facies	Mostly amphibolite facies tonalites, granodiorites and granites with minor occurrences of granulite facies paragneiss and mafic gneiss along the LF. Also contains some metavolcanics	Characterized by northeast trending belts of granulite facies paragneiss, tonalite gneiss and mafic gneiss
	No anorthosite or carbonatite suite rocks	No anorthoste but contains carbonatite complexes (Cargil, Clay Howles)	Anorthosite and several carbonatite complexes present (Shenango, Nemagosenda, Borden Lake, Lackner Lake)
Structural Elements i.e., boundary zones	Fault bounded on all sides. ILCZ (thrust) on eastern side, SLF (normal) on western side and WRF (normal) at southern limit.	Fault bounded by LF (normal) on western side and SLF (normal) on eastern side Has no apparent evidence of a reverse fault.	Fault bounded on all sides. ILCZ (thrust) on eastern side, SLF (normal) on western side and WRF (normal) at northern limit.

Dykes	Contains northerly trending Matachewan dykes		Some evidence of northwesterly trending Matachewan dykes to the south.
Pseudotachylite	Veinlets of pseudotachylite occur sporadically throughout this block	Not present, except in ILCZ	
Surface Density	Generally high with average densities of 3.05 g/cm^3	Generally low with average densities of 2.72 g/cm^3	High with average of 3.05 g/cm^3
Gravity Anomaly	2-5 mGals	25-35 mGals	35-45 mGals
Estimated thickness of granulites	1-4 km	25-30 km	25-30 km
Crustal thickness and Moho topography	No anomalous lower crustal structure associated with this block	Crustal bulge or thickened crust underneath region of high gravity anomaly (50 km)	Thick crust underneath region of high gravity anomaly (52 km)
Magnetic Anomaly	Strong (500 nT above background level)	Moderate (300 nT)	Subtle except for moderately strong, northeast-trending strips in the northern CB and strong anomalies around the carbonatite complexes

Near surface velocity structure	No significant change in velocities across this block.	Increase in velocities on the eastern side of the LF associated with uplifted granulites	High velocities associated with uplifted granulites
Geobarometry	High metamorphic pressures (7-8 kbar) associated with granulites	Intermediate pressures (4-6 kbars) except for localities where granulites are exposed (8 kbar)	High metamorphic pressures within the granulites (7-9 kbar)

REFERENCES

ARKANI-HAMED, J. and STRANGWAY, D.W. 1986. Effective magnetic susceptibility of the oceanic upper mantle derived from MAGSAT data. Geophysical Research Letters, 13, pp. 999-1002.

ARMSTRONG, R.L. 1982. Cordilleran metamorphic core complexes from Arizona to southern Canada. Annual Review of Earth and Planetary Sciences, 10, pp. 129-154.

ATTOH, K. 1980. Stratigraphic relations of the volcanic-sedimentary successions in the Wawa greenstone belt, Ontario. *In* Current research, part A. Geological Survey of Canada, Paper 80-1A, pp. 101-106.

BARANOV, V. and NAUDY, H. 1964. Numerical calculation of the formula of reduction to the magnetic pole. Geophysics, 29, No. 1, pp. 67-79.

BARTON, P.J. 1986. The relationship between seismic velocity and density in the continental crust- a useful constraint? Geophysical Journal of the Royal Astronomical Society, 87, pp. 195-208.

BENNETT, G., BROWN, D.D., GEORGE, P.T, and LEAHEY, E.J. 1967. Operation Kapuskasing. Ontario Department of Mines, Miscellaneous Paper 10, 98p.

BERKHOUT, A.W.J. 1973. Gravity in the Prince of Wales, Somerset and northern Baffin islands. *In* Proceedings of the symposium on the geology of the Canadian Arctic. *Edited by* J.D. Aitkens and D.J. Glass. Geological Association of Canada - Canadian Society of Petroleum Geologists, pp. 63-80.

BERRY, M.J. and FUCHS, K. 1973. Crustal structure of the Superior and Grenville Provinces of the northeastern Canadian shield. Bulletin of the Seismological Society of America, 63, pp. 1393-1432.

BOLAND, A.V., and ELLIS, R.M. 1989. Velocity structure of the Kapuskasing Uplift from seismic refraction studies, northern Ontario. Journal of Geophysical Research, 94, No. B6, pp. 7189-7204.

BOLAND, A.V., and ELLIS, R.M. 1988. Velocity structure of the Kapuskasing zone from seismic refraction studies. *In* Lithoprobe Workshop, KSZ 88, University of Toronto, pp.141-154.

BRIGGS, I.C. 1974. Machine contouring using minimum curvature. Geophysics, 39, No. 1. pp. 39-48.

BROOME, J. 1986. Display and enhancement of aeromagnetic data with examples from Guysborough County, Nova Scotia. *In* Interpretation of gravity and magnetic anomalies for non-specialists. *Organized by* A.K. Goodacre. Notes for Canadian Geophysical Union Short Course, pp. 212-252.

BROWN, R.L. and JOURNEAY, J.M. 1987. Tectonic denudation of the Shuswap metamorphic terrane of southeastern British Columbia. Geology, 15, pp. 142-146.

BURCHFIEL, B.C. and ROYDEN, L.H. 1985. North-south extension within the convergent Himalayan region. Geology, 13, pp. 679-682.

BURKE, K. and DEWEY, J.F. 1973. Plume generated triple junctions: Key indicators in applying plate tectonics to old rocks. Journal of Geology, 81, pp. 406-433.

CARD, K.D. 1979. Regional geological synthesis, central Superior Province. *In* Current research, Part A. Geological Survey of Canada, Paper 79-1a, pp. 87-90.

CARD, K.D. and CIESIELSKI, A. 1986. Subdivisions of the Superior Province of the Canadian Shield. Geoscience Canada, 13, pp. 5-13.

CHANDLER, V.W., McSWIGGEN, J.M., MOREY, G.B., HINZE, W.J., and ANDERSON, R.R. 1989. Interpretation of seismic reflection, gravity and magnetic data across middle Proterozoic Mid-Continent Rift System, northwestern Wisconsin, eastern Minnesota, and central Iowa. The American Association of Petroleum Geologists Bulletin, 73, No. 3, pp. 261-275.

CHRISTENSEN, N.I. and FOUNTAIN, D.M. 1975. Constitution of the lower continental crust based on experimental studies of seismic velocities in granulite. Geological Society of America Bulleting, v. 86, pp. 227-236.

COOK, D.G. 1983. The northern Franklin Mountains, N.W.T., Canada: a scale model for the Wyoming Province. *In* Rocky Mountains foreland basins and uplifts. *Edited by* J.D. Lowell. Rocky Mountain Association of Geologists, pp. 315-358.

COOK, F.A. 1985. Geometry of the Kapuskasing structure from a Lithoprobe pilot reflection survey. Geology, 13, pp. 368-371.

CORDELL, L. and HENDERSON, R.G. 1968. Interactive three-dimensional solution of gravity anomaly data using a digital computer. Geophysics, 33, No. 4, pp. 596-601.

COWARD, M.P. 1984. Major shear zones in the Precambrian crust; examples from NW Scotland and southern Africa and their significance. *In* Precambrian Tectonics Illustrated. *Edited by* A. Kröner and R. Grieling, International Union of Geological Sciences, pp. 207-235.

COWARD, M.P. and FAIRHEAD, J.D. 1980. Gravity and structural evidence for the deep structure of the Limpopo belt, southern Africa. Tectonophysics, 68, pp. 31-44.

DOBRIN, M.B. 1976. Introduction to Geophysical Prospecting. Third Edition. New York, McGraw-Hill, 446p.

DOBRIN and SAVIT, C.H. 1988. Introduction to Geophysical Prospecting. Fourth Edition. New York, McGraw-Hill.

DODS, S.D., TESKEY, D.J., and HOOD, P.J. 1985. The new series of 1:1000,000-scale magnetic-anomaly maps of the Geological Survey of Canada: Compilation techniques and interpretation. *In* The Utility of Regional Gravity and Magnetic Anomaly Maps. *Edited by* W.J. Hinze, Society of Exploration Geophysicists, pp. 69-87.

EARTH PHYSICS BRANCH. 1984. Field Procedures Manual. Geological Survey of Canada. Unpublished manuscript.

ELLIOTT, D. 1983. The construction of balanced cross-sections. Journal of Structural Geology, 5, p. 101.

ERNST, R.E. and HALLS, H.C. 1984. Paleomagnetism of the Hearst dyke swarm and implications for the tectonic history of the Kapuskasing Structural Zone, northern Ontario. Canadian Journal of Earth Science, 21, pp. 1499-1506.

FEININGER, T. 1986. Rock Density. *In* Interpretation of gravity and magnetic anomalies for non-specialists. *Organized by* A.K. Goodacre, Notes for Canadian Geophysical Union Short Course, pp. 50-68.

FORMAN, D.M. and SHAW, J.D. 1973. Deformation of the crust and mantle in central Australia. Bulletin of the Australian Bureau of Mineral Resources, Geology and Geophysics, 144, 20p.

FORSYTH, D., MOREL, P., HASEGAWA, H., WETMILLER, R., ADAMS, J., GOODACRE, A., NAGY, D., COLES, R., HARRIS, J., and BASHAM, P. 1983. Comparative study of the geophysical and geological information in the Timiskaming-Kapuskasing Area. Technical Report, TR-238, 52 pp. Atomic Energy of Canada, Chaulk River Ontario.

FOUNTAIN, D.M. 1976. The Ivrea-Verbano and Strona-Ceneri Zones, northern Italy: A cross section of the continental crust - new evidence from seismic velocities. Tectonophysics, 33, pp. 145-166.

FOUNTAIN, D.M., and SALISBURY, M.H. 1981. Exposed cross sections through the continental crust: Implications for crustal structure, petrology and evolution. Earth and Planetary Science Letters, 56, pp. 263-277.

FOUNTAIN, D.M. and SALISBURY, M.H. 1986. Seismic properties of the Superior Province crust based on seismic velocity measurements on rocks from the Michipicoten-Wawa-Kapuskasing terranes, Ontario. Geological Association of Canada, Abstracts and Programs, 11, pp. 69.

FOUNTAIN, D.M, SALISBURY, M.H, and PERCIVAL, J.A. 1990. Seismic structure of the continental crust based on rock velocity measurements from the Kapuskasing Uplift. Journal of Geophysical Research, 95, pp. 1167-1186.

FRASER, J.A, HEYWOOD, W.W. and MAZURSKI, M.A. 1978. Metamorphic map of the Canadian shield. Geological Survey of Canada Map 1475-A.

GARLAND, G.D. 1950. Interpretation of gravimetric and magnetic anomalies on traverses in the Canadian Shield in northern Ontario. Publications of the Dominion Observatory, Ottawa, 16, No. 1, 57p.

GEIS, W.T., COOK, F.A., GREEN, A.G., MILKEREIT, B., PERCIVAL, J.A., and WEST, G.F. 1990. Thin thrust sheet formation of the Kapuskasing Structural Zone revealed by Lithoprobe seismic reflection data. Geology, 18, pp. 513-516.

GEOLOGICAL SURVEY OF CANADA. 1984. Magnetic anomaly map, Timmins (NM-17), Map NM-17-M. Scale 1:1000,000.

GIBB, R.A. 1975. Collision tectonics in the Canadian Shield. Earth and Planetary Science Letters, 27, pp. 378-382.

GIBB, R.A. 1978. A gravity Survey of James Bay and its bearing on the Kapuskasing Gneiss Belt, Ontario. Tectonophysics, 45, pp. T7-T13.

GIBB, R.A. and WALCOT, R.I. 1971. A Precambrian suture in the Canadian Shield. Earth and Planetary Science Letters, 10, pp. 417-422.

GITTINS, J., MACINTYRE, R.M., and YORK, D. 1967. The ages of Carbonatite complexes in eastern Canada. Canadian Journal of Earth Sciences, 4, pp. 651-655.

GRANT, F.S. 1973. The magnetic susceptibility mapping method for interpreting aeromagnetic surveys (abstract). Presented at the 42nd annual society of Exploration Geophysicists meeting, Mexico city.

GRANT and WEST, G.F. 1965. Interpretation theory in applied geophysics. New York, McGraw-Hill, 584p.

GREEN, A.G., ANDERSON, N.L., and STEPHENSON, O.G. 1979. An expanding spread seismic reflection survey across the Snake Bay-Kakagi greenstone belt, NW Ontario. Canadian Journal of Earth Sciences, 16, pp. 1599-1612.

GOODWIN, A.M. 1962. Structure, stratigraphy and origin of iron formations, Michipicoten area, Algoma district, Ontario, Canada. Geological Society of America Bulletin, 73, pp. 561-586.

GOODWIN, A.M. 1972. The Superior Province. *In* Variation in tectonic styles in Canada. *Edited by* R.A. Price and R.J.W. Douglas. Geological Association of Canada Special Paper 2, pp. 527-624.

HALL, D.H. and HAJNAL, Z. 1973. Deep crustal studies in Manitoba. Bulletin of the Seismological Society of America, 63, pp. 885-910.

HALLS, H.C. 1982. Crustal thickness in the Lake Superior region. Memoirs of the Geological Society of America, 156, pp. 239-243.

HEAMAN, L.M. 1988. A precise U-Pb Zircon age for a Hearst dyke. Geological Association of Canada, Program with Abstracts, 13, pp. A53.

HOFFMAN, P.F. 1988. The United Plates of America, the Birth of a craton: Early Proterozoic assembly and growth of Laurentia. Annual Review of Earth and Planetary Science, 16, pp. 543-603.

HURICH, C.A., and SMITHSON, S.B. 1982. Gravity interpretation of the southern Wind River Mountains, Wyoming. Geophysics, 47, pp. 1550-1561.

INNES, M.J.S. 1960. Gravity and isostasy in northern Ontario and Manitoba. Publications of the Dominion Observatory, Ottawa, 21, No. 6, pp. 261-338.

INNES, M.J.S., GOODACRE, A.K., WEBER, J.R., and McCONNELL, R.K. 1967. Structural implications of the gravity field in Hudson Bay and vicinity. Canadian Journal of Earth Sciences, 4, pp. 977-993.

KANASEWICH, E.R. 1975. Time sequence analysis in geophysics. University of Alberta Press, Edmonton, 352 pp.

KERR, J.W. 1977. Cornwallis Fold Belt and the mechanism of basement uplift. Canadian Journal of Earth Sciences, 14, pp. 1374-1401.

LECLAIR, A.D. 1990. Puskuta Shear Zone and Archean crustal structure in the central Kapuskasing Uplift, northern Ontario. *In* Current Research, Part C, Geological survey of Canada, Paper 90-1C, pp. 197-206.

LECLAIR, A.D., and NAGERL, P. 1988. Geology of the Chapleau, Groundhog River and Val Rita blocks, Kapuskasing area, Ontario. *In* Current Research, Part C, Geological Survey of Canada, Paper 88-1C, pp. 83-91.

LECLAIR, A.D.and POIRIER, G.G. 1989. The Kapuskasing Uplift in the Kapuskasing Area, Ontario. *In* Current Research, Part C, Geological Survey of Canada, Paper 89-1C, pp. 225-234.

LETROS, S.W. 1980. Geological interpretation of high resolution aeromagnetic data in the Kirkland-Larder Lakes area. Msc. thesis, University of Toronto, Toronto, Ontario.

LETROS, S.W., STRANGWAY, D.W., TASILLO-HIRT, A.M., and GEISSMAN, J.W. 1983. Aeromagnetic interpretation of the Kirkland Lake- Larder Lake Portion of the Abitibi Greenstone Belt, Ontario. Canadian Journal of Earth Sciences, 20, pp.548-560.

LeQUENTREC, M.F., MARESCHAL, J.C. and PARPHENUK, O. 1989. A finite element model of the thermal evolution of the Kapuskasing Structure. Geological Association of Canada Mineralogical Association of Canada, Program with Abstracts, 14, pp. A103.

LEWCHUCK, M.T. and SYMONS, D.T.A. 1990. Paleomagnetism of the Clay Howells Carbonatite Complex: Constraints on Proterozoic motion in the Kapuskasing Structural Zone, Superior Province, Canada. Tectonophysics, 172, pp. 67-75.

LUDWIG, J.W., NAFE, J.E., and DRAKE, C.L. 1970. Seismic refraction, *In* The Sea. *Edited by* A.E. Maxwell, Wiley, New York, 4, pp. 53-84.

MACLAREN, A.S., ANDERSON, D.T., FORTESCUE, J.A.C., GAUCHER, E.G., HORNBROOK, E.H.W., and SKINNER, R. 1968. A preliminary study of the Moose River belt, northern Ontario. Geological Survey of Canada, Paper 67-38, pp. 12-36.

MACLAREN, A.S. and CHARBONNEAU, B.W. 1968. Characteristics of magnetic data over major subdivisions of the Canadian Shield. Proceedings of the Geological Association of Canada, 19, pp. 57-65.

MARESCHAL, M., CHAKRIDI, R., and CHOUTEAU, M. 1988. A magnetotelluric survey across the Groundhog River block: Progress report on the pseudo 1-D interpretation. *In* Lithoprobe Workshop II KSZ 88-9, University of Toronto, pp. 77-81.

MARILLIER, F. and VERHOEF, J. 1989. Crustal thickness under the Gulf of St. Lawrence, northern Appalachians, from gravity and deep seismic data. Canadian Journal of Earth Sciences, 26, pp. 1517-1532.

MATHUR, S.P. 1974. Crustal Structure in southwestern Australia from seismic and gravity data. Tectonophysics, 24, pp. 151-182.

MCGLYNN, J.C. 1970. The Superior Province. *In* Geology and Economic Minerals of Canada.*Edited by* R.J.W. Douglas, Geological Survey of Canada, Economic Geology Report, 1, pp. 59-71.

McGRATH, P.H. 1986. Terrestrial magnetism, its terminology, and manifestations from an interpreter's point of view. *In* Interpretation of gravity and magnetic anomalies for non- specialists. *Organized by* A.K. Goodacre, Notes for Canadian Geophysical Union Short Course, pp. 137-211.

MEREU, R.F., WANG, D., KUHN, O., FORSYTH, D.A., GREEN, A.G., MOREL, P., BUCHBINDER, G.G.R., CROSSLEY, D., SCHWARTZ, E., duBERGER, R., BROOKS, C., and CLOWES, R. 1986. The 1982 COCRUST seismic experiment across the Ottawa-Bonnechere graben and Grenville Front in Ontario and Quebec. Geophysical Journal of the Royal Astronomical Society, 84, pp. 491-514.

MIALL, A.D. 1983. Stratigraphy and tectonics of the Peel Sound Formation, Somerset and Prince of Wales islands: Discussion. *In* Current Research, Part A. Geological Survey of Canada, Paper 83-1A, pp. 493-495.

NKWATE, E.A. and SALISBURY, M.H. 1988. New gravity mapping of the Kapuskasing structure in the Val Rita and Groundhog River Blocks: Preliminary results. *In* Lithoprobe Workshop II KSZ 88-9, University of Toronto, pp. 55-64.

NORTHEY, D.J., and WEST, G.F. 1986. A crustal scale seismic refraction experiment over the Kapuskasing Structural Zone. Geological Association of Canada, Mineralogical Association of Canada, Program with Abstracts, 11, pp. 108.

OKULITCH, A.V., PACKARD, J.J. and ZOLNAI, A.I. 1986. Evolution of the Boothia Uplift, arctic Canada. Canadian Journal of Earth Sciences, 23, pp. 350-358.

PARKER, R.L. 1972. The rapid calculation of potential anomalies. Geophysical Journal of the Royal Astronomical Society, 31, pp. 447-455.

PERCIVAL, J.A. 1983. High grade metamorphism in the Chapleau-Foleyet area, Ontario. American Mineralogist, 68, pp. 667-686.

PERCIVAl, J.A. 1985. The Kapuskasing structure in the Kapuskasing-Fraserdale area, Ontario. Geological Survey of Canada, Paper 85-1A, pp. 1-5.

PERCIVAL, J.A. 1986. A possible exposed Conrad discontinuity in the Kapuskasing Uplift, Ontario. *In* Reflection Seismology, The Continental Crust. *Edited by* M. Barazangi and L.D. Brown. Geodynamic Series, American Geophysical Union, Washington D.C., 14, pp. 135-141.

PERCIVAL, J.A. 1990. A field guide to the Kapuskasing Uplift, a corss-section through the Archean Superior Province. *In* Exposed Cross-sections of the Continental Crust. *Edited by* M. Salisbury and D.M. Fountain. NATO ASI series, Kluwer Academic Publishers, Netherlands, pp. 227-283.

PERCIVAL, J.A. and CARD K.D. 1983. Archean crust as revealed in the Kapuskasing Uplift, Superior Province, Canada. Geology, 11, pp. 323-326.

PERCIVAL, J.A. and CARD, K.D. 1985. Structure and evolution of Archean crust in central Superior Province, Canada. Geological Association of Canada, Special Paper 28, pp. 179-192.

PERCIVAL, J.A and KROGH, T.E. 1983. U-Pb zircon geochronology of the Kapuskasing Structural Zone and vicinity in the Chapleau-Foleyet area, Ontario. Canadian Journal of Earth Science, 20, pp. 830-843.

PERCIVAL, J.A and McGRATH, P.H. 1986. Deep crustal structure and tectonic history of the northern Kapuskasing Uplift of Ontario: An integrated petrological-geophysical study. Tectonics, 5, pp. 553-572.

PERCIVAL, J.A., PARISH, R.R., KROGH, T.E., and PETERMAN, Z.E. 1988. When did the Kapuskasing Zone come up? *In* Lithoprobe workshop, KZ 88, University of Toronto, pp. 43-47.

SAGE, R.P. 1983. Geology of the Cargil Township Carbonatite Complex. Ontario Geological Survey, Open File Report 5400, 46p.

SALES, J.K. 1968. Crustal mechanics of Cordilleran foreland deformation: A regional and scale model approach. American Association of Petroleum Geologists Bulletin, 52, pp. 2016-2044.

SHIVE, P.N., and FOUNTAIN, D.M. 1988. Magnetic mineralogy in an Archean crustal cross section: Implications for crustal magnetization. Journal of Geophysical Research, 93, No. B10, pp. 12177-12186.

STEWART, W.D. and KERR, J.W. 1984. Geology of Somerset island north, Somerset island south, Boothia Peninsula north and central Boothia Peninsula. Geological Survey of Canada, Maps 1595A, 1596A, 1597A and 1598A.

STUDEMEISTER, P.A. 1983. The greenschist facies of an Archean assemblage near Wawa, Ontario. Canadian Journal of Earth Sciences, 20, pp. 1409-1420.

SWAIN, C.J. 1976. A Fortran IV program for interpolating irregularly spaced data using the difference equations for minimum curvature. Computers and Geosciences, 1, pp. 231-240.

TALWANI, M. and HEIRTZLER, J.R. 1964. Computation of magnetic anomalies caused by two dimensional structures of arbitrary shape. *In* Computers in the Mineral Industries Part 1, Stanford University Publications, Geological Sciences, 9, pp. 464-480.

TALWANI, M., WORZEL, J.L. and LANDISMAN, M. 1959. Rapid gravity computations for two dimensional bodies with application to the Mendicino Submarine fracture zone. Journal of Geophysical Research, 64, N0. 1, pp. 49-59.

TELFORD, W.M., GELDART, L.P., SHERIFF, R.E., and KEYS, D.A. 1976. Applied geophysics. Cambridge University Press, London, 860p.

THURSTON, P.C., SIRAGUSA, G.M., and SAGE, R.P. 1977. Geology of the Chapleau area, Districts of Algoma, Sudbury, and Cochrane. Ontario Division of Mines, Geoscience Report, 157, 293p.

TWYMAN, J.D. 1983. The generation, crystallization and differentiation of Carbonatite magmas: Evidence from the Argo and Cargil complexes, Ontario, Unpublished Ph.D. thesis, University of Toronto, Toronto, Ontario.

URQUHART, W.E.S. and STRANGWAY, D.W. 1985. Interpretation of part of an aeromagnetic survey in the Matagami area of Quebec. *In* The Utility of Regional Gravity and Magnetic Anomaly Maps. *Edited by* W.J. Hinze, Society of Exploration Geophysicists, pp. 426-438.

WASILEWSKI, P. and FOUNTAIN, D.M. 1982. The Ivrea Zone as a model for the distribution of magnetization in the continental crust. Geophysical Research Letters, 9, pp. 333-336.

WATSON, J. 1980. The origin and history of the Kapuskasing Structural Zone, Ontario, Canada. Canadian Journal of Earth Sciences, 17, pp. 866- 875.

WEBER, W. and SCOATES, R.J.F. 1978. Archean and Proterozoic metamorphism in the northwestern Superior Province and along the Churchill-Superior boundary, Manitoba. Geological Survey of Canada, Paper 78-10, pp. 5-16.

WEST, G.F. 1988. An interpretation overview of the KSZ refraction data. *In* Lithoprobe Workshop KSZ-88, University of Toronto, pp. 126.

WILLIAMS, H.R. 1978. The Archean geology of Sierra Leone. Precambrian Research, 6, pp. 251-268.

WILSON, C.W. and STEARNS, R.G. 1958. Structure of the Cumberland Plateau. Tennessee. Geological Society of America Bulletin, 69, pp. 1283-1296.

WILSON, J.T. 1968. Comparison of the Hudson Bay arc with some other features. *In* Science, History and Hudson Bay. *Edited by* C.S. Beals, Department of Energy Mines and Resources, Ottawa, pp. 1015-1033.

WILSON, H.D.B., and BRISBIN, W.C. 1965. Mid-North American ridge structures (abstract). Geological Society of America Special Paper, 87, pp. 186-187.

WOODARD, N.B., BOYER, S.E. and SUPPE, J. 1985. An outline of balanced cross-sections. University of Tennessee, Department of Geological Sciences, Studies in Geology, 11, 166 p.

WU, J., and MEREU, R.F. 1988. Crustal models of the Kapuskasing Structural Zone: Results from the 1984 seismic refraction experiment. *In* Lithoprobe Workshop, KSZ 88, University of Toronto, pp. 127-140.

YUNSHENG, S., STRANGWAY, D.W., and URQUHART, W.E.S. 1985. Geological interpretation of a high resolution aeromagnetic survey in the Amos-Barraute area of Quebec. *In* The Utility of Regional Gravity and Magnetic Anomaly Maps. *Edited by* W.J. Hinze, Society of Exploration Geophysicists, pp. 413-425.

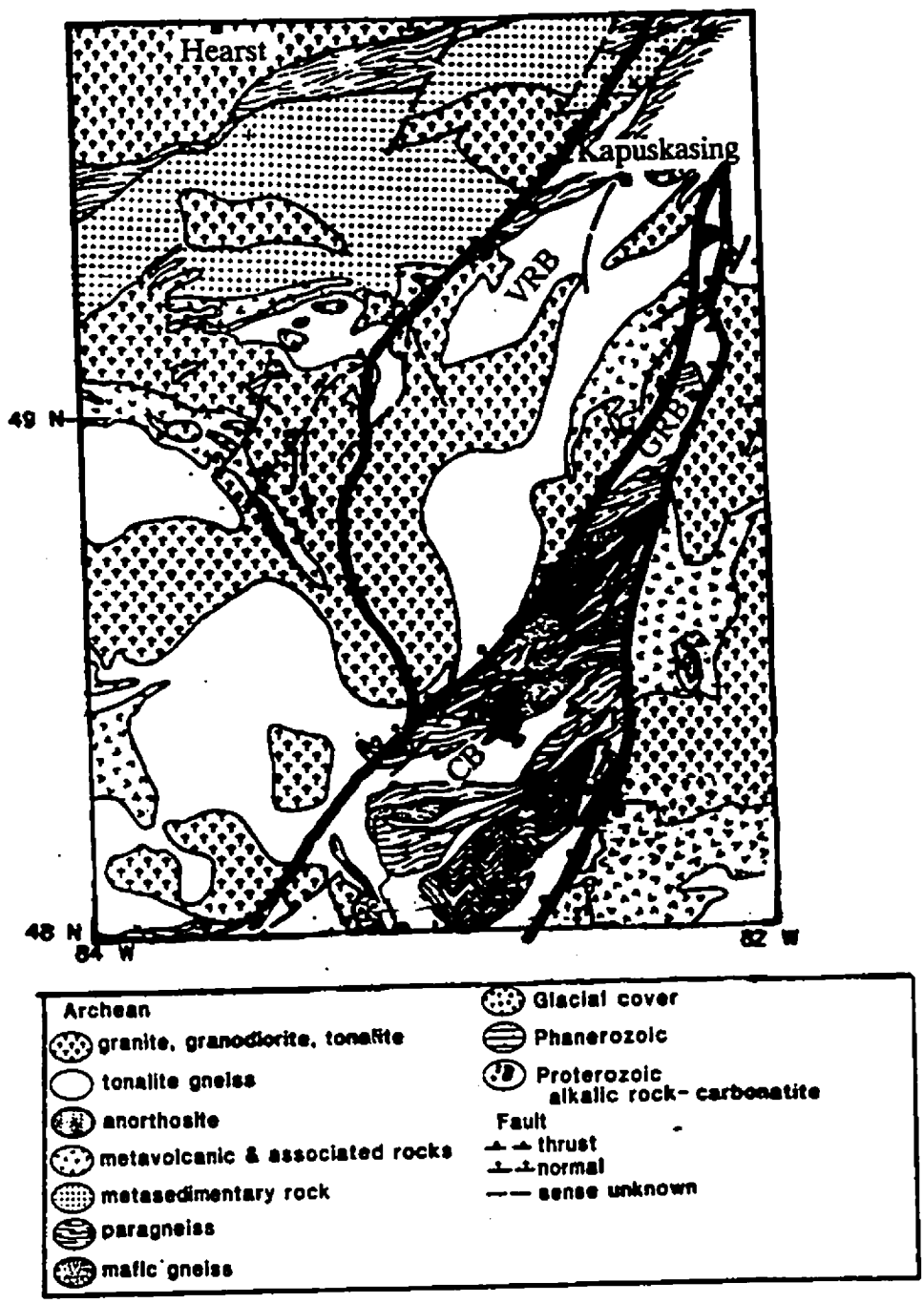

Figure 4-7. Geology map of the CB, GRB and VRB of the KSZ (adapted from Percival, 1990). Areas outlined in red indicate the block boundaries.

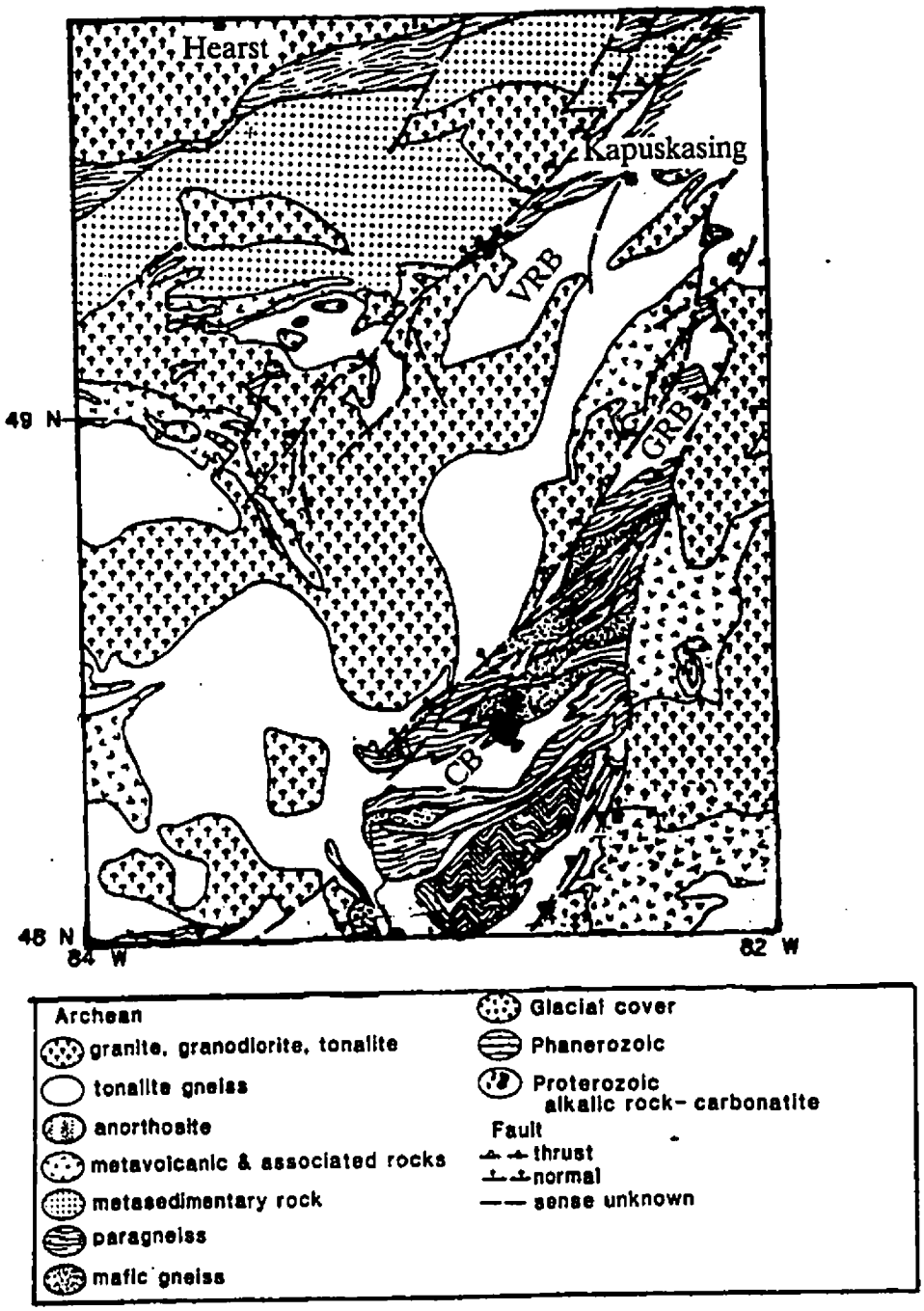

Figure 4-7. Geology map of the CB, GRB and VRB of the KSZ (adapted from Percival, 1990). Areas outlined in red indicate the block boundaries.